N° d'ordre : 40628

THESIS

Submitted to

Université Lille 1- Sciences et Technologies

by

Chaithanya D. Jain

For obtaining the PhD degree of the

Doctoral School SMRE: Sciences de la Matière, du Rayonnement et de l'Environnement

Laser photolysis coupled to detection by LIF and cw-CRDS: Application to spectroscopic and kinetic studies of OH, HO_2 and HONO

Defended on 20th October 2011

Jury committee

1. Dr. Christa Fittschen Research Director, CNRS, Université Lille 1 – Sciences et Technologies, France.	Thesis supervisor
2. Dr. Abdelwahid Mellouki Research Director, CNRS/ICARE, Orleans, France.	Referee
3. Dr. Ondřej Votava Research Director, J. Heyrovský Institute of Physical Chemistry Academy of Sciences of the Czech Republic, Prague.	Referee
4. Prof. Jean François Pauwels PC2A, Université Lille 1 – Sciences et Technologies, France.	Examiner
5. Dr. Brabara Noziere Researcher, IRCELYELYON/CNRS, Lyon, France.	Examiner
6. Dr. Birger Bohn Researcher, Institut für Energie- und Klimaforschung Forschungszentrum Jülich GmbH, Germany.	Examiner

To my beloved parents

for their everlasting love and support …

Abstract

OH and HO_2 radicals play a vital role in many oxidation processes in the atmosphere. The degradation of volatile organic compounds under tropospheric conditions is generally induced by the reaction with hydroxyl radicals, followed by reaction with oxygen. This thesis involved the study of the mechanisms and reaction pathways of some of these reactions using an experimental system of laser photolysis coupled to Laser Induced Fluorescence (LIF, for OH) and continuous wave Cavity Ring-Down Spectroscopy (cw-CRDS, for HO_2) detection techniques. The coupling of these detection techniques allowed studying the simultaneous, time resolved kinetics of OH and HO_2 radicals and spectroscopic measurements for different species by the cw-CRDS technique.

Different chemical systems studied using the above experimental technique include: 1) kinetics of the reaction of OH radicals with CH_3OH and CD_3OD, 2) HO_2 yield in the OH-initiated oxidation of SO_2, 3) an energy dependence study on the direct formation of HO_2 radicals from the photoexcitation (at 248 nm) of various aromatic hydrocarbons (benzene, toluene, xylene or mesitylene) in the presence of oxygen. In addition the spectroscopic application of the cw-CRDS technique has been used to measure the absorption cross-sections of selected absorption lines of H_2O_2, HONO, HO_2 and DO_2 in the near infrared region.

Keywords: Atmospheric chemistry – Radicals – Hydroxyl – Laser Induced Fluorescence – Flash Photolysis – Hydroperoxyl – CRD spectroscopy

Résumé

Les radicaux OH et HO_2 jouent un rôle essentiel dans beaucoup de processus d'oxydation dans l'atmosphère. La dégradation d'espèces chimiques dans les conditions troposphériques est généralement initiée par la réaction avec les radicaux OH, suivie par la réaction avec l'oxygène. Dans le cadre de cette thèse, deux techniques optiques de détection d'OH et HO_2 ont été appliquée à des études cinétiques et spectroscopiques. Pour cela, nous utilisons un système expérimental de photolyse laser couplée à des techniques de détection par continuous wave Cavity Ring-Down Spectroscopy (cw-CRDS, pour HO_2) et Fluorescence Induite par Laser (FIL, pour OH). Ce couplage permet de mesurer les cinétiques des radicaux OH et HO_2 simultanément, résolues dans le temps pour l'étude des mécanismes réactionnels.

Différents systèmes chimiques ont été étudiés en utilisant ce dispositif expérimental: 1) les cinétiques de la réaction d'OH avec CH_3OH et CD_3OD, 2) le rendement de HO_2 dans l'oxydation de SO_2 initiée par OH et 3) la formation des radicaux HO_2 par photoexcitation (à 248 nm) de différents hydrocarbures aromatiques (benzène, toluène, xylene ou mésitylène) en présence d'oxygène. Des applications spectroscopiques de la cw-CRDS pour mesurer les sections efficaces de H_2O_2, HONO, HO_2 et DO_2 dans le proche Infrarouge ont également été réalisées.

Mots-clefs : Chimie de l'atmosphère - Radicaux (Chimie) – Hydroxyle - Fluorescence Induite par Laser - Photolyse éclaire- Hydropéroxyle - Spectroscopie CRDS

Acknowledgements

I would like to start thanking my thesis supervisor, Dr. Christa Fittschen, for her support, patience and wise supervision during the preparation of this thesis. I owe her my profound admiration and respect.

Many thanks to Prof. Jean-François Pauwels, director of PC2A, and all other colleagues, who always gave me the encouragement to seek this Ph.D.

My sincere thanks to the referees and examiners of my thesis Dr. Abdelwahid Mellouki, Dr. Barbara Noziere, Dr. Birger Bohn for their invaluable time spent in reading my thesis and writing the report.

I would like to sincerely acknowledge Dr. Alexander Parker and Dr. Coralie Schoemaecker for their guidance, collaboration and encouragement at different stages of this work.

My sincere thanks to Dr. Ondřej Votava, J. Heyrovský Institute of Physical Chemistry, Academy of Sciences of the Czech Republic, Prague for being one of the referees and also for his invaluable guidance and technical support to improve the experimental technique used in this thesis.

I owe my sincere thanks to all the other members of my team for their everlasting help and support throughout my stay here. They truly deserve this as they made my life a lot easier here.

I would like to acknowledge European Union *via* Marie Curie EST, IRENI, CNRS and Nord Pas Calais region, France for providing the financial support for this thesis and their continuous contribution to the development of science, technology and higher education in France.

I would like to conclude by thanking my parents, Dharmaraja Jain and Poornima Jain, all my friends and relatives, for their everlasting love and support during my work.

Thank you again…

Contents

List of Figures

Abbreviations

AOM	**A**cousto **O**ptic **M**odulator
CRDS	**C**avity **R**ing-**D**own **S**pectroscopy
cw-CRDS	**c**ontinuous **w**ave **C**avity **R**ing-**D**own **S**pectroscopy
CPM	**C**hannel **P**hoton **M**ultiplier
cm^3	**c**ubic **c**entimetre
DFB	**D**istributed **F**eed **B**ack
FT	**F**ree **T**roposphere
FSR	**F**ree **S**pectral **R**ange
GPIB	**G**eneral **P**urpose **I**nterface **B**us
Hz	**H**ert**z**
IR	**I**nfra-**R**ed
LIF	**L**aser **I**nduced **F**luorescence
MFC	**M**ass **F**low **C**ontroller
NIR	**N**ear **I**nfra-**R**ed
nm	**n**ano**m**etre
PBL	**P**lanatory **B**ounday **L**ayer
PC	**P**ersonal **C**omputer
PCI	**P**eripheral **C**omponent **I**nterconnect
PMT	**P**hoto-**M**ul**T**iplier
PZT	**P**ie**Z**o **T**ransducer
ppbv	**p**arts **p**er **b**illion by **v**olume
ppmv	**p**arts **p**er **m**illion by **v**olume
pptv	**p**arts **p**er **t**rillion by **v**olume
PFO	**P**seudo **F**irst **O**rder
sccm	**s**tandard **c**ubic **c**entimetre per **m**inute
TDLAS	**T**unable **D**iode **L**aser **A**bsorption **S**pectrometer
TMB	1,3,5-**t**ri**m**ethyl**b**enzene
UV	**U**ltra **V**iolet
VOC	**V**olatile **O**rganic **C**ompound
YAG	**Y**ttrium **A**luminium **G**arnet

Chapter 1 - Introduction

This thesis describes a study of two radical intermediates OH and HO_2 which play a vital role in atmospheric chemical oxidation processes. Two well known techniques, laser induced fluorescence (LIF) and continuous wave cavity ring-down spectroscopy (cw-CRDS) coupled to a laser photolysis reactor have been used as the measurement tools for the kinetic measurements of OH and HO_2 radical intermediates respectively.

This introduction chapter gives a brief idea about the atmosphere, the chemistry of the atmosphere, the importance of the OH and HO_2 radical intermediates in the troposphere and a brief introduction to LIF and CRDS techniques. The following chapter 2 gives a detailed explanation about the development of the experimental technique, experimental procedures and the implementation. Chapter 3 explains the validation of the experimental technique by measuring well known rate constants. Chapter 4 describes the HO_2 radical formation from the photoexcitation of various aromatic compounds (benzene, toluene or xylene) in presence of oxygen at 248 nm. Chapter 5 gives details of spectroscopic applications of the cw-CRDS technique in the near infrared region.

1.1 The atmosphere

The atmosphere is a layer of gas surrounding the planet Earth that is retained by Earth's gravity. The word 'atmosphere' was introduced into the western languages in the course of the 17th century and comes from the Greek *"atmos"* meaning vapour and *"sphaira"* meaning ball. The atmosphere protects life on Earth by absorbing ultraviolet solar radiation, warming the surface through heat retention (greenhouse effect), and reducing temperature extremes between day and night. The atmosphere of the earth consists of a mixture of gases called air together with some particulate matter of different kinds. Dry air is composed of [1] N_2 (78%), O_2 (21%), Ar (1%). There are also trace gases like CO, CO_2, CH_4 and other volatile organic compounds (VOCs); nitrogen containing species such as NO, NO_2, NO_3, N_2O, peroxyacetylnitrate (PAN) and NH_3; sulphur species such as SO_2,

dimethylsulphide (DMS) and H_2S; and halogenated compounds such as CFCs, HCFCs, HCl, HF, CH_3Cl, CH_3Br and CH_3I. The concentration of these trace gases generally is very low and given in part per million (10^{-6}) by volume (ppmv), ppbv (10^{-9}) or pptv (10^{-12}). These trace gases originate from both natural and anthropogenic sources. Natural processes which produce trace gases include emissions from plants and trees, volcanic eruptions, thunderstorms, natural fires, and biological processes. Anthropogenic origin includes human activities such as transport, agriculture, industries and household activities. Unstable reactive species like ions, atoms and radicals are also present in very small concentrations. In addition there is a variable concentration of water vapour ranging from less than 1% to 4% [1]. Small particles in suspension are present throughout the atmosphere in the form of clouds and aerosols. Their sizes range from a few nm to some µm [1]. Clouds are mostly made up of water droplets or small ice particles. Atmospheric aerosols can be either primary (emitted directly to the atmosphere) or secondary (formed during the transformation of chemical species in the atmosphere). Typical primary aerosols are dust, sea salt, volcanic ashes or soot. Sulphuric acid, sulphates, nitrates, organic matter and biogenic VOCs are the typical precursors for secondary aerosols [1].

1.2 Structure of the atmosphere

The Earth's atmosphere is by no means uniform in composition, with varying temperature and pressure from the Earth's surface to altitudes in excess of 100 km. The partitioning of the atmosphere into different regions is based on the temperature profile as seen Figure 1.

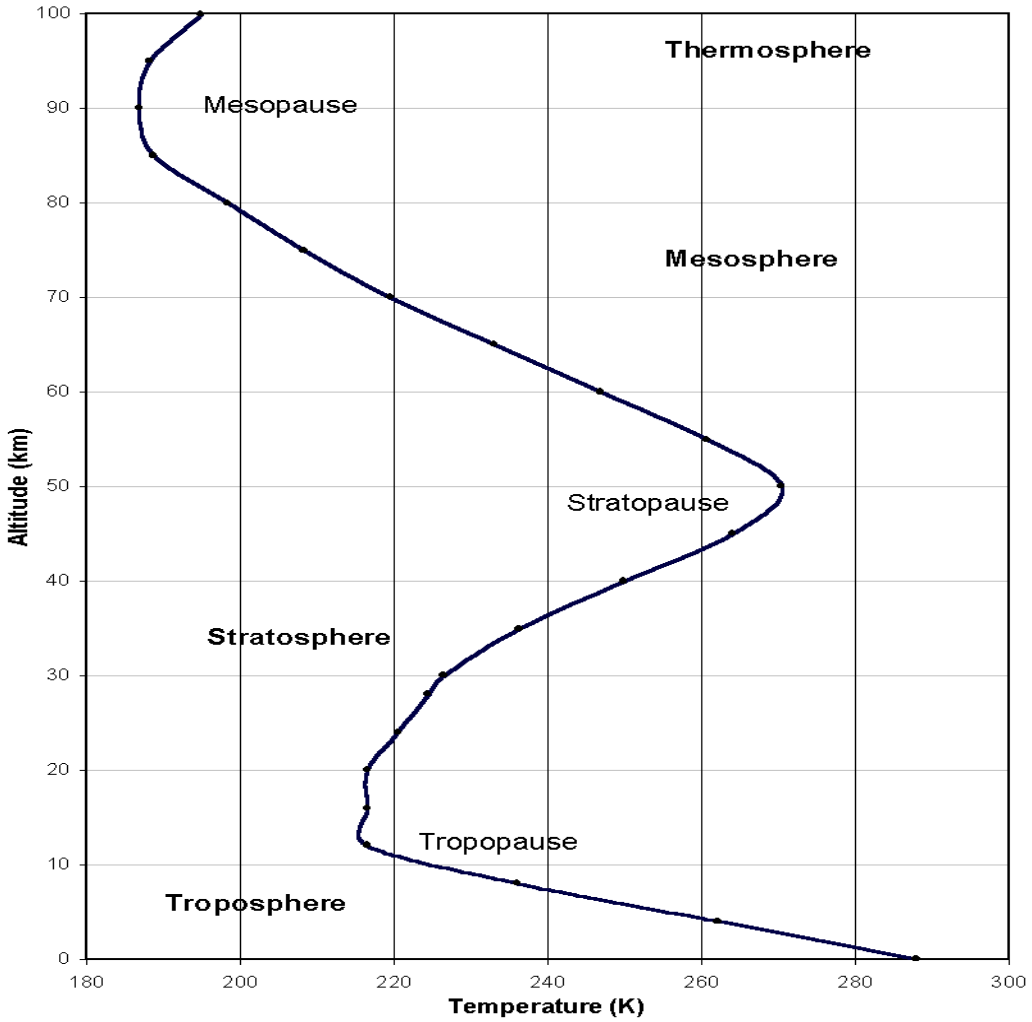

Figure 1: The temperature structure of the atmosphere. Temperatures show a complex dependence on altitude, decreasing with altitude at some heights but increasing at others. The turning points of the temperature gradient mark the boundaries between regions of the atmosphere [1]**.**

The different layers of the atmosphere are:

1.2.1 Troposphere

Troposphere ranges from 0 to approximately 9-15 km depending on the latitude and contains 75% of the gases in the atmosphere [1]. The term troposphere originated from two Greek words "*tropos*" which means turning or mixing and "*Sphaira"* means ball. Troposphere is the region where we live and the day to day phenomena associated with the weather take place. As height increases, the temperature decreases in the troposphere: the temperature drop is about 6.5 K for every kilometre above the earth's surface and is termed as environmental lapse rate (ELR). This is because the atmosphere is heated from

below as Earth's surface absorbs the solar radiation and re-emits the heat, which warms the atmosphere directly above it. This effect decreases with increasing heights. As a result the gas near the Earth's surface is heated and rises due to convection. Adiabatic expansion and the cooling of air take place as it rises in the troposphere resulting the vertical mixing. This mixing allows the transport of the species from the ground to the top of the troposphere in a few days depending on the weather conditions in the troposphere.

The troposphere may be subdivided into two regions, the planetary boundary layer (PBL) and the free troposphere (FT). The boundary layer is the closest region to the ground and reaches up to 0.5 – 2 km (less at night). This is the region of the atmosphere which is directly affected by the surface of the Earth. Turbulent mixing resulting from the radiative heating by the ground and increased deposition due to repeated contact of air masses with the ground are characteristics of PBL. PBL has a vital impact on the atmospheric composition as the majority of trace species are released from the planetary surface. The air masses in the PBL do not undergo an extensive transport as in the free troposphere; the short-lived species tend to be transformed in the area in which they were released.

The temperature change with height through the troposphere towards the stratosphere comes across a region called **tropopause**. This layer forms a boundary layer between troposphere and stratosphere where the environmental lapse rate changes from negative to positive. Beyond the tropopause is the stratosphere where temperature increases with altitude.

1.2.2 Stratosphere

The region from approximately 15 up to 50 km is called stratosphere. In the stratosphere the temperature increases with the altitude due to the absorption of UV radiation in a series of exothermic reactions involved in the formation and destruction of the ozone. As a result less and less UV light passes to the lower levels of the stratosphere creating layers with different temperatures. This brings the name stratosphere where the stratification of the temperature occurs. In the stratosphere the horizontal mixing of gaseous components proceeds much more rapidly than the vertical due to lack of convection [1]. The top of the stratosphere is called the **stratopause** which has a temperature of about 270 K. Beyond the stratopause the temperature decreases with height. The stratopause is the

boundary between the stratosphere and mesosphere and is approximately 50 to 55 km above the Earth's surface.

1.2.3 Mesosphere

The mesosphere extends from the stratopause up to 80–85 km. The temperature decreases with increasing altitude, due to decrease in the concentrations of oxygen and ozone (and thus less UV absorption). The temperature minimum at the boundary between the mesosphere and the thermosphere is called **mesopause**. The temperature in the mesopause drops to about 170 K making the coldest region of the atmosphere.

1.2.4 Thermosphere

80 km and up is the thermosphere. The temperature rises again due to the ionisation of the gas molecules by the absorption of short wavelength ($\lambda < 200$ nm) UV rays. This layer contains:

Ionosphere - This is the lower part of the thermosphere. It extends from about 80 to 550 km. Gas particles absorb ultraviolet and X-ray radiation from the sun and become electrically charged ions.

Exosphere - the upper part of the thermosphere. It extends from about 550 km for thousands of kilometres. This is the area where satellites orbit the earth.

1.3 Chemistry of the atmosphere

The chemistry of the atmosphere is very complex, which is a result of the many thousands of chemical species emitted to the atmosphere by natural and anthropogenic sources and the innumerable reactions they undergo. In between release and removal process from the atmosphere, these species will be transported horizontally and vertically. Chemical transformation of the released species also takes place depending on their stability. Degradation of one species generates another and the process continues until they are removed through removal process. There are three removal processes. The first one is the chemical transformation in an ideal case to constituents such as H_2O or CO_2. The second is dry deposition, whereby gases are absorbed by plants, water or soil. Dry deposition is of limited significance because it only applies to gases in the

boundary layer on a local scale. The third is wet deposition or removal by precipitation, and is only effective for species that are soluble in water.

Chemical conversions in the atmosphere are largely driven, directly or indirectly, by solar ultraviolet radiation so that the atmosphere is not just a reactor, but a photochemical reactor. The chemical changes are greatly influenced by temperature and pressure which change within the atmosphere. Not only the rates of reactions, but even the pathways open for reaction and thus the products formed may depend on temperature and pressure. As a result altitude, latitude and longitude may all play a part in determining which processes occur, or at least compete successfully with alternative pathways.

In this thesis the focus is given to the tropospheric oxidation processes involving OH and HO_2 radicals. Therefore most prominent chemical processes taking place in the troposphere and related to OH and HO_2 (together called HO_x) chemistry will be discussed in the next section.

1.4 OH and HO_2 radicals in the troposphere

The chemical conversions in the troposphere are mainly driven by the OH radicals during the day time. The high reactivity of OH radicals lead to the oxidation of chemical constituents like VOCs (methane and other hydrocarbons), H_2S, SO_2 and carbon monoxide to CO_2 and H_2O. Thus, reaction with OH radicals provides an efficient chemical removal mechanism for the troposphere.

The hydroxyl radical is a short-lived radical species because of its high reactivity. The average life time of the OH radical is approximately 1 second or less [2] depending on the local concentrations of VOCs. The day time average concentration of the OH is around $1x10^6$ molecules cm^{-3} and can decrease approximately to $1x10^5$ molecules cm^{-3} during night [3].

The hydroxyl radical is generated in the troposphere by the photolysis of ozone and subsequent reaction with H_2O in the following way:

$$O_3 + h\nu\ (<310\ nm) \longrightarrow O(^1D) + O_2(a, X) \qquad \text{R-1}$$

$$O(^1D) + H_2O \longrightarrow 2\ OH \qquad \text{R-2}$$

However, most of the O (^{1}D) produced will be quenched back to ground state as below:

$$O(^1D) + M \longrightarrow O(^3P) + M \quad \text{R-3}$$

Finally all ground state O (^{3}P) atoms will recombine with oxygen to form ozone:

$$O(^3P) + O_2 + M \longrightarrow O_3 + M \quad \text{R-4}$$

In presence of NO_x (NO and NO_2) ozone reacts with NO to form NO_2.

$$NO + O_3 \longrightarrow NO_2 + O_2 \quad \text{R-5}$$

The NO_2 formed will be photolysed to produce O (^{3}P) which in turn produces ozone *via* reaction (R-4) making it the only source for ozone in the troposphere [1].

$$NO_2 + h\nu\ (<400\ nm) \longrightarrow O(^3P) + NO \quad \text{R-6}$$

Other additional pathways which generate OH in the troposphere are given below:

$$HONO + h\nu\ (350\ nm) \longrightarrow OH + NO \quad \text{R-7}$$

$$Alkenes + O_3 \longrightarrow OH \quad \text{R-8}$$

Once the OH radical is formed it will initiate the degradation of VOCs in the troposphere. Main cases involve the reaction with methane and CO. About 70% (globally) of the OH reacts with CO and 30% of the OH reacts with methane.

As an example, the general reaction pathway for the oxidation of saturated hydrocarbons in the troposphere will be explained below: Reaction with OH radical starts with the abstraction of H atoms from the C-H bond to generate the alkyl radicals.

$$OH + RH \longrightarrow R + H_2O \quad \text{R-9}$$

The alkyl radicals formed in reaction (R-9) will then react with oxygen to form the corresponding alkylperoxy radicals.

$$R + O_2 \longrightarrow RO_2 \qquad \text{R-10}$$

These RO_2 radicals will react with NO (when NO_x concentration is higher than 100 ppt [4]) to form alkoxy radicals and NO_2.

$$RO_2 + NO \longrightarrow RO + NO_2 \qquad \text{R-11}$$

NO_2 produced will be photolysed to recycle ozone *via* reactions (R-6 and R-4). The alkoxy radicals produced in reaction (R-11) upon subsequent reaction with O_2 produce HO_2 radicals.

$$RO + O_2 \longrightarrow R'O + HO_2 \qquad \text{R-12}$$

where R' = R_{-H} produced from R. Reaction (R-12) is the principal pathway that produces HO_2 radical in the troposphere. HO_2 is converted back to OH in a reaction with NO converting NO to NO_2.

$$HO_2 + NO \longrightarrow OH + NO_2 \qquad \text{R-13}$$

Thus, HO_2 also plays a key role in tropospheric oxidation processes along with OH radicals. In tropospheric regions where the NO concentrations are less than 50 ppt, the main consumption pathways [4] for the alkylperoxy radicals produced in reaction (R-10) will be as below,

$$RO_2 + HO_2 \longrightarrow ROOH + O_2 \qquad \text{R-14}$$

Figure 2 summarises the production and inter-conversion of OH and HO_2 radicals in the troposphere.

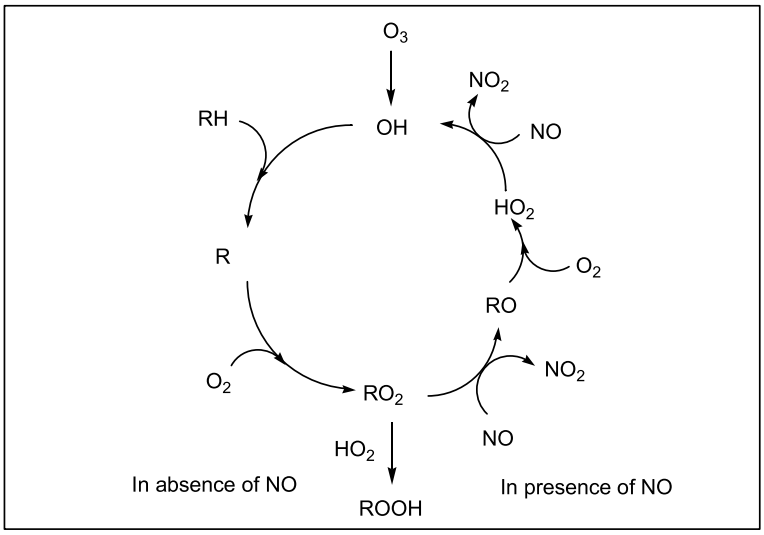

Figure 2 : Production, inter conversion and the products of OH and HO_2 radical chemistry in the atmosphere reproduced from the idea of [1].

This chain is finally terminated by the loss of HO_x in the system. This takes place by the following reactions,

$$HO_2 + HO_2 \longrightarrow H_2O_2 + O_2 \qquad \text{R-15}$$

$$RO_2 + HO_2 \longrightarrow ROOH + O_2 \qquad \text{R-14}$$

$$NO_2 + OH + M \longrightarrow HNO_3 + M \qquad \text{R-16}$$

The peroxides and HNO_3 may react with OH or removed by deposition resulting in the termination of the oxidation reaction chain.

This is a brief overview of the OH and HO_2 radical chemistry in the troposphere. In the present thesis, work has been carried out on the oxidation of SO_2 and aromatic hydrocarbons as well as spectroscopic measurements of HONO. More details on the importance of these species in the troposphere will be given before the results in chapters 3, 4 and 5 respectively.

1.5 OH and HO_2 radical detection and kinetic measurement techniques in the laboratory

As mentioned earlier atmosphere being a very complex system, it is very difficult to understand from only one type of study. Therefore, atmospheric studies are subdivided into many different areas such as meteorological studies, field

measurements, emission studies, atmospheric transport studies, deposition studies etc. In addition, laboratory kinetic measurements are also performed to measure the rate constants of the elementary reactions which will be helpful in understanding the mechanisms of atmospheric chemical conversions. The results from all the above studies are then used as the input parameters for computational chemical models to test our understanding about the atmosphere and try to reproduce the results observed during the measurements. These modelling studies can then be extended to predict climate change or the chemistry of the VOCs in the atmosphere. Therefore both field and laboratory measurements are very important in the context of atmospheric chemistry studies.

High reactivity of OH and HO_2 radicals becomes a challenge for their detection and kinetic measurements. This demands the techniques employed to have an excellent time resolution, selectivity towards these radical species and not affected significantly by interference from other species. Often the last criterion mentioned is the most difficult to achieve. There have been several methods employed successfully for the detection of OH and HO_2 radicals and their kinetic measurements in the laboratory. This section gives an overview of different detection and kinetic measurement techniques used in the laboratory for the study of OH and HO_2 radicals.

1.5.1 Experimental methods for kinetic measurements

Some of the common experimental methods used to measure kinetic data will be discussed here. Different detection techniques which can be coupled with these methods to detect OH and HO_2 radicals will be discussed separately in section 1.5.2.

Discharge Flow technique

In this technique the radical species are produced continuously with electric or microwave discharge within a fast flow system [5, 6]. These radicals are then highly diluted in the bath gas, flow at high speed (by pumping) along a reactor designed to allow the addition of reactants downstream. Different reaction times between the reactant and the radicals are achieved by adding the reactant to the flow tube at different distances through a movable injector. The radical concentration is detected at the end of the reactor. This results in a time resolved kinetic measurement. The reactant concentration is generally maintained in large

excess compared to the radical concentration in order to have pseudo first order conditions.

Flash photolysis method

This technique was first reported in 1949 by Norrish and Porter [7], since then it has been readily adopted to measure pulsed OH and HO_2 radical kinetics [8, 9]. The radicals are generated on a short time scale compared to the reaction time. This can be on a nanosecond time scale in case of laser flash photolysis or on a millisecond time scale if UV lamp is used. In-situ radical generation is achieved by the photo-dissociation of species such as H_2O, nitrous acid (HONO) or hydrogen peroxide (H_2O_2) by UV light [10, 11] for OH radicals and H_2O_2 or Cl_2 in presence of formaldehyde or H_2 [12] for HO_2 radicals. The gas mixture in the reactor contains the reactant species together with the radical precursor and thus allowing the in-situ generated radicals to react with the reactant. This is the technique used to measure OH and HO_2 radical kinetics in the present work.

Relative rate technique

This technique is based on monitoring the decays of two or more reactants [13] simultaneously. The difference in the decay rate of the reactant under investigation is compared to the decay rate of the reference compound following reaction with OH or HO_2.

$$\text{OH or } HO_2 + \text{Reactant} \longrightarrow \text{Products} \qquad \text{R-17}$$

$$\text{OH or } HO_2 + \text{Reference} \longrightarrow \text{Products} \qquad \text{R-18}$$

Rate laws for the reactions (R-18 and R-19) can be written as

$$\frac{-\mathrm{d}[\mathrm{Reactant}]}{\mathrm{dt}} = \mathrm{k}_{18}[\mathrm{Radical}][\mathrm{Reactant}] \qquad \text{E-1}$$

$$\frac{-\mathrm{d}[\mathrm{Refernce}]}{\mathrm{dt}} = \mathrm{k}_{19}[\mathrm{Radical}][\mathrm{Reference}] \qquad \text{E-2}$$

Integration and combination of the equations (E-1 and E-2) leads to the equation as given below:

$$\ln\left\{\frac{[\mathrm{Reactant}]_{t0}}{[\mathrm{Reactant}]_t}\right\} = \frac{k_{18}}{k_{19}}\left[\ln\left\{\frac{[\mathrm{Reference}]_{t0}}{[\mathrm{Reference}]_t}\right\}\right] \qquad \text{E-3}$$

where, t=time, k_{18} = rate constant of the reaction (R-18) and k_{19} = rate constant of the reaction (R-19). A plot of $\ln\{[Reactant]_{t0}/[Reactant]_t\}$ against $\ln\{[Reference]_{to}/[Reference]_t$ should give a straight line with the slope being k_{18}/k_{19} and an intercept of zero. The rate constant k_{18} can be then calculated from the slope using the known rate constant for the reference reaction (R-19). The disadvantage of this method is the uncertainty in the rate constant of the reference reaction. This experimental technique is generally used in simulation chambers for kinetic measurements [14, 15].

1.5.2 Detection techniques for OH and HO_2 radicals

There are several techniques available to detect OH and HO_2 radicals. These detection techniques can either be used to measure the atmospheric concentrations (atmospheric measurements [2]) or coupled with one of the experimental methods explained in section 1.5.1 to measure kinetics (laboratory measurements). The detection techniques for OH and HO_2 can be broadly divided into spectroscopic and non spectroscopic techniques. The selection of a particular detection technique depends on the chemistry, conditions and the availability of the resources. Following section describes some of the common spectroscopic and non spectroscopic techniques for OH and HO_2 radical detection.

1.5.2.1 Spectroscopic techniques

Spectroscopy is the use of interaction between a radiation and atoms, molecules or radicals to study them qualitatively or quantitatively. This interaction can cause absorption followed by light emission or other energy transfer processes. The absorption of light by a species can probe the species to a higher energy state called excited state. The energy absorbed by the species can be released by light emission at different wavelengths (fluorescence, phosphorescence) or at the same wavelength (scattering). When species absorb light, the incoming energy excites the species to a higher energy level. The type of excitation depends on the wavelength of the light. Electrons are promoted to higher orbital by ultraviolet or visible light, vibrations are excited by infrared light, and rotations are excited by microwaves. An absorption spectrum is the measurement of the absorption of light by a species as a function of wavelength. The absorption spectrum of an atom or molecule depends on its energy level structure, and absorption spectra are useful for identification of the species. Calculation of the

concentration of an absorbing species in a sample is accomplished by applying the Beer-Lambert Law. For low concentration absorptions if I_0 is the intensity of incident beam and I is the intensity of transmitted beam, then the intensity of transmitted beam is given by:

$$I = I_0 \exp(-\alpha l) \qquad \text{E-4}$$

where l=the length of the sample and α= absorption co-efficient of the sample. In case of the absorption caused by a single species then α can be replaced by $\alpha=\sigma N$ where σ=absorption cross-section and N=number density (molecules/unit volume) of the absorbing species.

Species that are excited to high energy levels can decay to lower levels by emitting radiation (emission or luminescence). It is called fluorescence if the transition is between states of the same spin and phosphorescence if the transition occurs between states of different spin. The emission intensity of an emitting substance is linearly proportional to analyte concentration at low concentrations, and can be used for quantification of emitting species. Following section briefly describes some of the common spectroscopic techniques used for the OH and HO_2 detection. More detailed explanation on Laser Induced Fluorescence (LIF) technique and continuous wave Cavity Ring-Down Spectroscopy (cw-CRDS) which are used to detect OH and HO_2 respectively in the present work will be given in sections 1.6 and 1.7.

Spectroscopy in the UV region

Common absorption spectroscopic techniques for OH and HO_2 detection which use the light in the UV region are:

Resonance Absorption (RA) technique (for OH)

This technique is based on absorption spectroscopy [16] and is used to detect OH radicals. In this case the light source consists of the fluorescence emission of OH radicals generated by electric or microwave discharge of H_2O-argon mixture, hence the name “resonance” absorption. The attenuation of the emitted OH radiation in the reactor is proportional to the OH radical concentration. This technique is selective, sensitive and inexpensive. The disadvantage is it is specific for one particular species.

Resonance Fluorescence (RF) technique (for OH)

This technique is based on the absorption emission spectroscopy and is used for the OH detection. It is similar to that of resonance absorption; the only difference is that fluorescence emission of OH radicals is measured following the excitation using the resonance lamp [17–19]. The OH radiation from an electric or microwave discharge of H_2O-argon mixture at low pressure is aligned to the detection cell. Such resonance lamp radiation emits rotational lines of various branches of the (0-0) band, $A^2\Sigma^+$-$X^2\pi$. The OH radicals are excited from the ground electronic state (S_0) to the first excited electronic state (S_1) using OH radiation. When the excited state OH radicals relax back to the ground electronic state, the excess energy is emitted in the form of fluorescence. A typical resonance fluorescence experiment consists of a microwave or electric discharge set up which emits the OH radiation, optical set up to align the beam into the detection cell, fluorescence collection optics and a photo detector. The fluorescence collected around 308 nm is collected in the A-X, 0-0 band using an interference filter will provide the OH radical concentration (calibration is required in the same conditions with a known concentration of OH if absolute concentration needs to be measured).

Direct UV absorption spectroscopy (for OH and HO_2)

UV absorption spectroscopy is the commonly used tool to detect HO_2. This technique uses the UV source (UV lamp). The intensity of the light with and without the sample and the ratio gives the transmittance. HO_2 radicals undergo electronic transitions by absorbing the UV light and the absorption on a specific wavelength is measured. However, HO_2 has a broad absorption spectrum in the UV region with absorption maximum at 205 nm ($\sigma_{205\ nm}$=4.65x10^{-18}cm^2 molecule^{-1} [20]) which can cause problems concerning the selectivity of the detection.

This technique can also be used to detect OH radicals. For OH detection source is a continuous wave UV laser, tuned to a transition of the OH radical (308 or 282 nm in general). The OH concentration monitoring is done by the time resolved long path absorption of OH on one of the rotational lines [21]. This technique is selective and sensitive. The disadvantage is laser emission bandwidth has to be adapted to the species under investigation and expensive.

Absorption spectroscopy in the IR region

Common absorption spectroscopic techniques which use light in the IR region are:

FT-IR spectroscopy (for HO_2)

This is an absorption spectroscopic technique which uses the infrared region of the electromagnetic spectrum and commonly used for the HO_2 detection. The source emits broad band infrared radiation. The IR radiation then passes through an interferometer which modulates the infrared radiation. The modulated IR beam passes through the sample (HO_2 in this case) where it is absorbed to various extents at different wavelengths. The transmitted intensity of the IR beam is then processed and Fourier transformed [22] (and hence the name FT-IR) to get the IR spectrum of the sample. This technique offers a number of advantages such as speed, broadband emission resulting the full range spectrum and improved data processing. Disadvantages include sensitivity and difficulty in obtaining the time resolved absorption spectrum with slow repetition rate which limits the use in kinetics.

Direct IR absorption spectroscopy (for OH and HO_2)

Near infrared and mid infrared region can also be used for the direct detection of OH [23–25] and HO_2 [26, 27] absorption. These techniques use ro-vibrational bands of OH and HO_2 radicals for the detection. Cavity enhanced methods like cw-CRDS (explained in details in section 1.7.4) in the near infrared region can also be used for the OH detection.

Wavelength modulation spectroscopy (for HO_2)

Tunable diode lasers in the near infrared region are used for the detection of HO_2 by wavelength modulation spectroscopy [28, 29]. In this technique the wavelength of a laser is modulated at a frequency *F* by sinusoidally modulating the input current of the laser diode. The Fourier analysis of the transmitted light power shows signal components at *F*, *2F*, *3F* etc. As a result, the wavelength modulated side (second harmonic) bands are widely separated and the detection of the HO_2 can be done on a single isolated sideband. The detector output is processed by a lock in-amplifier on a single component of the output signal where the HO_2

absorption is measured. The technique is very selective and sensitive but the low intensity of the sidebands cause problems for high concentrations.

1.5.2.2 Non spectroscopic techniques

Some of the common non spectroscopic techniques used for OH and HO_2 detection are given below:

Mass Spectrometry (for OH and HO_2)

This technique measures the mass-to-charge ratio of charged species and commonly used for OH detection. The principle consists of ionizing the chemical compound in order to generate a charged molecule or molecular fragments [30]. The ionised sample is then sorted according to its mass to charge ratio by a mass analyser. Separated charged particles are finally detected by a detector and the ion signal is processed into a mass spectrum.

A mass spectrometer can be used to detect OH radical directly [31] or indirectly through Chemical Ionisation Mass Spectrometry (CIMS). CIMS is an indirect measurement of OH radicals which uses chemical, rather than optical properties of OH radical and was first developed at Georgia Tech in 1989 [32] as a tool for quantitative atmospheric OH measurements. In this technique the OH is titrated into isotopically labelled $H_2{}^{34}SO_4$ that can be readily ionised and detected by selected-ion mass spectrometry.

$$OH + {}^{34}SO_2 + M \longrightarrow H^{34}SO_3 + M \qquad \text{R-19}$$

$$H^{34}SO_3 + O_2 \longrightarrow {}^{34}SO_3 + HO_2 \qquad \text{R-20}$$

$${}^{34}SO_3{}^{+} H_2O + M \longrightarrow H_2{}^{34}SO_4 + M \qquad \text{R-21}$$

$^{34}SO_2$ is added in excess to make sure the complete conversion of OH into $H^{34}SO_3$. The resulting $H_2{}^{34}SO_4$ is ionized by charge transfer reactions with NO_3^- ions produced from HNO_3. NO_3^- ions are in the form of clusters of $NO_3^-{\cdot}HNO_3$ and react with $H_2{}^{34}SO_4$ in the following way.

$$NO_3^-\ \ HNO_3 + H_2{}^{34}SO_4 \longrightarrow H^{34}SO_4^-\ \ HNO_3 + HNO_3 \qquad \text{R-22}$$

$H^{34}SO4^-{\cdot}HNO_3$ clusters are fragmented into HNO_3 and $H^{34}SO_4^-$ in a collisional dissociation chamber and the $NO_3^-/H^{34}SO_4$ ratio is measured by mass spectrometer which provides a measure of $[H_2{}^{34}SO_4]$ and hence [OH]. HO_2 can

also be detected using this technique where first HO_2 is converted to OH by the reaction with NO (R-13) and then the OH is titrated in the same procedure explained above. This technique is very sensitive and selective but needs calibration.

Electronic Spin Resonance (ESR) technique (for OH and HO_2)

This technique is used to detect chemical species that have one or more unpaired electrons [33]. These species exhibit the paramagnetism due to the presence of unpaired electrons. If an external magnetic field is applied, the interaction with an electron spin depends upon the magnetic moment associated with the spin; it can be either parallel or antiparallel. This provides a magnetic potential energy which splits the spin states by an amount proportional to the external magnetic field (Zeeman Effect). Transitions can be induced between spin states by supplying electromagnetic energy, usually in the microwave range of frequencies. The resulting absorption spectra are described as electron spin resonance (ESR) or electron paramagnetic resonance (EPR). The OH [34–36] HO_2 [37, 38] radicals have an unpaired electron and can thus be detected using ESR spectroscopy. The disadvantage of this method is the long measurement time which makes this technique not suitable for fast kinetic measurements.

Laser Magnetic Resonance (LMR) technique (for OH and HO_2)

The basic principle is similar to that of ESR technique unlike it uses a laser radiation in the far infrared region instead of microwave region to induce the transitions between the two spin levels [29, 41 and 42]. This technique can be used to detect OH and HO_2 [41]. Absorption is accomplished by tuning the molecule into resonance with the fixed frequency of a far infrared laser by means of a magnetic field. The absorption cell in an electro magnet is placed in the far infrared laser cavity and the laser beam passes through the cell to a detector. The common detector used is a liquid helium cooled germanium bolometer. The magnetic field is modulated in order to extract the absorption signal using the phase sensitive detection. The intensity of the signal is proportional to the concentration of the OH radicals. This technique is very sensitive and selective but at high concentrations the intensity will go down due to absorption and caused problem for the laser action.

Table 1 lists a comparison of different methods used for OH and HO_2 detection.

Type and Range	**Technique**	**Species**	**Detection limit (radicals cm^{-3})**	**Advantages**	**Drawbacks**
Spectroscopic techniques in the UV region	Resonance absorption	OH	~ 6×10^{11} [16]	Inexpensive, selective and sensitive	Specific for a given species
	Resonance fluorescence	OH	3×10^{8} [42]	Selective and sensitive	Calibration, specific for a given species
	Direct absorption	OH HO_2	OH: ~ 5×10^{11} [43] HO_2: ~ 1×10^{12} [44]	Direct, simple	Selectivity
	LIF	OH	1×10^{6} [45]	Selective, sensitive, good temporal resolution	Calibration, interference
Spectroscopic Techniques in the IR region	FTIR	HO_2		Broad band, full range spectrum	Moderate sensitivity, limited time resolved applications
	Direct absorption	OH HO_2	OH: ~2×10^{13} [23] HO_2: 4×10^{12} [27]	Selective, direct, simple	Moderate sensitivity, low intensity
	Wavelength modulation	HO_2	2×10^{11} [46]	Selective, direct	Low Intensity, moderate sensitivity
	cw-CRDS	OH HO_2	OH: 1×10^{11} [47] HO_2: 3×10^{9} [48]	Sensitive and selective	Low pressure operation, low intensity overtone absorption
Non spectroscopic techniques	Mass spectrometry	OH HO_2	OH: 1×10^{5} [2] HO_2: 2×10^{5} [2]	Selective and sensitive	Sampling, calibration, expensive, bulky
	ESR	OH HO_2	OH: 5×10^{5}/30 min[2] HO_2: 2×10^{7}/30 min[2]	Selective and sensitive	Complicated, large uncertainties, long measurement time
	LMR	OH HO_2	OH: ~1×10^{7}[49] HO_2: ~8×10^{7}[49]	Selective and sensitive	Intensity problem at high concentrations

Table 1: Comparison of different methods used for OH and HO_2 detection

1.6 Laser Induced Fluorescence (LIF) technique

In the present work a laser photolysis reactor coupled to Laser Induced Fluorescence (LIF) is used for the time resolved OH radical kinetic measurements. The important features of this experimental system are explained in chapter-2 and only the principle of LIF is explained here. Laser Induced fluorescence spectroscopy used for the OH detection is based on absorption emission spectroscopy and is well known for its sensitivity and selectivity.

The principle of LIF includes excitation of the target species from the ground electronic state (S_0) to the higher electronic state or excited state (S_1). The photon required for the excitation is emitted by a laser. There are different ways of relaxation for a molecule in its excited state (S_1). This can be summarized by the Jablonski diagram shown in Figure 3.

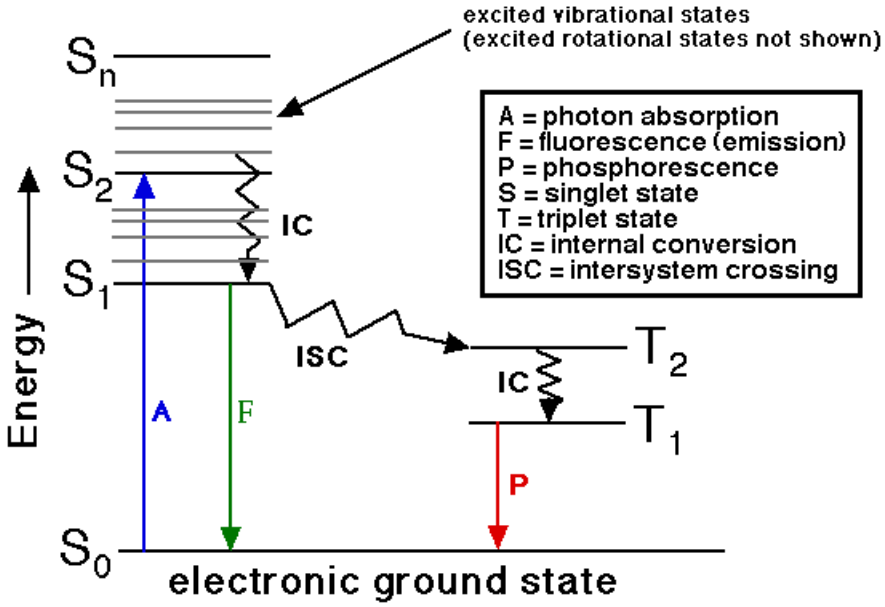

Figure 3: Jablonski diagram.

If the photon emission occurs between states of the same spin state (e.g. S_1 --> S_0 shown as green arrow pointing downwards in Figure 3) this is termed fluorescence. If the excited electron undergoes intersystem crossing which results in different spin states of the initial and final energy levels (e.g. T_1 --> S_0 shown as red arrow pointing downwards in Figure 3), the emission is called phosphorescence. The lifetimes of fluorescent states are generally very short (10^{-5} to 10^{-8} s) and phosphorescence somewhat longer (10^{-4} s to minutes). There are three non-

radiative deactivation processes which are significant: Internal conversion (IC), intersystem crossing (ISC) and vibrational relaxation. Internal conversion is the radiationless transition between electronic states of the same spin state. Intersystem crossing is a radiationless transition between different spin states. Vibrational relaxation is the relaxation from the higher vibrational level to the lower vibrational level within the same energy vibrational excited state.

In the present work, OH is excited in the (1-0) vibrational band of the A-X electronic transition near 282 nm, followed by detection of the red shifted fluorescence near 310 nm (1-1 and 0-0 A-X transitions). A schematic diagram of the LIF principle for OH detection is given in Figure 4, shows the typical transitions including excitation, relaxation through vibrational energy transfer and fluorescence.

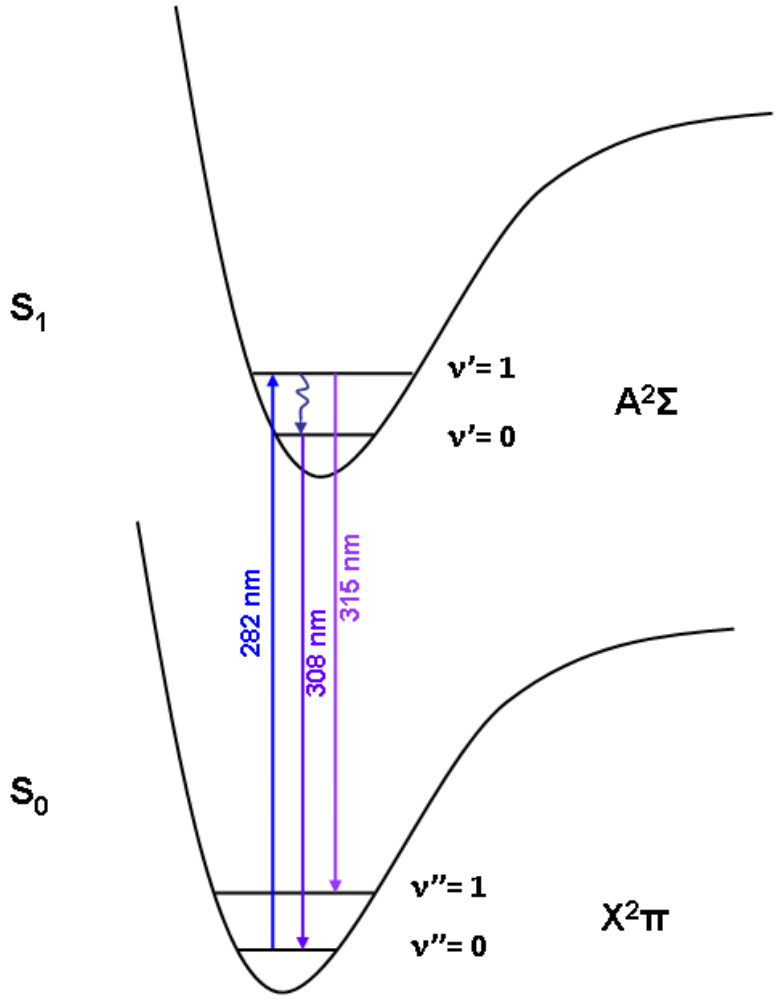

Figure 4: The principle of LIF technique for OH radical (excitation at 282 nm)

The fluorescence intensity observed is proportional to different parameters and can be given as:

$$I_{LIF} \propto G\theta_{21}\sigma[C]I_{laser} \quad \text{E-5}$$

where, I_{LIF} = intensity of the fluorescence signal, G = light collection efficiency, θ_{21} = fluorescence quantum yield, σ= absorption cross-section, [C] = concentration of the absorbing species and I_{laser} = laser intensity.

The fluorescence quantum yield depends on the emission and the quenching as given below.

$$\theta_{21} = \frac{A_{21}}{[A_{21} + Q + \Sigma \text{ other loss processes}]} \quad \text{E-6}$$

Where, θ_{21} = fluorescence quantum yield, A_{21} = spontaneous emission, Q= quenching and Σ other loss processes = radiationless relaxation.

LIF is commonly used as relative technique because performing quantitative fluorescence measurements of a given chemical species requires detailed knowledge about the quenching of all species present in the reaction mixture. A typical LIF setup consist of a laser as the source of light for excitation, an arrangement of optics to align the laser beam in the absorption medium, collection optics and a detector. Advantage over absorption spectroscopy is very good signal-to-noise ratio because of almost zero background which in turn leads to very high sensitivity.

1.7 Cavity Ring-Down Spectroscopy (CRDS) technique

Continuous wave Cavity Ring-Down Spectroscopy (cw-CRDS) coupled with laser photolysis reactor is used to detect HO_2 radicals in this thesis. The OH stretch overtone of the HO_2 radical around 6638 cm^{-1} is observed by cw-CRDS technique. The principle of the CRDS spectroscopy is explained in this section and the detailed explanation of the technique used in the present thesis will be explained in chapter-2.

Cavity Ring-Down (CRD) spectroscopy is a cavity enhanced absorption technique which can be performed with pulsed or continuous light sources. The CRDS was pioneered by O'Keefe and Deacon in 1988 [50]. This technique measures the light leaking out of the cavity consisting of two ultra reflective (better than 99.99% reflectivity) mirrors.

1.7.1 Optical cavity

An optical cavity, often called an optical resonator, is an arrangement of optical components to allow a light beam to circulate in a closed path. These optical cavities can be constructed in different ways [51]. There are two basic types available:

a) Linear (or standing wave) cavities, where light makes the round trip between two highly reflective end mirrors. When the light is circulating continuously between the two mirrors there are always counter propagating waves, which interfere with each other to form a standing-wave pattern and hence the name standing wave cavity.

b) Ring cavities, where the light makes round trip in different directions with mirrors placed at different angles. These cavities have no end mirrors.

1.7.2 Cavity modes

Transverse intensity of the light beam changes when it propagates through free space or transparent medium inside the cavity. However, if the cavity is stable there are certain electric field amplitude distributions which are self-consistent during propagation apart from a possible loss of power after the round trip. These are called cavity modes.

These cavity modes are obtained by the approximate solutions of the wave equation valid for weak focussing (paraxial approximation [51]) considering the optical frequency, beam axis, focus position and the beam radius. These are called Hermite Gaussian modes. The intensity distribution of such a mode has *n* nodes in the horizontal direction and *m* nodes in the vertical direction. If n=m=0 then the simplest among the modes, named Gaussian mode is obtained. This mode is also called as “fundamental mode *or* axial mode” and has the highest intensity. In addition to the Gaussian modes, a cavity also has higher-order modes with more complicated intensity distributions. The distance between the two axial or fundamental modes is called free spectral range (FSR). The optical intensity distribution of such modes with *n* nodes in the horizontal direction and *m* nodes in the vertical direction are given in Figure 5.

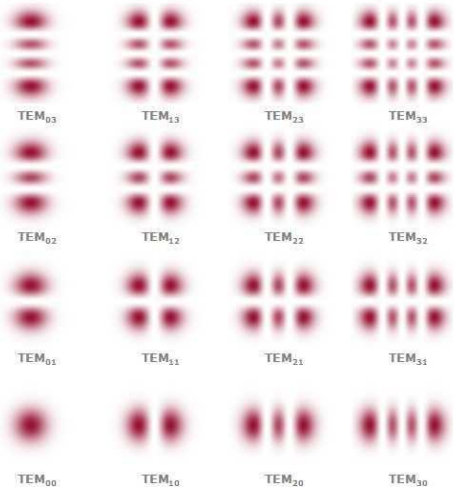

Figure 5: Intensity distributions of TEM_{nm} modes [51].

When we have an optical cavity and that cavity length obeys the relationship with the wavelength of the light emission as shown in equation (E-6) then the light inside the cavity builds up through constructive interference [50].

$$L = n\left(\frac{\lambda}{2}\right) \qquad \text{E-7}$$

where L= length of the cavity and λ= wavelength of the light emission. In other words, at least one of the cavity modes is in “resonance” with the wavelength of the light emission when the above criterion is satisfied.

1.7.3 The CRDS technique

In the CRDS light beam is aligned into the cavity and the injected light travels back and forth many times between the ultra reflective mirrors before fading out. This gives a path length of several kilometres using short cavity length. Every time the light is reflected a small fraction leaks out of the cavity, and it is this small fraction which is measured using a photo detector. Instead of measuring the total intensity as in the case of typical absorption spectroscopy here the light leaking out of the cavity with time is measured [50]. This eliminates the error occurring through the intensity fluctuations in an absorption measurement. The decay of the light intensity leaking out of the cavity is generally exponential and represents the residence time of the light inside the cavity, which will be then used to calculate the sample absorption coefficient.

In a simple picture where the duration of the laser pulse width is much shorter than the round trip time of the pulse in the cavity, the detector will see a train of pulses each slightly intense than the previous one. The separation between adjacent pulses is equal to the round trip time t_r=2L/c, where c is the speed of light and L is the length of cavity [52]. The intensity of the pulses will decrease due to absorption by the species in the cavity and the losses at the mirrors. For a laser pulse with intensity I_{laser} which is injected in the cavity with length L we can calculate the intensity at the detector as follow: The mirrors in the cavity are identical and have a reflectivity R and transmittance T. In an ideal case where the loss is only due to reflectivity of the mirrors and not from absorption or scattering then T=1-R. However, normally T is equal to 0.1 to 0.5 times of 1-R for the typical CRDS mirrors. After one pass through the cavity, the intensity of the first optical pulse at the detector is obtained from the Beer-Lambert law as below:

$$I_0 = I_{laser} T^2 \exp(-\alpha l) \qquad \text{E-8}$$

where α=absorption coefficient of the species in cm^{-1} and l= absorption path length in cm. The intensity of the second pulse is given as:

$$I_1 = I_0 R^2 \exp(-2\alpha l) \qquad \text{E-9}$$

where $R^2\exp(-2\alpha l)$ accounts for the total loss due to the additional complete round trip in the cavity. Therefore after n complete roundtrips the intensity at the detector will be:

$$I_n = I_0 R^{2n} \exp(-2n\alpha l) \qquad \text{E-10}$$

As the loss per pass is very small the discrete number of roundtrips n can be replaced by a continuous parameter of time t=n×2L/c and R^{2n} can be written as exp(2nlnR), insertion of these assumptions into E-9 leads to:

$$I_{(t)} = I_0 \exp\left(\frac{tc}{L}(\ln R - \alpha l)\right) \qquad \text{E-11}$$

Since the mirrors used in the cavity have a reflectivity close to unity, lnR ≈ - (1-R), then E-10 will be written as:

$$I_{(t)} = I_0 \exp\left(-\frac{tc}{L}(1 - R + \alpha l)\right) \quad \text{E-12}$$

The 1/e decay of the exponentially decaying light intensity called ring-down time τ can be defined as:

$$\tau_{abs} = \frac{L}{c\{(1-R)+\alpha l\}} \quad \text{E-13}$$

where τ_{abs} = Ring down time with absorbing species in the cavity in seconds. The absorption coefficient can be expressed as $\alpha = N\sigma$ then the E-12 transforms as:

$$\tau_{abs} = \frac{L}{c\{(1-R)+N\sigma l\}} \quad \text{E-14}$$

where σ = absorption cross section in cm^2 and N = number density of the absorbing species in molecules cm^{-3}. In an empty cavity the residence time is dependent only on the reflectivity of the mirrors and can be expressed as:

$$\tau_0 = \frac{L}{c(1-R)} \quad \text{E-15}$$

Using equations E-13 and E-14 absorption coefficient can be obtained as below:

$$\alpha = N\sigma = \frac{R_L}{c}\left(\frac{1}{\tau_{abs}} - \frac{1}{\tau_0}\right) \quad \text{E-16}$$

where R_L = ratio between the cavity length and the absorption path length. The residence of an empty cavity is longer than the residence time of a cavity with the absorbing species τ_{abs}. If we know the absorption cross-section of the absorbing species at that particular wavelength then the concentration of the sample species can be calculated using τ_0 and τ_{abs}.

This value constitutes an absolute measurement [50], and is unaffected by the fluctuations of the source intensity. In the “classical” CRDS technique a pulsed laser is used. The band width of a pulsed laser is generally larger than the FSR. Therefore there is always one or the other mode of the cavity in resonance with the laser emission resulting in the build-up of light in the cavity and ring-down events

can be measured. A schematic diagram of approximate cavity mode spacing and pulsed laser emission bandwidth are shown in Figure 6.

1.7.4 Continuous wave Cavity Ring-Down Spectroscopy (cw-CRDS)

Modifications to the CRDS technique over the past decade have introduced the use of continuous light sources in place of pulsed lasers [53, 54]. Relatively inexpensive and widely available Continuous Wave (CW) lasers can substitute for the costly, cumbersome pulsed lasers previously used in CRDS-based research. In this work a continuous wave (cw) diode laser is used instead of pulsed laser. Important requirements to use this technique in place of pulsed CRDS are; A) the necessity of an optical switch which turns off the light going into the cavity in order to record the ring-down time: in case of pulsed CRDS the laser emission is pulsed but in cw-CRDS the laser emission is continuous which demands a way to turn the light off, once the cavity comes into resonance with the laser emission. B) A system to bring a cavity mode into resonance with the laser emission: the band width of the continuous laser emission is smaller than the FSR, therefore the resonance with the cavity mode is achieved either by changing the cavity length or the wavelength periodically. Figure 6 shows a comparison between the band widths of atypical singe mode continuous laser, pulsed laser, cavity modes spaced by spectral range (FSR).

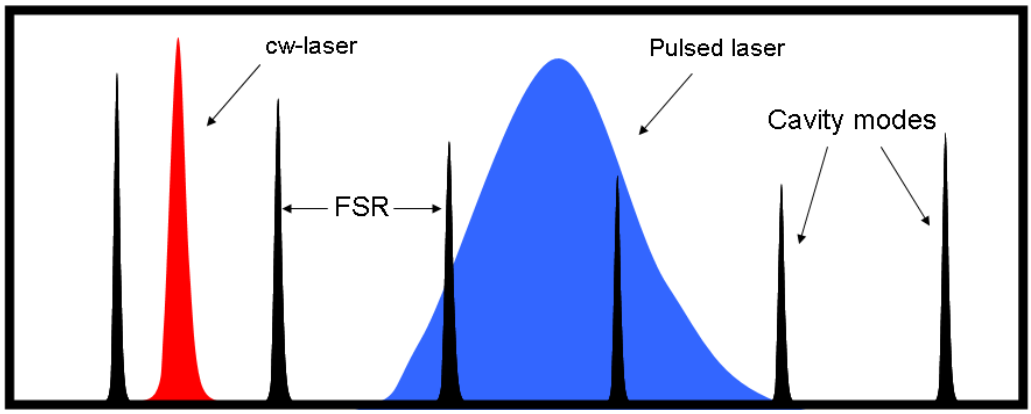

Figure 6: An approximate comparison between band widths of lasers and cavity modes obtained in an optical cavity.

The quantitative detection of a particular species has to be done at a fixed wavelength and hence the only option is the modulation of the cavity length. This can be changed periodically by placing one of the mirrors on a piezo transducer. Piezo transducers modulate the cavity length periodically upon the application of a triangular voltage and bring the cavity periodically into resonance with the laser light. As a result the light builds up inside the cavity through constructive interference and hence the light intensity leaking out of the cavity increases. Once the signal intensity measured by the photodiode exceeds a preset level, the light source is shut-off or diverted from the cavity using an optical switch (AOM: acousto optical modulator in our case) and the decay of the light intensity is measured. Figure 7 shows a basic schematic diagram of cw-CRDS technique containing a cavity made up of ultra reflective mirrors, continuous light source, an optical switch and a photo detector.

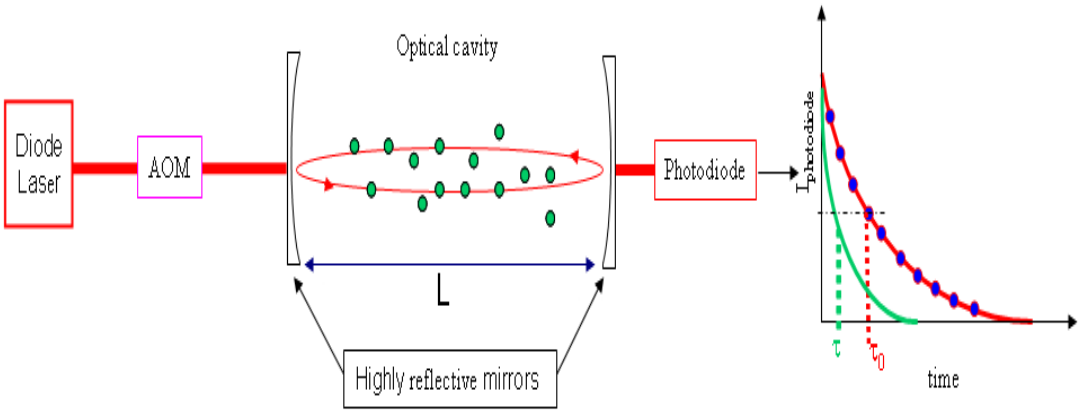

Figure 7: Schematic diagram basic cw-CRDS technique. AOM = Acousto Optical Modulator.

A typical signal detected by the photodiode at the approach of resonance is given in Figure 8. The light starts building up when the cavity length approaches the resonance with the laser wavelength. AOM deviates the light going into the cavity after a set threshold (laser off) and the decay of the light intensity inside the cavity is observed by a photo diode.

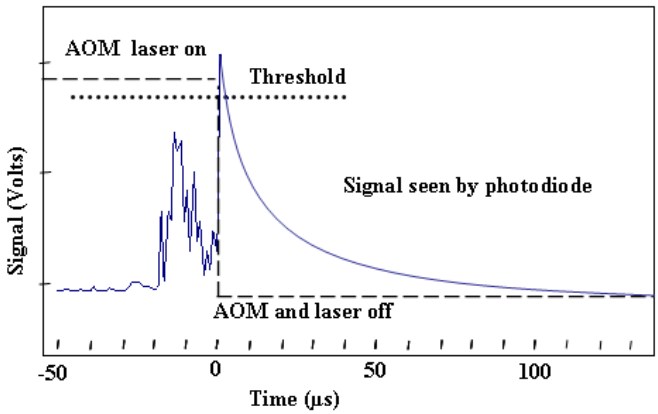

Figure 8: The concept of ring-down decay within the cavity after the laser source is shuttered. AOM = acousto optical modulator.

There are several advantages of the CRDS technique compared to classical absorption techniques. Since the absorption is determined from the time behaviour of the signal, it is independent of intensity fluctuations of the laser. Furthermore, the effective absorption path length, which depends on the reflectivity of the cavity mirrors, can be very long (up to several kilometres), while the sample volume can be kept small. Compared with other sensitive absorption techniques, especially those using modulation schemes, CRD spectroscopy has the additional advantage that the absorption is measured on an absolute scale.

1.8 Summary

This chapter has provided an overview of the atmosphere, its structure, its chemistry with an emphasis on the tropospheric chemistry of the OH and HO_2 radicals, different OH and HO_2 detection and kinetic measurement techniques and the basic theory behind the Laser Induced Fluorescence (LIF) and the Cavity Ring-Down Spectroscopy (CRDS) techniques.

Chapter 2 - Experimental technique

This chapter provides a detailed description of the instrumentation and the experimental techniques used for the entire work of this thesis. There are four main components to the experiment: the photolysis cell, the photolysis laser, the cw-CRDS system and the LIF system. A schematic view of the experimental system is given in Figure 9 and the details of the photolysis cell, LIF and CRDS techniques, different laser systems, and the measurement procedures along with the strategies are explained in the following sections.

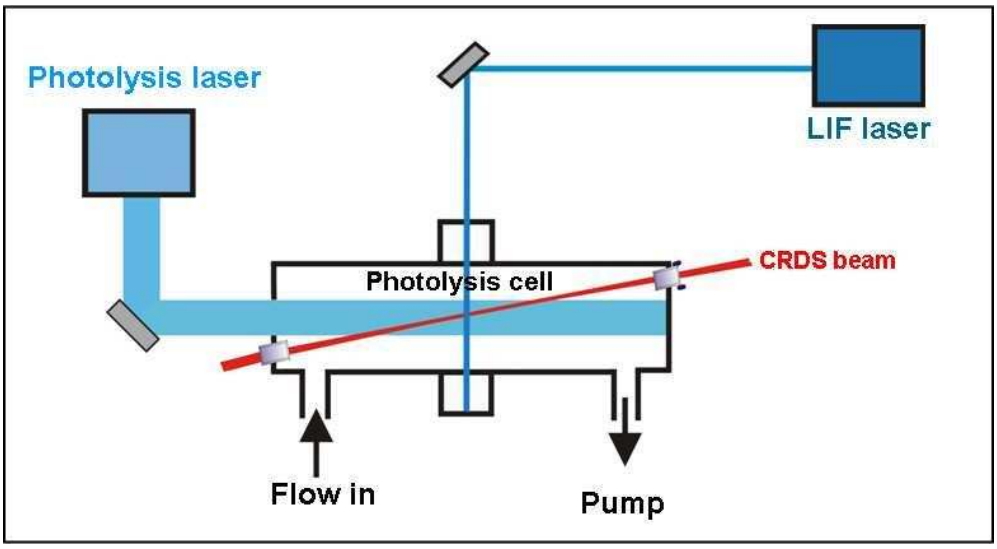

Figure 9: Schematic view of the experimental system.

2.1 Photolysis cell

The photolysis cell is a three axis stainless steel cell with one long axis (78 cm) and two short axes (27 cm), internally coated with Teflon to reduce heterogeneous radical loss. The cell is constructed using six stainless steel tubes each with an internal diameter of 6 cm, connected along the three perpendicular axes that pass through a cubic central structure to form a three dimensional cross. It is equipped with a coil heating system to perform higher temperature experiments if desired. A schematic diagram of the cell is given in Figure 10 [55].

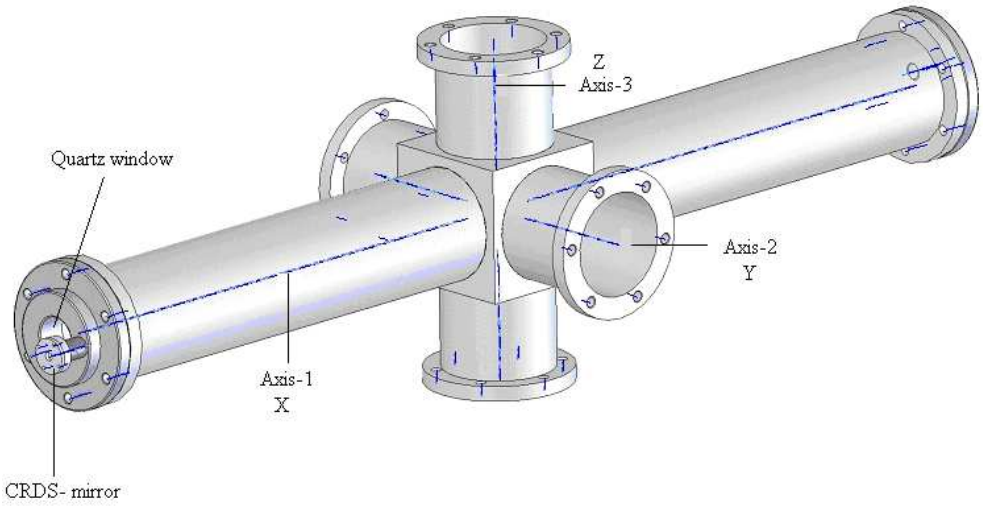

Figure 10: Schematic diagram of the reaction cell [55]**.**

The end flange of each long axis is designed to fulfil three functions: to seal the cell, to allow entry for the photolysis beam and to support the CRDS mirrors. Therefore each plate consists of three parts as shown in Figure 11.

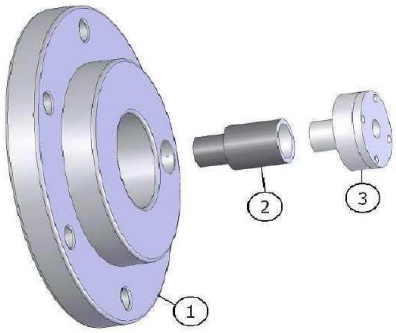

Figure 11: The end flange of the photolysis cell showing different parts [55]**.**

Part 1 is of the same diameter as the stainless steel tubes and directly fixed to the cell. This part has a circular opening of 3 cm in the centre where a quartz window (UV transparent) is fixed which allows the photolysis beam to enter the cell. There is a threaded opening as close as possible to the centre window into which the part 2 can be fixed.

Part 2 is in the form of a collar and has an outer diameter of approximately 1 cm. One end is threaded and can be screwed into part 1 in the opening mentioned above. This forms the junction between CRDS mirror support and the photolysis cell. Together the whole photolysis cell gives an overlap of 37 cm out of the 78 cm long axis of the CRDS and photolysis lasers with an angle of 4° defined between the plane of part 1 and the symmetry axis of parts 2 and 3. There is an additional

tube of 2 mm inner diameter attached perpendicularly to part 2 to have a constant helium flow in front of the mirrors to protect them.

Part 3 is the mirror holder. This is a cylindrical block containing two ends of different diameters. One end is inserted into the other end of part 2 and is held in position with a rubber o-ring. The use of the o-ring in the connection between parts 2 and 3 both seals the cell and allows just enough movement to be able to align the mirrors. The high reflectivity CRDS mirror is mounted inside the other end. The whole unit is mounted in a three-axis optical support with micrometric adjustment screws, with which the mirrors can be aligned *(X-Y-Z Newport U100-A series*).

The lower end of the vertical short axis is closed using a stainless steel cover flange and the upper end by a stainless steel cover with a window (diameter 6 cm) mounted centrally through which the fluorescence from the LIF is collected. Two lenses (Thor labs, focal length 75 mm) are mounted between the central cube of the cell and this plate to focus the fluorescence signal onto the detector, and an interference filter is mounted between the window and the detector to remove all extraneous light (e.g. scattered light from the photolysis laser and the LIF excitation laser) except that in the wavelength range of interest. One end of the horizontal short axis is closed using a stainless steel cover plate and the other end by a stainless steel cover plate with a quartz window (diameter 2.5 cm) at the centre to allow the LIF excitation laser beam to enter into the photolysis cell.

The CRDS and LIF laser beams are aligned at the centre of the photolysis beam to have the highest sensitivity possible for the experiment.

2.2 Photolysis laser

The photolysis is achieved by a high energy excimer laser from *Lambda Physik LPX 202i* series, operated at 248 nm. The term excimer is short for “excited dimer”. The excimer gain medium is a gas mixture, typically containing a noble gas (e.g. argon, krypton or xenon) and a halogen (e.g. fluorine, bromine or chlorine), apart from helium or neon as buffer gas [51]. A high voltage discharge between the electrodes in the laser device [56] transfers the energy to the excimer gas mixture which creates so-called *excimers* (excited dimers); molecules which represent a bound state of their constituents only in the excited electronic state, but not in the electronic ground state. This result in a dissociative ground state and associative exited state populated during the electrical discharge, causing the population

inversion. The high energy associative excited state can give up its excess energy through fast spontaneous or stimulated emission of light and return to the low energy dissociative ground state resulting in laser action.

Different gas mixtures are used for different wavelengths. Table 2 lists different gas mixtures and the corresponding wavelengths typically used in excimer lasers. KrF gas mixture has been used as the gain medium for the present work. 20 Hz repetition rate is accessible; however for practical reasons the repetition rate used is 1 Hz or less. The maximum pulse energy that can be obtained is around 1 Joule (with 1 Hz rep. rate) with a pulse to pulse energy fluctuation of ±3%. The pulse width and the beam dimensions are 34 ns (FWHM) and 1.5×3 cm respectively.

Excimer	Wavelength (nm)
XeCl	308
XeF	351
KrF	248
ArF	193
F_2	157

Table 2: Different gas mixtures used in the excimer laser and their respective emissions.

2.3 The LIF system

OH is excited in the (1-0) vibrational band of the A-X electronic transition near 282 nm, followed by detection of the red shifted fluorescence near 308 nm. The excitation beam comes from a frequency doubled dye laser (PrecisionScan PRSC-24-HPR, Sirah Laser) pumped by the frequency doubled output of a Nd:YVO_4 laser (Spectra Physics Navigator II YHP40-532QW), operating at a 10 kHz repetition rate with an average power of 30 mW. In order to avoid saturation of the LIF signal, the beam is attenuated by a neutral density filter roughly by a factor of 100 and thereafter expanded by a cylindrical lens into a sheet in order to excite a larger volume of OH radicals. The fluorescence is collected perpendicular to the laser beam using two lenses and an interference filter (308 ± 10 nm) and detected with a Channel Photon Multiplier (CPM) (Perkin Elmer MP-1982). The fluorescence signal is measured by photon counting during a 700 ns time window, starting 214 (± 20)

ns after the excitation laser pulse. The signal from the CPM is measured with a counting card (National Instruments PCI-6221) installed in a PC.

2.3.1 Laser in the LIF system

As mentioned above; the dye laser is pumped by the frequency doubled output of a Nd:YVO_4 laser. The Nd:YVO_4 laser is optically pumped using laser diodes and operated in the Q-switching mode. The Q-switching mode is used to produce high energy laser pulses [57]. This mode uses an optical switch inserted in the laser cavity waiting for a maximum population inversion in the neodymium ions before it opens. The high energy pulse is then efficiently frequency doubled to generate laser light at 532 nm, which is then used to pump the dye laser. The dye used in the laser is rhodamine 6G (to obtain 282 nm through frequency doubling of 564 nm) which fluoresces when exposed to light of a suitable frequency. The dye solution is circulated from a large reservoir. This is for two reasons, first the dye will be heated up if it is pumped continuously at 10 kHz and second organic dyes tend to degrade under the influence of light when they are continuously exposed. The dye solution is flowed through a cuvette, i.e., a quartz container. Dye fluorescence emission is inherently broad. In order to produce narrow bandwidth; laser output uses an optics grating as one end mirror of the laser cavity. This ensures the small reflection bandwidth and narrow linewidth emission which is then used to create the laser beam through stimulated emission. Figure 12 shows a schematic diagram of the dye laser used in the present work.

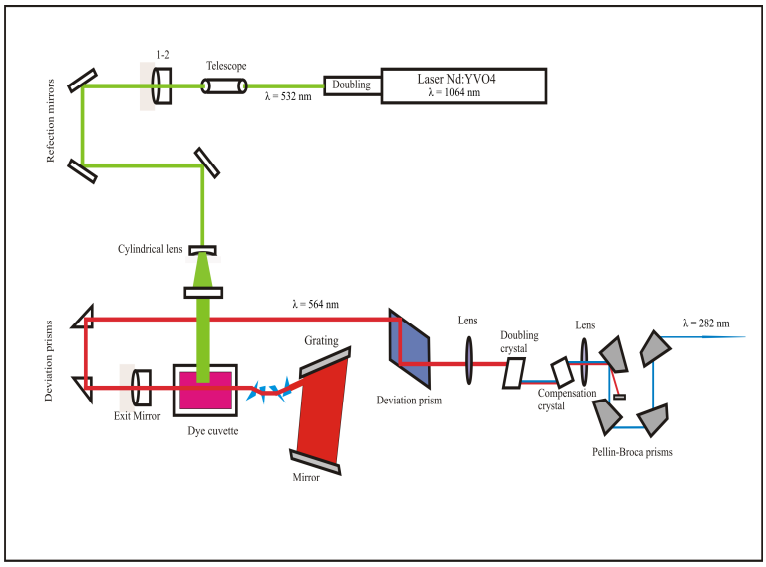

Figure 12: Schematic diagram of a dye laser pumped by Nd:YVO_4 laser [58].

Average output power of the dye laser at 10 kHz is 40 mW. Pulse width and band widths are 30 ns (FWHM) and 20 MHz respectively. The dye laser can be operated at a maximum frequency of 100 kHz; the selection of the operating frequency depends on the temporal resolution required for the measurement.

2.3.2 Frequency Doubling

Nonlinear crystal materials such as lithium niobate ($LiNbO_3$) [59], potassium titanyl phosphate (KTP = $KTiOPO_4$) [60], lithium triborate (LBO = LiB_3O_5) [61] lack the inversion symmetry. This can give rise to a phenomenon called second-harmonic generation or frequency doubling [62], where an input light wave or pump wave generates another wave with twice the optical frequency (i.e. half the wavelength) in the medium. The input wave is delivered from a laser beam, and the frequency-doubled (second-harmonic) wave is generated in the form of a beam propagating in a similar direction.

2.4 The cw-CRDS system

The cavity is formed in the reactor between two highly reflective mirrors (R = 99.9967%, Los Gatos). One of the cavity mirrors is mounted on a piezo-electric transducer (P-305.00, PI) in order to modulate the cavity length with a triangular signal. The amplitude of this signal is set slightly higher than the free spectral range to achieve the resonance requirement twice per period (see section 2.5.1.2). The near-infrared beam with output power ~20-25 mW is provided by one of the two fibred, distributed feed-back (DFB) diode lasers (Fitel-Furukawa FOL15DCWB-A81-W1509 DFB laser for 6635±12 cm^{-1} range and NTTElectronics-NLK1E5GAAA-S/N-723966 DFB laser for 7013±19 cm^{-1} range). The diode laser emission passes through a fibred optical isolator and a fibred 99% / 1% beam splitter. The 1% portion is connected to a fibred wavemeter (Burleigh WA-1100) with an accuracy of 0.01 cm^{-1} for monitoring the wavelength of the laser emission. The remaining 99% is coupled into the cavity through a short focal length lens for mode matching so as to excite the fundamental TEM_{00} mode. Two folding mirrors allow easy alignment of the beam, while an acousto-optical modulator (AOM, Gooch and Housego) mounted in between the folding mirrors allows the laser beam to be deviated within 350 ns with respect to a trigger signal. The optical signal transmitted through the cavity is converted into current by an avalanche

effect photodiode (Perkin Elmer C30662E). An in-house designed amplifier-threshold circuit converts the current signal to an exploitable voltage signal and triggers the AOM to deviate the laser beam when the cavity comes into resonance and the photodiode signal passes a user defined threshold. Figure 13 shows a schematic diagram of the cw-CRDS technique used in the present work.

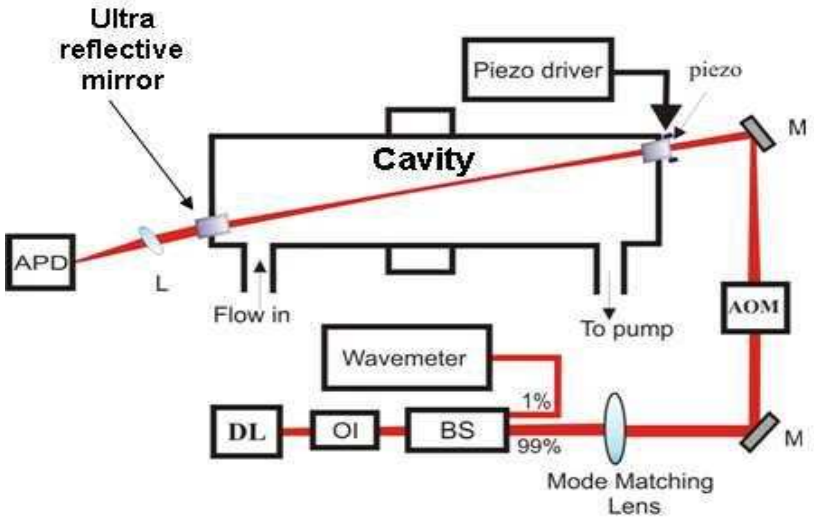

Figure 13: Schematic diagram of the cw-CRDS technique. APD = Avalanche Photo Diode, DL = Diode Laser, OI = Optical Isolator, BS = Beam Splitter, AOM = Acousto-Optical Modulator, M = Mirror and L = Lens.

2.4.1 Laser in the cw-CRDS system

A distributed feedback (DFB) laser diode in the near infra red region is used as the source for continuous wave cavity ring-down spectroscopy. DFB laser diodes have a semiconductor as the active laser medium. The laser action takes place *via* interband transition between valence band and conduction band in the semiconductor using an external voltage that is slightly higher than the band gap voltage [63]. In the presence of external voltage, the transition between the valence band and the conduction band occurs using the external voltage resulting in a population inversion. The electrons in the conduction band will move towards the bottom while the holes created in the valence band move towards the top. Finally the electrons in the bottom of the conduction band fall back into the holes on top of the valence band, emitting the excess energy in the form of light causing the laser action. Figure 14 shows a schematic diagram of the laser action in the semiconductor diode laser.

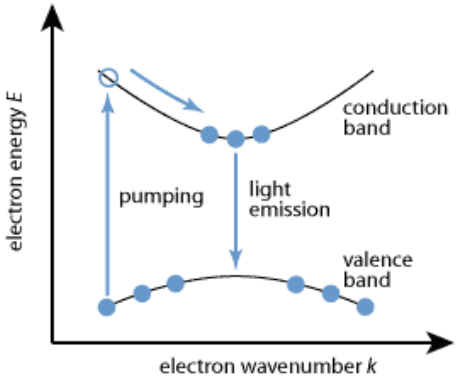

Figure 14: Laser action in a semiconductor diode laser [51].

The DFB lasers have a grating structure incorporated in the semiconductor chip. This grating restricts the laser emission and determines the lasing wavelength. The laser power and wavelengths are related to laser temperature and current. When the laser temperature and current are accurately controlled, the peak wavelength can be tuned along a given range, typically 25 cm^{-1} for a given diode. Maximum output power of the DFB lasers used in this work is around 40 mW with a fluctuation of ±2% at 25 ℃. Bandwidth of the laser emission is aro und 2 MHz.

2.4.2 Event filter switch

The photodiode signal and the AOM trigger signal are both connected to an in-house designed analogue switch circuit working as an event filter that only passes the photodiode signal when the AOM trigger signal is high, i.e. when the laser has been deviated and is “off”. This results in the photodiode signal being “cleaned” as shown in Figure 15. The circuit is based on the Texas Instruments TS5a21366 chip which has an ON-state impedance of 0.75 ohms, a turn-on time of ~200 ns and a total harmonic distortion of 0.002%.

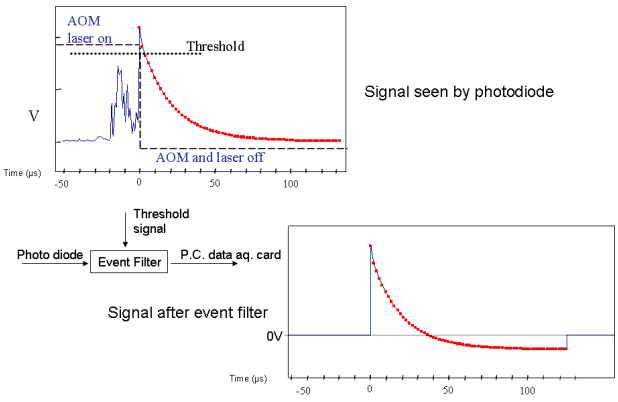

Figure 15: Schematic diagram showing the filtering of the photodiode signal with the analogue switch circuit.

The resulting filtered signal is connected to a fast 16 bit analogue acquisition card in a PC (National Instruments PCI-6259). The acquisition card has an acquisition frequency of 1.25 MHz and thus the ring-down signal is sampled every 800 ns. The data are transferred to PC in real time via PCI bus.

2.4.3 Piezo tracking servo

As mentioned earlier the piezo transducer modulates the cavity length periodically using a triangular voltage ramp to achieve the resonance between the cavity modes and the laser wavelength. Each piezo full scan ideally brings the cavity modes into resonance with the laser emission two times (Figure 16), once each on forward and backward scan. Using a piezo tracking servo (for technical details see paper in preparation) the piezo is made to track the position of a particular cavity mode on the piezo scan and stay tracking at the same position without completing the full scan. The tracking servo has its own threshold circuit and uses the signal from the photodiode to find resonance position when signal that passes a user defined threshold. Once the tracking servo finds resonance it overshoots the piezo scan for a very short time period and reverses its direction so that it can find the same resonance again without going for a full scan. This reduces the time taken to find another resonance, which is the case when the full sweep mode of the piezo is used. The tracker continues to do this until it looses the position of resonance (happens because of mechanical fluctuations of the cavity). Once it loses the ring down event it starts the full scan before it finds resonance again and repeats the same procedure. This will help to reduce the time taken by the piezo for the full scan which in turn increases the frequency of resonance for a given acquisition time and hence the ring-down events. The approximate increase in the number of ring-down events has been a factor of four compared to the number obtained for a full scan of the piezo. Figure 16 shows the result of a piezo scan with and without tracking and the corresponding ring-down events.

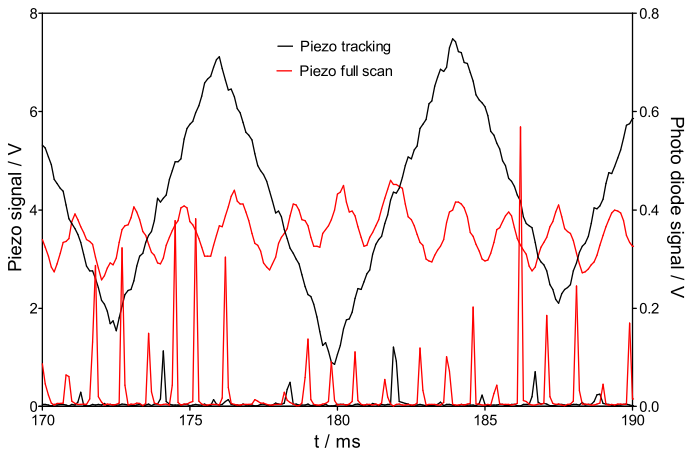

Figure 16: Ring-down events with and without piezo tracking.

Figure 17 shows an example of kinetic measurement of HO_2 recorded for 1 photolysis pulse after photolysing H_2O_2 at 248 nm and 40 Torr helium.

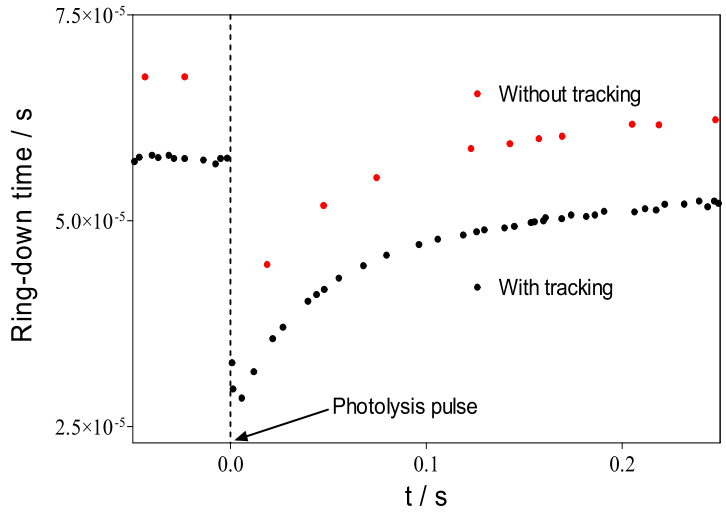

Figure 17: HO_2 kinetics with and without piezo tracking for one photolysis pulse. The signals are deliberately shifted for a better view.

2.5 Kinetic and spectroscopic applications of the experimental technique including measurement strategies

This experimental technique can be used for two distinct applications: (a) kinetics applications, permitting measurement of OH and HO_2 concentration-time profiles to measure rate constants, and (b) spectroscopic applications either in continuous mode for species with constant concentration or allowing the

synchronization of the acquisition of ring-down events (cw-CRDS) with the laser photolysis pulse to determine spectroscopic parameters of transient species.

2.5.1 Kinetic applications

This application has two different measurement strategies one allowing the simultaneous measurement of OH and HO_2 (section 2.5.1.1) and the other allowing the synchronisation of the cw-CRDS technique with photolysis laser (section 2.5.1.2)

2.5.1.1 Simultaneous, time resolved measurements of OH and HO_2 radical kinetics ("Simultaneous measurement mode")

In this section the measurement strategy for the synchronisation of the LIF and cw-CRDS techniques to measure OH and HO_2 kinetics simultaneously will be explained. A schematic view of the experimental set-up for simultaneous, time resolved kinetic measurements of OH and HO_2 radicals is given in Figure 18 and the details are described below.

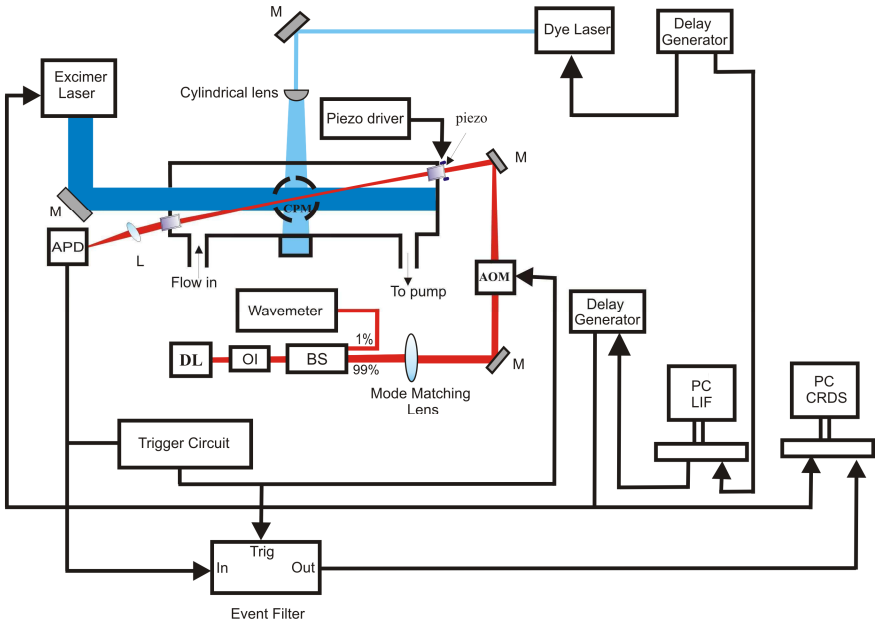

Figure 18: Schematic diagram for "simultaneous measurement mode". APD = Avalanche Photo Diode, DL = Diode Laser, OI = Optical Isolator, BS = Beam Splitter, AOM = Acousto-Optical Modulator, M = Mirror and L = Lens.

The principle of the LIF system is explained in section 2.3. The master timing unit in this configuration is DG1 (Figure 20), triggering the LIF laser continuously at 10 kHz. The control program written in Labview generates one measurement gate

pulse (or time window) during which time the fluorescence signal is measured (700 ns) for each pulse received from the delay generator (DG 1 in Figure 20) up to a maximum of measurement time multiplied by laser frequency (10 kHz) as shown in Figure 19.

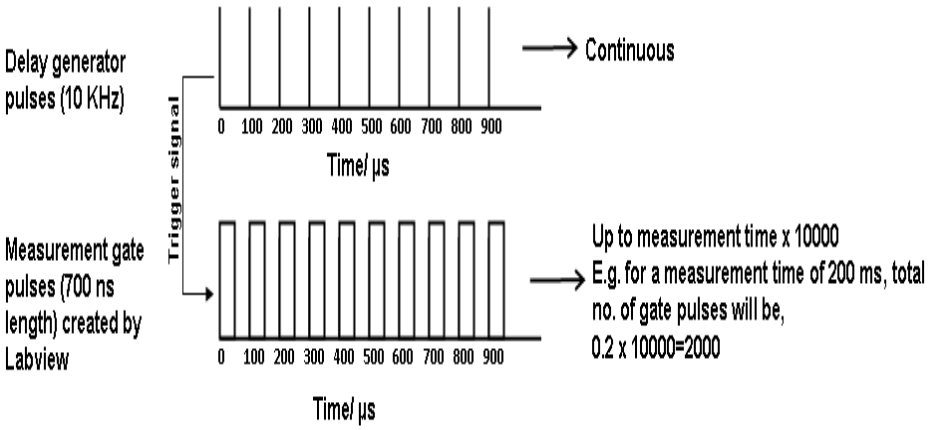

Figure 19: Fluorescence measurement gate pulse calculation in LIF system.

The relative delay between the excitation laser pulse and the start of the fluorescence measurement (as well as the duration of the LIF signal window) is controlled with the PC counting card via Labview (v8.2.2, National Instruments). The first measurement time window pulse then triggers a second delay generator (DG2 in Figure 20) which triggers the photolysis laser after a configurable delay. Thus it is possible to position the photolysis pulse where required relative to the train of LIF excitation pulses, with a time jitter of ± 20 ns. The delay between two photolysis pulses to renew the gas mixture inside the reactor is set using a dummy delay in the second delay generator. This way DG2 accepts a new trigger pulse only once the dummy delay (e.g. 1 s for 1 Hz repetition rate) is completed and ignores all the other pulses arriving at a rate of 10 kHz. To increase the signal to noise ratio, photon counts from equivalent time windows are summed for many photolysis pulses, typically for a total number of 500-600 photolysis pulses.

DG2 also triggers the data acquisition of the CRDS system without any delay. However, the ring-down events of the CRDS technique are running independently of the photolysis, i.e. no synchronization is done and the ring-down events occur randomly with respect to the photolysis pulse. Therefore it is necessary to determine the position of each ring-down event relative to the photolysis pulse as well as the corresponding ring-down time. As noted, the CRDS acquisition is triggered from the same delay generator that also triggers the photolysis laser and

starts at a fixed time before the photolysis laser pulse. The filtered photodiode signal is collected continuously at the 1.25 MHz sampling rate for the entire kinetics measurement period, typically for a few hundred milliseconds, and thus the acquisition samples all the ring-down events that occur during that period. The position of the photolysis pulse relative to the start of acquisition is therefore known and thus the time of each ring-down event relative to the photolysis pulse can be easily calculated from its position within the data file. As the photodiode signal has been filtered of all other signals except the ring-down events by the event filter unit, it is trivial to locate each event within the data file based on the sharp and well defined rising edge, as shown in Figure 15. All that remains is to calculate the ring-down time itself. The ring-down time is first estimated by linear regression of the logarithm of the first 20 μs of the decay. Next the full decay is fitted over a time range of seven previously calculated lifetimes with an external implementation of a Levenberg-Marquardt exponential fit [64] in Labview. This way, one obtains for each photolysis pulse a variable number of ring-down events, occurring at random delays with respect to the photolysis pulse. This is repeated for multiple photolysis pulses until a complete picture of the HO_2 profile with time is obtained. A schematic diagram of the full timing and synchronisation between the various subsystems is shown in Figure 20.

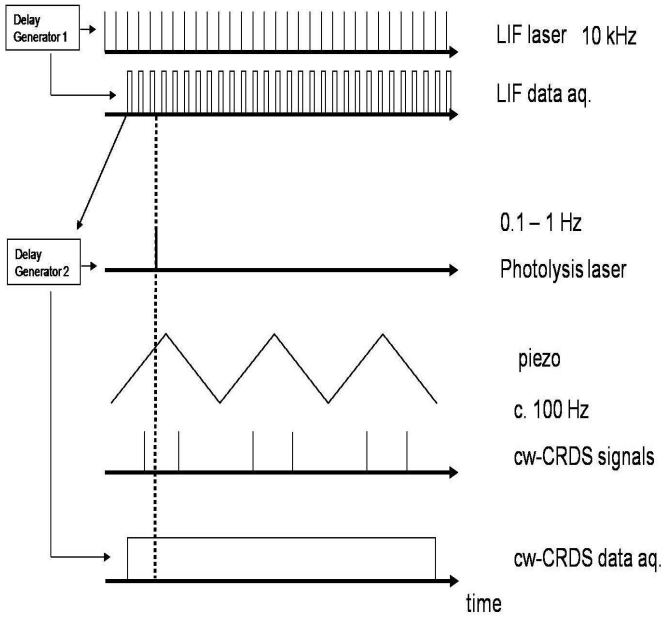

Figure 20: Schematic diagrams showing the timing and synchronisation of the photolysis pulse, LIF and cw-CRDS.

Figure 21 summarises the measurement strategy for the simultaneous measurement of OH and HO_2 radical kinetics using LIF and cw-CRDS techniques.

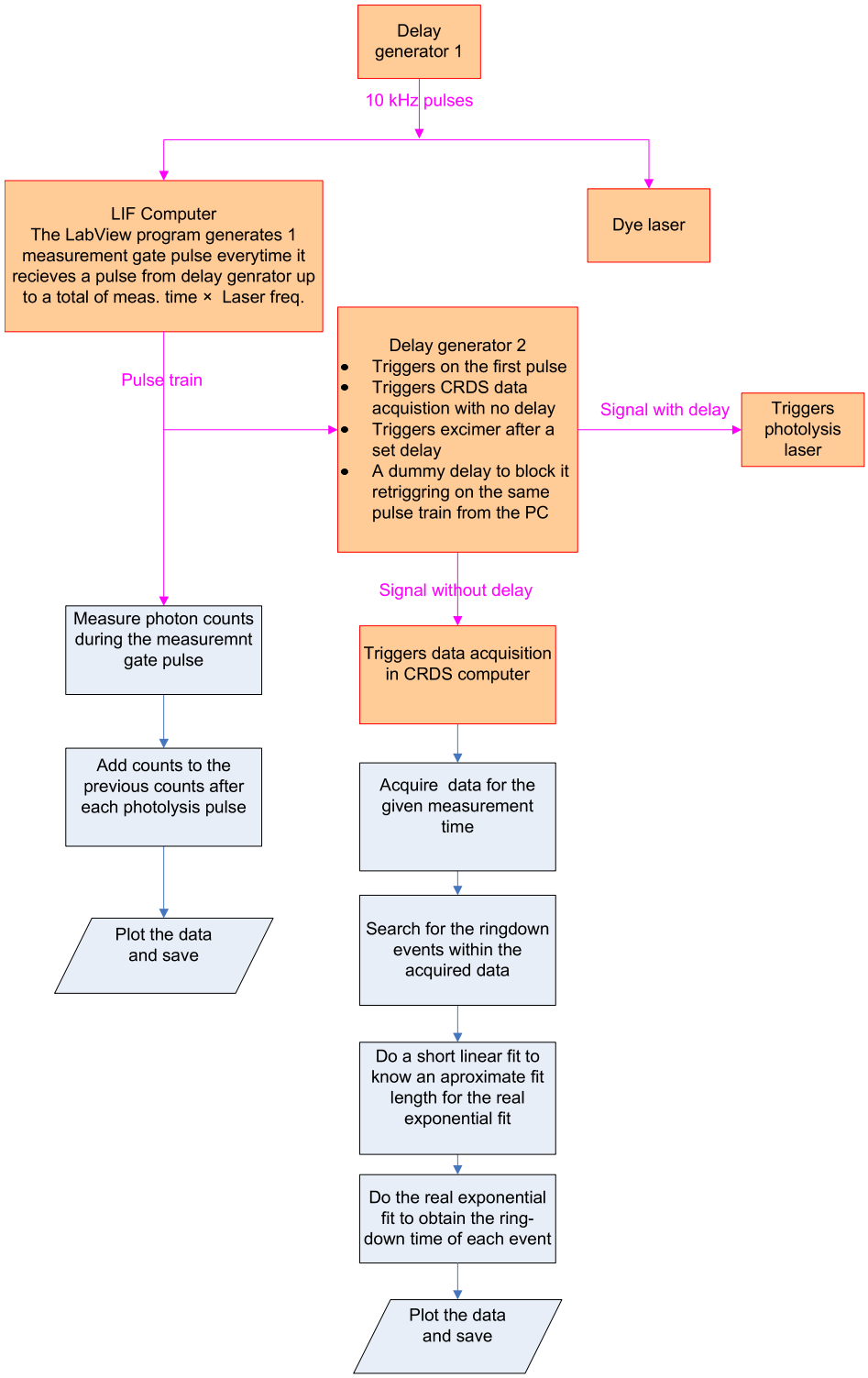

Figure 21: Flow chart showing the measurement strategy for simultaneous measurement of OH and HO_2.

The delay between the start of the acquisition and the photolysis pulse can be defined by the user in order to get many ring-down events before the photolysis pulse, i.e. the ring-down time of the empty cavity.

Figure 22 shows the typical signals of OH and HO_2 kinetics obtained from a simultaneous measurement of H_2O_2 photolysis at 248 nm and 40 Torr helium. The OH counts are obtained after averaging for ~600 photolysis laser shots and CRDS signals are obtained after averaging ~200 photolysis laser shots.

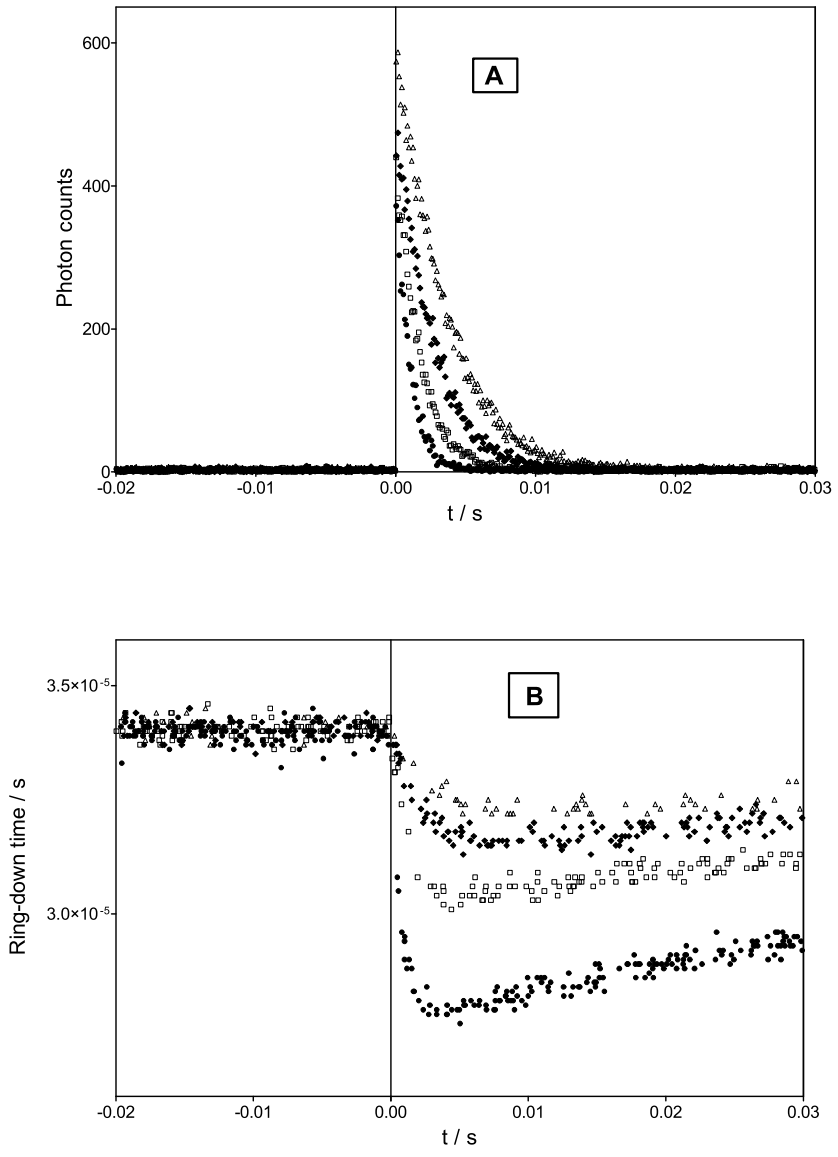

Figure 22: Typical signals obtained in a simultaneous measurement (A) OH profiles (B) HO_2 profiles at different H_2O_2 concentrations. ●: $[H_2O_2] = 4.8\times10^{14}$, $[OH]_0=2.4\times10^{12}$ cm^{-3}, : 3.1 and 1.3, ♦: 2.0 and 0.84, Δ: 1.5 and 0.65.

When a better signal-to-noise ratio is desired for HO_2 signals then ring-down events occurring in a same, user-defined time-window can be averaged using a data analysis program written in the Labview. Figure 23 shows a comparison of three different (1.0 ms, 0.5 ms and 0.25 ms) time window averages together with the raw HO_2 signal ($[HO_2]_{max} \approx 2\times10^{10}$ cm^{-3}) obtained from a kinetic measurement at 6638.20 cm^{-1}. The averaged signals are deliberately shifted for a better view.

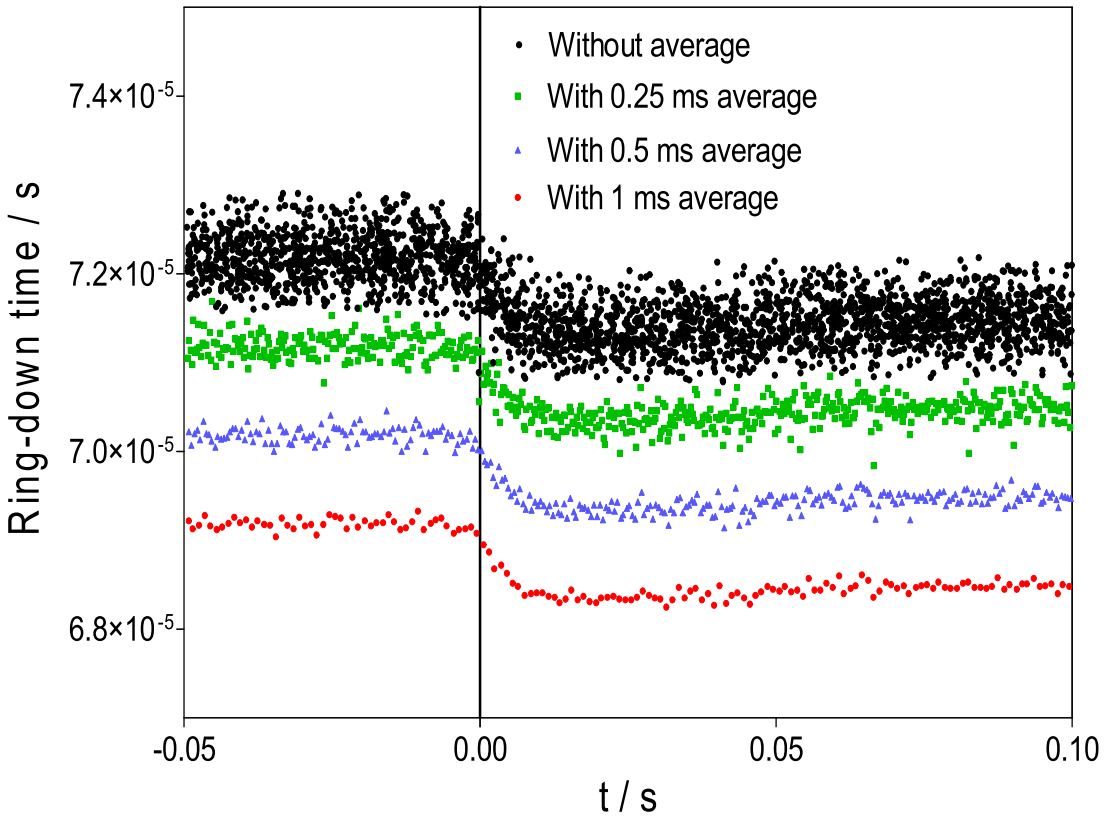

Figure 23: Comparison of different HO_2 signal averaging to get a better signal to noise ratio in a kinetic experiment.

The averaging is done according to the requirement and the dynamics of the signal. More averaging will end up with less number of points as shown in Figure 23. It is important to have enough points to describe well the time resolution of the concentration. Therefore two or more averaging sections with different time windows can be combined to get a signal with good time resolution in the beginning and a better signal to noise ratio at longer reaction times.

Effect of the photolysis pulse on the ring-down time

While studying the kinetics of HO_2, decay in ring-down time just before the photolysis pulse has systematically been observed, Figure 24 shows such an example of ring-down events with lower ring-down time than the baseline (ring-down events in the red circle).

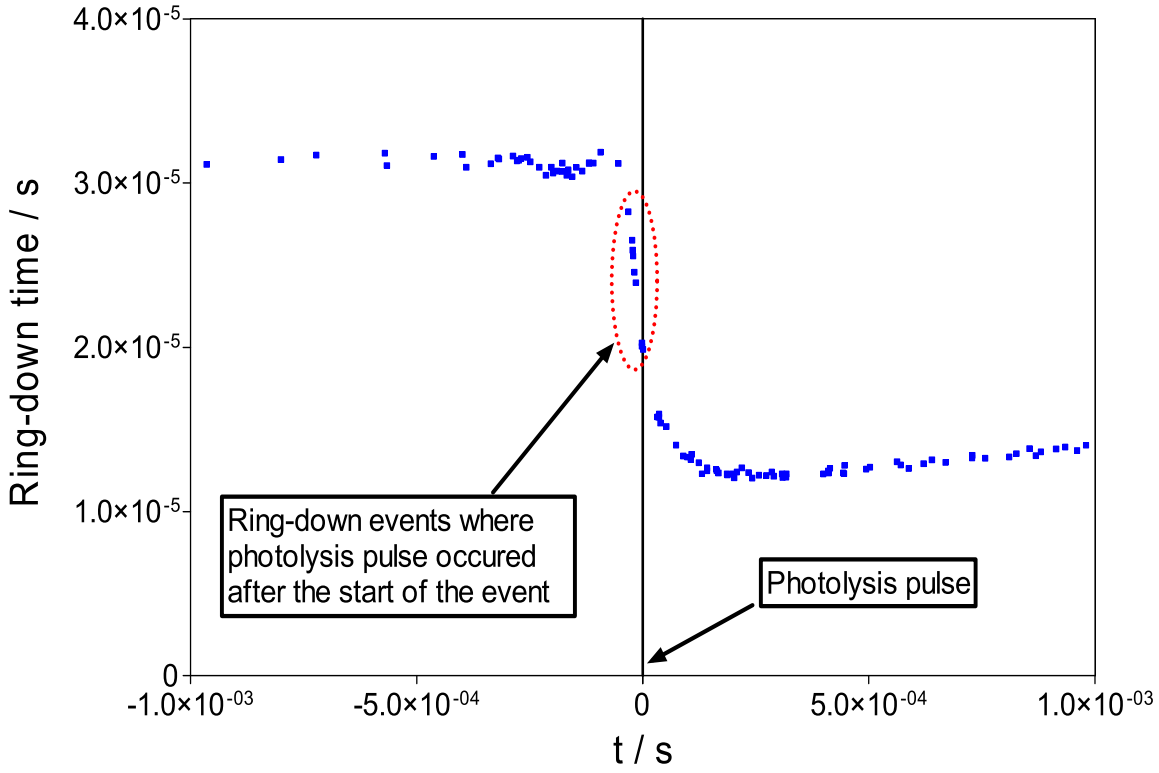

Figure 24: A kinetic measurement signal showing the effect of the photolysis pulse occurred after the start of the ring-down event.

The reason for this observation was not clear, whether these are real signals or some measurement error, for example a shift in the delay of the photolysis laser. As the ring-down events are occurring randomly with respect to the photolysis laser; it sometimes happens that the photolysis pulse occurs during a ring-down event. Figure 25 shows one such ring-down event where the photolysis pulse occurred with a delay of 21.6 µs after the start of a ring-down event.

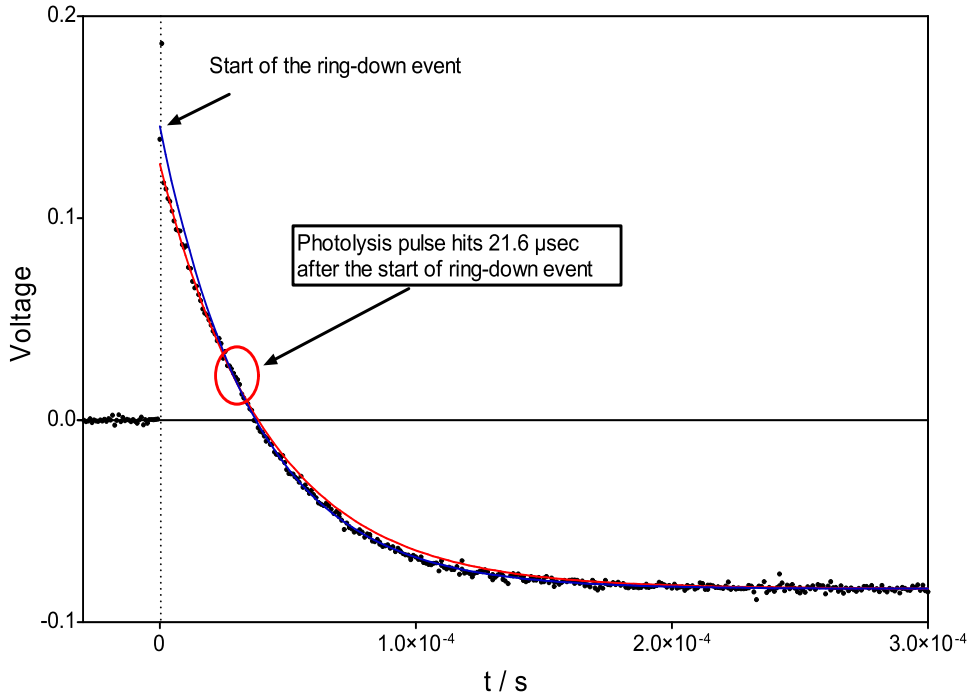

Figure 25: Effect of photolysis pulse on the ring-down event, showing the photolysis pulse occurring after the start of the ring down event. Red full line shows the fit without taking the points after the photolysis pulse and the blue line shows the fit without taking the points before the photolysis pulse.

Fitting for such a signal can be done in two ways as shown in Figure 25. If the fitting is done only for the data points before the photolysis pulse (i.e. for the first 21.6 µs) then the ring-down time obtained would be the same as obtained for all the events before the photolysis pulse as shown in Figure 24. If the fitting is done only for the data points after the photolysis pulse then the ring-down time obtained would correspond to the HO_2 concentration just after the photolysis pulse (Figure 24). However, in our data acquisition program such separation within a ring-down event is not possible and a single exponential fitting is done for the entire data acquired for the ring-down event. As a result a ring-down time with a value in between the ring-down times before and after the photolysis pulse is obtained (ring-down events in the red circle in Figure 24). This effect depends on the relative delay of the photolysis pulse to the beginning of the ring-down event: shorter the delay the more pronounced is the effect and vice versa. These ring-down events are removed before averaging all ring-down events before photolysis pulse to get the τ_0.

Figure 26 shows the OH and HO_2 kinetics profiles derived from the data in Figure 22.

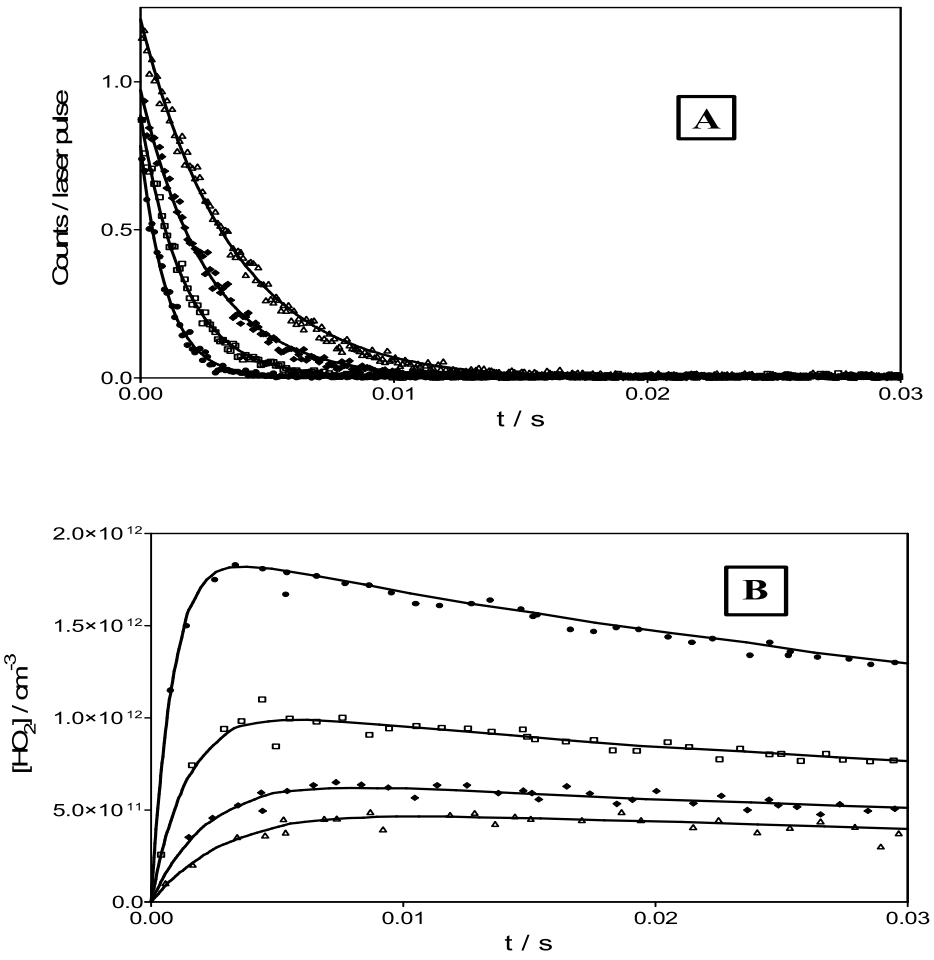

Figure 26: (A) Plot of OH fluorescence count/ laser shot vs time at different H_2O_2 concentrations, (B) plot of HO_2 concentration vs time at different H_2O_2 concentrations. •: $[H_2O_2] = 4.8\times10^{14}$, $[OH]_0=2.4\times10^{12}$ cm^{-3}, : 3.1 and 1.3, ♦: 2.0 and 0.84, Δ: 1.5 and 0.65.

The OH counts per laser shot are obtained after dividing the signal by the total number of laser shots. The background noise of OH signals, i.e. the photon counts observed before the photolysis laser, is averaged and subtracted from the fluorescence signals. For the HO_2 profiles the ring-down events that are affected by the photolysis pulse are removed and the average of all the ring-down events before the photolysis pulse is used to get the τ_0. The τ_0 will then be used to transform other ring-down times τ_t into time resolved concentration [A] as explained in section 1.7.3 of Chapter 1. The absorption cross sections used in the present work for HO_2 (on the absorption line at 6638.20 cm^{-1}) at different pressures

are calculated using Doppler coefficient (7.0889×10^{-3} cm^{-1}), the pressure broadening coefficient for Helium (0.057 cm^{-1} atm^{-1}) [65] and the integrated line strength (6.34×10^{-21} cm). Table 3 shows the different absorption cross sections used in this thesis for different pressures for HO_2 absorption at 6638.20 cm^{-1}.

Pressure / Torr	**$\sigma_{6638.20\ cm\text{-}1}$ / 10^{-19} cm^2 $molecule^{-1}$**
50	2.72
40	2.93
20	3.47
10	3.81

Table 3: Absorption cross-sections of HO_2 at different pressures.

2.5.1.2 Photolysis laser synchronisation with the ring-down events for time resolved measurements of HO_2 radical kinetics ("Grouped events mode")

The previous section has described the simultaneous measurement of OH and HO_2, during which the timing of the HO_2 measurements relative to the photolysis pulse, although well characterised, is essentially random. This is the so called "simultaneous measurement mode" of the cw-CRDS acquisition. However, it is also desirable to be able to synchronise the timing of the cw-CRDS measurements relative to the photolysis laser in order to study the details of the kinetic profile at short reaction time. Using the "simultaneous measurements mode", ring-down events occur randomly and thus it can be tedious to wait for enough ring-down events to accumulate at short reaction times. This is possible with our set-up when operating in "grouped events mode", although it is not possible to make simultaneous LIF measurement in this mode because the master time base is the CRDS events and not the LIF laser which requires a constant high repetition rate trigger signal. The schematic diagram for the "grouped events mode" measurements is the same as shown in Figure 20 with the LIF part removed.

Modulating the cavity length with the piezo transducer periodically fulfils the resonance condition and leads to ring-down events at approximately regular

intervals; this has been explained in detail by Thiébaud *et al.* [66]. This relationship is used to predict when the next ring-down events occur, as shown by signals (a) and (b) in Figure 27: two events are obtained per modulation period *T*, one on the positive slope at t_0, the other on the negative slope at t_1. The interval between these two events is governed by the offset of the modulation signal and by slow mechanical drifts of the mirror position, so it is difficult to predict the ring-down event at t_1 relative to the one at t_0. The interval between t_0 and t_2 on the other hand is, besides the jitter (approximately 2 ms), equal to the modulation period *T* and can be predicted. The AOM trigger signal is therefore used to trigger the delay generator which in turn triggers both the data acquisition and the photolysis laser after specified delays. The photolysis frequency is controlled using a dummy delay in the delay generator.

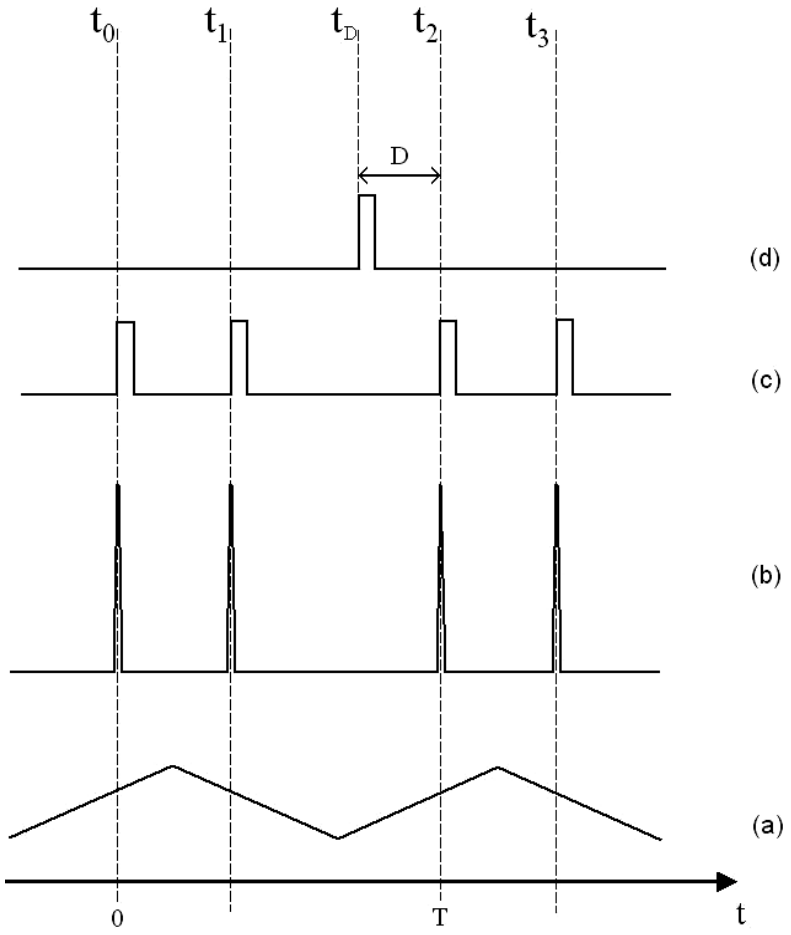

Figure 27: Timing scheme for spectroscopic measurements. (a) Triangular voltage applied to piezoelectric transducer (b) cavity modes recorded by the photodiode (c) ring-down trigger pulses (d) photolysis trigger pulse [9]**.**

A typical signal obtained using grouped events mode from the photolysis of a mixture of benzene and oxygen is given in the Figure 28.

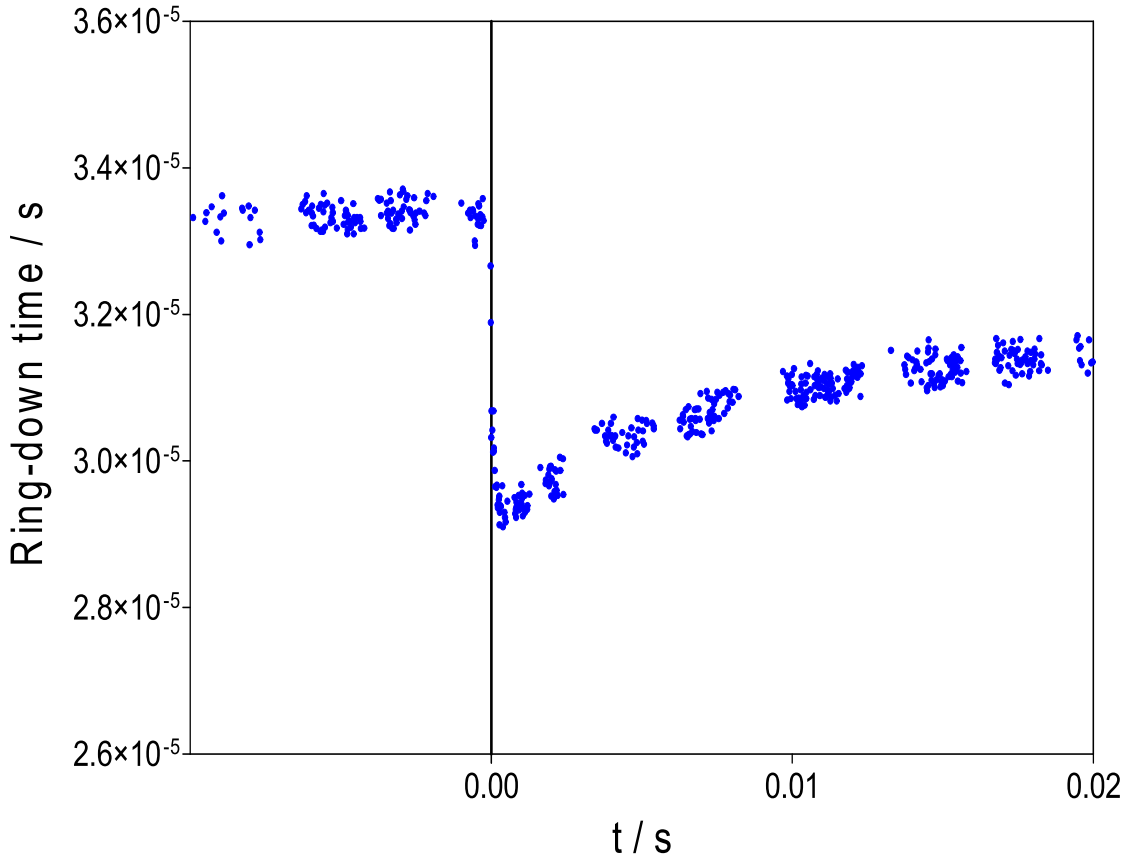

Figure 28: Signal obtained from a grouped events mode measurement.

However, this mode leads to grouped ring down events in few ms interval (depending on the modulation frequency of the piezo transducer) and hence it might be necessary to periodically change the delay of the photolysis laser in order to obtain the even distribution of ring-down events all-over: this is done automatically by setting the photolysis delay on the delay generator *via* GPIB from the Labview control program.

Figure 29 summarises the measurement strategy for the photolysis laser synchronised with the ring-down events for time resolved measurements of HO_2 radical kinetics.

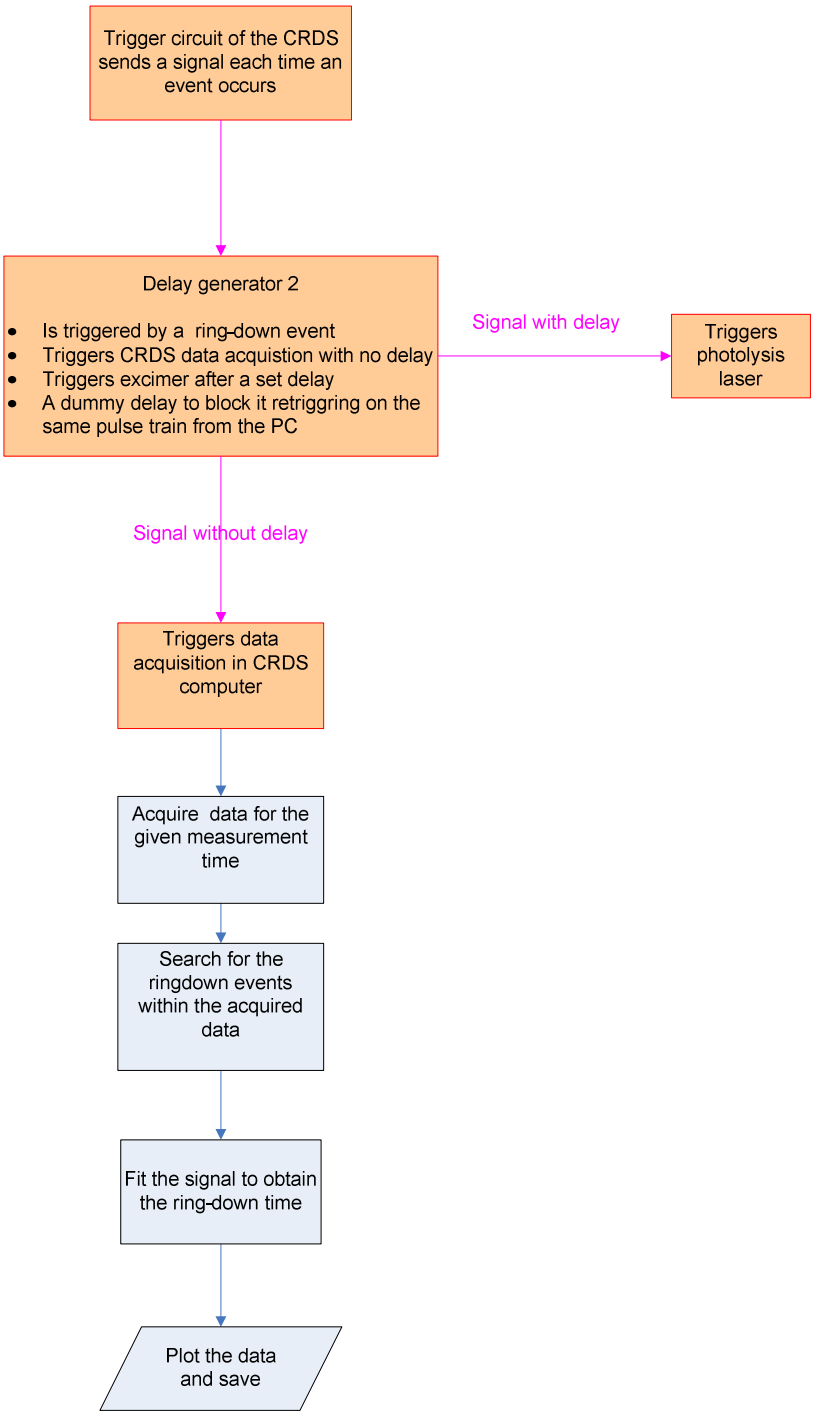

Figure 29: Flow chart showing the measurement strategy for grouped events measurement.

In summary two strategies have been described for kinetic applications; one of them allows simultaneous, time resolved kinetics of OH and HO_2 radicals and the other allows the grouping of HO_2 radical kinetic measurements relative to the photolysis laser. The latter is also used for spectroscopic applications of CRDS technique. The spectroscopic applications will be explained in following sections.

2.5.2 Spectroscopic applications

The cw-CRDS technique can be used to measure absorption spectra. For transient species there are two distinct ways of generating the chemical species under investigation. The first is to generate a constant concentration of the species of interest either external to the reactor or by continuous photolysis within the reactor, while the second is to generate a transient concentration of a species *in-situ* by the use of the photolysis laser and measure the time resolved spectrum of the transient species. Two different measurement strategies are used to measure the absorption spectra in the two cases.

2.5.2.1 With a constant concentration

In this approach, a steady state concentration of the absorbing species is maintained in the reactor. The wavenumber of the CRDS laser is repeatedly stepped through the range of interest, and at each wavenumber a user defined number of ring-down events are averaged. The wavenumber tuning is achieved by changing the current of the laser diode which is itself controlled by sending a variable voltage to the diode controller from the data acquisition card installed in the PC. The wavenumber measured by the wavemeter is saved once every 10 such increments, because each individual increment is very small (0.001 cm^{-1}) and the resolution of the wavemeter is not precise enough to record this very small change. Therefore the wavenumber is only measured in larger increments and the data are interpolated during the analysis to obtain the wavenumber for each data point. The resolution of the spectrum can be controlled by stepping the wavenumber at the desired resolution, with a maximum possible resolution of around 0.001 cm^{-1}. Figure 30 shows a schematic diagram of the continuous spectrum measurement experimental technique.

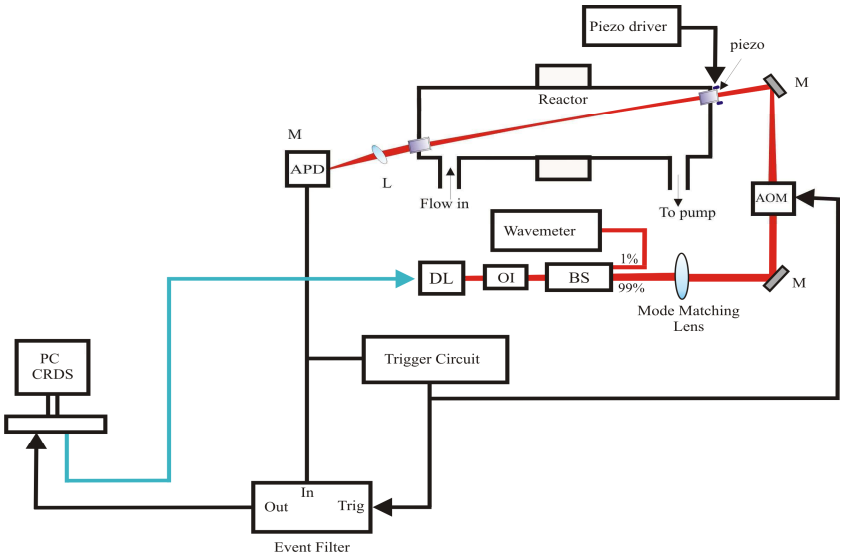

Figure 30: Schematic diagram of the absorption spectrum of the species generated by continuous photolysis or injected into the cavity; APD = Avalanche Photo Diode, DL = Diode Laser, OI = Optical Isolator, BS = Beam Splitter, AOM = Acousto-Optical Modulator, M = Mirror and L = Lens.

Figure 31 summarises the strategy for absorption spectrum measurement of the chemical species with a constant concentration.

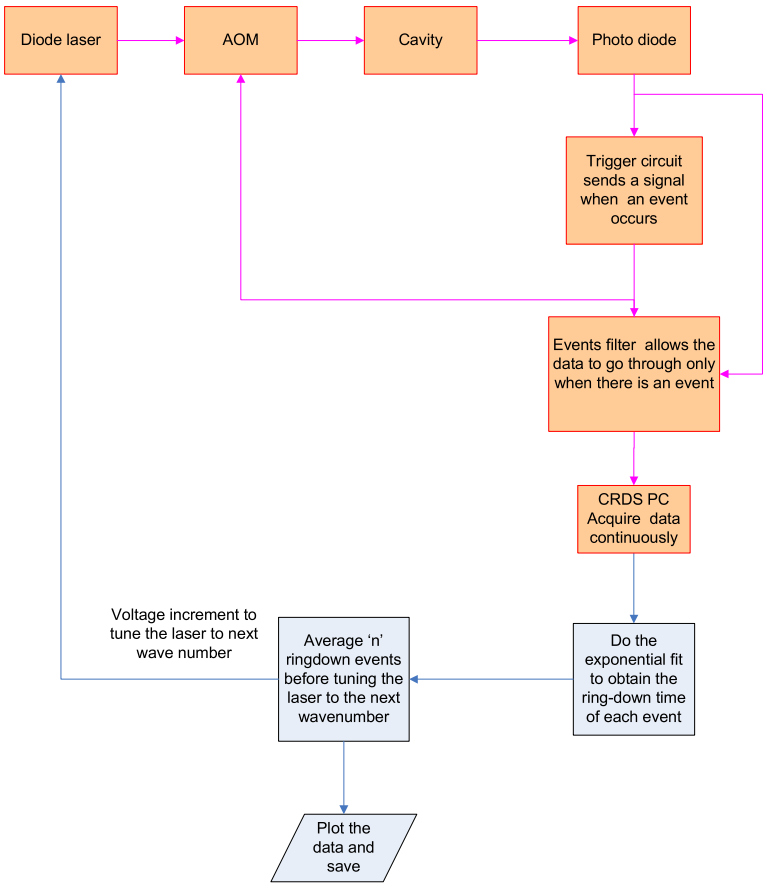

Figure 31: Measurement strategy flow diagram for the absorption spectra of the species with a constant concentration.

2.5.2.2 With transient concentration

This configuration is used to measure the absorption spectra of species with transient concentration generated in-situ, for example by the laser photolysis. The application can be done in two distinct ways as explained below:

Ring-down events average mode

This mode is used for the measurement of baseline absorption in the aromatic experiments (Chapter 4) and calibration of line strengths of HO_2 and DO_2 in the 7013 cm^{-1} range (Chapter 5). The timing strategy used for the synchronisation with the photolysis laser is the same as detailed in section 2.5.1.2. Figure 32 shows a schematic diagram of the experimental set-up for the absorption spectrum measurement of species with transient concentration.

.

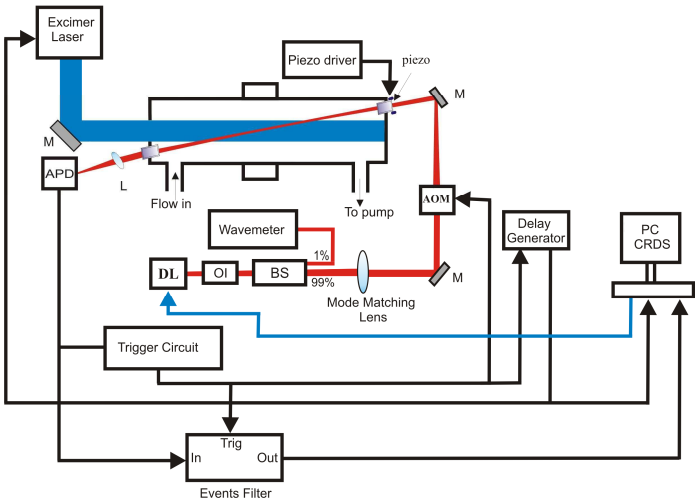

Figure 32: Schematic diagram of the ring-down events average mode; APD = Avalanche Photo Diode, DL = Diode Laser, OI = Optical Isolator, BS = Beam Splitter, AOM = Acousto-Optical Modulator, M = Mirror and L = Lens.

The AOM trigger signal is also used to trigger the delay generator which in turn triggers both the data acquisition and the photolysis laser after specified delays. A time resolved kinetic of the transient species is measured on each wavelength and the required number of ring-down events that fall within a specific time window after the photolysis pulse are then averaged along with events prior to the photolysis for the background. The photolysis frequency is controlled through a dummy delay set on the delay generator. Typically 30-40 events are averaged before tuning to the next wavelength, giving a scan speed of 1.0 cm^{-1} h^{-1} at a resolution of 0.002 cm^{-1}. Figure 33 shows a typical time-resolved signal recorded

on one of the wavelengths during the unknown reactive intermediate absorption spectrum measurement from o-xylene photodissociation studies (section 4.1.1). In this case three different time windows of averaging are used. The first time window averages all the ring-down events before the photolysis pulse to get the baseline (baseline average), second time window averages all the ring-down events occurring within 1 ms after the photolysis pulse (short average) and the third time window averages all the ring-down events during more than one millisecond after the photolysis pulse (long average).

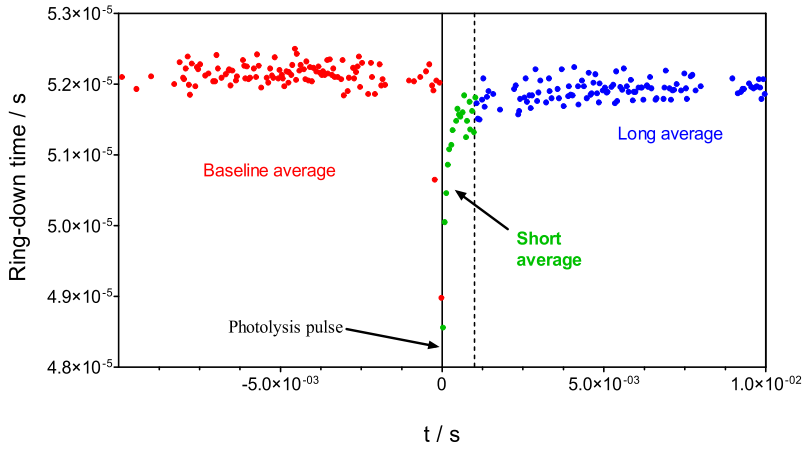

Figure 33: Typical signal obtained in a ring-down events average mode with different average time windows.

The signal shown in Figure 33 yields one data points each corresponding to the baseline average, short average and long average for the wavelength where the time resolved kinetics is measured. The resulting spectrum from these signals is given in Figure 34 (details are discussed in Chapter 4).

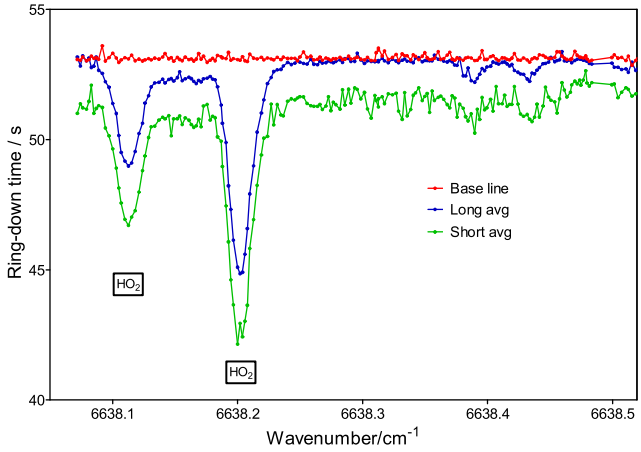

Figure 34: Spectrum obtained from a ring-down events average mode

The ring-down event average mode is generally used for transient species with fast decay times where the data acquisition on a long time scale is not possible. Furthermore, in this mode the time resolved kinetics of the transient species on each wavelength is not saved, instead the ring-down event averages of different time windows are saved.

Figure 35 summarises the strategy for measuring the absorption spectra using ring-down events average mode.

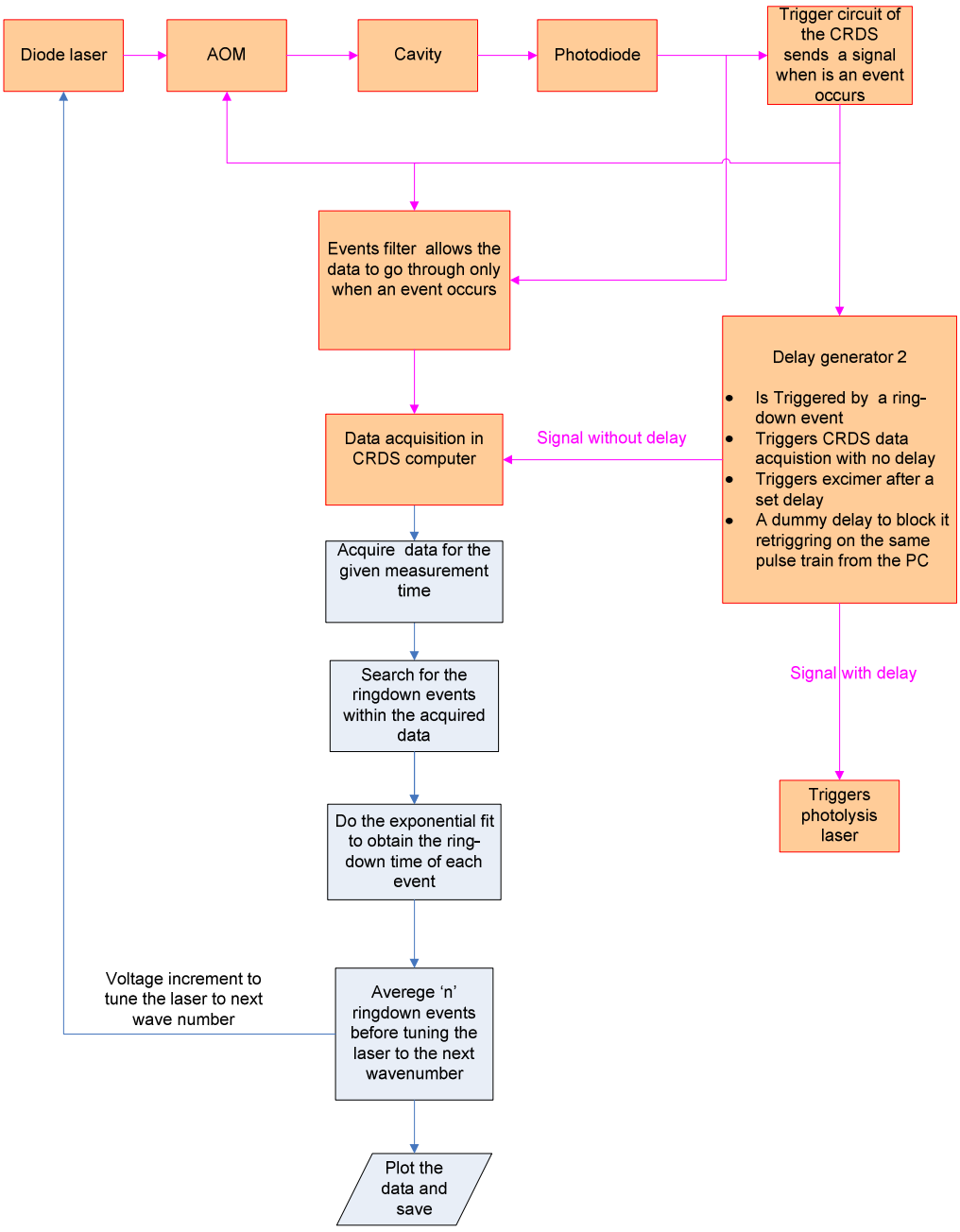

Figure 35: Measurement strategy flow diagram for absorption spectra of the species with transient concentration measured ring-down events average mode.

Ring-down events fitting mode

Measurement of the long lived transients such as, HONO spectrum (details in Chapter 5) have been carried out using ring-down events fitting mode This mode is used for species with slow decay times and require longer measurement times while measuring spectra e.g. for more than one second acquisition time. A large, variable number of ring-down events will occur during this long acquisition time, and therefore the time required to fit all these events will both be long and variable. If the ring-down event average procedure were to be used, then the dummy delay on the delay generator would have to be set to be in excess of the longest potential fitting time so as to be sure that it would not be retriggered before fitting was complete (as acquisition cannot start again until the fitting is done). This can lead to lots of time being wasted if the fitting time is quicker than the worst case scenario dummy delay.

Therefore under these conditions the acquisition program becomes the timing master. It does not wait to be triggered by the threshold circuit before starting acquisition and the delay generator is no longer triggered by the threshold circuit, but instead by the acquisition program. The acquisition program sends a pulse synchronised with the start of acquisition to the delay generator to trigger it. In this way the timing of the ring-down events relative to the photolysis pulse are still known, and as the acquisition program starts another acquisition period as soon as the fitting is complete, the time lost is minimised. The initial version of the fitting program took 30 to 40 seconds to fit the approximately 1000 ring-down events that are acquired in four seconds thus greatly limiting the photolysis frequency possible. Improvements to the fitting program have since been made, and the same number of events can now be fitted in a few hundred milliseconds. Further optimisations could be performed to make the acquisition and fitting run in parallel, although with the increase in speed of the fitting that has been achieved, this is no longer necessary.

The schematic diagram for this mode is similar to Figure 32, only the delay generator is triggered by the control program written in Labview. Typical time resolved kinetics obtained on one of the wavelengths during the HONO spectrum measurement using ring-down events fitting mode is shown in Figure 36.

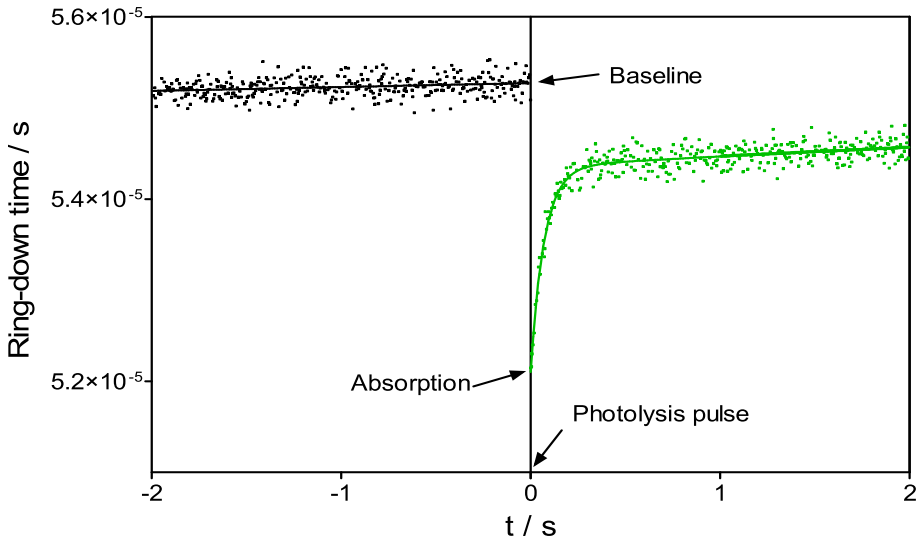

Figure 36: Typical signal obtained from a ring-down events fitting mode

In order to extract $\tau_{t=0}$ and τ_0, the time resolved signals as shown in Figure 36 were analyzed for each wavelength by a data analysis program written in lab view. τ_0 was obtained as the intercept of the linear regression of all the ring-down events occurred during the 2 seconds before the photolysis pulse. For extracting $\tau_{t=0}$, all ring-down events occurred after the photolysis pulse were fitted by a two phase association fit (details in Chapter 5) and extrapolated the fit to time zero to get the intercept which corresponds to $\tau_{t=0}$. The signal shown in Figure 36 yields one data points each corresponding τ_0 and $\tau_{t=0}$ for the wavelength where the time resolved kinetics is measured.

The main difference between the ring-down events fitting mode and the ring-down events average mode is that in the former mode the entire time resolved kinetics corresponding to each wavelength is saved and analysed. This helps in analysing the signal after looking at its dynamics where in the latter mode this is not possible. The drawbacks of the ring-down event fitting mode are: data analysis is time consuming, the ring-down events can not be positioned relative to the photolysis pulse instead they occur randomly and it may not be applicable for transient species with very fast decay times.

Figure 37 summarises the strategy for measuring the absorption spectra using ring-down events fitting mode.

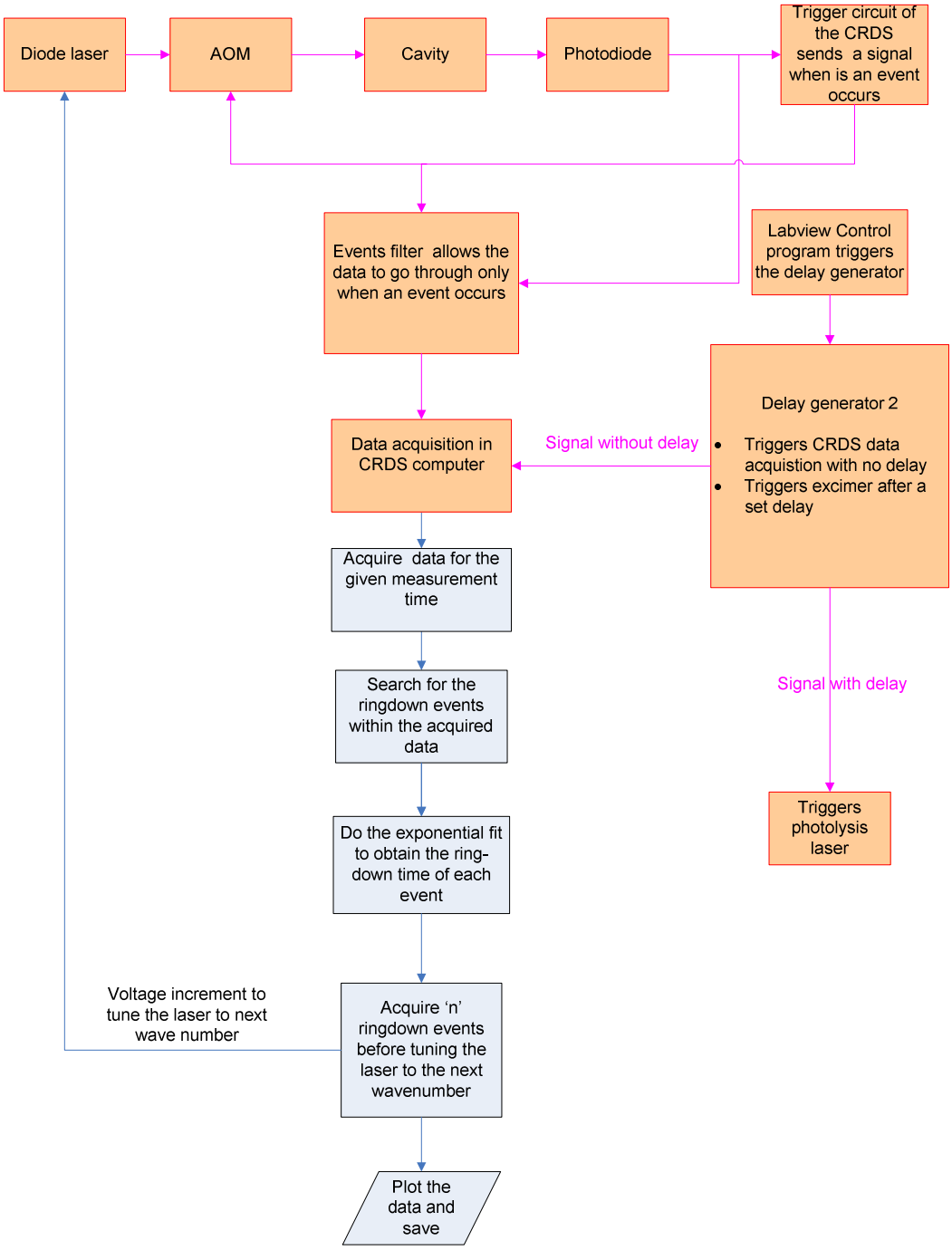

Figure 37: Measurement strategy flow diagram for absorption spectra of the species with transient concentration measured ring-down events fitting mode.

2.6 List of Labview programs for different measurements

The kinetic and spectroscopic measurements and the data analysis of this work are performed by using different programs written in Labview software 8.2.2 version. The following is the list of all the Labview programs used for different measurement configurations and data analysis.

2.6.1 Programs associated with measurements

- Kinetics.vi; this program is used to measure the HO_2 radical kinetics when the cw-CRDS technique is synchronised with the LIF measurements for simultaneous, time resolved OH and HO_2 kinetic measurements.
- Photon counting-kinetics synchronised with excimer.vi; this program is used to measure the OH radical kinetics when the LIF technique is synchronised with the cw-CRDS measurements for simultaneous, time resolved OH and HO_2 kinetic measurements.
- Kinetics-grouped events.vi; this program is used to measure the HO_2 radical kinetics when the photolysis laser is synchronised with the CRDS ring-down events. This allows the user to position the photolysis pulse with respect to the ring-down events.
- Laser control.vi; this program is used to scan the excitation laser of the LIF technique to find the OH absorption wavelength and lock the laser to the OH absorption line.
- Photon emission counting.vi; this program is used to count the photons from the CPM in regular time bins for a specific total measurement time for phosphorescence or some light emission studies from different chemical species e.g. count photons in 100 µs bins for a total measurement time of 0.5 s
- Spectrum-continuous photolysis.vi; this program is used to measure the absorption spectrum using the cw-CRDS technique for a species with a constant concentration.
- Spectrum-pulsed photolysis new.vi; this program is used to measure the absorption spectrum using the cw-CRDS technique synchronised with the photolysis pulse. The photolysis pulse will be triggered by one of the ring-down events after a set delay to measure the baseline.
- Spectrum-pulsed photolysis-LV triggered.vi; this program is generally used for long measurement time absorption spectroscopy where data size is big and the program needs to wait until the data processing is finished as explained in section 2.5.2.2.
- Tau0.vi; this program is used to measure the ring down time and the S/N ratio while aligning the cavity in the cw-CRDS technique. The data is acquired continuously and processed to get the ring-down time for each ring-down event. A

user defined number of ring-down events are averaged and the value is used for the S/N ratio calculation.

- Modul triang.vi; this program is used to control the piezo transducer motion to achieve the resonance between the cavity mode and the light emitted by the laser in cw-CRDS technique.

2.6.2 Programs associated with data analysis

- moykin.vi; this program is used to average all the ring-down events falling in a selected time window from the kinetic measurement data obtained by cw-CRDS technique as shown in Figure 23.
- fit voltage to wavenumber-interpolate.vi; as explained in section 2.5.2.1 the wavenumber is acquired for every 10 increments of voltage and the ring-down time is saved for each individual voltage increment. This yields two different data files, one with voltage and ring-down time for each individual increment and the other with voltage and wavenumber for every 10 increments. This program is used to interpolate to the two data files to get the wavenumber corresponding to the ring-down time recorded for each individual increment of voltage.
- fit voltage to wavenuber-interpolate pulsed photolysis.vi; this program is used to interpolate the data of transient concentration absorption spectrum to get the wavenumber corresponding to the ring-down time recorded for each individual increment of voltage.
- HO_2 concentration calculation.vi; this program is used to convert the CRDS kinetic data into absolute concentration profiles of HO_2. The file containing the ring-down times as a function of delay, manually cleaned from the ring-down times affected by the photolysis pulse (page 53), is the input to the program along with other input parameters like absorption cross-section, absorption path length and the time scale. The program calculates the average of all the ring-down events before the photolysis pulse to determine τ_0 and then converts all τ_t values to HO_2 concentrations using equation (E-16).
- Baseline fit.vi; In the event that an additional absorbing species are produced by the photolysis pulse, the average of the data before photolysis can no longer be taken as the baseline and a more complicated procedure must be used. The procedure and its rationale are described in chapter 4.

- Kinetics fit for the recorded spectrum k imposed; this program is used to analyse the data for the spectra using long acquisition. The details will be given in chapter 5.

2.7 Summary

This chapter has provided an overview of the techniques used in this thesis for measuring OH and HO_2 radicals in the laboratory. The LIF and cw-CRDS techniques which are used to study the simultaneous, time resolved kinetic measurements of OH and HO_2 radicals in this thesis have been explained in detail along with measurement procedures and timing strategies for the different measurement configurations. A list of different Labview programs used for different measurements in the present work is also given.

Chapter 3 - Validation of the experimental technique

Coupling of the LIF and cw-CRDS detection techniques with laser photolysis to measure simultaneous, time resolved kinetics of OH and HO_2 radicals has been implemented during this thesis. Experiments have been carried out with the goal of validating our new experimental system for simultaneous and time resolved kinetic measurements of OH and HO_2. This chapter presents results obtained from the validation experiments and first applications of the new experimental system.

3.1 Validation of LIF and cw-CRDS techniques coupled to a laser photolysis reactor

Few experiments have been reported on the simultaneous, time-resolved and selective detection of both species: Taatjes and co-workers have studied several systems by coupling laser photolysis to a detection of HO_2 radicals by infrared absorption of the overtone of the O−H stretch near 1.5 μm using wavelength modulation spectroscopy. OH radicals have been monitored simultaneously by either direct absorption of the vibrational fundamental at 3484.6 cm^{-1} using an F-center laser [67, 68] or by LIF [69]. The quasi-simultaneous detection of both radicals by coupling laser photolysis to a detection of HO_2 radicals by cw-CRDS and OH radicals by using the “classical” LIF has been reported in an earlier work of our research group [70]. The OH-radicals were probed at a given delay after the photolysis pulse and covering the entire concentration time profile step by step through changing the delay between both lasers. This method is rather time consuming and asks for the same repetition rate of both lasers, in general 10 Hz. Such a rapid photolysis rate however was not compatible with the cw-CRDS acquisition mode mainly for two reasons [9]: (a) the synchronisation mode between photolysis laser and cw-CRDS ring down technique was realized by using an oscilloscope for data acquisition with subsequent transfer of large data sets to a PC, not feasible at 10 Hz and (b) for cw-CRDS measurements the photolysis beam must cross the reactor through the long axis which makes it nearly impossible to renew the gas mixture between two photolysis shots at a rate of 10 Hz. Hence in the earlier configuration [9] it was necessary to switch the photolysis axis when changing from one method to the other in order to obtain both, OH and HO_2 concentration time profiles. Therefore an improved experimental set-up allowing for

truly simultaneous and time resolved measurements of OH and HO_2 radical kinetics after laser photolysis has been developed in the course of this thesis. There are two major improvements:

(1) OH radicals are now detected by LIF using a high repetition rate dye laser (10 kHz). This type of laser gives access to the entire OH concentration time profile after each photolysis shot with a time resolution of 100 µs. Averaging is still required with this modified system over many photolysis pulses, so the absolute time benefit of this modification compared to the classical set-up is limited. The major advantage is that the repetition rate for the photolysis laser can be lowered to a frequency compatible with the detection of HO_2 radicals by cw-CRDS. This facilitates renewing the gas mixture in the reaction cell between two photolysis pulses.

(2) The acquisition mode of the cw-CRDS set-up has been improved by replacing oscilloscope with a data acquisition card for the fast data transfer through a home-made event-filter. This allows the direct data acquisition by the PC while maintaining the synchronisation of the ring-down events with the photolysis laser.

3.1.1 Validation of LIF

The LIF technique alone using the high repetition rate excitation laser was first validated by measuring the rate constants of the reaction of OH with methanol and deuterated methanol. The reactions of CH_3OH and CD_3OD with OH radicals can be represented as:

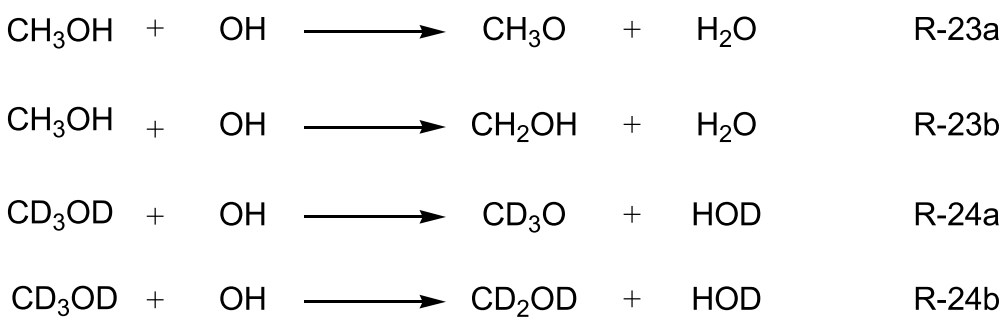

These reactions have been chosen for two reasons: first of all, a new experimental set-up should be validated by reproducing well-known results (R-23) that have been measured many times. The rate constant of the reaction (R-23) is well-known and has been reviewed and a recommended value is available [71].

Therefore reaction (R-23) is a good candidate. The motivation for measuring k_{27} comes from the fact that CD_3OD has been used as a reference compound in smog chamber experiments [72] and only two papers on the rate constant of the abstraction of deuterium from the deuterated homologue of methanol (CD_3OD) have been published [19, 73] previously. Furthermore, there is a considerable difference between the two values: 3.23 and 1.93×10^{-13} cm^3 $molecule^{-1}$ s^{-1} have been reported for k_{24} at 293K by Wallington *et al.* [19] and McCaulley *et al.* [73] respectively. This encouraged this work to obtain a third value for this rate constant. CH_3OH and CD_3OD have been introduced from the premixed (in He) gas bulbs through calibrated flow meters and H_2O_2 has been introduced by bubbling helium through 50% H_2O_2/water mixture.

3.1.1.1 OH radical generation

OH radicals have been produced by 248 nm photolysis of H_2O_2. It is well known [71], that OH radicals react rapidly with H_2O_2

$$H_2O_2 + h\nu(248\ nm) \longrightarrow 2\ OH \qquad \text{R-25}$$

$$OH + H_2O_2 \longrightarrow HO_2 + H_2O \qquad \text{R-26}$$

A large excess of CH_3OH over the radical concentration has been used to maintain the pseudo first-order conditions. As a consequence, radical decay kinetics follows the equation:

$$-\frac{d[OH]}{dt} = \left(k_{23}[CH_3OH] + k_{26}[H_2O_2] + k_d\right)\times[OH] \qquad \text{E-17}$$

with k_{23} being the second-order rate constant for the reaction of OH with CH_3OH, k_{26} being the second-order rate constant for reaction (R-26) and k_d representing the loss of OH radicals due to diffusion out of the detection volume or reactions with other impurities. The exponential decays of OH with

$$k_{obs} = k_{23}[CH_3OH] + k_{26}[H_2O_2] + k_d \qquad \text{E-18}$$

being the pseudo first order decay rate (s^{-1}) are obtained considering that $[CH_3OH]$ and $[H_2O_2]$ are constant.

3.1.1.2 Kinetic measurements

Figure 38 shows the decays for OH radicals in the presence of different concentrations of CH_3OH.

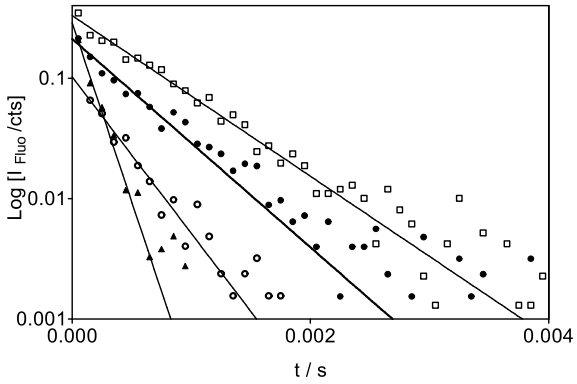

Figure 38: OH radical decays in the presence of different concentrations of CH_3OH as a function of time.

In Figure 38 the fluorescence intensity has been normalized to the number of accumulated photolysis laser shots: it can be seen, that one fluorescence photon was on average obtained for every 3 to 10 photolysis shots. A slight decrease with increased CH_3OH concentration would be expected due to increased fluorescence quenching. However, the decrease in intensity for the decay $[CH_3OH] = 1.9\times10^{15}$ molecules cm^{-3} was probably due to a slight drift in the fluorescence excitation wavelength caused by the instability of the dye laser. From exponential decays like those shown in Figure 38 the pseudo-first order rate constants have been obtained by non-linear regression. These pseudo-first order rate constants were then plotted against the CH_3OH concentration (Figure 39) in order to obtain the second-order rate constants k_{26} and k_{27} from a linear regression. The intercept of the regression line corresponds to the sum of $k_{26}[H_2O_2]+k_d$, i.e. the loss of OH radicals without any added reactant.

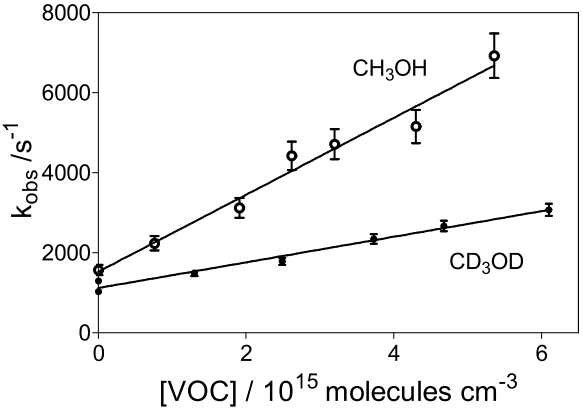

Figure 39: Plot of pseudo-first order rate constants against the CH_3OH/CD_3OD concentrations. The error bars represent the 95% confidence levels between the fit and the data points.

From Figure 39 the following rate constants for reactions (R-23) and (R-24) have been obtained at 295 K:

$CH_3OH + OH$: $k_{23} = (9.6\pm0.7)\times10^{-13}$ cm^3 $molecule^{-1}$ s^{-1}

$CD_3OD + OH$: $k_{24} = (3.2\pm0.2)\times10^{-13}$ cm^3 $molecule^{-1}$ s^{-1}

A very good agreement has been found between the rate constant k_{26} and recent recommendations for this rate constant [71, 74]: $(9.1\pm0.9)\times10^{-13}$ $cm^3molecule^{-1}s^{-1}$. For the reaction of CD_3OD, only two earlier references are known with values of k_{24}=3.23 and 1.93×10^{-13} cm^3 $molecule^{-1}$ s^{-1} by Wallington *et al.* [19] and McCaulley *et al.* [73] respectively. The agreement of the value obtained in the present work with Wallington *et al.* [19] is excellent, whilst the value of McCaulley *et al.* [73] is much lower. Wallington *et al.* [19] have used a similar technique; OH radical generation by vacuum UV photolysis of H_2O using N_2-pulsed discharge flash lamp at 0.25 Hz repetition rate and detection of OH radicals by resonance fluorescence. McCaulley *et al.* [73] used a flow tube at 3 Torr with generation of OH radicals by microwave discharge of H_2 and added NO_2 downstream. Reactions (R-23) and (R-24) being abstraction reactions, the pressure difference should not have any influence on the rate constant.

However an argument for the disagreement with the value of McCaulley *et al.* [73] can be made taking the fact that, under our conditions the “acidic” D-atoms from CD_3OD can be exchanged with H in contact with water from the H_2O_2 water mixture. In that case the measured rate constant is a combined value of reactions $CD_3OH + OH \rightarrow CD_3O + H_2O$ and R-24b instead of R-24a and R-24b. The rate constant for the R-23a and R-23b are 1.4×10^{-13} and 7.7×10^{-13} $cm^3molecule^{-1}s^{-1}$ respectively [75]. If the rate constant by McCaulley were correct, a rate constant for the reaction $CD_3OD+OH \rightarrow CD_3O + HDO$ of 2.8×10^{-14} can be estimated (same fraction). Using this estimated rate constant, we can calculate a rate constant for reactions including the exchange as: $(1.93 - 0.28 + 1.4)\times10^{-13} = 3.1\times10^{-13}$ $cm^3molecule^{-1}s^{-1}$ which is close to our value. Therefore one can suspect the same might have happened in the work by Wallington *et al.* [19] but it has not been discussed. Further more the gas phase exchange rate of D by H for methanol under our condition is not very well known; hence we can’t conclude which one of the rate constants for the reaction CD_3OD+OH is correct.

This experiment validated the modified LIF technique using the new high repetition rate laser by measuring the well known rate constant of the reaction (R-23). The rate constant obtained is in good agreement with the recommended value suggesting the reliability of the experiment. Then the experiment has been extended to measure the rate constant of reaction (R-24). In section 3.1.2, the validation of the simultaneous kinetics measurements of OH and HO_2 will be presented.

3.1.2 Simultaneous, time resolved measurements of OH and HO_2 and their application to the photolysis of H_2O_2

The capabilities of this new set-up have been demonstrated on a simple and well-known system, the photolysis of H_2O_2 at 248 nm. This experiment has been chosen not only to demonstrate the capability of the new experimental set-up, but also to measure the absorption cross sections of H_2O_2 in the near infra-red region to have a handy tool to quantify H_2O_2 concentration in the photolysis reactor for future experiments. The absorption cross sections of two selected absorption lines of H_2O_2 in the near IR have been determined by cw-CRDS, using the relative OH-decay from LIF measurements for the determination of the H_2O_2 concentration. HO_2 profiles are used to calculate the impact of secondary reactions in order to validate the spectroscopic applications of cw-CRDS technique.

3.1.2.1 OH and HO_2 radical generation and their kinetics

The same method used in section 3.1.1.1 is used to generate radicals. The carrier gas used was helium and H_2O_2 was introduced into the cell by bubbling 20 sccm of the Helium flow through a 50% H_2O_2/H_2O solution. The H_2O_2 concentration was varied by varying the dilution helium flow. Previous studies [76–78] on the photolysis of H_2O_2 at 248 nm have shown that the only photolysis products are OH radicals *via* following reaction.

$$H_2O_2 + h\nu(248\ nm) \longrightarrow 2\ OH \qquad \text{R-25}$$

The OH radicals formed in (R-9) subsequently react with H_2O_2

$$OH + H_2O_2 \longrightarrow HO_2 + H_2O \qquad \text{R-26}$$

The rate constant of this reaction is well known [79], $k_{28} = 1.7 \times 10^{-12}$ cm^3 $molecule^{-1}$ s^{-1} and therefore the H_2O_2 concentration can be evaluated by measuring the OH decay under pseudo-first order conditions. However, subsequent rapid reactions such as

$$OH + HO_2 \longrightarrow H_2O + O_2 \qquad \text{R-27}$$

have to be taken into account, especially when using high photolysis energies. Typical OH and HO_2 profiles are shown in Figure 40: in the upper Figure 40 (A) the OH decays are shown for four different H_2O_2 concentrations, in the lower Figure 40 (B) the simultaneously obtained HO_2 profiles are shown.

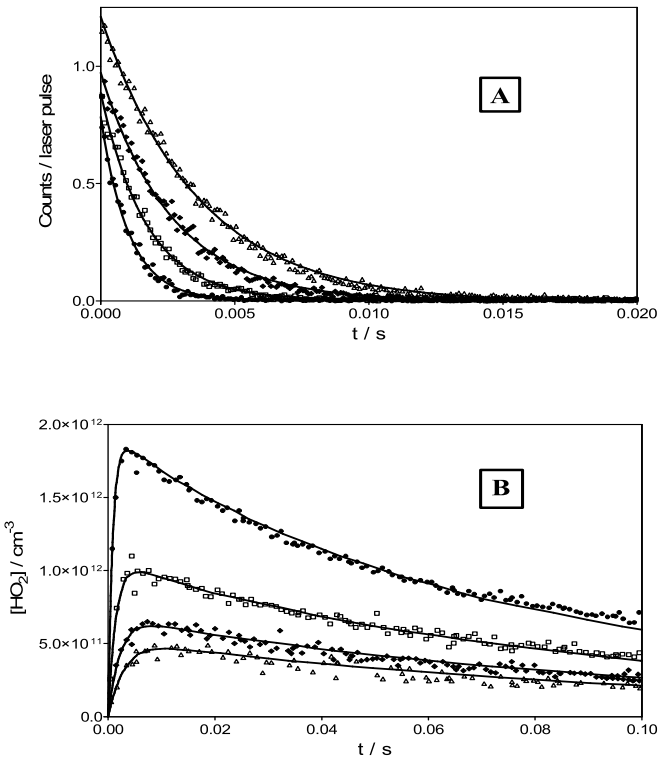

Figure 40: (A) Plot of OH fluorescence count/ laser shot vs time at different H_2O_2 concentrations, (B) plot of HO_2 concentration vs time at different H_2O_2 concentrations. •: $[H_2O_2]$ = 4.8×10^{14} molecules cm^{-3}, $[OH]_0$=2.4×10^{12} cm^{-3}, : 3.1 and 1.3, ♦: 2.0 and 0.84, Δ: 1.5 and 0.65.

The OH-concentration decay rate increases with increasing H_2O_2 concentration, but also the peak LIF intensities (expressed in counts per photolysis shot) decrease with increasing H_2O_2 concentration: this is due to faster OH fluorescence quenching with the increase in H_2O concentration. The H_2O_2 concentration has been obtained through a one-iteration procedure: a first guess of the H_2O_2 concentration was obtained from an exponential fit of the OH-decays in Figure 40 (A) considering only reaction (R-26) and assuming pseudo-first order (PFO) conditions, this leads directly to $[H_2O_2]_{PFO}$. However, reaction (R-27) being fast, the "real" OH-decay is also influenced by this reaction, and the deviation from PFO-conditions increases with increasing radical concentration or increasing

photolysis energy, both resulting in increased OH and HO_2 concentrations. The $[H_2O_2]_{PFO}$ concentration has been used as input parameter for modelling the absolute HO_2-concentration-time profiles from Figure 40 (B) using a simple model. as given in the Table 4 below :

No.	**Reaction**	**Rate constant**	**Reference**
R-25	$H_2O_2 + h\nu \rightarrow 2\ OH$	$\phi = 2$	Vaghjiani *et al.* [77], Thiebaud *et al.* [76]
R-26	$H_2O_2 + OH \rightarrow H_2O + HO_2$	1.8×10^{-12} cm^3 molecule^{-1} s^{-1}	Sander *et al.* [79]
R-27	$HO_2 + OH \rightarrow O_2 + H_2O$	1.1×10^{-10} cm^3 molecule^{-1} s^{-1}	Sander *et al.* [79]
R-28	$OH + OH + M \rightarrow H_2O_2 + M$	1.0×10^{-12} cm^3 molecule^{-1} s^{-1}	Sander *et al.* [79]
R-15	$2\ HO_2 \rightarrow H_2O_2 + O_2$	1.45×10^{-12} cm^3 molecule^{-1} s^{-1}	Sander *et al.* [79]
R-29	$HO_2 \rightarrow$ loss	10 s^{-1}	
R-30	$OH \rightarrow$ loss	10 s^{-1}	

Table 4: Reaction mechanism used to fit the HO_2 concentration time profiles.

In the beginning, OH radicals will predominantly react with H_2O_2 to form HO_2 radicals (R-26). As the reaction advances and HO_2 radical concentration increases, reaction (R-27) becomes more important during the time interval where OH is still present and HO_2 is already present. In the absence of other reaction partners, the HO_2 yield depends on (a) the decay rate of OH radicals, i.e. on the initial H_2O_2 concentration and (b) on the total radical concentration: both factors influence the loss of radicals (OH and HO_2) through their impact on reaction (R-27) [80]. Finally at longer reaction times, the HO_2 radicals recombine (R-15). HO_2 and OH radicals will also be lost from the reaction zone and the observation volume through diffusion out of the detection volume (R-29 and R-30).

These fits return absolute initial OH concentrations, which in turn will be used as input parameters to refit the OH-decays from Figure 40 (B), now taking into account the full model [80]. These improved fits give the “real” H_2O_2 concentration, which is always lower than $[H_2O_2]_{PFO}$, because now the OH-decay is partially explained by secondary reactions such as (R-27). Another iteration refining the HO_2-profile was not necessary, because the HO_2 profile was not sensitive to the initial H_2O_2 concentration. Under our conditions, the difference between $[H_2O_2]_{PFO}$ and “real” $[H_2O_2]$ as obtained by the full model was 16% and 6% for the highest

and lowest initial concentration, respectively. This way absolute H_2O_2 concentration using time resolved OH and HO_2 profiles have been obtained. The measurement of the absolute absorption cross-sections of H_2O_2 on two selected lines using the H_2O_2 concentration time profiles will be described in the following section.

3.1.2.2 Measurement of absorption cross-sections of H_2O_2 lines in the near infrared region

The H_2O and the H_2O_2 / H_2O spectrum has been recorded using cw-CRDS technique in the wavelength range accessible with our laser diode (6623.5-6645.5 cm^{-1}). The water absorption spectrum was measured to compare with the H_2O_2/H_2O spectrum and to separate the H_2O from the H_2O_2 absorption lines. A part of the spectra is shown in Figure 41(A) (full spectrum is given in appendix A.1).

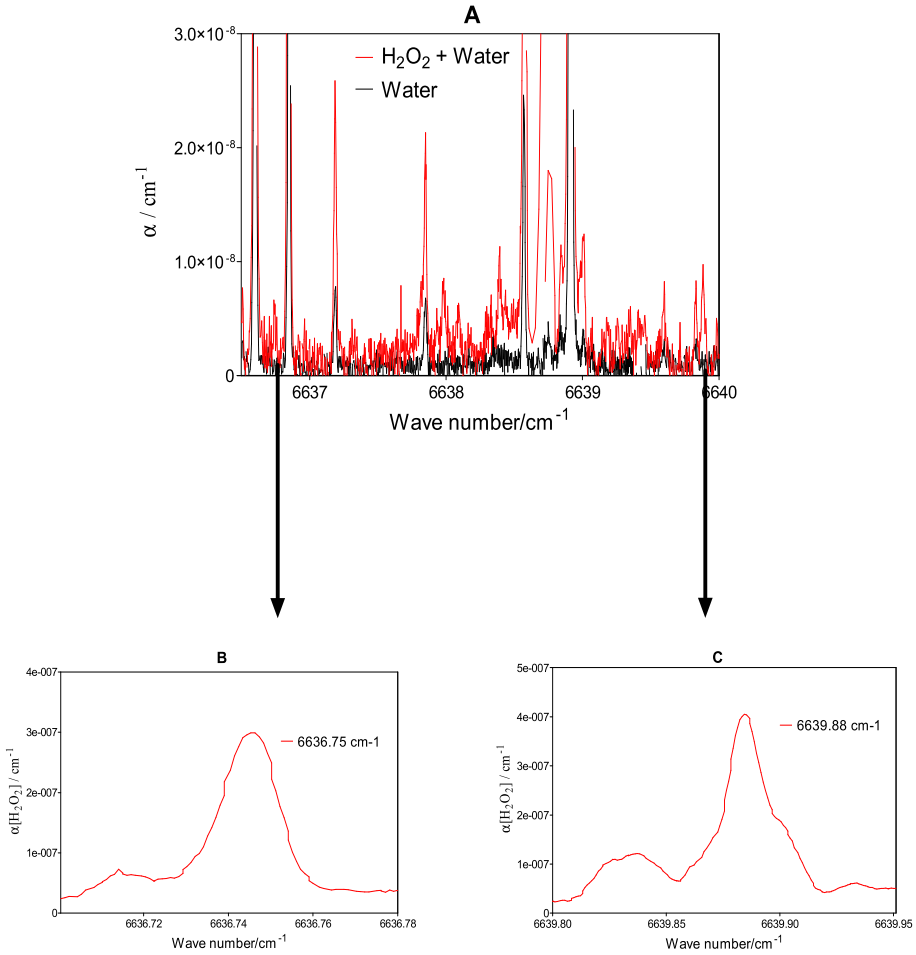

Figure 41: (A) spectra of water and H_2O_2 from 6636.5 to 6640 cm^{-1} at 50 Torr helium, (B) and (C) zooms of H_2O_2 lines at 6636.75 and 6639.88 cm^{-1} respectively.

32 ring-down events were recorded and averaged at each wavelength before incrementing the diode laser wavelength by 0.0015 cm^{-1}. Water is a strong absorber in this wavelength region (as shown in Figure 41). Therefore two H_2O_2 lines (Figure 41(B) and Figure 41(C)), which are not disturbed by the predominant water absorption, have been selected to quantify H_2O_2 using cw-CRDS technique. The absorption spectra for both lines have been recorded at different H_2O_2 concentrations. The baseline has to be measured in the absence of H_2O_2 due to the dense absorption spectrum of H_2O_2 as shown in Figure 42. The H_2O_2 peak absorption lines are not isolated and hence the absorbance does not go to zero next to the peak absorption lines. If the ring down time before or after the peak absorption line is taken as the baseline then it will lead to an error in the calculation.

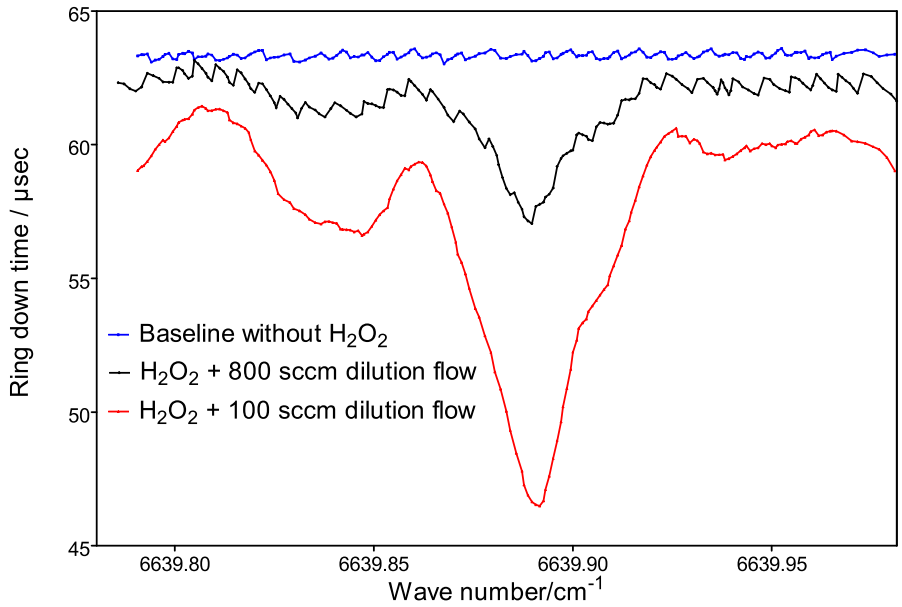

Figure 42: H_2O_2 absorption on 6639.88 cm^{-1} at two different concentrations showing the dense absorption of H_2O_2 on either sides of the absorption peak.

The absolute concentrations of H_2O_2 have been obtained by the procedure explained in section 3.1.2.1. The peak absorbencies measured for different concentrations of H_2O_2 on the two selected lines were then plotted against the H_2O_2 concentrations (Figure 43). The error bars for the α-values correspond to S/N = 1 of the baseline and the error bars for the H_2O_2 concentrations are from the errors in the OH decay fits used for H_2O_2 concentration calculation.

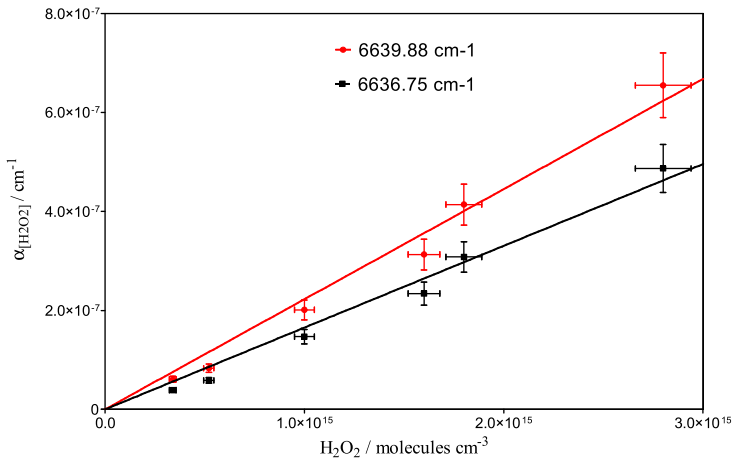

Figure 43: Plots of absorption coefficient on two different H_2O_2 absorption lines versus H_2O_2 concentrations.

Using the slopes of the plots shown in Figure 43, the peak absorption cross-sections at 6636.75 and 6639.88 cm^{-1} in 50 Torr Helium were calculated to be (1.65 ± 0.2) and (2.23 ± 0.16) x 10^{-22} cm^2 respectively. Errors represent the 95% confidence level between the experimental data points and the fit. The absorption cross section of the line at 6636.75 cm^{-1} is somewhat smaller than at 6639.88 cm^{-1}; however, the latter line seems to be the convolution of two different H_2O_2-absorption lines, which is also possibly the reason for the higher uncertainty of the obtained absorption cross section. For this reason, care has to be taken while using this absorption line for measurements at different pressures. Therefore a study on the pressure broadening has been carried out in helium at three different pressures (10, 50 and 74 Torr). Table 5 shows the absorption cross-sections of two H_2O_2 absorption lines (6636.75 and 6639.88 cm^{-1}) at different pressures.

Wavenumber/cm^{-1}	σ / 10^{-22} cm^2 at 10 Torr	σ / 10^{-22} cm^2 at 50 Torr	σ / 10^{-22} cm^2 at 74 Torr
6636.75	2.42 ± 0.1	1.65 ± 0.2	1.35± 0.16
6639.88	3.14 ± 0.05	2.23 ± 0.16	1.81± 0.15

Table 5: Absorption cross-sections of H_2O_2 absorption lines at different pressures.

Using the measured absorption cross-sections of selected H_2O_2 lines at different pressures, the line strength and the pressure broadening coefficient in helium have been calculated. For practical purposes, Table 6 lists the line strength and pressure broadening coefficient for the two (6636.75 cm^{-1} and 6639.88 cm^{-1})

H_2O_2 absorption lines, obtained from a best fit of the pressure dependant absorption cross sections to a Voigt profile.

Wave number / cm^{-1}	Line strength / 10^{-24} cm	Pressure broadening co-efficient / cm^{-1} atm^{-1} (He)
6636.75	4.1	0.068
6639.88	5.5	0.068

Table 6: Line strength and pressure broadening co-efficient for the two (6636.75 cm^{-1} and 6639.88 cm^{-1}) H_2O_2 absorption lines.

This study has been further extended to measure a few more H_2O_2 absorption lines in the near infrared region at 10 Torr helium as part of a collaboration with *Laboratoire Reactions et Genie des Procedes (LRGP), ENSIC, Nancy*. Table 7 lists the absorption cross sections of different absorption lines at 10 Torr helium.

Wavenumber / cm^{-1}	σ /10^{-22} cm^2 at 10 Torr Helium
6642.21	1.32 ± 0.1
6642.14	1.88 ± 0.2
6642.06	1.05 ± 0.25
6638.75	1.18 ± 0.075
6638.66	0.781 ± 0.02

Table 7: Absorption cross sections of H_2O_2 measured at 10 Torr helium in the near infrared region.

These experiments allowed the validation of synchronised LIF and cw-CRDS kinetic measurements by measuring simultaneous, time resolved kinetics of OH and HO_2 using H_2O_2 as the precursor. The absolute absorption cross-sections of H_2O_2 absorption lines in the near infrared region have been measured using absolute concentrations of the H_2O_2 extracted from the OH and HO_2 kinetic data. In the following section the utility of this experimental system has been demonstrated in another application by measuring the HO_2 yield in the OH-initiated oxidation of SO_2.

3.2 Yield of HO_2 radicals in the OH-initiated oxidation of SO_2

The formation of new aerosol particles in the atmosphere has been the subject of intense studies in the field and in the laboratory for many years. Different formation mechanisms have been proposed, but still it is not clear which of them is dominating in the troposphere [81] and the participating substances have not yet been fully identified. Large discrepancies between model-predicted nucleation rates for the favoured binary system H_2SO_4-H_2O and much higher atmospheric nucleation data have been explained by additional species such as ammonia [81]. However, nucleation events in the lower troposphere were found to be closely connected to the appearance of H_2SO_4 for concentrations of 10^7 molecules cm^{-3} and below, measured at various sites [82]. Recent laboratory studies have suggested that the OH-initiated oxidation of SO_2 is much more effective for the process of particle formation and growth than equivalent concentrations of H_2SO_4 vapor [83–85]. It has therefore been suggested that reaction products other than H_2SO_4, i.e. intermediate species in the OH-initiated SO_2 oxidation process, might trigger the particle formation [85].

The commonly accepted homogeneous oxidation mechanism of SO_2 under atmospheric conditions includes the following reactions:

$$OH + SO_2 + M \longrightarrow HSO_3 + M \qquad \text{R-31}$$

$$HSO_3 + O_2 \longrightarrow SO_3 + HO_2 \qquad \text{R-32}$$

$$SO_3 + 2\,H_2O \longrightarrow H_2SO_4 + H_2O \qquad \text{R-33}$$

whereby (R-32) is written as an overall reaction, but proceeds more likely through a two-step mechanism [86].

$$HSO_3 + O_2 + M \longleftrightarrow HSO_5 + M \qquad \text{R 34a, -34a}$$

$$HSO_5 + M \longleftrightarrow SO_3 + HO_2 \qquad \text{R 34b, -34b}$$

A hypothesis has therefore been proposed by Kurten *et al.* [87] stating that the intermediate HSO_5 radicals might live long enough to build a complex with H_2O:

$$HSO_5 + H_2O + M \longleftrightarrow HSO_5\text{-}H_2O + M \qquad \text{R-35}$$

This addition complex could subsequently trigger nucleation through the formation of larger clusters with other water molecules or through formation of peroxodisulfuric acid, $H_2S_2O_8$ by self-reaction. However, a recent series of theoretical papers including quantum chemical calculation for deducing thermo-chemical data of intermediates possibly involved in the SO_2 oxidation mechanism [88–90] combined with master-equation calculations of the kinetics of the chemically activated HSO_5 radical under atmospheric conditions [86] concluded that the lifetime of the HSO_5 radicals is not long enough to undergo bimolecular reactions. In the meantime, Sipilä *et al.* [91] have undertaken new laboratory experiments to unravel the mystery of increased nucleation power of freshly formed H_2SO_4 compared to H_2SO_4 from a liquid reservoir and have identified the geometrical configurations of the experimental set-ups; from these results they rule out a major participation of HSO_5 radicals in the nucleation process, in agreement with the work of Gonzalez-Garcia and Olzmann [86].

In this work, HO_2 radical yields during the OH-initiated oxidation of SO_2 in presence of O_2 (R-31, R-32) has been measured. HO_2 radicals as product of this reaction sequence have already been identified indirectly in an early work [92] through recycling of HO_2 radicals back to OH radicals by addition of NO in flow tube experiments. However, in the present work, the selective and direct detection of HO_2 radicals by cw-CRDS coupled to laser photolysis has been carried out. The yield of HO_2 radicals in reaction (R-32) has been determined by modelling the measured HO_2 profiles to a simplified reaction mechanism.

Photolysis of H_2O_2 at 248 nm leads to the formation of two OH radicals which in the absence of other reaction partners, predominantly transformed into HO_2 radicals as explained in section 3.1.2.1. A typical HO_2 profile obtained from such an experiment is shown as the lower curve in Figure 44: the increase in HO_2 concentration at short reaction times is governed by reaction (R-26), while the decrease at longer reaction times is, under our conditions, mainly due to diffusion: the self-recombination is a slow process at typical HO_2 concentrations of 10^{12} cm^{-3}.

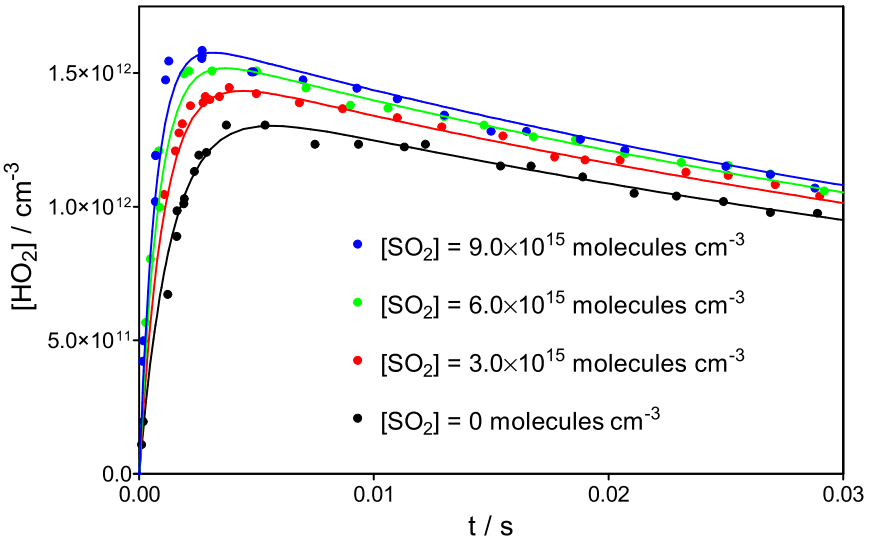

Figure 44: HO_2 concentration-time profiles following the photolysis of 3.2×10^{14} molecules cm^{-3} H_2O_2 (lower curve, black dots) and in the presence of three different SO_2 concentrations. Full lines describe a simulation using a model (consisting R-31, R-32a, R-32b and the reactions in Table 4) with a branching ratio of 1 for reaction (R-32a).

Rate constants for the reactions (R-15, R-26, R-27 and R-28) are fairly well known (see Table 4), and from a fit of HO_2 concentration time profiles to the reaction mechanism (section 3.1.2.1) one can therefore obtain the initial H_2O_2 and OH concentration: The HO_2 profiles are not very sensitive to the initial H_2O_2 concentration; therefore the initial H_2O_2 concentration has also been obtained by measuring the OH decays using LIF. The H_2O_2 concentration determined this way was $[H_2O_2]_0 = 3.2 \times 10^{14}$ cm^{-3}, the initial OH radical concentration was found from the fit of the HO_2 signal to be $[OH]_0 = 1.9 \times 10^{12}$ cm^{-3}. The OH radical concentration, calculated from Beer-Lambert law using the measured laser photolysis energy of 28 mJ cm^{-2} and the well-known absorption cross section for H_2O_2 at 248nm ($\sigma_{H_2O_2,248nm} = 9.37\times10^{-20}$ cm^2) [77] leads to an initial OH concentration estimate of $[OH]_0 = 2.1 \times 10^{12}$ cm^{-3}, in good agreement with the value obtained from fitting the HO_2 concentration time profiles.

Addition of SO_2 and the effect on HO_2 and OH profiles

Addition of SO_2 to the reaction mixture will lead to a competition between (R-26) and

$$OH + SO_2 + M \longrightarrow HSO_3 + M \qquad \text{R-31}$$

Reaction (R-31) is pressure dependant [93] and under our conditions still in the fall-off range with a rate constant of k_{31} = 8.3 × 10^{-14} cm^3 $molecule^{-1}$ s^{-1} at 40 Torr He [94]. Attempts of measuring simultaneously the OH-decay by LIF and the HO_2 formation by cw-CRDS in order to more reliably validate the reaction mechanism and the HO_2-formation yield have failed due to an intense, long-lived light emission following the photolysis pulse, masking the OH-fluorescence signal. The decay rate of this emission has been k ≈ 92 s^{-1} independent of the excitation energy and only slightly dependant on the SO_2 concentration ($k_{quenching?}$=2×10^{-15} cm^3s^{-1}). Hippler *et al.* [95] have measured the temperature dependant SO_2 absorption spectrum and have used the strong temperature dependence of the absorption minimum at around 240 nm in order to study the collisional energy transfer of highly excited SO_2 [96]. Even though the SO_2 absorption coefficient is at a minimum at around 248 nm [97] with an absorption cross section of σ_{248nm} = 9.5×10^{-20} cm^2, complicated photochemistry following 248 nm excitation has already been reported by Fulle *et al.* [93] and others. Figure 45 shows the emission monitored through the interference filter at 308±10 nm following 248nm excitation of 3×10^{16} molecules cm^{-3} SO_2 at variable excitation energies.

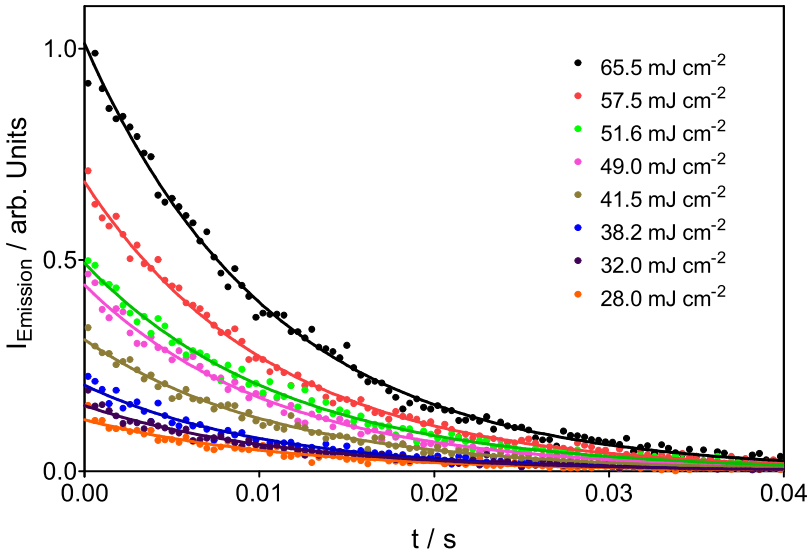

Figure 45: Light emission observed at 308 ± 10 nm after 248 nm excitation of 3×10^{16} molecules cm^{-3} SO_2 at different excitation energies.

This emission has its origin in multi-photon absorption of SO_2, as can be seen in Figure 46: the observed emission intensity is plotted as a function of the excitation energy and suggests the implication of 3 photons, possibly with partial saturation.

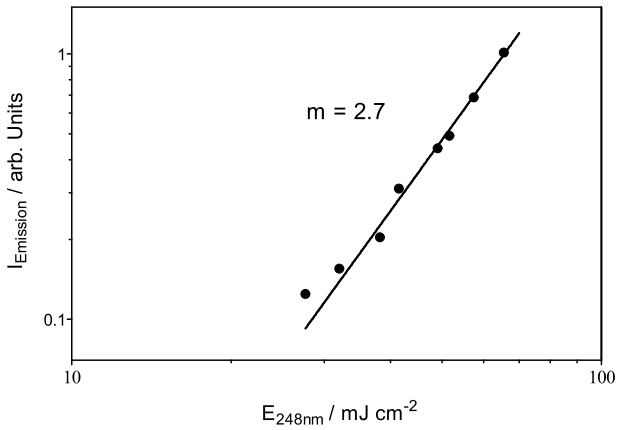

Figure 46: Emission intensity at 308 ± 10 nm as a function of 248 nm excitation energy.

Wilson *et al.* [98] have studied the multiphoton photofragmentation of SO_2 at 248 nm and have observed emission of SO fluorescence in the wavelength range of 250 – 400 nm. As the lowest channel for the dissociation of SO_2 into SO lies at 219 nm [99], the authors have suggested a sequential 2-photon absorption with subsequent excitation of the hot SO (v" = 2, J" ≈ 15-25), having a transition within the bandwidth of a free-running excimer laser [100]. The subsequent fate of the generated O-atoms is probably under our conditions the recombination with O_2: even though the recombination of O-atoms with SO back to SO_2 is fast, this reaction is strongly pressure dependant and in the fall-off range under our conditions [101]. In order to minimize the impact of the photofragments on the reaction mechanism, the photolysis energy has been lowered to 28 mJ cm^{-2}, i.e. the lowest photolysis energy from the experiments in Figure 45. In addition, the HO_2-yield measurements have been conducted at low SO_2 concentrations which will further minimize the impact of possible photofragments: the highest SO_2 concentration was three times lower than the concentration used for the experiments in Figure 45. Even under these conditions, the SO emission from the photofragmentation was still visible such that clean and reliable OH-decays could not be obtained. However, this is not a real problem, as OH decays are not essential for studying the title reaction: the gain from OH-decay measurements in the presence of SO_2 would have been mainly cross checking the SO_2 concentration in the reaction cell. We therefore have relied on the calibrated flow meters for calculating the SO_2 concentration.

HSO_3 radicals formed in reaction (R-31) will react under our conditions ($[O_2]$ = 1×10^{17} molecules cm^{-3}) within a few µs with O_2 through two possible pathways

$$HSO_3 + O_2 \longrightarrow SO_3 + HO_2 \qquad \text{R-32a}$$

$$HSO_3 + O_2 \longrightarrow \text{Products} \qquad \text{R-32b}$$

In Figure 44 are plotted three experiments with different SO_2 concentrations added to the initial H_2O_2 mixture: it can be seen that the HO_2 concentration increases with increasing concentration of SO_2. This can be easily understood, because the main loss process for the radical pool preventing the complete conversion of OH radicals into HO_2 is reaction (R-27), and this reaction becomes less and less important with increasing SO_2 concentration as the OH radicals decay faster and faster, now through both, reaction (R-31) and (R-26). The increase in HO_2 concentration with SO_2 depends of course on the branching ratio between both pathways, (R-32a) and (R-32b): the full lines in Figure 44 represent a simulation of the reaction mechanism shown in Table 1 with a $k_{32a} / (k_{32a} + k_{32b}) = 1$, i.e. a 100% yield of HO_2 radicals in the oxidation of HSO_3 radicals.

In Figure 47 the sensitivity of HO_2 concentration time profiles is demonstrated against the branching ratio of reaction (R-32): for the experiment with $[SO_2] = 6.0\times10^{15}$ cm^{-3} three simulations are shown, the upper curve is the same than in Figure 44 with $k_{32b} = 0$, while the middle (red) and lower (blue) curve consider a branching ratio of 0.05 and 0.1 for reaction (R-32b), respectively.

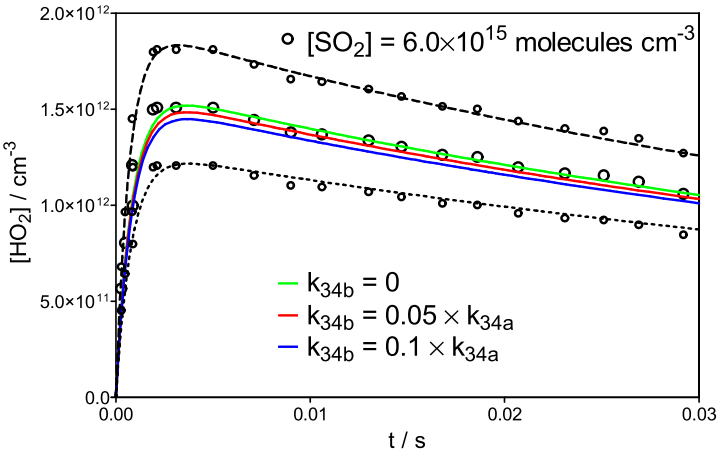

Figure 47: HO_2 concentration-time profiles following the photolysis of 6.0×10^{15} molecules cm^{-3} SO_2 (green curve from Figure 45): green line describe a simulation using a model (consisting R-31, R-32a, R-32b and the reactions in Table 4) with a branching ratio of 1 for reaction (R-32a), red and blue line consider branching ratios of 0.05 and 0.1 for reaction (R-32b), respectively. Upper dashed and lower dotted curve: simulation of a 20% uncertainty in the initial radical concentration.

One can observe that a branching ratio of 0.05 for reaction (R-32b) might still be acceptable within the scatter of the data points, but a branching ratio of 0.1 is clearly not consistent with the HO_2 concentration time profile. A systematic error of the absolute HO_2 concentration has only a minor impact on this conclusion, because the result is drawn from the observation of the change of HO_2 concentration in the presence of SO_2 compared to the HO_2 concentration in the absence of SO_2. The HO_2 concentration is obtained from the geometrical configuration of the photolysis cell, i.e. the overlap of photolysis beam and cw-CRDS beam path, and the absorption cross section of HO_2 at 6638.20 cm^{-1}. The HO_2 absorption cross sections have been determined using the same set-up [65, 66], i.e. using the same geometrical configuration; therefore any uncertainty would cancel out. That said, a recent measurement of the pressure dependant absorption cross sections of HO_2 radicals by Tang *et al.* [26] using TDLAS is in excellent agreement with our measurements. Therefore, we consider that the HO_2 concentration in our experiments is known to better than ± 20%. But even a systematic error of 20% in the HO_2 concentration would only have a minor impact on the branching ratio for reaction (R-32): a decrease of 20% in the HO_2 concentration, i.e. an absorption cross section 20% higher than admitted, can be compensated for by a branching ratio of 0.08 for reaction (R-32b), while an increase of 20% in the HO_2 concentration can only be compensated for by an increase of 30% for the rate constant of (R-31) (1.1×10^{-13} instead of 8.3×10^{-14} cm^3 $molecule^{-1}$ s^{-1}), still within the uncertainty range of the rate constant for (R-32). Both cases are shown as dashed and dotted lines in Figure 5. Another source of systematic error is an uncertainty in the rate constant of (R-31): the evaluation by the IUPAC committee [102] $k_{0,31,N_2}$ is based on the low pressure measurements by Wine *et al.* [94] and recommends an uncertainty of log (k_{31}) = ±0.3, i.e. a factor of 2. Considering the same uncertainty for the measurements of Wine *et al.* [94] in helium the impact of this uncertainty can be evaluated on the extraction of the branching ratio of (R-32): an increase of k_{31} by a factor 2 can be compensated for by a branching ratio of 0.1 for reaction (R-32b), while a decrease of k_{33} by a factor 2 can not be brought into agreement with our experimental observations. Such a decrease of k_{33} leads not only to an underestimation of the HO_2 concentration but also to a rate of formation for HO_2 radicals too slow compared to the experimental

profiles. From these considerations it can be concluded that the measurement of HO_2 concentration time profiles performed in this work is in good agreement with a yield of 1.0 ± 0.1 for the formation of HO_2 radicals in the OH-initiated oxidation of SO_2 in the presence of O_2. This result is in agreement with the currently accepted mechanism as well as with a recent Master-Equation study [86], predicting a lifetime of $HOSO_4$ radical too short for undergoing bimolecular reactions.

3.3 Conclusions

The validation of the new experimental set up has been carried out by measuring the rate constants of well known reactions. The results show a good agreement with the results published previously confirming the reliability of the experimental set up. The studies were extended to measure absorption cross sections for selected lines of H_2O_2 in the near infrared regions which will be helpful for the quantification of H_2O_2 in future laboratory studies.

The HO_2 yield in the OH initiated oxidation of SO_2 has been investigated in this work by direct observation of HO_2 concentration time profiles after 248 nm photolysis of $H_2O_2/SO_2/O_2$ mixtures. Initial OH concentrations have been obtained from a fit of the absolute HO_2 concentration time profiles following the 248 nm photolysis of H_2O_2 / O_2. Upon addition of SO_2 to this reaction mixture an increase in the HO_2 concentration is observed: simulations of these profiles to a simple reaction mechanism are in excellent agreement with a HO_2-yield of 1.0 ± 0.1 for the reaction of HSO_3 radicals with O_2.

Chapter 4 - HO_2 formation from aromatic compounds

Aromatic hydrocarbons (benzene, toluene, xylenes: BTX) are an important class of volatile organic compounds emitted to the atmosphere from vehicle emissions, various industrial processes and from the use of organic solvents [103]. The natural emissions include biomass burning [104] and volcanoes [105]. The presence of aromatic hydrocarbons in the atmosphere was first detected by Lonnemann *et al.* [106] at Los Angeles basin in 1968. Model studies show that aromatic hydrocarbons contribute more than 30% to the photochemical oxidant and smog formation in urban areas [1]. Besides photo-oxidant formation, aromatic hydrocarbons are also assumed to make a significant contribution to the secondary organic aerosol formation [107].

The determination of the influence of these aromatic hydrocarbons is a challenging task, since many of the details of the complex mechanistic pathways are not well known [103]. Many studies have been carried out to understand the mechanisms of the photo-oxidation of these aromatics and include the simulation of experimental observations in photo-reactors [108, 109]. It is proposed that the principal pathway of aromatic hydrocarbon degradation is initiated by the reaction with OH radicals [110, 111]. The oxidation occurs principally *via* two reaction channels either addition to the ring or H abstraction from the substituent group in case of substituted aromatic compounds [110]. Reaction through addition is the dominant channel, about 90% of the reaction takes place through addition. The addition on benzene to form hydroxycyclohexadienyl (HCHD) radical can be written as below:

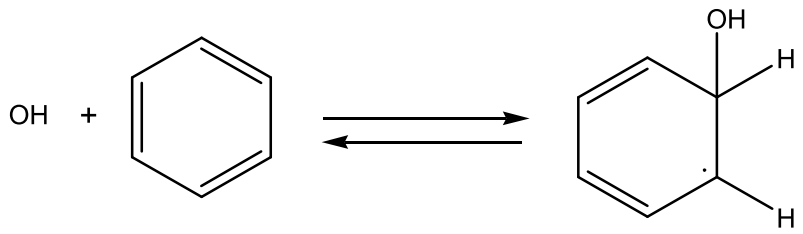

R-36

The OH adduct from reaction (R-36) subsequently reacts with oxygen to peroxy radical or phenol through H abstraction. The peroxy radical formed can undergo subsequent reactions in a more complex mechanism yielding different products.

The most recent mechanism proposed by Nehr *et al*. [107] for the OH initiated oxidation of benzene is shown in Figure 48. The chemistry of the ring-opening routes is still very speculative in nature and many different ring-opening routes have been proposed and proved experimentally. Products reported in the literature have been mainly focussed on the analysis of the OH initiated photo-oxidation of benzene and toluene.

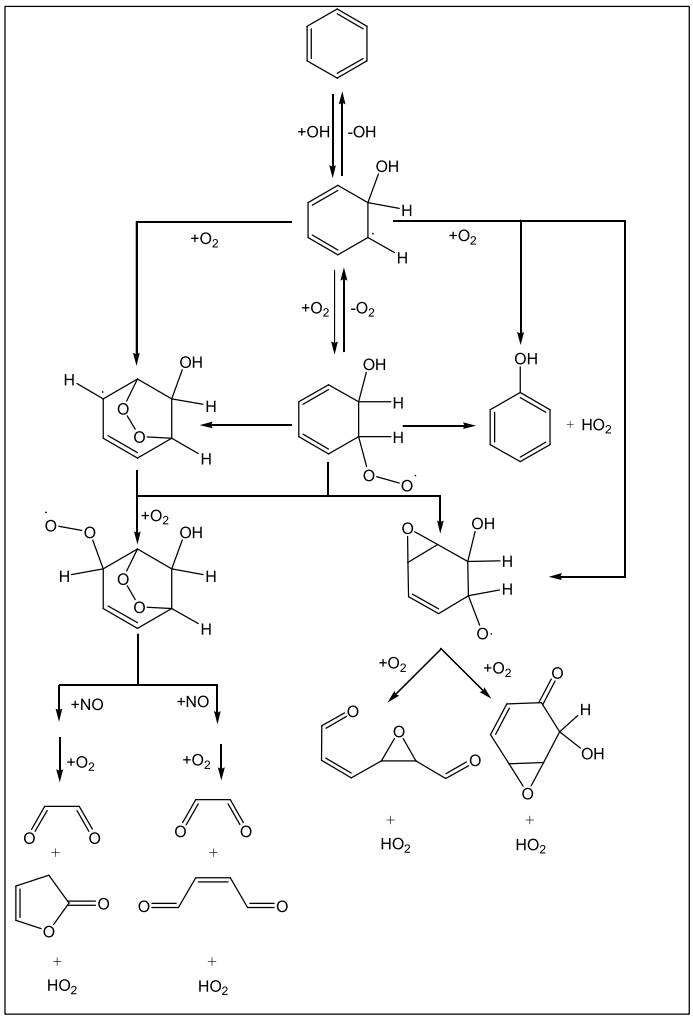

Figure 48: Currently accepted mechanism for the OH initiated degradation of benzene. Reproduced from Nehr *et al.* [107].

Different branching ratios have been reported through different studies for the channel which yields phenol and HO_2 from HCHD radical. It was believed to be 16% [103] then 53% [112] through chamber experiments and later 51% [113] and 61% [114] *via* flow tube experiments. This discrepancy about the branching ratio of the OH initiated benzene degradation channel which yields phenol has given the motivation to the earlier work from our research group [70] to reinvestigate the branching ratio. Laser photolysis reactor coupled to cw-CRDS technique was used

to detect HO_2 radicals and observed the direct formation of HO_2 radicals after 248 nm laser irradiation of a mixture of C_6H_6 and O_2 without OH radical addition to the reaction system. The study was carried out at low photolysis energy (around 15 mJ cm^{-2}) and the energy dependence of the HO_2 yield has not been investigated. The origin of the HO_2 radicals was not clearly determined; however from the time resolved measurements they concluded that the reaction of H-atoms with O_2

$$H + O_2 + M \longrightarrow HO_2 + M \qquad \text{R-37}$$

can not be responsible for the observed HO_2 radicals: the rate constant of this reaction under typical conditions (50 Torr He) is much too slow (2.7×10^{-14} cm^3 $molecule^{-1}$ s^{-1}) [115] and therefore the authors concluded that a fast reaction between excited C_6H_6 and O_2 is responsible for the HO_2 formation. Recently, Kovacs *et al.* [116] have observed the formation of H-atoms after 248 nm excitation of benzene and toluene. By varying the excitation energies in the range 11.5 to 77 mJ cm^{-2} they have shown that 2-photon absorption is responsible for this process. Even though earlier work from our research group [70] has excluded the reaction (R-37) as the origin for the observed HO_2 radicals, Kovacs *et al.* [116] suggested that the observed HO_2 radicals might originate from a reaction of O_2 with 2-photon excitation products other than H-atoms.

The direct HO_2 formation from the irradiation of a mixture of benzene and oxygen at 248 nm may not have a direct influence on atmospheric chemistry because wavelengths as short as 248 nm are not present in ambient light in the lower regions of the atmosphere. However H_2O_2 photolysis at 248 nm is commonly used to study the OH initiated oxidation of aromatic hydrocarbons in the laboratory. The interpretation of experimental results can be affected if there is direct formation of HO_2 from the photo irradiation of a benzene and oxygen mixture. This supplied the motivation for the present work: investigating the phenomenon in more details to understand the HO_2 formation process in more details.

In the present work a detailed study has been done on the direct formation of HO_2 radicals from the photoexcitation of various aromatic compounds (benzene, toluene, o-xylene and mesitylene) in presence of oxygen. Different experiments such as energy dependence, oxygen dependence and concentration dependence have been carried out to understand the direct HO_2 formation phenomenon. All the aromatic compounds were premixed with helium in gas bulbs and injected to the reactor through calibrated flow meters.

4.1 Laser energy dependence study on HO_2 formation

In order to study the laser energy dependence of the HO_2 formation, a series of experiments has been performed keeping pressure, O_2 and aromatic compound concentration constant and varying the photolysis laser energy.

Figure 49 shows typical HO_2 concentration-time profiles obtained by photolysing benzene in the presence of oxygen at different energies. The raw data have been treated in such a way that all ring-down events falling into 50 µs time slots have been averaged.

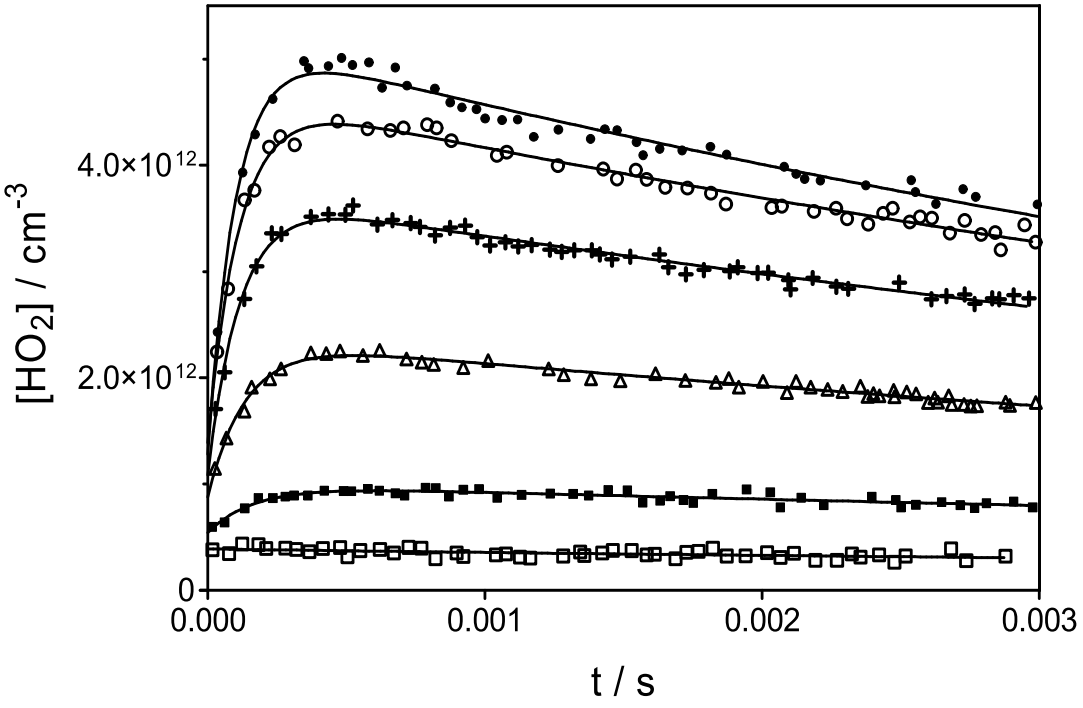

Figure 49: HO_2 concentration-time profiles at different photolysis pulse energies, from top to bottom: 53, 47, 40, 30, 17 and 10 mJ cm^{-2}. [C_6H_6] = 6.47×10^{14} molecules cm^{-3}, [O_2] = 1.35×10^{17} molecules cm^{-3}.

The main observations from this figure is the fact that apparently HO_2 radicals are formed on two different time scales: a very rapid, initial HO_2 formation named $[HO_2]_{ini}$ with a build-up time that can not be resolved on the time resolution of our experiment, followed by a slower, secondary HO_2-build up named $[HO_2]_{sec}$. The signals have been fitted using an association-dissociation fit (full lines in Figure 49) for the HO_2 concentration-time profiles, i.e. assuming a pseudo-first order formation and consumption of HO_2 radicals

$$[HO_2] = [HO_2]_{ini} \times e^{-k_{slow}t} + [HO_2]_{sec} \times \frac{k_{fast}}{k_{slow} - k_{fast}} (e^{-k_{fast}t} - e^{-k_{slow}t}) \qquad \text{E-19}$$

From these fits, the initial, rapid HO_2 concentration $[HO_2]_{ini}$ can be obtained as the intercept while the amplitude of the association reaction is attributed to the secondary HO_2 concentration $[HO_2]_{sec.}$ Figure 50 shows the energy dependence of the initial and secondary HO_2 concentrations.

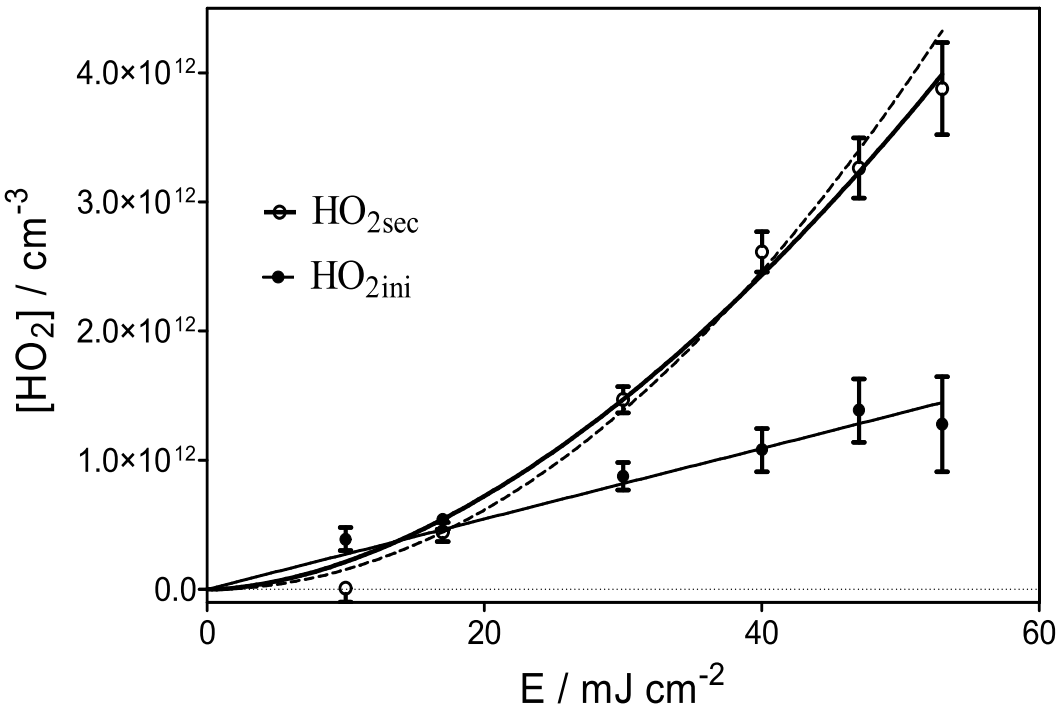

Figure 50: $[HO_2]_{ini}$ and $[HO_2]_{sec}$ as a function of the photolysis pulse energy as obtained from the fits in Figure 3a.). Full lines are best fits, dashed line represent square dependence of $[HO_2]_{sec}$.

As shown in Figure 50 the secondary HO_2 fitted nicely with the square of the photolysis energy in a power fit using the equation given below,

$$y = a \times x^n \qquad \text{E-20}$$

where 'a' is a pre-exponential constant and 'n' is scaling exponent. However, the rapid, initial HO_2 concentration increased linearly with photolysis energy and was hence published on the interpretation of one photon process [117].

4.1.1 Absorption due to unknown reactive intermediate

However, when the energy dependence study has been extended to other aromatic compounds like toluene and o-xylene, the HO_2 concentration profile

showed an unusual behaviour at lower energies. Figure 51 shows the energy dependence study on o-xylene.

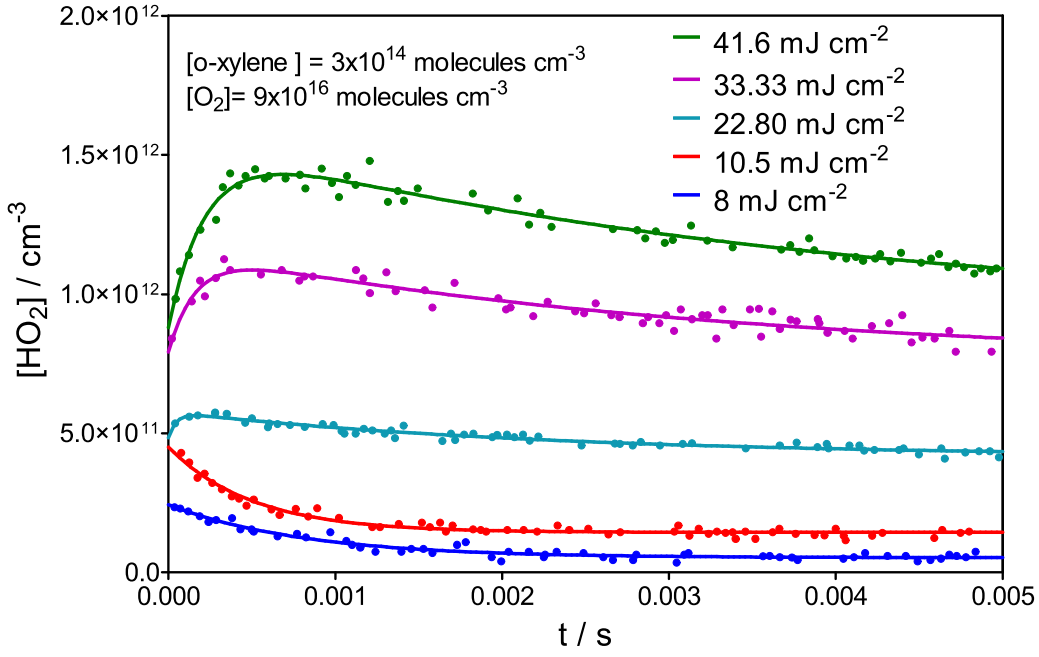

Figure 51: Laser energy dependence of HO_2 concentration obtained from the photolysis of a mixture of o-xylene and oxygen, showing an unusual behaviour at the lower energies.

It can be clearly seen in Figure 51 that at lower energies the HO_2 concentration does not build up as we have seen for the higher energies instead it decays very fast. The reason for this unusual behaviour was not clear: such a fast decay of HO_2 radicals with decreasing photolysis energy can not be explained through any chemical reaction. Therefore, we suspected formation of an additional unknown short-lived intermediate (originated from photolysis of the aromatic compound) absorbing at the same wavelength as HO_2. At higher energies the effect will be negligible compared to the HO_2 absorption, but at lower energies this species might over compensate the "real" HO_2 signal leading to the HO_2 profiles as shown Figure 51. To check the unknown reactive intermediate absorption on the other wavelengths, experiments have been carried out at a wavelength next to the HO_2 absorption line (6638.30 cm^{-1}). The absorption from the unknown reactive intermediate has also been observed on 6638.30 cm^{-1}. Figure 52 shows the signals obtained from the photolysis of o-xylene and oxygen mixture on two different absorption lines, 6638.20 cm^{-1} (HO_2) and 6638.30 cm^{-1}.

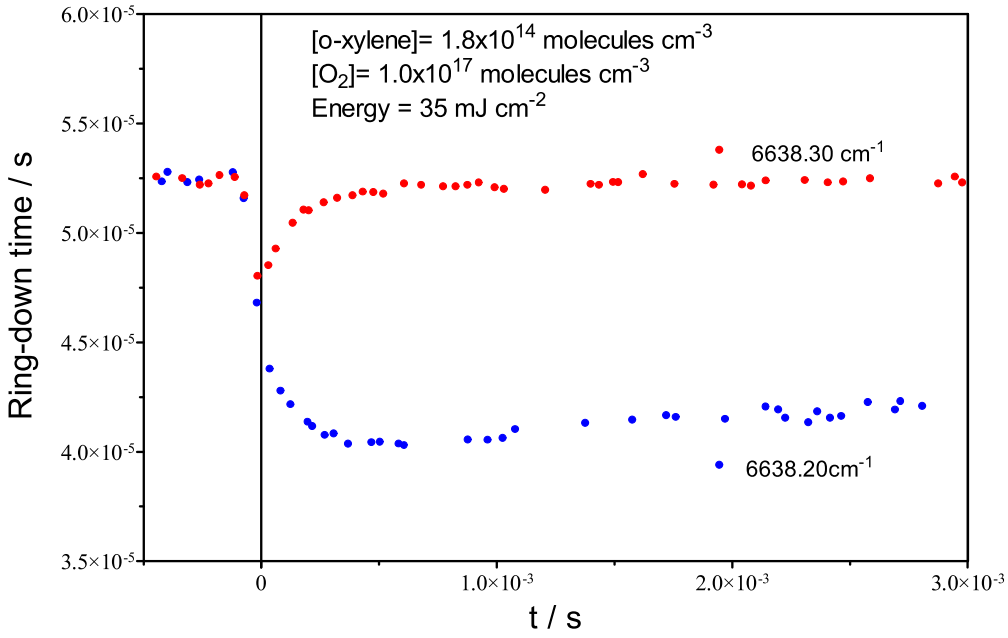

Figure 52: Signals from the photolysis of o-xylene and oxygen mixture at 6638.20 cm^{-1} and 6638.30 cm^{-1}.

From here onwards the HO_2 signal at 6638.20 cm^{-1} is termed as “online signal” and the absorption of the unknown reactive intermediate at 6638.30 cm^{-1} is termed as “offline signal” throughout the manuscript. This experiment also hinted that the absorption from the unknown reactive intermediate may have broad band absorption near the HO_2 absorption line. To confirm the broad band absorption of the unknown reactive intermediate and its effect on the HO_2 signal, a spectrum of a mixture of o-xylene and oxygen after photolysis has been recorded in the range 6638.00-6638.5 cm^{-1}. The spectrum has been measured using the ring-down event average method as explained in section 2.5.2.2. Figure 53 show the resulting spectrum. Three different averages are used, the first average has been done on all points before the photolysis to obtain the baseline, second average (short average) has been done on all the points falling in the 1 ms time window after the photolysis pulse and the third average (long average) has been done on all the points during more than 1 ms after the photolysis pulse. Once 10 ring-down events have occurred in the short average time window, the laser was tuned to the next wavenumber. The short and long averages have been carried out in order to see the effect of the short lived unknown reactive intermediate on HO_2 signal. The HO_2 concentration decays only slowly under these conditions, therefore the long-average spectrum still shows HO_2 absorption features whereas the unknown

reactive intermediate is short-lived (see Figure 51) and hence can be separated by carrying out two different averages as shown in Figure 53. The green line shows the absorption due to both, HO_2 and the unknown reactive intermediate obtained from short average while the blue line shows the signal for HO_2 alone using the long average. The HO_2 signal goes back to the baseline outside the HO_2 absorption peaks, whereas the absorption due to unknown reactive intermediate is constant throughout the range including the HO_2 absorption lines.

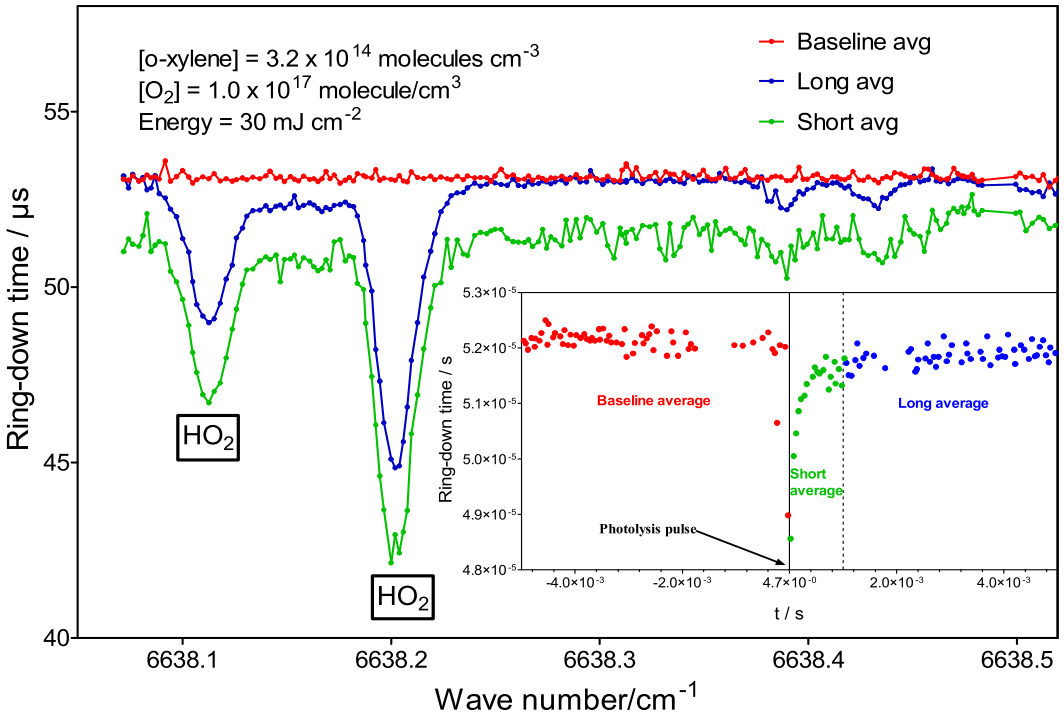

Figure 53: Spectrum of a mixture of o-xylene and oxygen after photoexcitation at 248 nm. Inset plot showing how each point on the spectrum has been extracted from the time resolved kinetics after the photoexcitation of a mixture of o-xylene and oxygen at 248 nm.

This experiment has shown that there is a considerable effect on the HO_2 absorption signal from the absorption due to an unknown reactive intermediate. This will eventually affect our results if this effect is not taken in to account because the online signal observed is the sum of the absorptions due to HO_2 as well as the unknown reactive intermediate. Therefore the use of τ_0, obtained from the average of all the ring-down events before the photolysis pulse, to convert ring down times to HO_2 concentration is no longer valid for this reaction system and needs to be corrected.

4.1.1.1 Correction of unknown reactive intermediate absorption while converting the HO_2 signals to concentration

To correct the effect caused by the unknown reactive intermediate absorption on HO_2 concentration profiles, both online and offline signals have been recorded for each experiment as shown in Figure 54 (A).

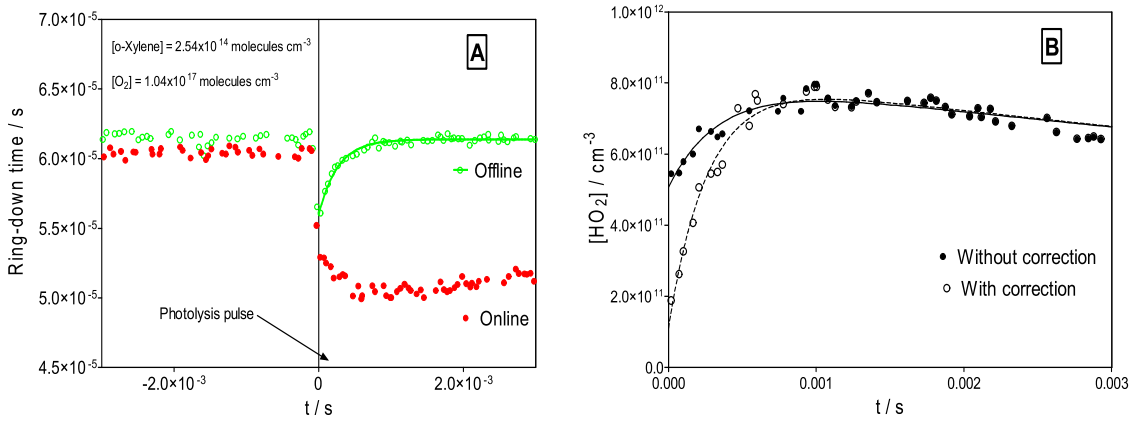

Figure 54: (A) Online offline signals obtained from the photolysis of o-xylene in presence of oxygen at 27mJcm^{-2}. (B) Online HO_2 signals converted to concentration with and without taking the correction of the unknown reactive intermediate absorption.

All the ring-down events after the photolysis pulse in the offline signal are then fitted using the equation (E-21):

$$Y = Y_0 + [P - Y_0] \times [1 - \exp(-k \times x] \qquad \text{E-21}$$

where Y_0= intercept, P=plateau, k=rate and x=time. The results obtained by the fit are the rate, the intercept and the plateau. However, the offline absorption signal was decaying very fast and was fitted only for a few milliseconds in order to get the best fit. Hence, the fit was not done on a time scale long enough to get a good value for the plateau. Therefore the plateau was fixed to the average of all ring-down events before the photolysis pulse in the offline signal. The obtained fit parameter will then be used to calculate a new $\tau_{0,t}$, now different for each ring down time obtained at time t for the online signal. The new $\tau_{0,t}$ for each ring-down event at time 't' for the online signal has then been calculated using the equation:

$$\tau_{0,t} = Y_0 + (P - Y_0) \times [1 - \exp(-k \times t)] \qquad \text{E-22}$$

where Y_0=intercept and k=rate obtained by the fit, P=plateau (average of all the ring-down events before the photolysis pulse) and t=time corresponding to the delay of the ring-down event relative to the photolysis pulse measured on the HO_2 absorption line. There is also a difference in the ring down time before the photolysis pulse between online signal and offline signal (Figure 54 (A)) due to absorption of the aromatic compound. This difference has been calculated and subtracted from the new τ_0 to get the exact τ_0 for the online signal. This new τ_0 is then used to convert the ring-down time at time t to HO_2 concentration using equation (E-16). All this has been done using an analysis program written in Labview (Baseline fit.vi section 2.6.2). The resulting concentration-time profile with the correction for the unknown reactive intermediate absorption is shown along with the concentration profiles where the correction has not been taken care in Figure 54 (B). It can be noted clearly that there is a significant influence on the concentration profile of the initial HO_2 while the effect is less important for the secondary HO_2. This will change our predictions on the origin of the initial HO_2 which will be discussed in section 4.1.3. The unknown reactive intermediate species absorption effect was causing the unusual decay of the HO_2 online signals in the lower energy experiments (Figure 50). Now with the correction the signals show normal trend (as shown at higher energies) even at the lower energy experiments as shown in Figure 55.

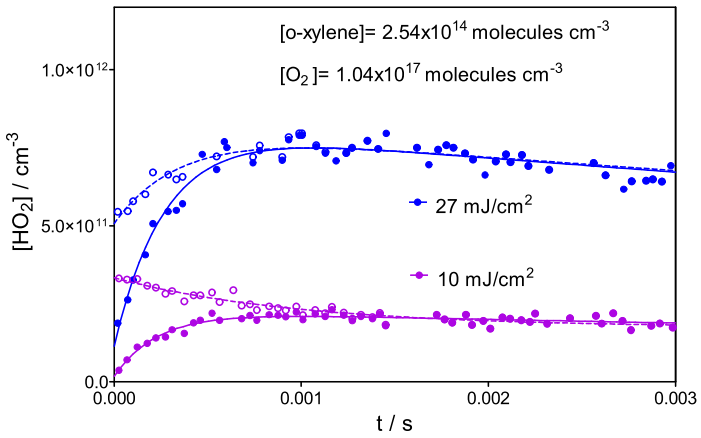

Figure 55: HO_2 online signals showing the effect of unknown reactive intermediate absorption correction. Open symbols and dotted lines represent the signals without correction.

This observation increased our interest to study more about the unknown reactive intermediate absorption at different conditions in order to understand it in a

better way and to remove the probable error while converting the ring down signals into HO_2 concentration.

4.1.2 Studies on unknown reactive intermediate absorption at different conditions

In order to understand the nature of the unknown reactive intermediate absorption more experiments for different aromatic compounds at different experimental conditions such as oxygen concentrations, photolysis energy and aromatic compound concentrations were carried out. The unknown reactive intermediate absorption increased with the substitution on the aromatic ring, i.e. more absorption observed in case of o-xylene which has two substituent methyl groups compared to benzene which has no substituent methyl group (Figure 56). Very little unknown reactive intermediate absorption was observed in case of benzene and could be the probable reason for overlooking this effect in our earlier work carried out only on benzene [117].

4.1.2.1 Energy dependence study on unknown reactive intermediate absorption

The energy dependence studies have been carried out on different aromatic compounds at different energies to know the effect on the unknown reactive intermediate absorption as shown in Figure 56 .

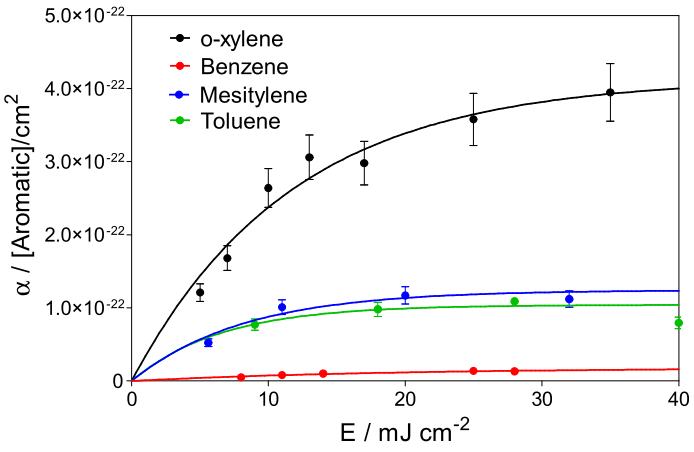

Figure 56: Laser energy dependence of the unknown reactive intermediate absorption (measured at 6638.30 cm^{-1}) at different energies. Error bars represent the statistical errors only.

The offline signals of the unknown reactive intermediate have been recorded and then analysed to get the absorption coefficient. The τ_0 for the unknown

reactive intermediate absorption was obtained from the average of all the ring-down events before the photolysis pulse and the absorption just after the photolysis pulse was obtained by fitting all the points after the photolysis pulse using the equation (E-21) given above and extrapolating the fit to time zero to get the intercept. Using the τ_0 and $\tau_{t=0}$, the absorption coefficient (α) is calculated using the equation (E-16). The results showed an increase up to 10 mJcm^{-2}, after that it seems like the reactive intermediate absorption was saturated. The largest absorption was observed for o-xylene and smallest for benzene among benzene, toluene, o-xylene and mesitylene. The calculated absorption coefficient is divided by the concentration of the aromatic compound. However, this should not be confused with the absorption cross-section because here the absorption coefficient observed is not for aromatic compound, but rather for a reactive intermediate whose absolute concentration is not known. Due to the saturating effect of the unknown reactive intermediate absorption around 10 mJcm^{-2}, the lower energy concentration profiles are more affected than the higher energy concentration profiles because the online signal is larger for the higher energy concentration profiles while the offline signal stays the same, as shown in Figure 57.

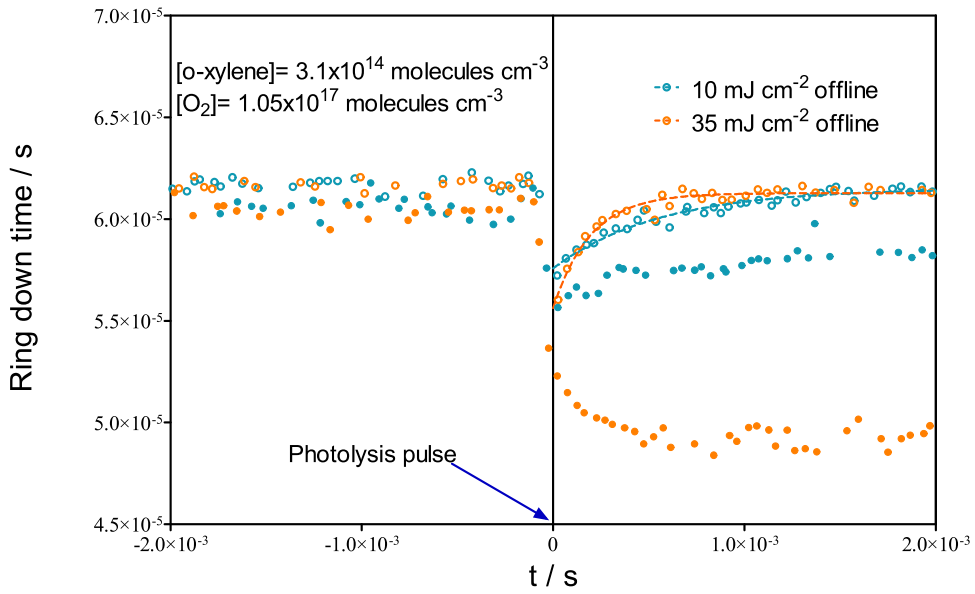

Figure 57: Online (filled symbol) and offline (open symbol) signals at two different energies.

As a result a larger correction for 10 mJcm^{-2} has to be made compared to 35 mJcm^{-2}, which shows the importance of taking into account the unknown reactive intermediate absorption.

4.1.2.2 Concentration dependence of the unknown reactive intermediate absorption

In the next step, the concentration dependence of the unknown reactive intermediate absorption was investigated. The experiments on toluene and o-xylene showed a similar trend as shown by the energy dependence. The signal saturated at aromatic compound concentration above $2x10^{14}$ molecules cm^{-3}. Figure 58 shows the concentration dependence of the absorption coefficient of the unknown reactive intermediate species on the initial toluene and o-xylene concentration. In the case of o-xylene the maximum concentration is limited by the concentration of the o-xylene/helium gas mixture in the bulb. O-xylene has a vapour pressure of ~8 Torr at 25℃ which limits the concentration of the gas mixture.

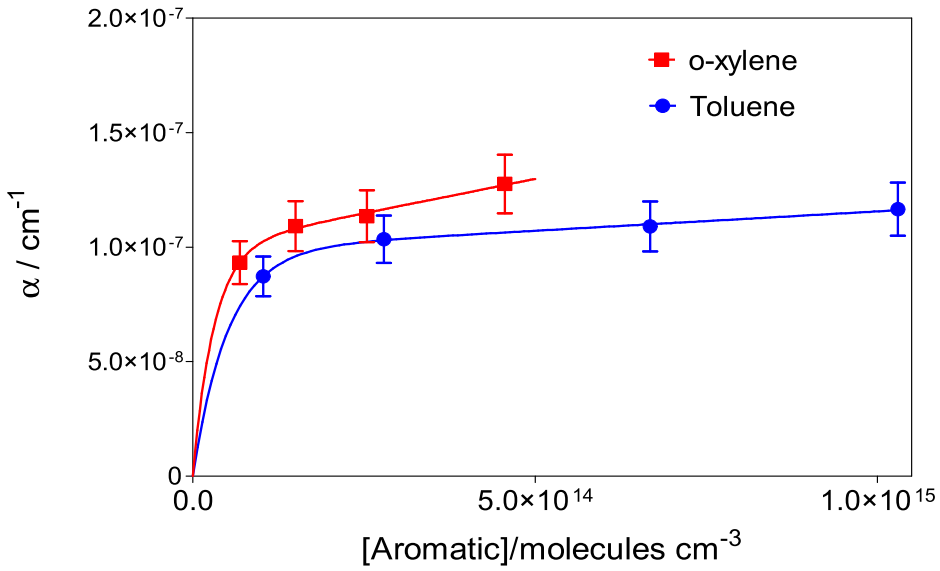

Figure 58: Concentration dependence of the offline absorption at different toluene and o-xylene concentrations. Error bars represent the statistical errors only.

The decay of the unknown reactive intermediate absorption was dependent on the concentration of the aromatic compound. Figure 59 shows the plot of decay rate constant of the unknown reactive intermediate absorption against aromatic compound concentration.

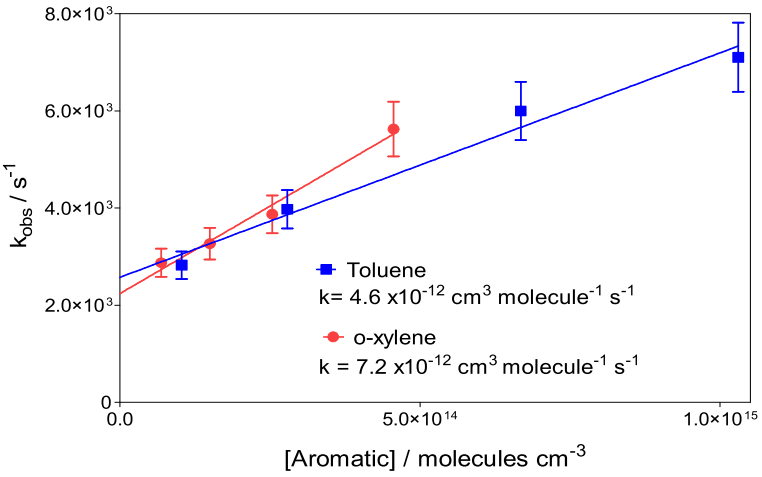

Figure 59: Plot of decay rate constant of the unknown reactive intermediate absorption as a function of aromatic compound concentration. Error bars represent the statistical errors only.

The rate co-efficient observed was in the order of magnitude of a chemical conversion (~10^{-12} Figure 59) but to distinguish between quenching and a reaction was difficult due to the lack of knowledge about the species absorbing.

4.1.2.3 Oxygen dependence of unknown reactive intermediate absorption

On the other hand an oxygen dependence study on unknown reactive intermediate absorption showed a linear increase with the change in the oxygen concentration. Figure 60 shows a plot of unknown reactive intermediate absorption as a function of oxygen concentration measured for different aromatic compounds.

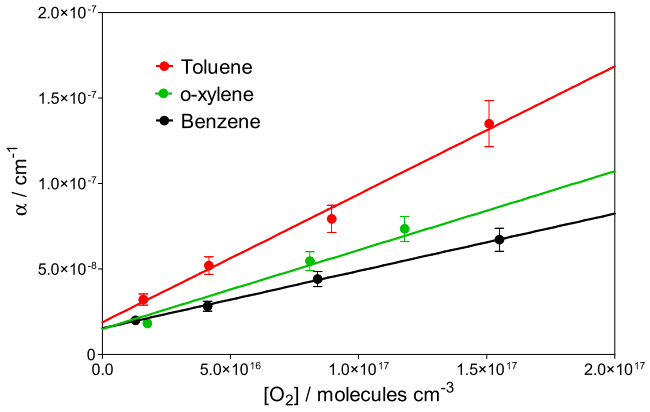

Figure 60: Plot unknown reactive intermediate absorption (6638.30 cm^{-1}) as a function of oxygen concentrations measured for different aromatic compounds. Error bars represent the statistical errors only.

However, the origin of the unknown reactive intermediate absorption has not been revealed due to the limitations of the experimental system. The absorption can be observed through the cw-CRDS technique but further studies to understand the origin of the unknown reactive intermediate which might cause this broad band absorption was not possible due to the lack of photolysis product knowledge [117]. Therefore the investigations on the origin of this baseline absorption fall outside the frame of this work.

4.1.3 Energy dependence study of HO_2 formation with correction for unknown reactive intermediate absorption

The energy dependence study which has been explained in the publication [117] was repeated on different aromatic compounds including benzene, now considering the unknown reactive intermediate absorption correction. Higher aromatic concentrations have been used compared to the earlier work [117] to have a larger signal in order to minimise unknown reactive intermediate absorption effect. The results were different, as mentioned earlier because the impact on the initial HO_2 was higher compared to the secondary HO_2 as shown in Figure 61.

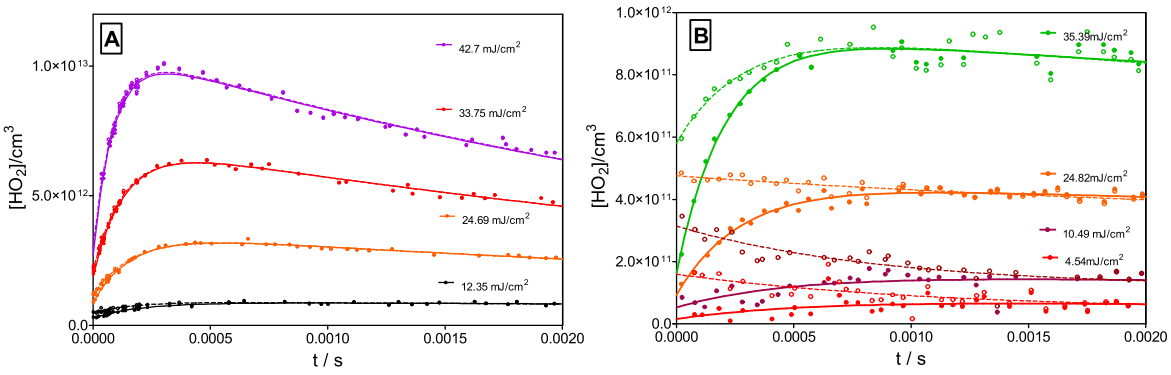

Figure 61: Examples of energy dependence on HO_2 concentration obtained from benzene (A) and o-xylene (B). Open symbols and dotted lines represent the HO_2 concentrations profiles without correction, full symbols and full lines represent the HO_2 concentration profiles after the correction. Experiments were carried out with $3.35x10^{15}$ molecules cm^{-3} of benzene and $3.1x10^{14}$ molecules cm^{-3} of o-xylene in presence of $1.0x10^{17}$ molecules cm^{-3} O_2.

Figure 62 shows an example plot of initial and secondary HO_2 concentrations (with and without correction) obtained from the fit (equation E-19) against the photolysis energy.

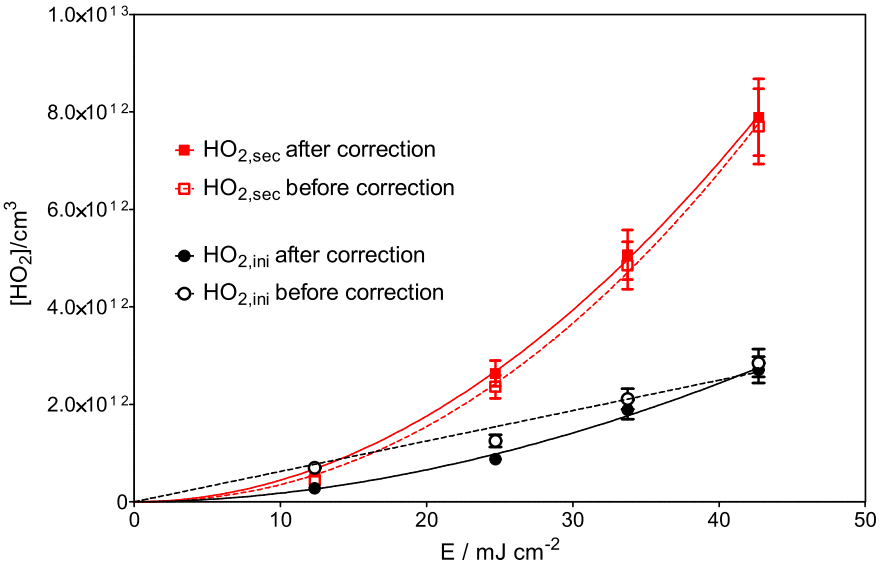

Figure 62: An example of Plot of [HO_2] against photolysis energy with and without correction obtained for benzene. Experiments were carried out with 3.35x10^{15} molecules cm^{-3} of benzene in presence of 1.0x10^{17} molecules cm^{-3} of oxygen. Error bars represent the statistical errors only.

Both the HO_2 concentrations fitted nicely with the square of the power fit (E-20) after considering the correction. The values obtained for the low energy initial HO_2 concentrations are lower compared to the values without correction and the impact decreased with the increase in the energy. The difference in the influence of unknown reactive intermediate absorption on initial and secondary HO_2 can also be clearly observed (Figure 62). Therefore after including the unknown reactive intermediate absorption correction it can be concluded that both the HO_2 come from two photon excitation process. This changes our assumption [117] of the involvement of two different kinds of the photo excitation processes in the formation of HO_2 radicals.

A saturation effect for both the HO_2 concentrations has also been observed after 45 mJcm^{-2}. Figure 63 shows the saturation effect at higher energy concentration profiles.

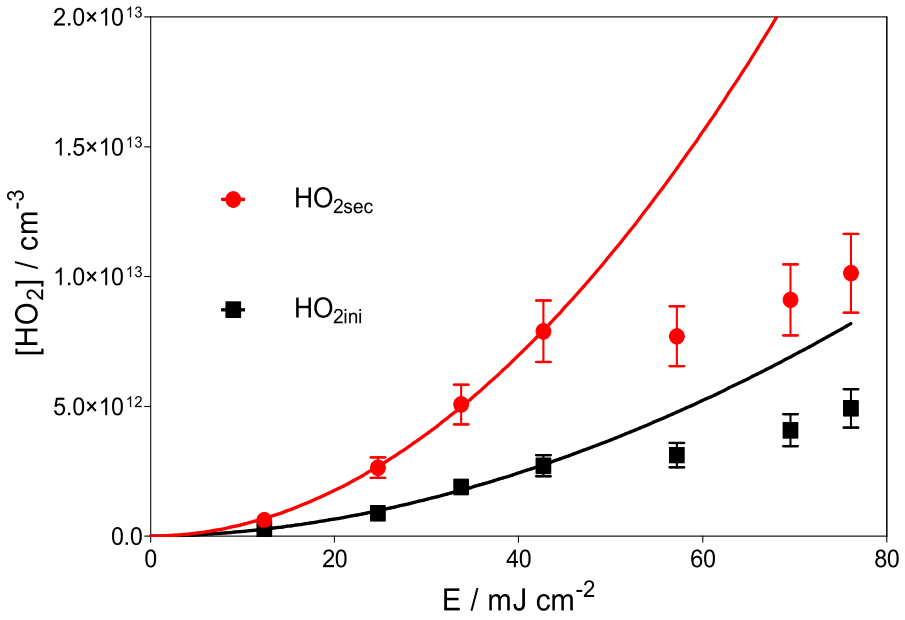

Figure 63: Plot of [HO_2] against photolysis energy showing the saturation at higher energies. The benzene and oxygen concentrations used were 3.35x10^{15} molecules cm^{-3} and 1.0x10^{17} molecules cm^{-3} respectively. Error bars represent the statistical errors only.

Above 45 mJ/cm^2 photolysis energy both the HO_2 yields were not increasing as expected and looked almost the same for all the energies. This saturation effect was also a part of the problem while predicting the initial HO_2 origin in our earlier work [117]. The lower energy concentrations for the initial HO_2 were higher in their value (Figure 62) because of the compensation caused by the unknown reactive intermediate absorption and the values at higher energy were lower due to saturation. This caused the plot of initial HO_2 against the photolysis energy look like a straight line and interpreted as single photon process. Now, with the correction and leaving the saturation effect at higher energies apart, both the HO_2 fit properly for the two photon absorption process. However, this saturation effect has not been observed by Kovacs *et al.* [116] even though their energy range extended to even higher values that what was used in the present work. We don't have any explanation for this difference.

Similar results have been observed for other aromatic compounds like toluene, o-xylene and mesitylene. The two photon processes as the origin of HO_2 radicals after the photo excitation of a mixture of aromatic compound and O_2 has been observed in all the cases after taking care of unknown reactive intermediate absorption and the saturation effect. The results of energy dependence study on different aromatics are shown in Figure 64.

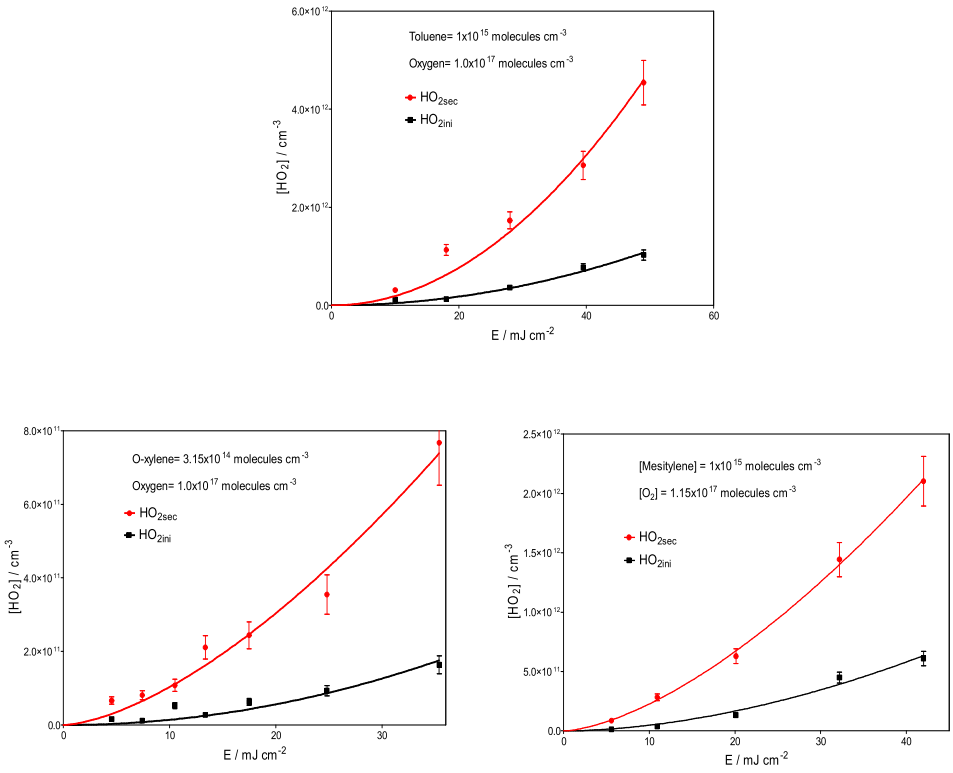

Figure 64: Results of energy dependence study on different aromatic compounds. Error bars represent the statistical errors only.

For practical purposes, Table 8 lists the pre-exponential factor 'a' from the equation (E-20) divided by the concentration of the aromatic compounds for initial and secondary HO_2 fits after forcing them for a 'n' value 2. All the aromatic compounds yield more or less the same initial and secondary HO_2. One experiment with low oxygen ($1.1x10^{16}$ molecules cm^{-3}) shows low yields of HO_2 in both the processes, which will be explained in section 4.2.

Compound	Initial HO_2 'a'/ [aromatic] / 10^{-7}	Secondary HO_2 'a' / [aromatic] / 10^{-6}	[Aromatic] / 10^{15} molecules cm^{-3}	[O_2] / 10^{17} molecules cm^{-3}
Benzene	4.8	1.3	3.3	1.0
Benzene	5.8	1.8	0.65	1.3
Benzene	2.8	0.73	3.4	0.112
Toluene	4.8	2.0	1.0	1.0
O-xylene	4.5	1.6	0.315	1.0
Mesitylene	3.2	2.0	1.0	1.15

Table 8: Pre-exponential factor 'a' (E-20) divided by the aromatic compound concentration for the initial and secondary HO_2 fits for different aromatic compounds.

4.1.4 HO_2 formation from single photon (C_6H_6*) and two photon (C_6H_6**) excited benzene in presence of O_2

This experiment has been carried out to confirm that two photon absorption is involved in the formation of both, initial and secondary HO_2 radicals from excited benzene in the presence of O_2. In this experiment, different combinations of initial benzene concentrations and photolysis energies have been used (see Table 8) in such a way, that the theoretical single photon and two photon excited benzene concentrations are identical. The single photon absorption cross section at 248.4 nm for benzene is well known ($2.6x10^{-19}$ cm^2/molecule [118]), but three different absorption cross sections have been published for the absorption of a second photon, ranging from $\sigma_{248\ nm,\ 2\ Photon} = 2.26\times10^{-18}$ cm^2 through 2.5×10^{-17} cm^2 to 3.4×10^{-17} cm^2 as published by Yokoyama *et al.* [119], Kovacs *et al.* [116] and Reilly and Kompa [120] respectively. Therefore, an approximate value $1.0x10^{-17}$ cm^2 has been taken for the second photon absorption

Photolysis energy / mJ cm^{-2}	**[C_6H_6] / 10^{15} molecules cm^{-3}**	**[C_6H_6*] / 10^{13} molecules cm^{-3}**	**[C_6H_6**] / 10^{12} molecules cm^{-3}**
20 (red symbols and line in Figure 65)	2.0	1.3	2.9
40 (blue symbols and line in Figure 65)	0.56	0.72	2.9
40 (green symbols and line in Figure 65)	1.0	1.3	5.1

Table 9: Theoretical C_6H_6* and C_6H_6concentrations calculated for different initial C_6H_6 concentrations at different photolysis energies.**

The expected result was that experiments with same C_6H_6** concentration should fall on top of each other if a two photon process is at the origin of both, initial and secondary HO_2. From our former conclusion, initial HO_2 from 1-photon process and secondary HO_2 from 2-photon process, one would expect, that the initial HO_2 is the same for experiments with the same $C_6H_6^*$ while the secondary HO_2 would be the same for the same $C_6H_6^{**}$. The results observed are shown in Figure 65.

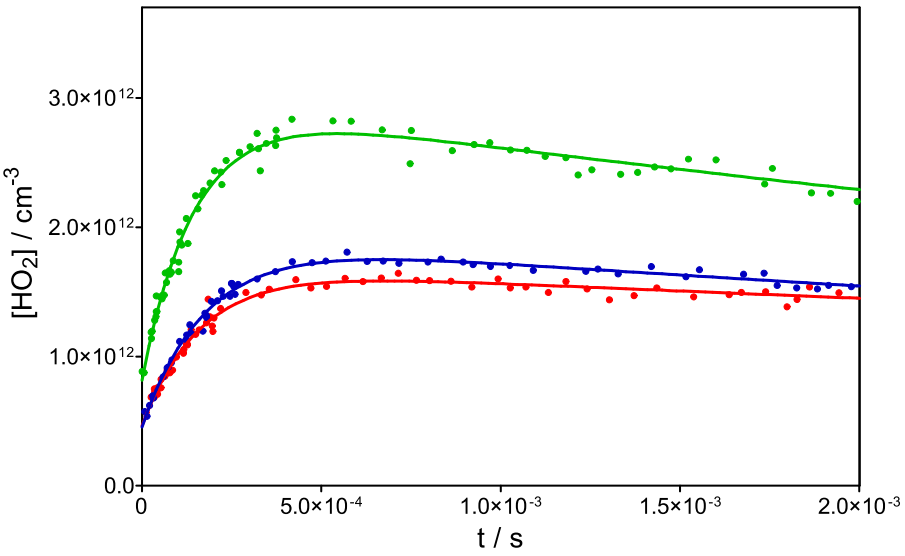

Figure 65: HO_2 profiles for different C_6H_6* and C_6H_6 concentrations. The O_2 concentration was kept constant at 1x10^{17} molecules cm^{-3}, for all the experiments.**

It can be clearly noted that the experiments with the same C_6H_6** (blue and red coloured signals in Figure 65) concentrations are falling one on top of the other, independent of the photolysis energy. There is a slight difference in the concentration of the secondary HO_2, can be explained on the grounds of concentration dependence study (in section 4.3) where, with higher aromatic compound concentration lower secondary HO_2 yield has been observed. On the other hand the experiments with the same C_6H_6* concentrations are totally different. This is because in order to get the same C_6H_6* concentrations at different energies the initial benzene concentration has to be changed and this resulted in a higher C_6H_6** concentration for the higher energy experiment. Therefore we get a higher HO_2 yield for the one with the highest C_6H_6** concentration. This confirms that both, initial and secondary HO_2 originate from a two photon process.

4.1.5 Energy dependence of the HO_2 formation and decay rates

The primary HO_2 formation is too fast and can not be resolved with the temporal resolution of the cw-CRDS technique. However the rates of secondary HO_2 formation and the decay of the HO_2 can be studied. Figure 66 shows for different aromatic compounds the rate of $[HO_2]_{sec}$ formation, i.e. k_{fast} obtained from fits to (E-19) after correction for the unknown reactive intermediate absorption .

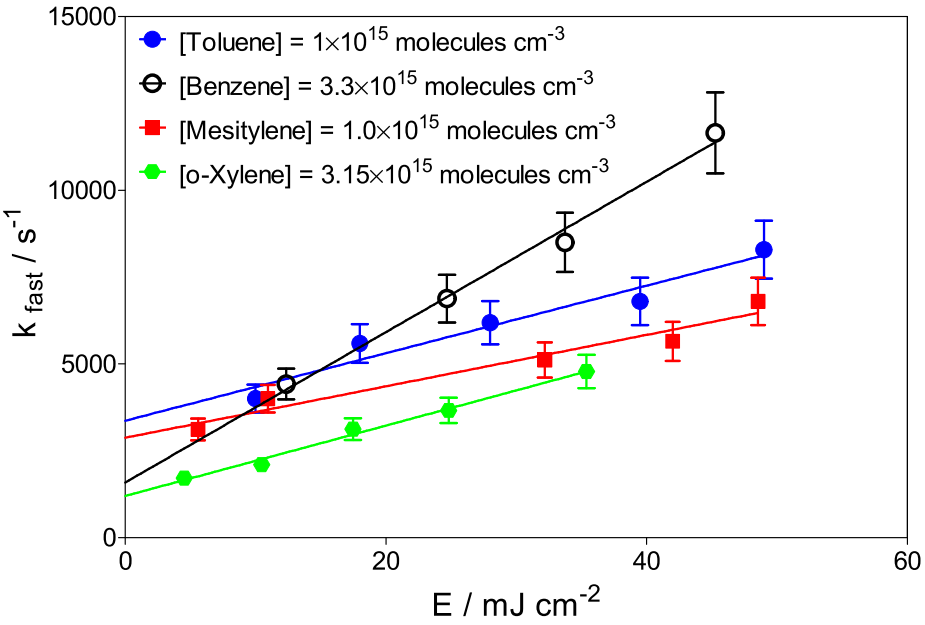

Figure 66: Plots of secondary HO_2 formation rate against photolysis energy for different aromatic compounds ($[O_2]$ = 1×10^{17} molecules cm^{-3}) obtained from the energy dependence studies. Error bars represent the statistical errors only.

Even though there is a trend for a slight increase of the rate with increasing energy, the energy range is too small to reliably confirm this trend. Further discussion on the rate of HO_2 formation will be given in the discussion of the O_2 dependence in section 4.2.

Rate of HO_2 decay, i.e. k_{slow} also increases with increasing photolysis energy as shown in Figure 61. The decay is much faster as a decay from the HO_2 self-recombination if that was the only consumption reaction: for comparison a dashed line in Figure 67 is added which represents the HO_2 concentration time profile that one would observe for the highest HO_2 concentration if HO_2 self-recombination were the only consumption reaction; it is obvious that this reaction is only of very minor importance under the conditions of these experiments, i.e. HO_2-concentration and time scale of the experiments. The same is true for the diffusion of radicals out of the observation volume: from previous experiences this process can be ruled negligible on the time scale of the experiments in Figure 67.

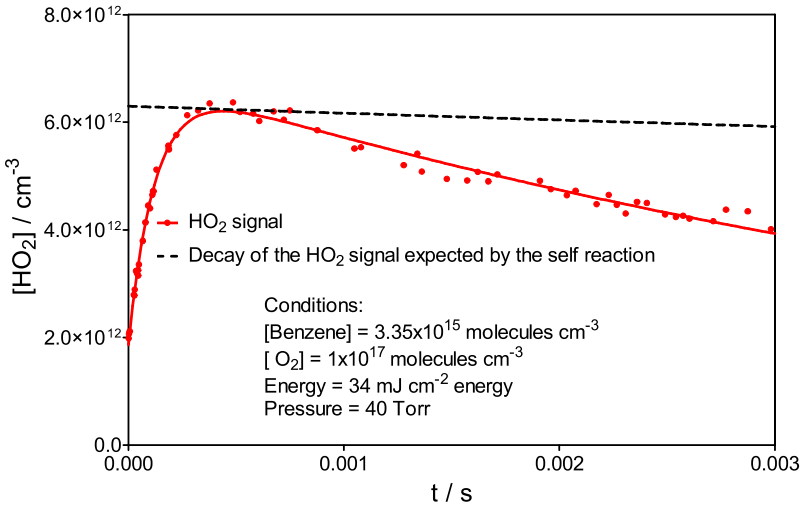

Figure 67: HO_2 decay observed under the experimental conditions and the expected decay if one considers only self recombination reaction of HO_2.

Therefore it can be assumed that mainly the co-products of the HO_2 radicals are responsible for the HO_2 decay. As for the products of the 2-photon absorption, little is known: recently, H-atoms have been detected under comparable experimental conditions by Kovacs *et al.* [116], however they report this product to be only a minor channel (1%). The only other study on this subject comes from Yokoyama *et al.* [119] using molecular beam photofragmentation, i.e. collision free conditions and thus very different from our experimental conditions. They report numerous fragments with C_3H_3 being the major product after 2-photon absorption. Atkinson and Hudgens [121] have investigated the reaction between propargyl, C_3H_3, and O_2 under our experimental conditions, reporting a pressure dependant rate constant yielding $k_{C3H3+O2} = 1.3\times10^{-13}$ cm^3 molecule^{-1} s^{-1} at 40 Torr Helium, i.e. propargyl radicals will react under Figure 61 conditions within less than 100 µs. The product of this reaction is not known, however the pressure dependence observed by Atkinson and Hudgens points towards the addition of O_2 to form peroxy radicals. To summarize, most of the photofragments will probably be converted rapidly into peroxy radicals, which subsequently probably react predominantly with HO_2 radicals. This is a sound assumption because it is recognized that rate constants for reactions between RO_2 and HO_2 radials are roughly a factor of ten faster ($\approx10^{-11}$ cm^3 molecule^{-1} s^{-1}) than the corresponding self reactions RO_2 + RO_2 or HO_2 + HO_2 ($\approx10^{-12}$ cm^3 molecule^{-1} s^{-1}) [122]. In Figure 68 the decay rates, i.e. k_{slow} as obtained from the fits of energy dependence studies

on different aromatic compounds are plotted as a function of the sum of initial and secondary HO_2 radical concentration, i.e. the HO_2 concentration is used as a proxy for the overall concentration of photofragments. The model yields a straight line with rate constants in the order of magnitude of 10^{-11} cm^3 $molecule^{-1}s^{-1}$, which is a rate constant generally expected for HO_2 + RO_2 reactions. A faster decay rate is observed in case of o-xylene and mesitylene compared to toluene and benzene. This can be explained on the basis of possibility of more than one photofragment produced by o-xylene and mesitylene.

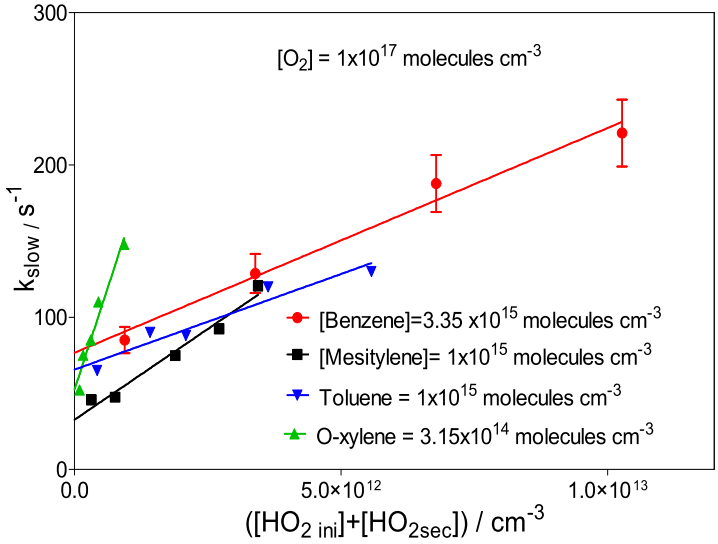

Figure 68: Decay rate k_{slow} of HO_2 radicals as a function of sum of $[HO_2]_{ini}$ + $[HO_2]_{sec}$ for different aromatic compounds. Error bars represent the statistical errors only.

However a further interpretation of the decays seems to be idle as the nature of the photofragments are not known nor is there any reliable knowledge about the fate of these fragments and their reactivity with HO_2 radicals.

4.2 Oxygen dependence study on HO_2 formation

The next to study was the oxygen dependence on the HO_2 concentration time profiles. The experiments were carried out on benzene at different oxygen concentrations and different pressures.

4.2.1 Oxygen dependence on initial HO_2

The O_2 dependence of $HO_{2,ini}$ is in excellent agreement with earlier work of research group [70] where it was found that the HO_2 quantum yield does not vary much as long as the O_2 concentration is above a certain threshold (around 3×10^{16}

cm^{-3}). Figure 69 shows the results obtained from an oxygen dependence study on benzene.

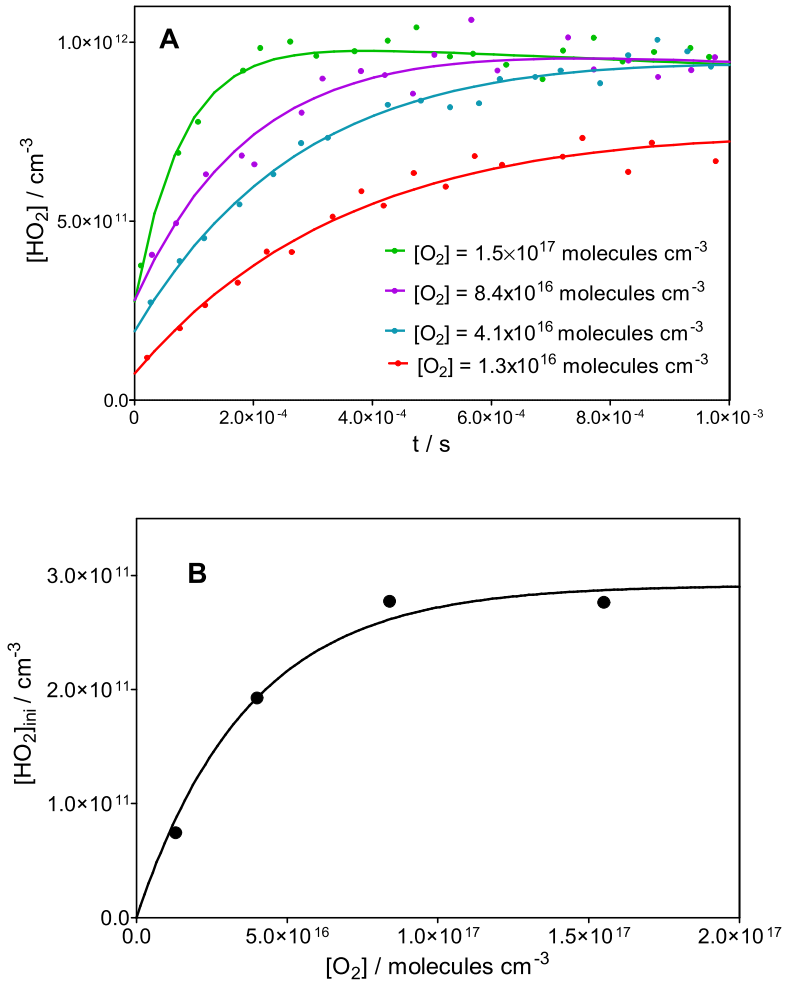

Figure 69: Oxygen dependence study on benzene. A) HO_2 profiles at different oxygen concentrations. B) $[HO_2]_{ini}$ as a function of oxygen concentration . All the experiments were carried out with 2.18x10^{14} molecules/cm^3 benzene and 30 mJ cm^{-2} photolysis energy.

The reason for this behaviour is not clear. It can be assumed that this is due to a competition between a reaction of excited species with O_2 to form HO_2 and a fast decay of the excited species to lower energetic states or to other products.

4.2.2 Oxygen dependence on secondary HO_2

The oxygen dependence study at two different pressures (22 and 102 Torr) has been carried out to obtain the rate constant for the secondary HO_2 formation reaction in order to verify if the secondary HO_2 formation originates from H+O_2 as suggested by Kovacs *et al.* [116]: the rate constant of H-atoms with O_2 is strongly

pressure dependant. The observed first order rate constants of the HO_2 formation, k_{fast}, for both pressures are plotted in Figure 70. The full symbols show the data directly obtained by the fitting procedure (E-19). It can be clearly seen that the reaction is pressure dependant.

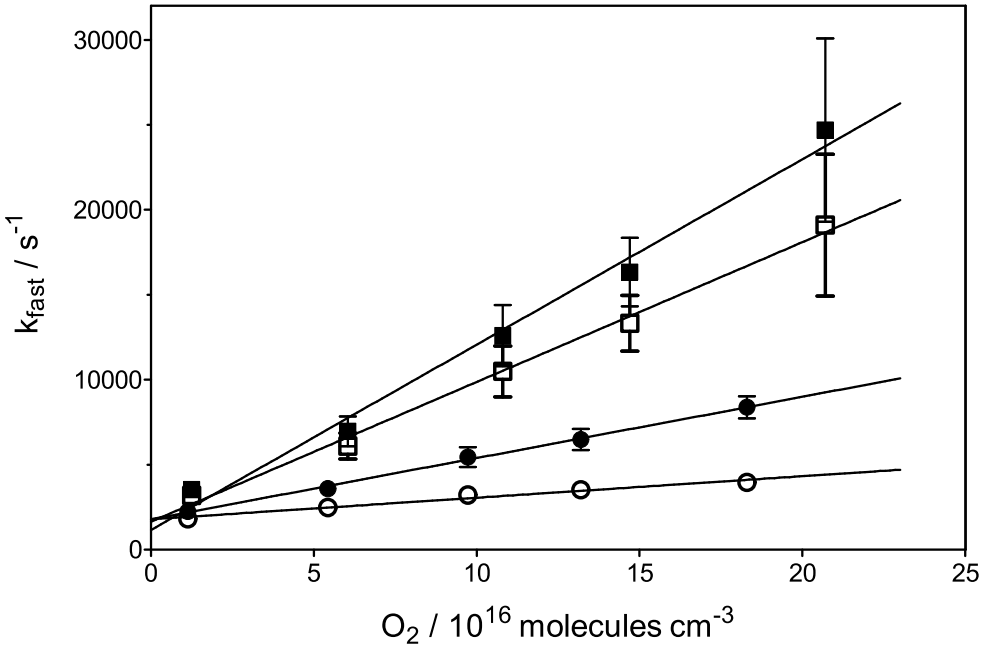

Figure 70: Rate constant of secondary HO_2 formation as a function of [O_2] and pressure: ■: 102 Torr, ●: 22 Torr, filled symbols: raw data, open symbols: corrected for [O_2] collision efficiency.

This strong pressure dependence along with the observed H-atom formation from 2-photon excitation of C_6H_6 by Kovacs *et al.* [116] suggests that (R-37) might be at the origin of the secondary HO_2 formation. Comparing the rate constant obtained from Figure 70 with literature values for (R-37) could support this assumption. The rate constant for the HO_2 formation at both pressures is found to be

22 Torr $\quad k = (3.4 \pm 0.3) \times 10^{-14}$ cm^3 s^{-1}

102 Torr $\quad k = (10.0 \pm 1.6) \times 10^{-14}$ cm^3 s^{-1}

While these rate constants vary with pressure, the absolute values are slightly higher than the recent measurements from Fernandes *et al.* [115]: k_{39}= 1.17 and 5.54× 10^{-14} cm^3 $molecules^{-1}$ s^{-1} for 22 and 102 Torr Helium, respectively. However, the raw data from Figure 70 need to be corrected: collision efficiencies for O_2 and Helium are different, and at higher O_2 concentrations and especially at 22 Torr, the

O_2 concentration (≈ 2×10^{17} molecules cm^{-3}) is no longer negligible compared to Helium (≈ 6×10^{17} molecules cm^{-3}). We therefore have corrected the raw-data using the low pressure rate constants for (R-37) $k_{0,O2}$ and $k_{0,He}$ from Fernandes *et al.* [115]. The O_2-dependent portion of the measured k_{fast} has than been treated for each experiment as the proportional sum of contributions, He and O_2, and the "pure" helium portion has been extracted. These theoretical values are shown as open symbols in Figure 70 and lead to the following rate constants:

22 Torr $k = (2.1 \pm 0.2) \times 10^{-14}$ cm^3 $molecule^{-1}$ s^{-1}

102 Torr $k = (8.7 \pm 1.2) \times 10^{-14}$ cm^3 $molecule^{-1}$ s^{-1}

It is probable that in our system the secondary HO_2 is formed at least partially in a complex mechanism, involving the reaction of O_2 with fragments other than H-atoms, thereby affecting the rate constant. A hint towards a complex mechanism is the fact that, as can be seen in Figure 70, the linear regressions of the straight lines do not pass through zero, but present for both pressures an intercept of 1500 ± 200 s^{-1}. Therefore, H-atoms are either scavenged in competing reactions other than (R-37)

$$H + O_2 + M \longrightarrow HO_2 + M \qquad \text{R-37}$$

$$H + X \longrightarrow HX \qquad \text{R-38}$$

with X being C_6H_6 or photo fragments, or HO_2 is partially formed in a fast reaction sequence

$$X \longrightarrow Y \qquad \text{R-39}$$

$$O_2 + Y \longrightarrow HO_2 + Z \qquad \text{R-40}$$

with (R-39) being the rate limiting step with k_3 = 1500 ± 200 s^{-1}. An argument against the first possibility is that $[HO_2]_{sec}$ as a function of O_2 evolves in the same manner for both pressures (as shown in Figure 71), which would not have been the case if H-atoms are scavenged in a pressure independent reaction (R-38): at 102 Torr the competition between (R-37) and (R-38) would be much more in favour of (R-37) than in the 22 Torr experiments, hence $[HO_2]_{sec}$ would increase faster with increasing O_2 at 102 Torr than at 22 Torr.

$$H + O_2 + M \longrightarrow HO_2 + M \qquad \text{R-39}$$

$$H + X \longrightarrow HX \qquad \text{R-40}$$

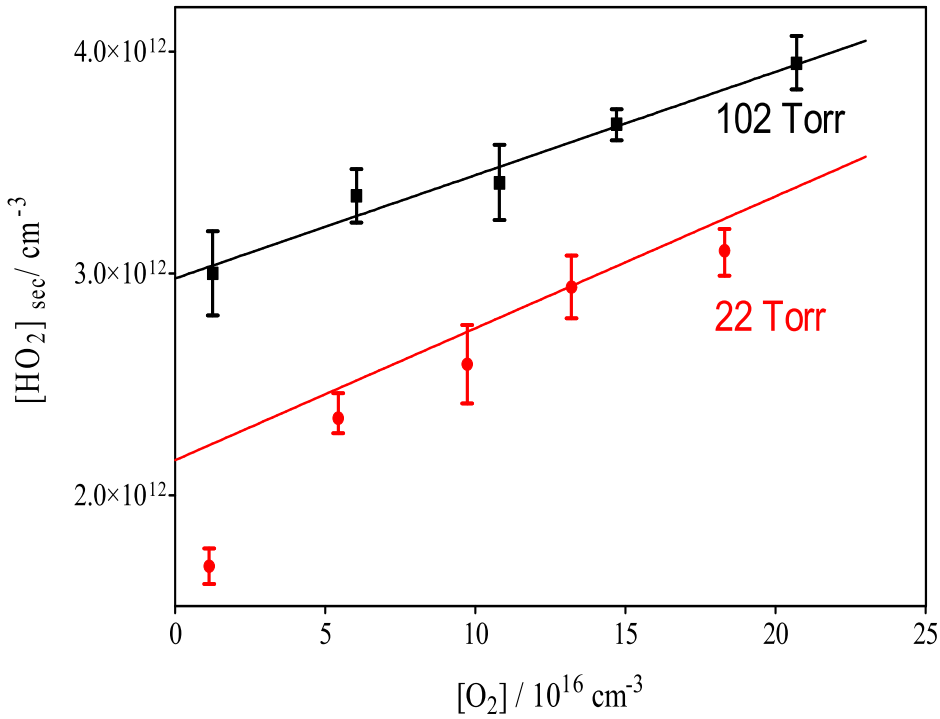

Figure 71: HO_{2sec} concentration as a function of $[O_2]$ and pressure.

However, scavenging of H-atoms with photofragments would be in agreement with the observed increase in k_{fast} with photolysis energy as shown in Figure 66. On the other hand, observations made by Kovacs *et al.* [116] are not in agreement with any rapid scavenging of H-atoms through (R-38). Therefore, the latter hypothesis of $HO_{2,sec}$ being formed in at least two different reactions, (R-37) and (R-38)-(R-39) seems more likely. It should be noted that a major contribution of (R-37) to the formation of secondary HO_2-radicals is in complete disagreement with the findings of Kovacs *et al.* [116]: they have deduced from the calibration of H-atom fluorescence signals that the H-atom formation is only a very minor reaction product (< 1%) after 2-photon absorption, and this under similar experimental conditions. In this work, we find from absolute cw-CRDS measurements much higher quantum yields for the HO_2-formation after 2-photon absorption (42 – 235 %, depending on which $\sigma_{248\ nm,\ 2\ Photon}$ is used for the calculation). This disagreement is far beyond the experimental uncertainties, but from the currently available experimental data we can not explain this disagreement. Experiments identifying the photofragments of 2-photon excitation would be very helpful in the interpretation of the observed HO_2 concentration-time profiles.

An increase of about 50% for both HO_2 concentrations with pressure increasing from 22 to 102 Torr is also observed which is more difficult to explain: a possible quenching of the excited state which leads to HO_2 formation can not explain this observation, as it would act in the other direction, i.e. a decrease in HO_2 concentration with increasing pressure. Also, a pressure dependence of the HO_2-forming reaction seems to be very unlikely especially in the case of the initial, rapid HO_2: HO_{2ini} is formed very fast at all pressures, the reaction is completed within less than 10 µs using O_2-concentrations of 3×10^{16} molecules cm^{-3}, corresponding to rate constants much faster than 10^{-11} cm^3 $molecule^{-1}$ s^{-1}. This makes a strong pressure dependence of the rate constant very unlikely. Therefore we rather suspect a systematic error in the absorption cross sections used for both pressures: in order to calculate the absorption cross section at the maximum of an absorption line at a given pressure from the line strength (6.34×10^{-21} cm^{-1}), line broadening has to be taken into account. However, broadening coefficients for HO_2 radical absorption lines are sparse [65, 66, 123], and only one measurement in helium [66] is known for the absorption line at 6637.29 cm^{-1}: γ_{He} = 0.057 $cm^{-1}atm^{-1}$. Concerning the absorption line used in this work (6638.20 cm^{-1}) nothing is known about its broadening coefficient. Therefore the only published broadening coefficient for HO_2 radicals in helium [66] to calculate the absorption cross sections for both pressures: $\sigma_{22Torr} = 3.4\times10^{-19}$ cm^2 and $\sigma_{102Torr} = 1.9\times10^{-19}$ cm^2. However it is known that the broadening coefficients depend on the quantum state for the given transition: for example, broadening coefficients between 0.14 - 0.09 $cm^{-1}atm^{-1}$, a variation of 50%, have been found for N_2 [123]. A lower broadening coefficient for the absorption line used in this work (6638.20 cm^{-1}) would increase the absorption cross sections for both pressures, but proportionally more for the 102 Torr measurements. Hence, the absolute concentrations at 102 Torr would decrease more than those at 22 Torr.

4.3 Aromatic compound concentration dependence of HO_2 formation

The investigation on the concentration dependence of the HO_2 formation has been carried out on benzene and o-xylene as representative molecules. The reason for only selecting these two molecules was that the energy dependence experiments had shown a similar behaviour for all different aromatic compounds.

The experiment with different benzene concentrations was carried out at 40 mJ cm^{-2} photolysis energy and $[O_2]$ = 1.2x10^{17} molecules cm^{-3}, whereas for o-xylene 27 $mJcm^{-2}$ of photolysis energy and $[O_2]$ = 1.1x10^{17} molecules cm^{-3} were used. The results are shown in Figure 72. All the HO_2 concentration profiles have been divided by the concentration of the aromatic compound.

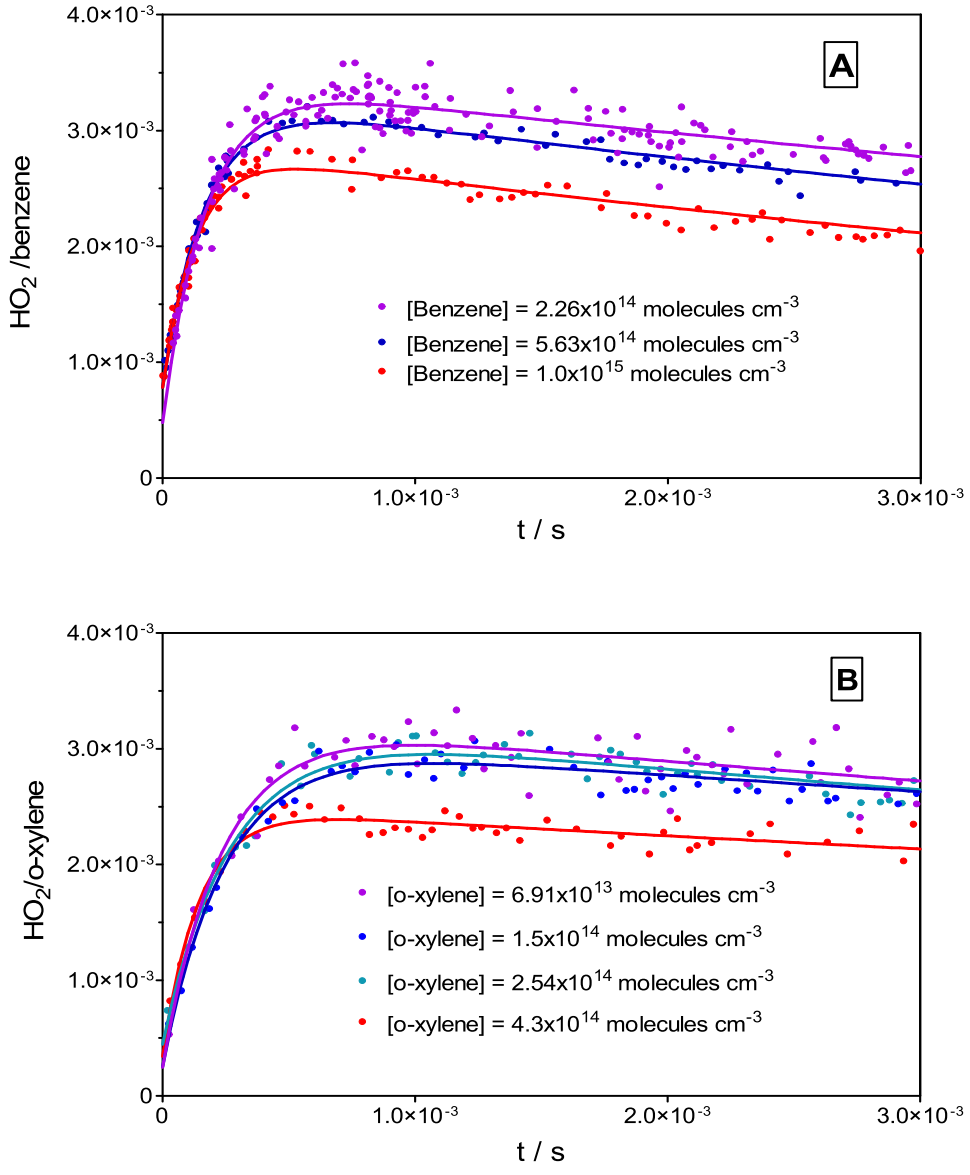

Figure 72: Concentration dependence study on HO_2 formation from benzene and o-xylene. A) HO_2 profile obtained for three different concentrations of benzene. B) HO_2 profile obtained for four different concentrations of o-xylene. The energy and the oxygen concentrations were kept constant for all the experiments. All the signals have been divided by aromatic compound concentrations.

All HO_2 profiles in Figure 72 (A and B) have almost the same initial HO_2 concentration whereas the secondary HO_2 build up decreases with the increase in the concentration of the aromatic compound. This can be explained by a probable mechanism given below.

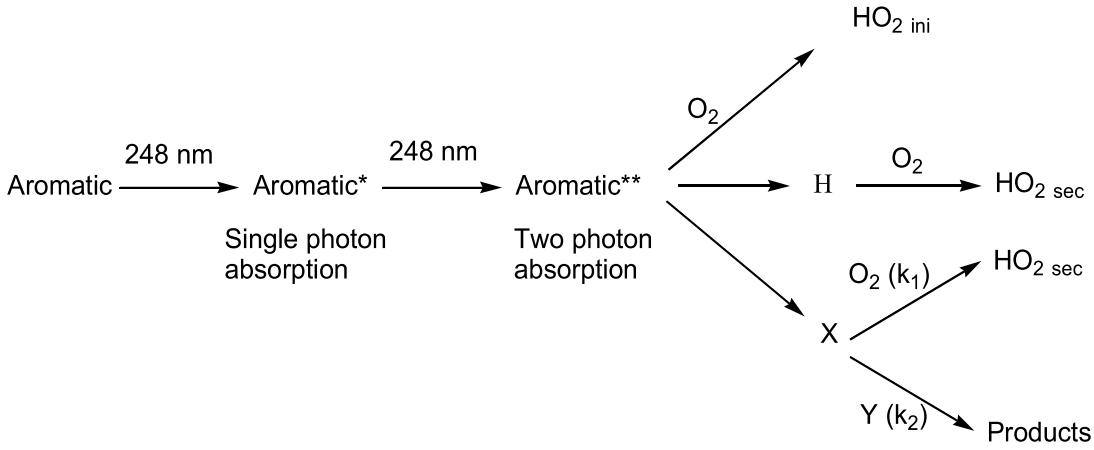

The initial HO_2 is directly formed from a reaction of two photon excited aromatic compound and oxygen, in competition with an O_2-independent path leading to X. However, the secondary HO_2 formation as mentioned depends partially on the reaction of H atoms with O_2 and partially on reactions (R-39 and R-40). Therefore the secondary HO_2 formation will be controlled by the sum of the two rates (k_1 and k_2) of the reactions indicated in the mechanism. There is a competition between the reaction of X (e.g. alkyl radicals) with O_2 and the photofragments (Y) which can scavenge X as well. This could explain the decrease of secondary HO_2 yield with a decrease in O_2. The explanation can also be given to the observation of saturation with increasing O_2: if O_2 concentration increases to a level where its reaction with X is dominant then any further increase in the oxygen concentration will not increase the HO_2 yield. Finally, the decrease in the build up of secondary HO_2 concentration with increasing aromatic concentration can be discussed on the grounds of reaction of X with products of the photolysis (Y). More photolysis products will be formed at higher aromatic compound concentration and can compete with oxygen for the HO_2 formation resulting in secondary HO_2 yield not reaching to the maximum observed for the lower concentrations.

4.4 Conclusions

The energy dependence study of the formation of HO_2 radicals by the irradiation of various aromatic hydrocarbons in the presence of oxygen at 248 nm has revealed that the origin of the HO_2 radical involves two photon excitation processes after correcting for an unknown reactive intermediate absorption. There is a primary reaction in which, on the timescale of our experiment, HO_2 radicals are formed instantaneously. Secondary HO_2 is formed on a longer time scale.

The origin of the unknown reactive intermediate is difficult to explain due to the lack of the photolysis product information. A linear trend with the change in the oxygen concentration for the unknown reactive intermediate absorption is observed. The absorption is saturated at photolysis energies higher that 10 $mJcm^{-2}$ concentrations of the aromatic compounds above $2x10^{14}$ molecules cm^{-3}.

The rate constant for the secondary HO_2 formation is in reasonable agreement with literature values for the reaction between H-atoms and O_2, however the yield is not in agreement with the H-atom yield, observed by Kovacs et al. [116].

The direct HO_2 formation from a mixture of aromatic compound and oxygen also showed that experiments on the OH-initiated oxidation study of aromatic compounds, using H_2O_2 photolysis at 248 nm as OH radical source, could be affect by this process. This could be avoided by the use of HONO as the precursor for OH radicals, as it can be photolysed at 351 nm, a wavelength were aromatic hydrocarbons do not absorb. This encouraged the measurement of the HONO absorption spectrum in the near infrared range in order to have a handy tool to measure absolute concentration of HONO. The HONO spectrum measurement will be discussed in chapter 5.

Chapter 5 - Spectroscopic applications of the cw-CRDS technique

Cavity Ring-Down Spectroscopy (CRDS) has proved to be a powerful technique for the trace analysis and spectroscopic studies of molecules and clusters as discussed in recent reviews [124, 125]. This technique has been used for the measurement of the atmospherically interesting species like NO_3, HO_2 formaldehyde etc [126, 127]. The availability of cheap and reliable components like DFB lasers and detectors are making this technique more and more popular and an attractive spectroscopic tool in the near IR region [9, 53]. Even the small absorption cross sections expected for overtone transitions occurring in near infrared region [9] can be compensated for by the high sensitivity of the cavity enhanced methods. Moreover, the ring-down time is usually independent of light intensity, so that sensitivity is not limited by optical intensity fluctuations, as is typical in most other forms of laser spectroscopy. These two features account for the high sensitivity of CRDS. The spectroscopic resolution of cw-CRDS is in general superior compared to pulsed CRDS, owing to the smaller optical bandwidth of cw laser output [128]. The HO_2 spectrum has been measured in the 6635 cm^{-1} region using this experimental set up [66] in order to get the absolute absorption cross-sections which can then be used for the absolute concentrations of HO_2 in the laboratory studies. The necessity of HONO as the precursor for OH to study the OH initiated degradation of aromatic compounds at 351 nm and the reported absorption lines for HO_2 and DO_2 lines in the 7013 cm^{-1} range motivated the extension of the spectroscopic studies to HONO (6630cm^{-1} range) and calibration of the absorption lines of HO_2 and DO_2 (7020 cm^{-1} range). The obtained spectroscopic data can then be used as a tool for kinetic measurements and absolute concentration calculations of these species. This chapter presents details of the absorption spectrum measurement using the cw-CRDS technique.

5.1 HONO measurement in the 6635 cm^{-1} range

Nitrous acid (HONO) is an important chemical species in the atmosphere as well as in laboratory studies. In the atmosphere of the polluted areas it is a major photochemical precursor for OH radicals in the early morning [129], but has also

been detected in remote areas such as the South Pole [130]. HONO can be produced in a simple gas phase reaction between OH radicals and NO, but heterogeneous reactions seem to be more important and heterogeneous formation has been shown to occur on ice [131], but also on photo catalytic surfaces [132, 133]. In laboratory studies, it has been identified as an heterogeneously formed, important OH radical precursor in atmospheric simulation chambers [134], but also as a by-product in the photolysis of CH_3ONO[135], another important OH-radical precursor for chamber studies. HONO can also be an interesting OH-precursor for laser photolysis studies, because it generates OH radicals after 351 nm excimer photolysis, thus avoiding possible unwanted complications arising at shorter, but more commonly used wavelengths [70, 117].

HONO is often detected and quantified by spectroscopic methods: UV-VIS absorption using open path DOAS technique has been very successful for atmospheric measurements [136], but FTIR spectroscopy has also been used, especially in laboratory studies [137]. While the qualitative absorption spectra of HONO have been studied by many authors in the UV-VIS and IR range [138–142], the major difficulty using spectroscopic detection methods is the uncertainty linked to the absolute absorption cross sections: HONO exists in an equilibrium with other components such as NO, NO_2, HNO_3 and H_2O, and is a rather unstable molecule, decomposing easily through heterogeneous reactions. Therefore, determining the absolute HONO concentration contained in an absorption cell is rather difficult. Febo *et al.* [143] have developed a method allowing the generation of stable HONO flows with very high purity, and this method has subsequently been used to determine absorption cross sections in the UV[144] and in the IR [145].

HONO is known to exist in equilibrium between two different forms, *trans*- and *cis*-HONO in a ratio of approximately 2 to 1 in favour of the *trans* form [146]. The rovibrational parameters of both isomers, including the $2\nu_1$ overtone of the OH stretch, have been published [139, 140]: the band centre of the $2\nu_1$ overtone of the *cis*-isomer has been located at around 6665 cm^{-1}, close to well-known and relatively intense $2\nu_1$ overtone features of the HO_2 radical [26, 66], an important intermediate in the oxidation of VOCs. The knowledge of absolute absorption cross sections for some HONO absorption lines in this wavelength range would allow for future, simultaneous measurements of HONO and HO_2 in laboratory studies.

Only one fairly indirect measurement of absorption cross sections for HONO is available in this range: Djehiche *et al.* [135] have detected HONO by cw-CRDS at 6625.69 cm^{-1} as reaction product during the photolysis of CH_3ONO in a simulation chamber. Through simultaneous measurements of CH_2O and subsequent modelling they deduced the theoretical HONO concentration, postulating that it is formed in a reaction of OH radicals with the precursor CH_3ONO. From this fairly indirect approach they have estimated the absorption cross section for *cis*-HONO to $\sigma_{6625.69\ cm^{-1}} = 4.2 \times 10^{-21}$ cm^2, assuming that only 1/3 of the formed HONO is in *cis*-configuration.

In this work the measurement of the HONO spectrum in the range 6623.6 - 6645.6 cm^{-1} is carried out using two different, complementary methods for generating HONO: pulsed and continuous. The pulsed method has allowed determining absolute absorption cross sections, while the continuous method led to a better signal-to-noise ratio.

5.1.1 Pulsed HONO spectrum measurement

This method includes in-situ HONO preparation by laser photolysis and the measurement of HONO absorption spectrum. HONO has been produced in-situ by photolysis of hydrogen peroxide H_2O_2 in presence of excess NO. Under these conditions, OH radicals initially formed from the H_2O_2 photolysis are converted nearly quantitatively to HONO in a fast reaction sequence.

Photolysis of H_2O_2 at 248 nm leads to the formation of two OH radicals (section 3.1.2.1) [76, 77]. The H_2O_2 concentration used for the HONO generation is monitored regularly by cw-CRDS through its absorption line at 6639.88 cm^{-1} ($\sigma = 2.23 \times 10^{-22}$ cm^2) and is $[H_2O_2] = 2.9 \times 10^{15}$ cm^{-3}, while the time resolved HO_2 profiles are measured at 6638.20 cm^{-1} ($\sigma_{40\ Torr} = 2.93 \times 10^{-19}$ cm^2). A fit of these HO_2-profiles using the well-known rate constants (section 3.1.2.1) leads to an initial OH concentration of $[OH]_0 = 3.3 \times 10^{13}$ cm^{-3}. Calculation of the OH concentration using the photolysis energy (52 mJ cm^{-2}) and H_2O_2 absorption cross section at 248 nm ($\sigma_{H_2O_2,\ 248\ nm} = 9.37 \times 10^{-20}$ cm^2) [147] leads to $[OH] = 3.52 \times 10^{13}$ cm^{-3}, in very good agreement with the value obtained from cw-CRDS measurements.

Addition of NO to the reaction mixture will lead to a competition between (R-26) and

$$OH + NO + M \longrightarrow HONO + M \qquad \text{R-41}$$

Reaction (R-41) is still in the fall-off range at pressures of 40 Torr He with a low pressure rate constant [148] of $k_{41,0} = 6.0\times10^{-31}\times$ [He] cm^6 $molecule^{-2}$ s^{-1}. However, HO_2 radicals formed in the presence of NO in competition through (R-26) will rapidly be transformed back to OH through the fast reaction

$$HO_2 + NO \longrightarrow OH + NO_2 \qquad \text{R-13}$$

The competing reaction channel

$$HO_2 + NO + M \longrightarrow HNO_3 + M \qquad \text{R-42}$$

has been found to be very minor at room temperature at 200 Torr N_2 [149], so it can safely been neglected under our conditions (40 Torr He). Another possible competing reaction for OH radicals is

$$OH + HONO \longrightarrow HO_2 + NO_2 \qquad \text{R-43}$$

will gain some importance at longer reaction times with a rate constant [150] of k_{45} = 7.0 $\times$ 10^{-12} cm^3 $molecule^{-1}$ s^{-1}. The rate constants for (R-26) (k_{26}= 1.7×10^{-12} $cm^3molecule^{-1}s^{-1}$) [102] and (R-41) (k_{41} = 6.0×10^{-31} cm^6 $molecule^{-2}$ s^{-1} = 8.4×10^{-13} cm^3 $molecule^{-1}$ s^{-1} at 40 Torr) [148] are comparable, leading at concentrations of H_2O_2 (2.9×10^{15} cm^{-3}) and NO (5.1×10^{15} cm^{-3}) to similar pseudo-first order rate constants of $k_{26,41}^{1st} \approx 5000s^{-1}$. A simple simulation shows that under these condition 88.4% of initial OH radicals will be transformed into HONO within around 1 ms, i.e. immediately on the time scale of Figure 74 7.2 % of the initial OH radicals react through (R-27) and 4.4% react through (R-43), we can thus calculate [HONO] = 0.884 $\times$ $[OH]_0$ = 2.9 x 10^{13} molecules cm^{-3}.

The systematic error introduced by uncertainties in the reaction mechanism is considered to be small: an error in the initial OH-radical concentration would of course have a direct, linear impact on the obtained HONO concentration; however the impact on the HONO yield itself through a changed impact of (R-27) and (R-43) is negligible. The initial OH concentration is mainly obtained from the absolute HO_2 concentrations, measured by cw-CRDS, while the H_2O_2 concentration, measured through pseudo-first order OH decays and by absorption in the near IR, has only a minor impact on the extraction of the initial OH concentration. The absorption cross section of HO_2 is thought to be known to better than ±20% [26, 66], therefore the initial OH concentration to be known with the same accuracy. A possible systematic error source for the conversion of OH radical into HONO is impurity of

NO_2, arising from an oxidation of NO by trace amounts of O_2: NO_2 reacts with both, OH and HO_2, in addition reactions and would therefore decrease the HONO concentration. To illustrate the impact of such an impurity, typical experimental traces, together with model simulations, are shown for an experiment in 10 Torr of N_2 (Figure 73). The graph A in Figure 73 shows experimental OH profiles together with simulations in absence and presence of NO (2.5×10^{15} molecules cm^{-3}): in presence of NO, the OH decay is, under these conditions, slowed down due to cycling of HO_2 radicals by (R-13). Impurities of NO_2 however increase the decay rate of OH radicals drastically due to a reaction of NO_2 with both, OH and HO_2 radicals: the dashed line in the upper graph represents an impurity of 2.5×10^{13} molecules cm^{-3}, i.e. 1 % of the NO concentration. An impurity on this order of magnitude would be noticeable in our OH decays, and we therefore estimate an upper limit of the NO_2 impurity of 1% of the NO concentration. Graph B Figure 73 shows the corresponding HO_2 profiles: the red curve in the absence of NO is the basis for the calculation of the initial OH radical concentration, and it can be seen from the black dots that after NO addition HO_2 decreases rapidly to concentration below our detection limit. The upper blue line shows the simulated HONO profile, which under these conditions corresponds to a HONO yield of [HONO] = 0.943 $\times$ $[OH]_0$ (a lower initial radical concentration compared to the conditions used for the complete spectrum leads to a decrease of the impact of (R-27). The green line shows the simulated HONO profile obtained in the presence of a 1% NO_2 impurity (2.5×10^{13} molecules cm^{-3}): under these conditions, the HONO yield drops to 0.89, i.e. a decrease of 5%. From the combined uncertainties (σ_{HO_2}, rate constants and NO_2 impurity) we estimate the uncertainty of the HONO concentration, and thus on the obtained absorption cross sections, to be $\pm$30%.

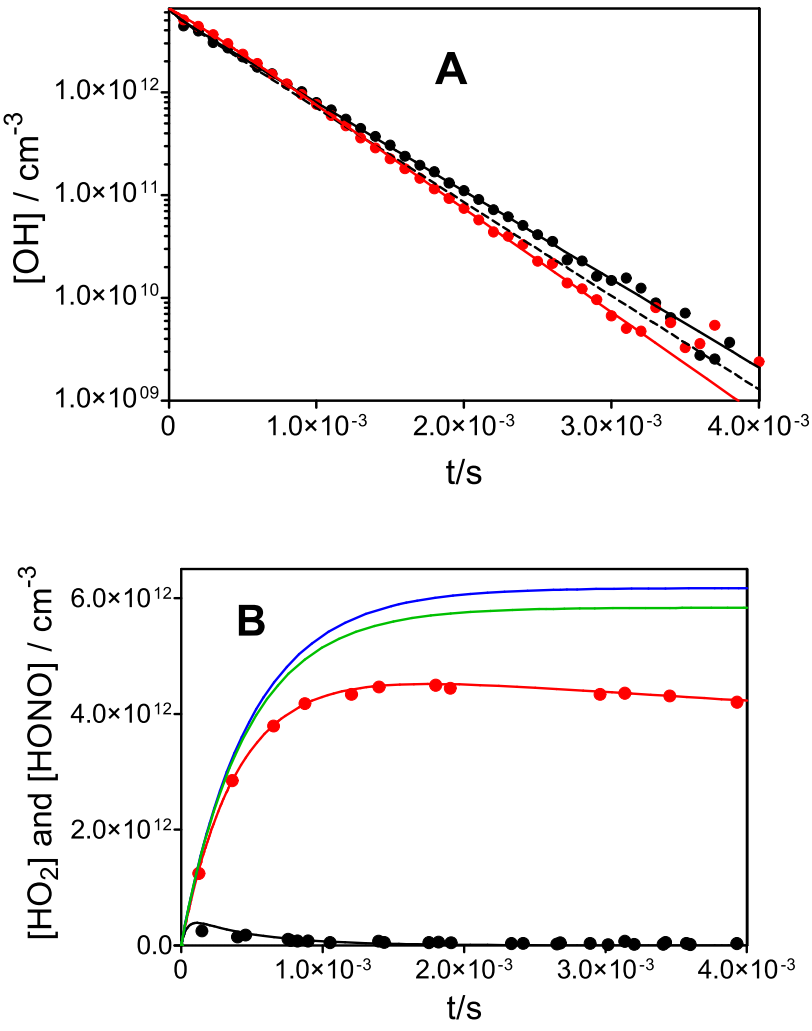

Figure 73: OH and HO_2 profiles for an experiment at 10 Torr N_2 with $[H_2O_2]$ = 1.1×10^{15} molecules cm^{-3}, $[OH]_0$ = 6.55×10^{12} cm^{-3}. Graph A shows OH-decays red dots [NO] = 0, black dots [NO] = 2.5×10^{15} molecules cm^{-3}, full lines represents simulation with rate constants as given in text, dashed line simulation with additional impurity of $[NO_2]$ = 2.5×10^{13} molecules cm^{-3}, graph B shows experimental HO_2 profiles with simulations, red symbols and line show the HO_2 profile without NO, black symbols and line show the HO_2 profile with NO, blue line simulated HONO profile without NO_2 impurity, green line HONO profile in presence of NO_2 impurity.

The ring-down events have to be measured relative to the photolysis pulse as explained in section 2.5.2.2. A lab view program started the data acquisition and triggered simultaneously a delay generator which in turn triggered after 2 seconds the Excimer laser. The total data acquisition was for a total period of 4 seconds, i.e., 2 seconds before and 2 seconds after the photolysis pulse (as shown in Figure 74) In order to renew the gas mixture between two laser pulses and to pump out

most of the HONO produced during the previous laser pulse, photolysis was carried out at a repetition rate of maximal 0.08 Hz. To ensure that the data acquisition and the fitting of the individual ring down events had been completed before the next photolysis pulse, the lab-view program was made to verify that data acquisition and fitting of the ring down events is finished before starting the next data acquisition cycle, as described in section 2.5.2.2. A minimum of 500 ring-down events have been acquired over the full 4 seconds measurement time (asking in average for 2 – 5 photolysis pulses) before the cw-CRDS laser was tuned to the next wavenumber by the control program. The whole spectrum was measured with a resolution of 0.005 cm^{-1}, i.e. 4600 time resolved traces as shown in Figure 74 have been recorded.

From the time resolved cw-CRDS signals (a typical example is shown Figure 74), the absorption coefficient $\alpha_{t=0}$ and, now with knowledge of the photolytically generated HONO concentration, the absorption cross section σ can be extracted using equation (E-16). In order to extract $\tau_{t=0}$ and τ_0, the time resolved signals as shown in Figure 74 were analyzed for each wavelength by a data analysis program written in lab view.

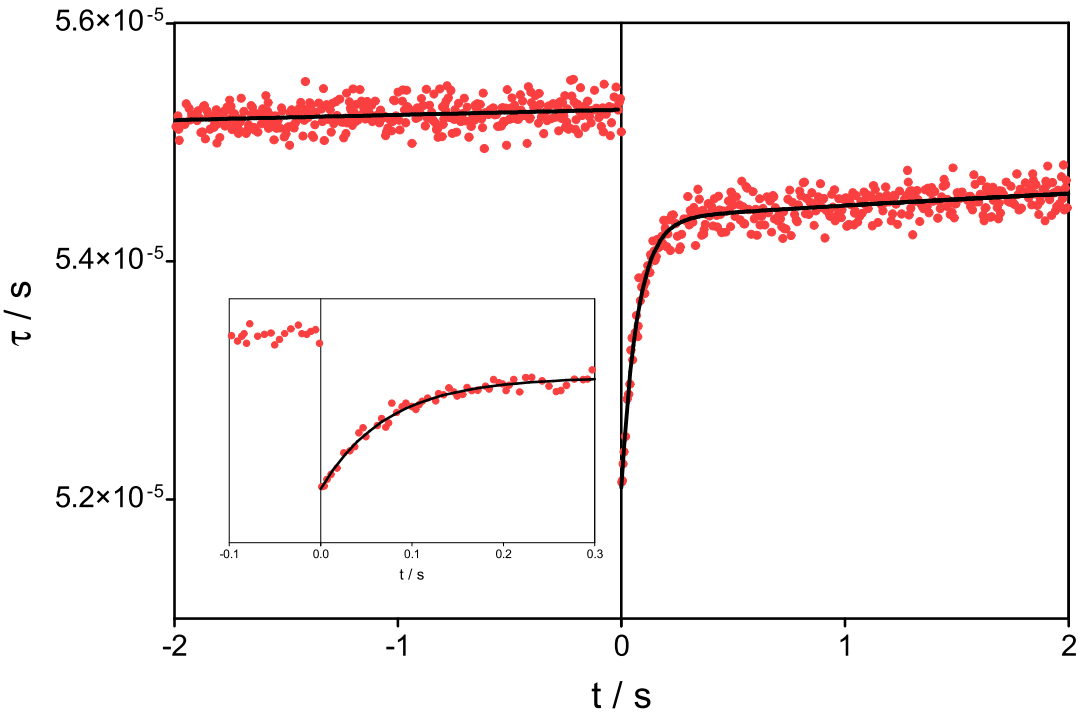

Figure 74: Typical time resolved absorption signal for HONO formed from H_2O_2 photolysis in the presence of NO. The inset shows a zoom of the first 300 ms.

τ_0 was obtained as the intercept of the linear regression of all the ring-down events occurred during the 2 seconds before the photolysis pulse. For extracting $\tau_{t=0}$, all ring-down events occurred after the photolysis pulse were fitted by a two phase association

$$\tau_t = \tau_{t=0} + a(1 - e^{-k_{fast}t}) + b(1 - e^{-k_{slow}t}) \qquad \text{E-23}$$

HONO is a stable product; therefore the two empirical rate constants k_{fast} and k_{slow} can be interpreted by two different loss processes. The rapid decay with an average rate of k_{fast}=12 s^{-1} can be linked to the diffusion of HONO out of the photolysis volume. This process is completed after roughly 200 ms, i.e., after this delay the HONO generated only in the volume limited by the size of the photolysis beam has diffused into the entire volume. The following slow loss k_{slow} with an average rate of $k_{slow} \approx 0.16$ s^{-1} can possibly be approximated as the loss of HONO through processes such as the renewal of the gas mixture by pumping and heterogeneous losses on the reactor wall. In order to evaluate if this assumption is reasonable, a simple estimation is carried out: the photolysis cell has an inner diameter of 6 cm leading to a surface of 28.3 cm^2, while the photolysis beam has a surface of 4.5 cm^2, i.e. a ratio of 6.2 between photolysed over total volume (for simplicity the side arms of the reaction cell have not been taken into account, which would increase this ratio). Taking a typical time resolved signal such as shown in Figure 74 the ratio of the absorption coefficients α can be calculated taking into account, that R_L (E-16) evolves from 2.22 just after the laser pulse (0.82 / 0.37) to 1.05 (0.82 / 0.78) at long reaction times, a ratio of $\alpha_{t=0}$ over $\alpha_{t=200\ ms}$ of 7.2 is in good agreement with the above calculated volume ratio. Therefore it is evident that the time resolved evolution of the absorption coefficient is due to diffusion phenomena only. This can further be confirmed by the pressure dependence study of the HONO absorption measured in two different bath gases (helium and nitrogen) at 3 different pressures. The rates of fast decay of HONO decrease with the increase in the pressure in both gases and are faster in helium compared to nitrogen. Figure 75 shows the HONO signal decay due to diffusion in two different bath gases at 3 different pressures and the rates at different pressures are listed in Table 10.

Pressure (Torr)	Rate of diffusion k_{fast} / s^{-1} (in nitrogen)	Rate of Diffusion k_{fast} / s^{-1} (in helium)
10	9	18
40	7	12
74	3	6

Table 10: HONO diffusion rates in nitrogen and helium bath gases at different pressures.

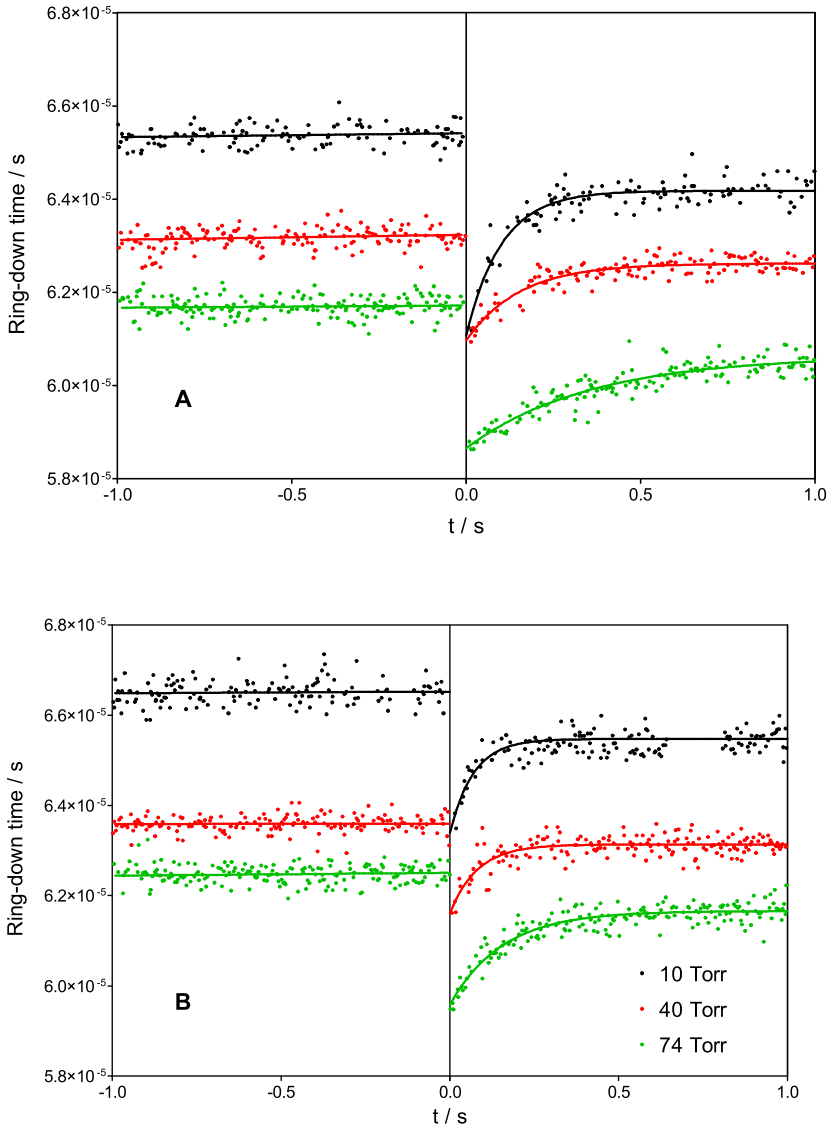

Figure 75: Plot of HONO absorption measured at 6642.5 cm^{-1} by pulsed photolysis showing the difference in the diffusion rate at 3 different pressures in two different bath gases, A) in nitrogen B) in helium. The shift in the signals is due to the change in the baseline with the pressure.

It can be noticed that the renewal of the gas mixture is probably not totally completed just before the next photolysis pulse i.e., some HONO is still left in the photolysis cell (the baseline is not completely flat). This however has no influence on the calibration of the absorption measurement, because the laser photolysis technique accounts only for HONO that is formed from the actual photolysis pulse, all possible residual HONO will also contribute with the same intensity to the baseline. The same is true for any absorption due to other species present in the photolysis cell such as H_2O: these absorptions will not be visible, because it affects τ_0 and $\tau_{t=0}$ in the same way (Figure 80).

In order to illustrate the measurement principle, a small portion of the obtained spectrum (although not typical for the whole spectrum, because measured with a higher resolution of 0.001 cm^{-1}) is presented in Figure 76.

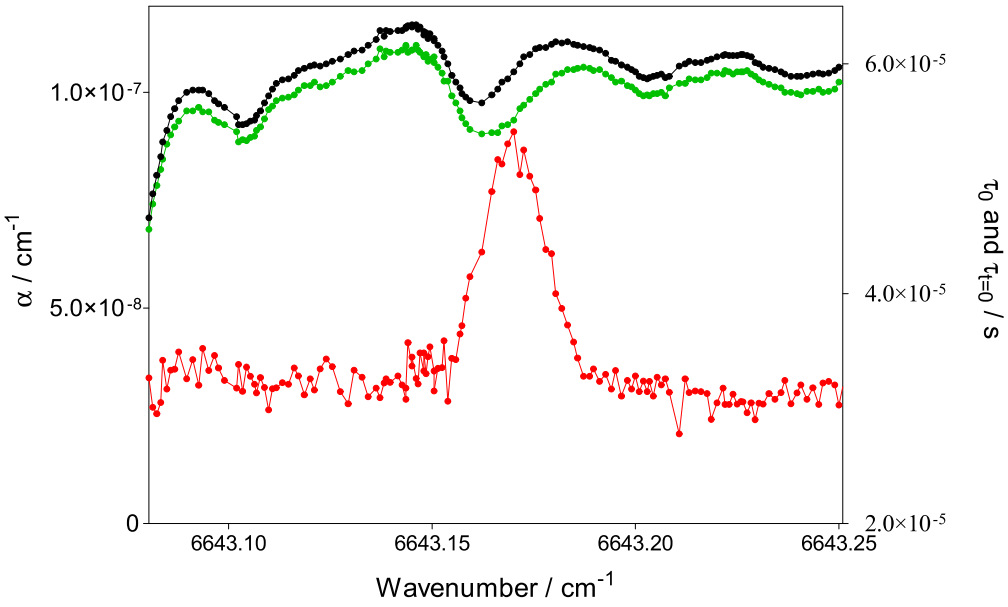

Figure 76: HONO spectrum obtained by laser photolysis: upper, black line is baseline (τ_0), middle, green line is $\tau_{t=0}$, obtained through fits of individual, time resolved HONO profiles to equation [E-23] (right Y-scale) and red line is absorption coefficient α obtained from equation [E-16] (left Y-scale).

Each dot is the result of one time resolved HONO signal as shown in Figure 74. The upper black line is the baseline, as obtained from ring down events acquired just before the photolysis pulse. The middle, green dots have been obtained as $\tau_{t=0}$ from fits of the individual, time resolved HONO profiles to equation (E-23). The lower red line represents the absorption coefficient α as calculated from equation

(E-16). In this manner the spectrum accessible with our DFB laser (6623.6 - 6645.6 cm^{-1}) has been measured with a resolution of 0.005 cm^{-1} and is presented in Figure 77 (zoomed spectrum is shown in Appendix A.3).

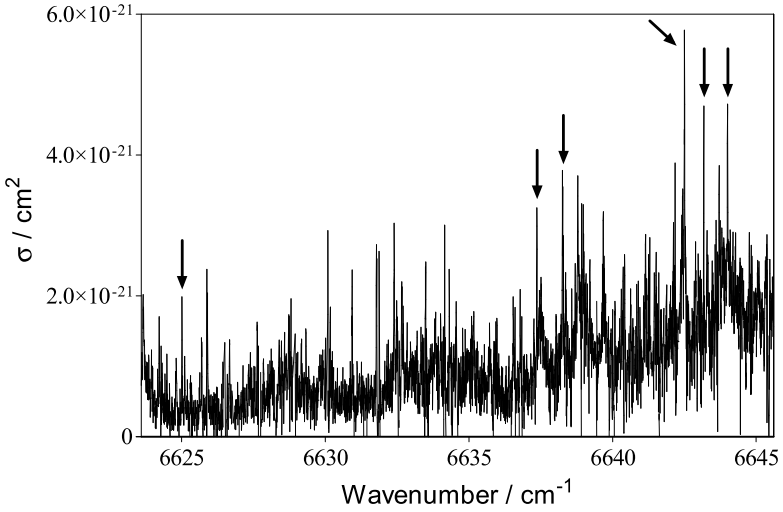

Figure 77: Full spectrum of HONO accessible with the DFB diode, obtained by pulsed HONO generation and calibrated to the six individual absorption lines indicated by an arrow.

The repetition rate of the experiment was very low (0.08 Hz maximal), therefore the total measurement time for the spectrum shown in Figure 77 spread over 2 weeks. The generated HONO concentration depends directly on the H_2O_2 concentration and on the photolysis energy. To ensure that the HONO concentration was constant over the whole measurement period, the H_2O_2 concentration has regularly been checked by measuring its absorption line at 6639.88 cm^{-1}. The photolysis energy was also measured by a calibrated power meter. Occasionally, HO_2 concentration-time profiles were recorded in the absence of NO, verifying simultaneously the H_2O_2 concentration and the photolysis energy.

It has been mentioned that the spectrum shown in Figure 77 was measured for practical reasons at a low spectral resolution with a poor signal-to-noise ratio. However, this spectrum has been used to choose six of the most intense absorption lines to be re-measured very carefully with high spectral resolution in order to obtain a significant calibration. Six absorption lines, indicated by an arrow in Figure 77, have therefore been measured again using a higher resolution (0.001 cm^{-1}, the same as shown in Figure 4) and taking special care on the verification of the absolute HONO concentration: before starting the acquisition of each line, the HO_2 and OH concentration-time profiles as well as the H_2O_2 absorption around 6639.88 cm^{-1} have been measured in the absence of NO. The six individual lines

are shown in appendix A.2 and the peak absorption cross-sections of these lines in 40 Torr Helium are listed in Table 11. It can be seen from Figure 76 that a broad absorption underlies the individual absorption lines: this background absorption is unequivocally HONO, because it is generated by the photolysis pulse and is probably due to an unresolved, dense spectrum. Sometimes it is not possible to record a baseline in the absence of HONO; therefore the percentage of the peak absorption cross sections due to this background absorption is added in Table 11.

Wavenumber /cm^{-1}	σ / 10^{-21} cm^2	Background absorption / %
6625.01	1.6 ± 1.0	26
6637.36	3.5 ± 1.6	38
6638.26	3.8 ± 1.6	30
6642.51	5.8 ± 2.2	37
6643.17	4.2 ± 1.7	33
6644.00	4.8 ± 1.9	52

Table 11: Absorption cross-sections of some selected HONO absorption lines in the near infrared region. Errors have been estimated from the signal-to-noise ratio ($\Delta\alpha = 1.5\times10^{-8}$ cm^{-1}) plus 30% for other errors such as drift in H_2O_2 concentration, photolysis energy and uncertainties in the retrieval of the HONO concentration. In the third column is added the percentage of this absorption cross section that is due to the congested background absorption.

It should be noted that the HONO is in equilibrium between its *cis*- and *trans*-isomer, i.e. only around 1/3 of the photolytically generated HONO is present in form of the *cis*-isomer. This fact has not been taken into account in the calculation of the absorption cross sections, because the result of this work should be seen as a tool enabling the easy quantification of HONO in laboratory experiments. Under this point of view it seems idle to take into account the *cis-trans* equilibrium.

5.1.1.1 Continuous measurement of HONO generated from HCl and $NaNO_2$

It has been already explained (in section 5.1.1) that the spectrum obtained by generating HONO in a pulsed manner could, for practical reasons, be obtained with a poor signal-to-noise ratio only. The pulsed method has other advantages, noticeably (a) the absolute HONO concentration can be known from a calibration

relative to HO_2 profiles and that (b) other stable species present in the cell such as H_2O or products formed in an equilibrium with HONO or from heterogeneous reactions at longer reaction times, will not be detected: all absorption features appearing directly after the photolysis pulse are inherent to HONO. In order to obtain a spectrum with better signal-to-noise ratio, the whole spectrum has been measured again using a continuous source of HONO: humidified N_2 was flown first over a 5.2 M HCl solution (kept at 12℃) and then o ver a 0.5 M $NaNO_2$ solution. In the first trial a variant published by Barney *et al.* [145] in which humidified N_2 is flown over 5.2 M HCl (kept at 0℃) and solid $NaNO_2$ was tried. However, the HONO concentration that could be generated by this method was too low to obtain a spectrum with a satisfying signal-to-noise ratio. Therefore, a slight modification using $NaNO_2$ in solution has been employed: this way, much higher concentrations of HONO could be obtained. Figure 78 shows a schematic diagram of continuous HONO generation.

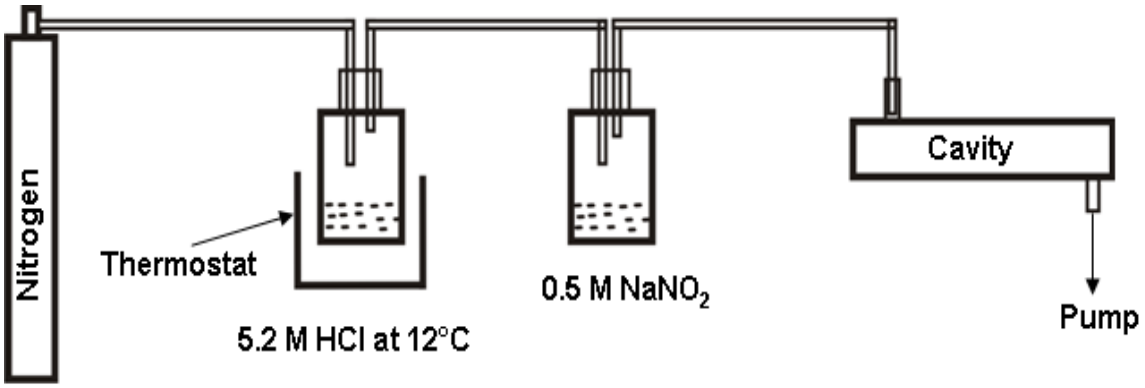

Figure 78: Schematic diagram of continuous HONO generation.

A drawback of this modification is (a) the high water concentration in the reactor (H_2O has strong absorption lines in this wavelength region) and (b) the instability of the HONO concentration on the longer time scale: a slow increase in the HONO concentration on the hour-time scale was observed, possibly due to an increase in $NaNO_2$ concentration following the slow evaporation of water. This change in HONO concentration was too fast to allow measuring the whole spectrum considering identical HONO concentrations. Therefore the spectrum has been measured in seven individual portions and each portion was calibrated to a reference: one of the HONO lines (6643.17 cm^{-1}) was chosen as reference line

and was regularly measured before and after the acquisition of each portion of the spectrum; the absorption coefficient of the entire portion was calibrated subsequently to the intensity of this line.

Once the whole spectrum has been measured and all individual portions were calibrated to the reference line, the absorption coefficients (α) of the six HONO lines were plotted against the absolute absorption coefficients σ of the same lines obtained by the pulsed method and tabulated in Table 11. This should present a linear relationship if the reference line calibration for the continuous spectrum was valid: as can be seen in Figure 79, this seems to be the case. The slope of a linear regression of this plot represents the HONO concentration generated by the continuous method: $(1.58 \pm 0.2) \times 10^{13}$ molecules cm^{-3}.

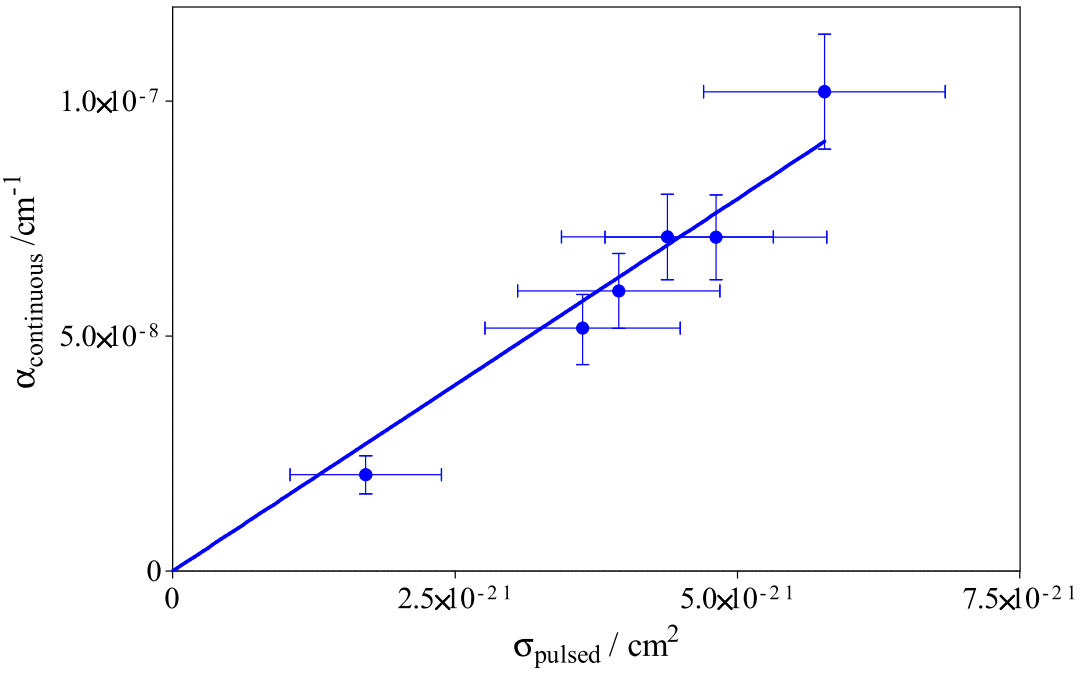

Figure 79: Plot of absorption coefficient α obtained by continuous HONO production against the absorption cross sections σ obtained by pulsed HONO generation for the six lines shown as supplementary data.

A comparison of the spectra, obtained with both methods, is shown for a small portion (full spectrum is shown in Appendix A.3) in Figure 80.

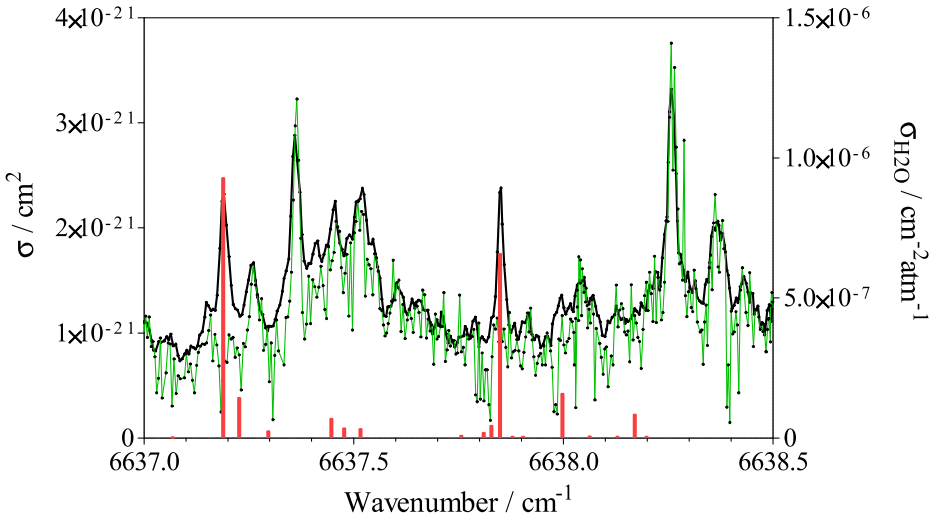

Figure 80: Small portion of HONO spectrum, obtained by both methods: green line shows the spectrum obtained by laser photolysis method, black line shows the spectrum obtained by continuous HONO production, red spikes show H_2O spectrum, as obtained by Macko *et al.* [151].

The green line represents the spectrum obtained using the pulsed method, the black line represents the spectrum obtained by the continuous method. For comparison, the position of H_2O absorption lines as published by Macko *et al.* [151] are added to the graph (red spikes). It can be seen that the H_2O lines are clearly visible in the continuous HONO spectrum, but do not appear in the pulsed HONO spectrum. The HONO absorption features on the other hand (for example 6638.26 or 6639.36 cm^{-1}) are clearly visible in both spectra (continuous and pulsed). There is, however, a limitation even to the pulsed method: very strong H_2O-absorption lines can decrease the intensity of the ring-down events below the trigger threshold and preventing measuring HONO absorption features.

The result of this work can be compared to the only published absorption cross section, deduced by Djehiche *et al.* [135] for the line at 6625.69 cm^{-1}: $\sigma = 4.2 \times 10^{-21}$ cm^2. After going through the whole spectrum this seems to be a small line with an absorption cross section of $\sigma = 3.2 \times 10^{-21}$ cm^2 (Djehiche *et al.* [135] have taken into account the *cis-trans* equilibrium, while in this work it is not taken into account, hence σ is to be multiplied by 3 for comparison). The 30% higher absorption cross section from Djehiche *et al.*[135] is in excellent agreement, looking at the very indirect method that they have used to extract the absorption cross section.

5.1.2 Pressure dependence of HONO absorption

The goal of this work was to provide a tool for measuring absolute HONO concentrations in laboratory experiments under reduced pressures. For this reason, the pressure broadening of the most intense line at 6642.51 cm^{-1} in the pressure range 10 – 74 Torr has been investigated with He and N_2 as bath gas. In Figure 81 are shown the two lines obtained at 10 Torr N_2 (upper graph) and at 74 Torr N_2 (lower graph). It is obvious (and has already been discussed) that the background absorption is a convolution of non-resolved absorption lines, leading to broad background absorption. This has been illustrated by adding the result of a least-square fit of the experimental data to individual, Voigt-shaped absorption lines, obtained by the free software fitting program Fityk (Version 0.9.8) [152] in Figure 81.

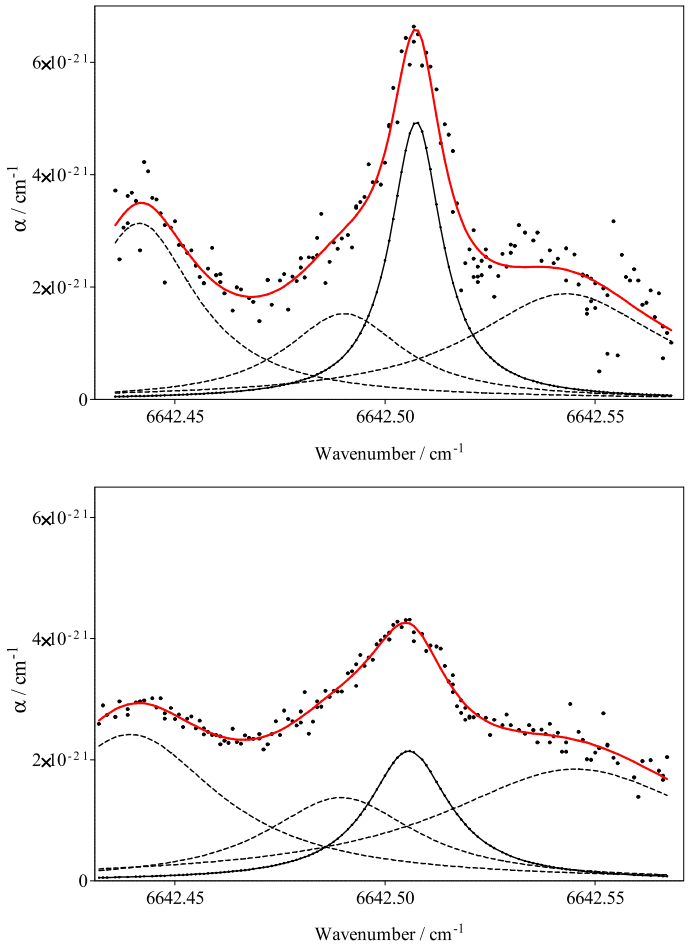

Figure 81: HONO absorption line at 6642.51 cm^{-1}. Upper graph at 10 Torr N_2, lower graph at 74 torr N_2. The black lines represent the individual absorption lines identified by the Fityk program through a fit of the experimental data (black dots) to a Voigt profile.

From Figure 81 it is obvious that it will not be useful to extract line strengths and pressure broadening coefficients for individual lines in order to propose a reliable tool to extrapolate absorption cross sections under various experimental conditions. Instead, the absorption cross sections in the centre of the strongest absorption line are presented in Table 12 for the three individual pressures and two bath gases, He and N_2. It is not always possible to measure the baseline in the absence of HONO (for example in atmospheric simulation chambers) and therefore the pressure dependant minimum absorption cross-section at 6642.46 cm^{-1} is also given.

Pressure / Torr	He		N_2	
	$\sigma_{6642.51\ cm^{-1}}$ / $10^{-21}cm^2$	$\sigma_{6642.46\ cm^{-1}}$ / $10^{-21}cm^2$	$\sigma_{6642.51\ cm^{-1}}$ / $10^{-21}cm^2$	$\sigma_{6642.46\ cm^{-1}}$ / $10^{-21}cm^2$
10	7.0 ± 2.6	1.8 ± 1.0	6.6 ± 2.5	1.8 ± 1.0
40	5.8 ± 2.2	2.1 ± 1.1	5.1 ± 2.0	2.3 ± 1.2
74	4.6 ± 1.8	2.3 ± 1.2	4.3 ± 1.8	2.4 ± 1.2

Table 12: Pressure dependant absorption cross sections at the centre of the strongest line at 6642.51 cm^{-1}. For practical purposes, the absorption cross section at 6642.46 cm^{-1} is also given.

5.2 Calibration of selected HO_2 absorption lines in the 7013 cm^{-1} range

The hydroperoxyl radical HO_2, plays an important role in low temperature oxidation processes in the atmosphere or combustion. This made the kinetics as well as the spectroscopy of HO_2 to receive significant interest in recent years. Higher initial HO_2 concentrations lead to the self-reaction of HO_2 because the self reaction is relatively fast [29, 153]. This demands a sensitive and time resolved measurement technique. UV absorption spectroscopy has become a widely used technique to monitor the HO_2 radical but the broad and structureless absorption of HO_2 in this wavelength range leads to many overlaps and becomes a limiting factor. This encouraged the development of spectroscopic measurements in the

infrared region where narrow and resolved absorption lines of small structures such as the HO_2 radical are found [154, 155]. Therefore, several experiments have been reported using a laser diode in the near-IR where the O-H stretching overtone $2\nu_1$ band absorption is used to detect HO_2 radicals [9, 29, 66, 156, 157]. An electronic transition of HO_2 can be found near 7013 cm^{-1}, this transition having the advantage, that DO_2 [158] and OH [159] absorption is observed in the same wavelength range. Being able to detect all three radical intermediates (HO_2, DO_2 and OH) with the same DFB laser and mirror set can be very useful for future applications of the cw-CRDS technique. Therefore, a few selected HO_2 absorption lines [123, 155, 160] for the electronic transition of HO_2 radicals in this wavelength range have been calibrated in this work.

HO_2 has been produced by 248 nm photolysis of a mixture of $COCl_2/CH_3OH/O_2$ at 20 Torr Helium. All flows were monitored through calibrated flow controllers. The reaction sequence which leads to the HO_2 formation is as follows.

$$COCl_2 + h\nu\ (248\ nm) \longrightarrow 2\ Cl + CO \qquad \text{R-44}$$

$$Cl + CH_3OH \longrightarrow CH_2OH + HCl \qquad \text{R-45}$$

$$CH_2OH + O_2 \longrightarrow CH_2O + HO_2 \qquad \text{R-46}$$

First, the absorption of a few selected HO_2 absorption lines (6998.41, 7020.72 and 7020.77 cm^{-1}) were measured using the 7013 cm^{-1} laser diode and the ring-down event average method as explained in 2.5.2.2. The baseline was obtained by averaging all the ring-down events before the photolysis pulse and the absorption due to HO_2 was measured averaging all the ring-down events that fall during a 2 ms time window immediately after the photolysis pulse. 25 ring-down events have been averaged in the 2 ms time window before tuning the laser to next wavelength. Once the measurement of spectra for the selected lines in the 7013 cm^{-1} range was finished, the laser diode was changed to the 6635 cm^{-1} range diode. The changing of the diodes did not take long and hence we considered that the experimental conditions, i.e. the HO_2 concentration, were maintained. After finishing the measurement, the absorbencies of the two measured spectra were calculated using equation (E-16). Figure 82 shows an example of the absorption spectra of HO_2 measured in the two ranges. The poor signal to noise ratio

observed for the 7013 cm^{-1} spectrum measurement was due to a lower mirror reflectivity in the 7013 cm^{-1} range compared to the 6630 cm^{-1}, leading to lower τ_0 (10 µs) at 7013 cm^{-1} compared to the 6630 cm^{-1} range (50 µs). The mirrors were selective for the 6635 cm^{-1} and not for the 7013 cm^{-1}.

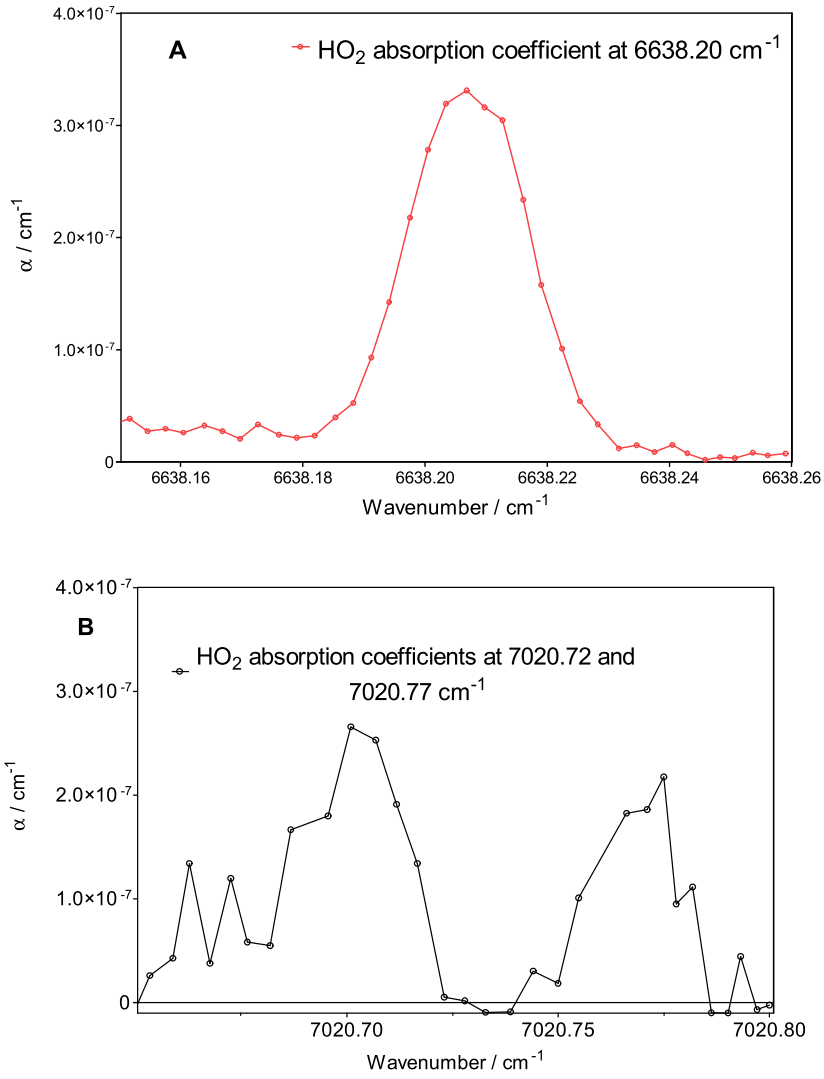

Figure 82: HO_2 absorption lines at 6635 and 7013 cm^{-1} ranges: (A) HO_2 line at 6638.20 cm^{-1} and (B) HO_2 lines at 7020.72 and 7020.77 cm^{-1}.

The absolute concentration of HO_2 at 20 Torr helium was calculated using the absorption coefficient measured at 6638.20 cm^{-1} using the well-known absorption cross section [66]. Once the absolute concentration of HO_2 was known then the absorption cross-sections for the selected lines at 20 Torr in the 7013 cm^{-1} range have been calculated using equation (E-16). HO_2 absorption cross sections measured using this method at 20 Torr helium are listed in Table 13. The errors in

the absorption cross section indicate the errors occurred due to the signal to noise ratio in the spectrum measurement.

Wavenumber /cm^{-1}	σ / 10^{-19} cm^2 at 20 Torr helium
6998.41	2.6 ± 0.15
7020.72	2.63 ± 0.2
7020.77	1.93± 0.2

Table 13: Absorption cross sections of HO_2 in the 7013 cm^{-1} range at 20 Torr helium.

Care must be taken while using these absorption cross sections at different pressures. In such cases the pressure broadening effect needs to be taken into account.

5.3 Calibration of selected DO_2 absorption lines in the 7013 cm^{-1} range

Due to its important role in the combustion processes and atmospheric chemistry HO_2 has been the subject of a large number of experimental and theoretical studies [155]. However for DO_2, not much work is done; Tuckett *et al,* [158] measured the first medium-resolution emission spectrum of DO_2. In 2002 Fink *et al.* [158] measured the accurate spectroscopic data of DO_2 using the Fourier-transform emission spectrum of DO_2 in 7013 cm^{-1} range. One of the DO_2 (7022.98 cm^{-1}) lines from Fink *et al.* [158] has been calibrated using the cw-CRDS technique for different pressures. DO_2 line strength measurements at different pressures have been carried out using the method based on time resolved kinetics as described by Thiebaud *et al.* [66] for HO_2. The DO_2 line calibration will help the DO_2 detection and kinetic measurements in the future applications of the cw-CRDS technique.

5.3.1 In-situ preparation of DO_2 using laser photolysis

DO_2 has been generated in-situ by the photolysis of a mixture of $COCl_2/CD_3OD/O_2$/He at 248 nm. Phosgene was introduced from a $COCl_2$/He mixture (4.95%), stored in a glass bulb. All gas flows into the cell were controlled by calibrated flow controllers. The reaction sequence involved in the in-situ generation of DO_2 is given below,

$$COCl_2 + h\nu\ (248\ nm) \longrightarrow 2\ Cl + CO \qquad R\text{-}44$$

$$Cl + CD_3OD \longrightarrow CD_2OD + DCl \qquad R\text{-}47$$

$$CD_2OD + O_2 \longrightarrow DO_2 + CD_2O \qquad R\text{-}48$$

The DO_2 absorption coefficient was measured by the cw-CRDS technique at 7022.98 cm^{-1} using the similar method used for HO_2 absorption line calibration (section 5.2). The pressure broadening of the absorption line at 7022.98 cm^{-1} was carried out at four different pressures.

5.3.2 Pressure broadening study of DO_2 absorption line at 7022.98 cm^{-1}

The calibration of the HO_2 absorption line using the kinetics of HO_2 self reaction has been explained by Thiebaud *et al.* [66]. The same procedure was used to calibrate the DO_2 absorption line using the DO_2 self reaction kinetics. Figure 83 shows an example of the kinetics of DO_2 observed at 7022.98 cm^{-1} at 20 Torr helium. The absorption coefficient α was calculated using equation (E-16).

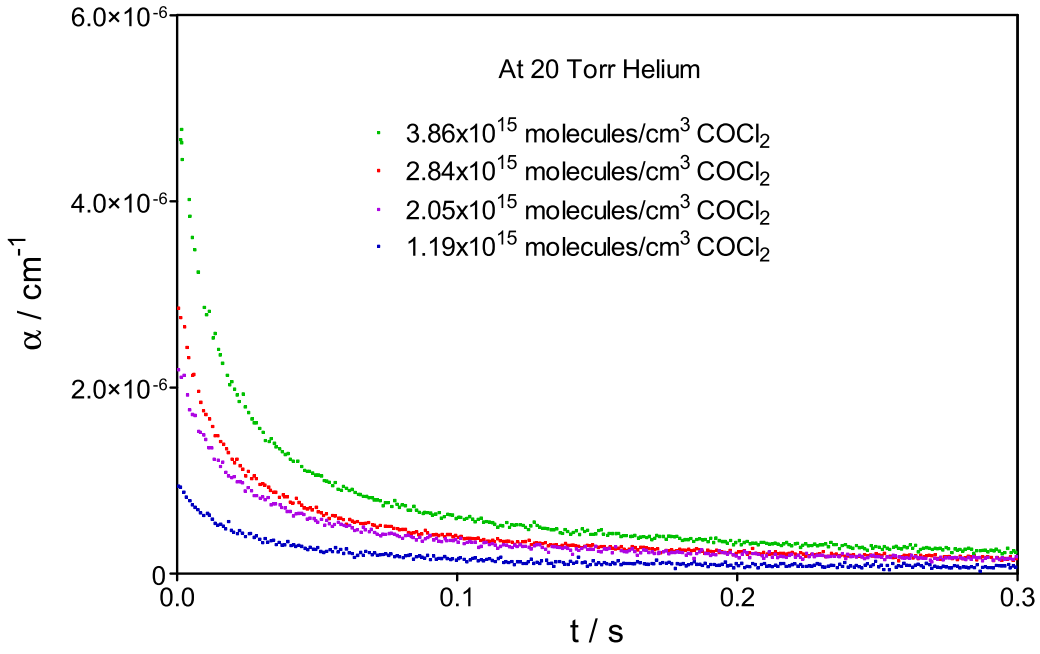

Figure 83: Plot of absorption coefficient of DO_2 at 7022.98 cm^{-1} against time obtained from the time resolved kinetic measurements.

Under the experimental conditions the decay of the DO_2 radical concentration in the reactor was mainly due to the self reaction of DO_2 as shown below.

$$DO_2 + DO_2 \longrightarrow D_2O_2 + O_2 \qquad \text{R-49}$$

In addition to the above reaction losses due to the diffusion out of photolysis volume have to be taken into account as well:

$$DO_2 \longrightarrow \text{Diffusion} \qquad \text{R-50}$$

Approximating the diffusion process to an exponential loss, the HO_2 concentration time profile is governed by the constant of reaction (R-49) and the diffusion as given below:

$$\frac{d[DO_2]}{dt} = -2k_{49}[DO_2]^2 - k_{diff}[DO_2] \qquad \text{E-24}$$

At higher concentrations of the reagents, the decay was faster and the major loss was due to the reaction (R-49). The decay of DO_2 can be approximated to a linear equation as below:

$$\frac{1}{[DO_2]_t} = \frac{1}{[DO_2]_0} + \left(\frac{kdiff}{[DO_2]_0} + 2k_{49}\right)t \qquad \text{E- 25}$$

where $[DO_2]_0$ is the DO_2 concentration at time zero and $[DO_2]_t$ at time t. Now a plot of $1/[DO_2]_0 = f(t)$ results in a straight line with a slope of $k_{diff}/[DO_2]_0+2k_{49}$ and intercept of $1/[DO_2]_0$. Therefore, different kinetic experiments at different DO_2 concentrations allow the distinction between the diffusion and the self reaction.

Now, a plot of $1/\alpha$ as function of time follows the equation

$$\frac{1}{\alpha} = \frac{1}{[DO_2]_t \sigma_\lambda} = f(t) \qquad \text{E-26}$$

and should give a straight line with a slope,

$$m = k_{diff}/[DO_2]_0\sigma_\lambda + 2k_{49}/\sigma_\lambda$$

and an intercept,

$$I = 1/[DO_2]_0\sigma_\lambda.$$

Figure 84 shows the plot of $1/\alpha$ as a function of time for the signals from Figure 83 .

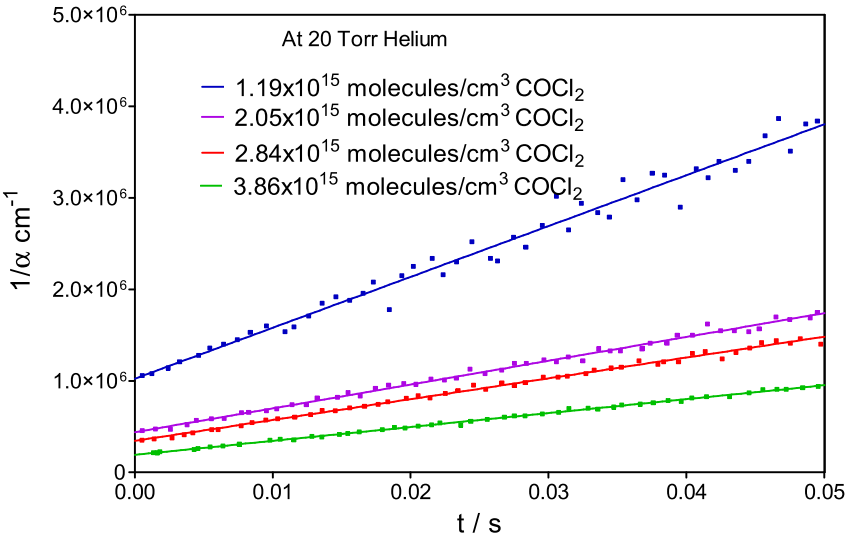

Figure 84: Plot of 1/ α as a function of time for the signals of Figure 83. Full lines represent the linear regression fit through the points.

The linearity in the above fits was in good agreement at shorter time scales. However on a longer time scale and lower concentrations there was a deviation from the linearity. This indicates that at these conditions diffusion was not negligible and the approximation of the reaction (R-49) was not valid any more. The increase in the slope of the plot with the decrease in the concentration of DO_2 was due to the increase of radical loss due to the diffusion process relative to the loss due to reaction with decreasing concentration [66]. The absorption cross section for each pressure was then deduced by plotting the intercept against the slope of Figure 84 type plots. One such plot for 20 Torr is shown in Figure 85.

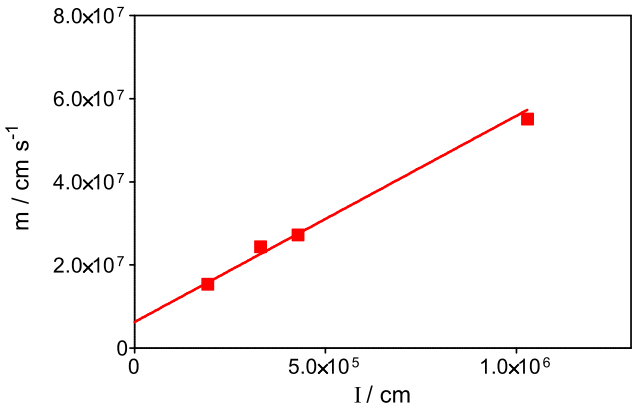

Figure 85: Plot of slope m as a function of intercept I from the Figure 84 obtained for four different initial concentrations of DO_2 at 7022.98 cm^{-1}.

Similar measurements were carried at four different (20, 38, 56 and 78 Torr) pressures and concentrations of DO_2. Figure 85 type data were fitted to a linear regression giving weight to the higher concentration data, as the effect of the diffusion process is minimized at higher concentrations. The intercept of this straight line is equal to an extrapolation to infinity of the initial DO_2 concentration and hence negligible diffusion condition. Therefore, the intercept from the plot shown in Figure 85 is equal to $2k_{49}/\sigma_\lambda$ with k_{49} being the rate constant of self reaction between DO_2. The rate constant of the DO_2 self reaction has been reported [161] and the enhancement due to the presence of other molecules like CD_3OD could be neglected under our conditions [66]. Therefore the reported rate constant of $k_{49} = 4.3x10^{-13}$ cm^3 $molecules^{-1}$ s^{-1} [161] has been used to calculate the absorption cross sections. Table 14 lists the obtained absorption cross sections for all four different pressures, the error limits indicate the 95% confidence levels for the intercept from the Figure 85 type plots. The decrease in the absorption cross-section with increase in the pressure due to the pressure broadening of the absorption is clearly visible.

Pressure / Torr He	**σ / 10^{-19} cm^2**
20	1.37±0.15
38	1.27±0.2
56	1.23±0.12
78	1.04 ±0.1

Table 14: Absorption cross-sections of DO_2 at 7022.98 cm^{-1} measured at four different pressures.

Using the absorption cross-sections obtained for the different pressures and by supposing a Voigt profile of the absorption lines, the line strength and the pressure broadening coefficient for the DO_2 absorption line at 7022.98 cm^{-1} can be calculated to 2.43 x 10^{-21} cm and 0.04 cm^{-1} atm^{-1}, respectively. This experiment has calibrated one of the lines for the DO_2 absorption in the 7013 cm^{-1} range and can be used for the future applications.

5.4 Conclusions

Spectroscopic applications of the cw-CRDS technique are used to measure different chemical species of atmospheric interest. The results of these measurements are then used for the kinetic as well as absorption spectroscopic measurements of the respective species.

The near IR spectrum of a portion of the $2\nu_1$ absorption band of the *cis*-isomer of HONO has been measured at a total pressure of 40 Torr Helium in the range 6623.6 - 6645.6 cm^{-1}, using two different methods for generating HONO. Absolute absorption cross sections for selected nitrous acid lines have been determined through calibration of the generated HONO concentration against the well-known HO_2 absorption cross section. The strongest line in this wavelength range has been found at 6642.50 cm^{-1} with $\sigma = (5.8 \pm 2.2) \times 10^{-21}$ cm^2. Using current cw-CRDS set-ups, HONO concentrations of as low as 1×10^{12} cm^{-3} (corresponding to $\alpha = 5 \times 10^{-9}$ cm^{-1}) can easily be quantified at 40 Torr He. Pressure broadening up to 74 Torr has been measured of the most intense line for He and N_2 as bath gas. The results show, that absorption spectroscopy in the near IR-range is not suitable for atmospheric measurements due to too small absorption cross section combined with strong pressure broadening. However, it can provide an interesting tool for laboratory studies.

Three selected lines for the HO_2 radical have been calibrated to get the absolute absorption cross sections in the 7013 cm^{-1} range. The absorption cross sections of HO_2 lines can be used for the absorption and kinetic measurements using cw-CRDS technique in the future.

One of the DO_2 absorption lines at 7022.98 cm^{-1} has been calibrated for pressure broadening. This would allow the detection and kinetic measurements of the DO_2 radical which would be quite handy considering the fact that there are also calibrated HO_2 absorption lines in the same range. Both DO_2 and HO_2 can be measured by the cw-CRDS technique using the same laser diode.

Conclusions and Future work

This section combines the conclusions of the work described in the preceding chapters and makes suggestions for potentially "fruitful" areas of future research. Several studies have been described within this thesis. Whilst specific conclusions on the work undertaken may be found within the relevant chapter, here it may be useful to address some more general conclusions.

The experimental technique

The work described in chapter 3 is on the validation and demonstration of the newly developed experimental technique for the time resolved, simultaneous kinetic measurements of OH and HO_2 radicals. The reliability of the technique has been tested by measuring well known rate constants. The utility demonstration has been shown by measuring time resolved, simultaneous OH and HO_2 kinetics from H_2O_2 photolysis as well as the HO_2 yield in the OH-initiated SO_2 oxidation study. Apart from the kinetic applications, the experimental technique can also be used for spectroscopic applications to measure the absorption spectra of species with constant or transient concentration through continuous or pulsed photolysis methods. The measured H_2O_2 absorption cross-sections as a part of validation of the spectroscopic application can be used to calculate the absolute concentration of H_2O_2 in future experiments.

There is lot of scope for future work using this experimental technique. Different reaction systems involving the OH and HO_2 radical intermediates can be studied for their reaction dynamics and role in atmospheric chemistry. Adding more to the utility of this technique, the cw-CRDS set-up can be used as the detection technique for OH radicals instead of LIF. The O-H stretch overtone of OH radicals can be detected by absorption measurement in the NIR region [159]. The sensitivity of CRDS may not reach that of LIF, but the radical concentration can be increased according to the need in the laboratory studies to have a detectable concentration. There are two distinct advantages to this approach. First the OH concentration measurement will be absolute eliminating the calibration used in LIF technique. Second, both OH and HO_2 radical kinetics can be monitored using the cw-CRDS technique alone. Such an attempt has already been made during this thesis, but has not been continued due to a lack of selective CRDS mirrors in the

7013 cm^{-1} range giving better τ_0 and hence better sensitivity. Figure 86 shows the absorption line of OH radicals at 7028.83 cm^{-1} as well a kinetic decay measured using the cw-CRDS technique.

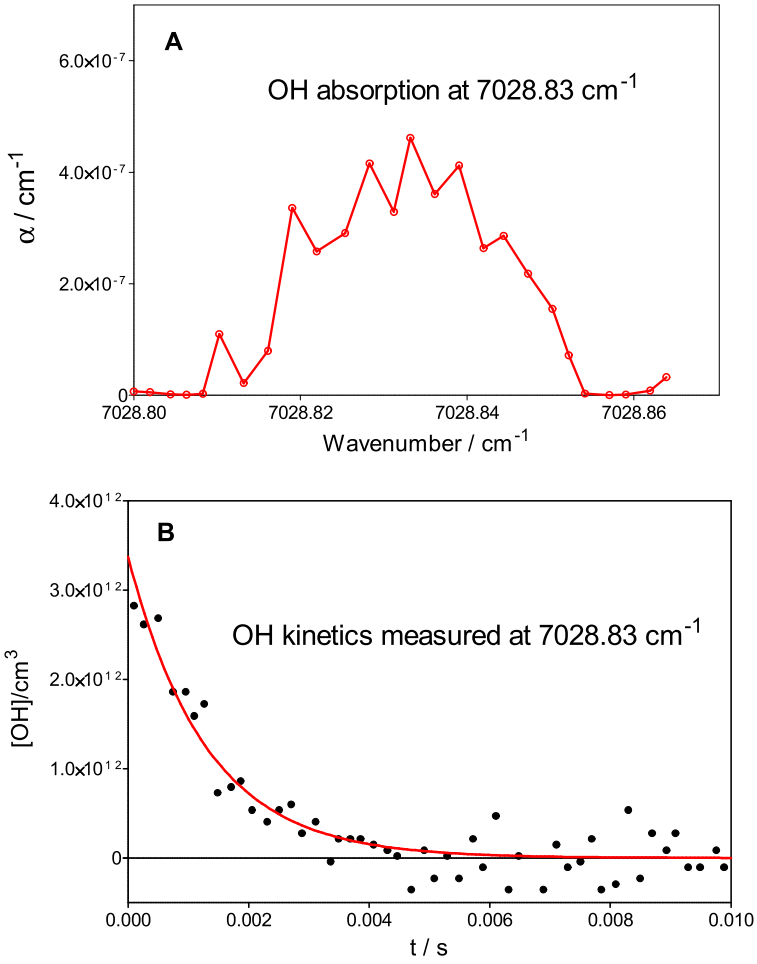

Figure 86: OH absorption (A) and kinetics (B) at 7028.83 cm^{-1} from the photolysis of H_2O_2 at 45 Torr measured by the cw-CRDS.

It can be noted that the signal to noise ratio in Figure 86 is very poor due to the low ring-down time obtained from the mirrors (Los Gatos 99.9968% reflectivity at 7246.3 cm^{-1}), yielding a maximum ring-down time of 10 µs for τ_0. The signals in Figure 86 were obtained from a difference in ring-down time of $\Delta\tau$ = 0.6 µs (with absorption cross section for OH at 7028.83 cm^{-1} σ_{OH}=1.5x10^{-19} cm^2 at 45 Torr [159]) which is very close to the signal to noise ratio of the technique. Therefore with a pair of selective mirrors that can give better τ_0, this problem can be solved to get better sensitivity for OH radicals. This would also be helpful for the HO_2 and

DO_2 radical kinetic studies as they are also calibrated in the same wavelength range, making the way forward for the other additional utilities of this experimental technique.

Study on aromatic compounds

The work discussed in chapter 4 is the core work of this thesis describing the direct HO_2 formation from the photo-excitation of a mixture of an aromatic compound and oxygen at 248 nm. Different studies on different aromatic compounds showed that the HO_2 radical formation originates from a two-photon excitation process. This study has its importance in the laboratory studies on OH-initiated oxidation of aromatic compounds. The H_2O_2 photolysis at 248 nm is generally used as the source of OH radicals when studying the oxidation of aromatic compounds. HO_2 yield from these studies can be used [107] to predict the branching ratios of different oxidation channels. If there is direct formation of HO_2 without the addition of initial OH radicals then this prediction will be erroneous. In such cases the direct HO_2 yield has to be taken into account while proposing the branching ratios in an aromatic oxidation mechanism.

This study opens up new perspectives for the study of the oxidation of aromatic compounds. First of all deuterated isotopologues like C_6D_6 can be studied with the availability of a calibrated DO_2 absorption line in the 7013 cm^{-1} range, the DO_2 formation kinetics and yield can be studied and compared with HO_2 formation. Furthermore using substituted aromatic compounds such as toluene with deuterated side chain, the HO_2 and DO_2 formation studies can be performed. The influence of the side chain can be studied by comparing with HO_2 formation from non-deuterated toluene.

Another area for future work on aromatic compounds is the study of their OH-initiated degradation using the 351nm photolysis of HONO as the precursor for OH radicals. This will eliminate the direct HO_2 formation following the 248 nm irradiation of aromatic compound and oxygen mixture. The absorption cross-sections measured for HONO in the near IR region will be used to calculate the absolute concentration of HONO which in turn will be used to calculate the OH radical concentration.

More work can be carried out on the unknown reactive intermediate absorption after the photolysis to identify the absorbing species which might help to understand the HO_2 formation mechanism in a better way.

In addition the influence of aromatic compound on the OH radicals from H_2O_2 photolysis at 248 nm can be studied to confirm the observation reported by Bohn *et al.* [21]. In their study they have reported that the benzene concentration has an unexpected influence on the initial OH radical concentration. The concentration of OH radicals, generated from the 248 nm photolysis of H_2O_2, was found to increase significantly after addition of benzene to the reaction mixture. The increase is linear up to a factor of 6 at about $3x10^{15}$ molecules cm^{-3} benzene for $2x10^{14}$ molecules cm^{-3} H_2O_2 and then levels off at higher concentrations. The reason for this has been predicted as absorption of 248 nm light by benzene leading to an electronically and vibrationally excited singlet state $S_1(^1B_{2u})$, followed by effective intersystem crossing into lowest lying triplet state $T_1(^3B_{1u})$. The increase in the OH concentration is tentatively attributed to a benzene sensitized decomposition of H_2O_2. They also mentioned that addition of lowest concentrations of oxygen ($7.5x10^{16}$ molecule cm^{-3}) has suppressed this effect and the reason quoted was the possible quenching of the singlet state benzene by oxygen. This observation can be studied directly using LIF and also can be extended to study its influence on HO_2 profiles using the cw-CRDS technique.

Spectroscopic applications

Spectroscopic applications of the cw-CRDS have been explained in chapter 5 through the measurement of HONO and the calibration of HO_2 and DO_2 lines in the 7013 cm^{-1} range. The HONO spectrum measurement has given a handy tool for the measurement of absolute concentration of HONO. This will help in calculating the OH radical concentration if HONO is used as the precursor molecule for generating OH by photolysing at 351 nm. The calibrated HO_2 and DO_2 lines in 7013 cm^{-1} range will help in future HO_2 and DO_2 kinetic studies using the same laser diode for both isotopologues, which in turn avoids the need for a diode change ensuring the same conditions for two different kinetic measurements.

The cw-CRDS is becoming more and more popular for its spectroscopic applications. Future work can be done on spectral measurements of different species with atmospheric interest.

To end, this thesis has added to the importance of OH and HO_2 radicals in the atmosphere through the investigation of different systems. Whilst there is much we do know, much more that needs to be to understood, which brings a lot of scope for the future work in the atmospheric science.

---* * *---

Bibliography

1. Atmospheric Chemistry Books: For example, Wayne, Richard P. (Oxford University Press 2000); Seinfeld, John H. (John Wiley & Sons 2006); Finlayson-Pitts, B.J. (Academic Press, San Diego 2000).
2. Heard, D.E., Pilling, M.J.: Measurement of OH and HO_2 in the Troposphere. Chemical Reviews. 103, 5163-5198 (2003).
3. Emmerson, K.M., Carslaw, N.: Night-time radical chemistry during the TORCH campaign. Atmospheric Environment. 43, 3220-3226 (2009).
4. Sadanaga, Y., Matsumoto, J., Kajii, Y.: Photochemical reactions in the urban air: Recent understandings of radical chemistry. Journal of Photochemistry and Photobiology C: Photochemistry Reviews. 4, 85-104 (2003).
5. Bedjanian, Y., Riffault, V., Poulet, G.: Kinetic Study of the Reactions of BrO Radicals with HO_2 and DO_2. The Journal of Physical Chemistry A. 105, 3167-3175 (2001).
6. Abbatt, J.P.D., Fenter, F.F., Anderson, J.G.: High-pressure discharge flow kinetics study of OH+CH_3SCH_3, CH_3SSCH_3 $\longrightarrow$ products from 297 to 368 K. The Journal of Physical Chemistry. 96, 1780-1785 (1992).
7. Norrish, R.G.W., Porter, G.: Chemical Reactions Produced by Very High Light Intensities. Nature (London, United Kingdom). 164, 658 (1949).
8. Parker, A.E., Jain, C., Schoemaecker, C., Szriftgiser, P., Votava, O., Fittschen, C.: Simultaneous, time-resolved measurements of OH and HO_2 radicals by coupling of high repetition rate LIF and cw-CRDS techniques to a laser photolysis reactor and its application to the photolysis of H_2O_2. Applied Physics B. 103, 725-733 (2010).
9. Thiébaud, J., Fittschen, C.: Near infrared cw-CRDS coupled to laser photolysis: Spectroscopy and kinetics of the HO_2 radical. Applied Physics B: Lasers and Optics. 85, 383-389 (2006).
10. Parker, A., Jain, C., Schoemaecker, C., Fittschen, C.: Kinetics of the reaction of OH radicals with CH_3OH and CD_3OD studied by laser photolysis coupled to high repetition rate laser induced fluorescence. Reaction Kinetics and Catalysis Letters. 96, 291-297 (2009).
11. Ren, X., Gao, H., Zhou, X., Crounse, J.D., Wennberg, P.O., Browne, E.C., LaFranchi, B.W., Cohen, R.C., McKay, M., Goldstein, A.H., Mao, J.: Measurement

of atmospheric nitrous acid at Bodgett Forest during BEARPEX2007. Atmos. Chem. Phys. 10, 6283-6294 (2010).

12. Cox, R.A., Burrows, J.P.: Kinetics and mechanism of the disproportionation of hydroperoxyl radical in the gas phase. The Journal of Physical Chemistry. 83, 2560-2568 (1979).
13. Tuazon, E.C., Carter, W.P.L., Atkinson, R., Pitts Jr., J.N.: The gas□phase reaction of hydrazine and ozone: A nonphotolytic source of OH radicals for measurement of relative OH radical rate constants. International Journal of Chemical Kinetics. 15, 619-629 (1983).
14. Vera, T., Muñoz, A., Ródenas, M., Vázquez, M., Borrás, E., Marqués, M., Mellouki, A., Treacy, J., Sidebottom, H.: Atmospheric fate of hymexazol (5-methylisoxazol-3-ol): Simulation chamber studies. Atmospheric Environment. 45, 3704-3710 (2011).
15. Muñoz, A., Vera, T., Sidebottom, H., Mellouki, A., Borrás, E., Ródenas, M., Clemente, E., Vázquez, M.: Studies on the Atmospheric Degradation of Chlorpyrifos-Methyl. Environmental Science & Technology. 45, 1880-1886 (2011).
16. Hibert, C., Gaurand, I., Motret, O., Pouvesle, J.M.: [OH(X)] measurements by resonant absorption spectroscopy in a pulsed dielectric barrier discharge. Journal of Applied Physics. 85, 7070 (1999).
17. Brune, W.H., Schwab, J.J., Anderson, J.G.: Laser magnetic resonance, resonance fluorescence, resonance absorption studies of the reaction kinetics of $O+OH \longrightarrow H+O_2$, $O+HO_2 \longrightarrow OH+O_2$, $N+OH \longrightarrow H+NO$, $N+HO_2 \longrightarrow$ at 300 K between 1 and 5 torr. The Journal of Physical Chemistry. 87, 4503-4514 (1983).
18. Anderson, J.G., Kaufman, F.: Kinetics of the reaction OH + NO_2 + M --> HNO_3 + M. Chemical Physics Letters. 16, 375-379 (1972).
19. Wallington, T.J., Kurylo, M.J.: Flash photolysis resonance fluorescence investigation of the gas-phase reactions of hydroxyl radicals with a series of aliphatic ketones over the temperature range 240-440 K. The Journal of Physical Chemistry. 91, 5050-5054 (1987).
20. Wallington, T.J., Dagaut, P., Kurylo, M.J.: UV absorption cross sections and reaction kinetics and mechanisms for peroxy radicals in the gas phase. Chemical Reviews. 92, 667-710 (1992).

21. Bohn, B., Zetzsch, C.: Gas-phase reaction of the OH-benzene adduct with O_2: reversibility and secondary formation of HO_2. Phys. Chem. Chem. Phys. 1, 5097-5107 (1999).
22. James, J.F.: A Student's Guide to Fourier Transforms. Cambridge University Press, U.K. (2002).
23. Pesce, G., Rusciano, G., Sasso, A.: Detection and spectroscopy of OH fundamental vibrational band based on a difference frequency generator at 3 [mu]m. Chemical Physics Letters. 374, 425-431 (2003).
24. Bahng, M.-K., Macdonald, R.G.: Determination of the Rate Constant for the $OH(X^2\Pi)$ + $OH(X^2\Pi)$ → $O(^3P)$ + H_2O Reaction over the Temperature Range 293−373 K. The Journal of Physical Chemistry A. 111, 3850-3861 (2007).
25. Nizkorodov, S.A., Harper, W.W., Nesbitt, D.J.: Fast vibrational relaxation of OH(v=9) by ammonia and ozone. Chemical Physics Letters. 341, 107-114 (2001).
26. Tang, Y., Tyndall, G.S., Orlando, J.J.: Spectroscopic and Kinetic Properties of HO_2 Radicals and the Enhancement of the HO_2 Self Reaction by CH_3OH and H_2O. The Journal of Physical Chemistry A. 114, 369-378 (2010).
27. Miyano, S., Tonokura, K.: Measurements of nitrogen-broadening coefficients in the [nu]3 band of the hydroperoxyl radical using a continuous wave quantum cascade laser. Journal of Molecular Spectroscopy. 265, 47-51 (2011).
28. Christensen, L.E., Okumura, M., Hansen, J.C., Sander, S.P., Francisco, J.S.: Experimental and ab Initio Study of the $HO_2{\cdot}CH_3OH$ Complex: Thermodynamics and Kinetics of Formation†. The Journal of Physical Chemistry A. 110, 6948-6959 (2006).
29. Christensen, L.E.: Kinetics of $HO_2+HO_2 \rightarrow H_2O_2+O_2$: Implications for Stratospheric H_2O_2. Geophysical Research Letters. 29, (2002).
30. Watson, J.T., Sparkman, O.D.: Introduction to Mass Spectrometry: Instrumentation, Applications, and Strategies for Data Interpretation. Willey Interscience Publication, USA (2007).
31. Morris, E.D., Stedman, D.H., Niki, H.: Mass-spectrometric study of the reactions of the hydroxyl radical with ethylene, propylene, and acetaldehyde in a discharge-flow system. Journal of the American Chemical Society. 93, 3570-3572 (1971).

32. Eisele, F.L., Tanner, D.J.: ION-ASSISTED TROPOSPHERIC OH MEASUREMENTS. J. Geophys. Res. 96, 9295-9308 (1991).
33. Belay, A.: Fluorescence and Electron Paramagnetic Resonance (EPR)Spectroscopy:Basic Principles, the Different Techniques and Applications. LAP LAMBERT Academic Publishing (2011).
34. Pauwels, J.F., Carlier, M., Sochet, L.R.: Experimental study of the structure of a methanol-air flame. Colloq. Int. Berthelot-Vieille-Mallard-Le Chatelier, [Actes], 1st. 1, 162-65 (1981).
35. Westenberg, A.A.: Intensity Relations for Determining Gas-Phase OH, Cl, Br, I, and Free-Electron Concentrations by Quantitative ESR. The Journal of Chemical Physics. 43, 1544 (1965).
36. Westenberg, A.A., De Haas, N.: Quantitative ESR Measurements of Gas-Phase H and OH Concentrations in the H-NO_2 Reaction. The Journal of Chemical Physics. 43, 1550 (1965).
37. Carlier, M., Pauwels, J.F., Sochet, L.R.: Application of ESR techniques to the study of gas-phase oxidation and combustion phenomena. Oxidation Communications. 6, 141-56 (1984).
38. Rozenshtein, V.B., Gershenzon, Y.M., Il'in, S.D., Kishkovitch, O.P.: Reactions of HO_2 with NO, OH and HO_2 studied by EPR/LMR spectroscopy. Chemical Physics Letters. 112, 473-478 (1984).
39. Howard, C.J.: Laser magnetic resonance study of the gas phase reactions of OH with CO, NO, and NO_2. The Journal of Chemical Physics. 61, 1943 (1974).
40. Howard, C.J.: Rate constants for the gas–phase reactions of OH radicals with ethylene and halogenated ethylene compounds. The Journal of Chemical Physics. 65, 4771 (1976).
41. Hougen, J.T., Radford, H.E., Evenson, K.M., Howard, C.J.: Analysis of the laser magnetic resonance spectrum of HO_2. Journal of Molecular Spectroscopy. 56, 210-228 (1975).
42. Wang, J.J., Keyser, L.F.: HCl Yield from the OH + ClO Reaction at Temperatures between 218 and 298 K. J. Phys. Chem. A. 105, 6479-6489 (2001).
43. Masten, D.A., Hanson, R.K., Bowman, C.T.: Shock tube study of the reaction $H+O_2 \longrightarrow OH+O$ using hydroxyl laser absorption. J. Phys. Chem. 94, 7119-7128 (1990).

44. Crawford, M.A., Wallington, T.J., Szente, J.J., Maricq, M.M., Francisco, J.S.: Kinetics and Mechanism of the Acetylperoxy + HO_2 Reaction. J. Phys. Chem. A. 103, 365-378 (1999).

45. Siese, M., Becker, K.H., Brockmann, K.J., Geiger, H., Hofzumahaus, A., Holland, F., Mihelcic, D., Wirtz, K.: Direct Measurement of OH Radicals from Ozonolysis of Selected Alkenes: A EUPHORE Simulation Chamber Study. Environ. Sci. Technol. 35, 4660-4667 (2001).

46. Noell, A.C., Alconcel, L.S., Robichaud, D.J., Okumura, M., Sander, S.P.: Near-Infrared Kinetic Spectroscopy of the HO_2 and $C_2H_5O_2$ Self-Reactions and Cross Reactions. J. Phys. Chem. A. 114, 6983-6995 (2010).

47. Guoli, Z., Aimin, Z., Jiating, W., Zhongwei, L., Yong, X.: Measurement of OH Radicals in Dielectric Barrier Discharge Plasmas by Cavity Ring-Down Spectroscopy. Plasma Science and Technology. 12, 166-171 (2010).

48. Thiébaud, J., Parker, A., Fittschen, C., Vincent, G., Zahraa, O., Marquaire, P.-M.: Detection of HO_2 Radicals in the Photocatalytic Oxidation of Methyl Ethyl Ketone. The Journal of Physical Chemistry C. 112, 2239-2243 (2008).

49. Hills, A.J., Howard, C.J.: Rate coefficient temperature dependence and branching ratio for the OH+ClO reaction. The Journal of Chemical Physics. 81, 4458 (1984).

50. O'Keefe, A., Deacon, D.A.G.: Cavity ring-down optical spectrometer for absorption measurements using pulsed laser sources. Review of Scientific Instruments. 59, 2544 (1988).

51. Paschotta, R.: Encyclopedia of Laser Physics and Technology, http://www.rp-photonics.com/encyclopedia.html.

52. Berden, G., Engeln, R. eds: Cavity Ring-Down Spectroscopy: Techniques and Applications. John Wiley & Sons, Inc, UK (2009).

53. Romanini, D., Kachanov, A.A., Sadeghi, N., Stoeckel, F.: CW cavity ring down spectroscopy. Chemical Physics Letters. 264, 316-322 (1997).

54. Romanini, D., Kachanov, A.A., Stoeckel, F.: Diode laser cavity ring down spectroscopy. Chemical Physics Letters. 270, 538-545 (1997).

55. Thiébaud, J.: Développment d'un spectromètre à cavité optique de haute finesse couplé à la photolyse laser-Mesures spectrscopiques et cinétiques du

radical HO_2, Thesis submitted to Université Lille 1 - Sciences et Technologies, France, (2007).

56. Lambda Physik Lasertechnik: USER MANUAL LPX 100i / 200i Series, (1998).
57. Taylor, N.: LASER: The inventor, the Nobel laureate, and the thirty-year patent war. Simon & Schuster (2000).
58. Sirah Dye Laser: Service Manual: Pulsed Dye Laser, (2009).
59. Shoji, I., Kondo, T., Kitamoto, A., Shirane, M., Ito, R.: Absolute scale of second-order nonlinear-optical coefficients. Journal of the Optical Society of America B. 14, 2268-2294 (1997).
60. Bierlein, J.D., Vanherzeele, H.: Potassium titanyl phosphate: properties and new applications. Journal of the Optical Society of America B. 6, 622-633 (1989).
61. Chen, C., Wu, Y., Jiang, A., Wu, B., You, G., Li, R., Lin, S.: New nonlinear-optical crystal: LiB_3O_5. Journal of the Optical Society of America B. 6, 616-621 (1989).
62. Franken, P.A., Hill, A.E., Peters, C.W., Weinreich, G.: Generation of Optical Harmonics. Physical Review Letters. 7, 118 (1961).
63. Chow, W.W., Koch, S.W.: Semiconductor-Laser Fundamentals. Springer, Berlin (1999).
64. Halmer, D., von Basum, G., Hering, P., Mürtz, M.: Fast exponential fitting algorithm for real-time instrumental use. Review of Scientific Instruments. 75, 2187 (2004).
65. Ibrahim, N., Thiebaud, J., Orphal, J., Fittschen, C.: Air-broadening coefficients of the HO_2 radical in the $2\nu_1$ band measured using cw-CRDS. Journal of Molecular Spectroscopy. 242, 64-69 (2007).
66. Thiebaud, J., Crunaire, S., Fittschen, C.: Measurements of Line Strengths in the $2\nu_1$ Band of the HO_2 Radical Using Laser Photolysis/Continuous Wave Cavity Ring-Down Spectroscopy (cw-CRDS). The Journal of Physical Chemistry A. 111, 6959-6966 (2007).
67. Taatjes, C.A.: Uncovering the Fundamental Chemistry of Alkyl + O_2 Reactions via Measurements of Product Formation. The Journal of Physical Chemistry A. 110, 4299-4312 (2006).

68. DeSain, J.D., Klippenstein, S.J., Taatjes, C.A., Hurley, M.D., Wallington, T.J.: Product Formation in the Cl-Initiated Oxidation of Cyclopropane. The Journal of Physical Chemistry A. 107, 1992-2002 (2003).

69. DeSain, J.D., Klippenstein, S.J., Miller, J.A., Taatjes, C.A.: Measurements, Theory, and Modeling of OH Formation in Ethyl + O_2 and Propyl + O_2 Reactions. The Journal of Physical Chemistry A. 108, 7127-7128 (2004).

70. Aluculesei, A., Tomas, A., Schoemaecker, C., Fittschen, C.: On the direct formation of HO_2 radicals after 248 nm irradiation of benzene C_6H_6 in the presence of O_2. Applied Physics B: Lasers and Optics. 92, 379-385 (2008).

71. Huie, R.E., Sander, S.P., Ravishankara, A.R., Golden, D.M., Kolb, C.E., Kurylo, M.J., Molina, M.J., Moortgat, G.K., Finlayson-Pitts, B.J., Wine, P.H.: Chemical Kinetics and Photochemical Data for Use in Atmospheric Studies Evaluation Number 15, (2006).

72. Szabó, E., Tarmoul, J., Tomas, A., Fittschen, C., Dóbé, S., Coddeville, P.: Kinetics of the •OH-radical initiated reactions of acetic acid and its deuterated isomers. Reaction Kinetics and Catalysis Letters. 96, 299-309 (2009).

73. McCaulley, J.A., Kelly, N., Golde, M.F., Kaufman, F.: Kinetic studies of the reactions of atomic fluorine and hydroxyl radical with methanol. The Journal of Physical Chemistry. 93, 1014-1018 (1989).

74. Atkinson, R., Baulch, D.L., Cox, R.A., Crowley, J.N., Hampson, R.F., Hynes, R.G., Jenkin, M.E., Rossi, M.J., Troe, J.: Evaluated kinetic and photochemical data for atmospheric chemistry: Volume II – gas phase reactions of organic species. Atmospheric Chemistry and Physics. 6, 3625-4055 (2006).

75. Atkinson, R., Baulch, D.L., Cox, R.A., Crowley, J.N., Hampson Jr, R.F., Kerr, J.A., Rossi, M.J., Troe, J.: Summary of Evaluated Kinetic and Photochemical Data for Atmospheric Chemistry. IUPAC Subcommittee on Gas Kinetic Data Evaluation for Atmospheric ChemistryWeb Version December 2001. 1-56 (2001).

76. Thiebaud, J., Aluculesei, A., Fittschen, C.: Formation of HO_2 radicals from the photodissociation of H_2O_2 at 248 nm. The Journal of Chemical Physics. 126, 186101 (2007).

77. Vaghjiani, G.L., Ravishankara, A.R.: Photodissociation of H_2O_2 and CH3OOH at 248 nm and 298 K: Quantum yields for OH, O(^{3}P) and H(^{2}S). The Journal of Chemical Physics. 92, 996 (1990).

78. Schiffman, A., Nelson, D.D., Nesbitt, D.J.: Quantum yields for OH production from 193 and 248 nm photolysis of HNO_3 and H_2O_2. The Journal of Chemical Physics. 98, 6935 (1993).

79. Sander, S.P., Abbatt, J.P.D., Barker, J.R.: Chemical Kinetics and Photochemical Data for Use in Atmospheric Studies. JPL publications. 10-6, (2011).

80. Johansson, O., Bood, J., Aldén, M., Lindblad, U.: Hydroxyl radical consumption following photolysis of vapor-phase hydrogen peroxide at 266 nm: Implications for photofragmentation laser-induced fluorescence measurements of hydrogen peroxide. Applied Physics B. 97, 515-522 (2009).

81. Kulmala, M., Pirjola, L., Makela, J.M.: Stable sulphate clusters as a source of new atmospheric particles. Nature. 404, 66-69 (2000).

82. Weber, R.J., McMurry, P.H., Mauldin, R.L., Tanner, D.J., Eisele, F.L., Clarke, A.D., Kapustin, V.N.: New Particle Formation in the Remote Troposphere: A Comparison of Observations at Various Sites. Geophys. Res. Lett. 26, 307-310 (1999).

83. Berndt, T., Böge, O., Stratmann, F., Heintzenberg, J., Kulmala, M.: Rapid Formation of Sulfuric Acid Particles at Near-Atmospheric Conditions. Science. 307, 698 -700 (2005).

84. Berndt, T., Stratmann, F., Bräsel, S., Heintzenberg, J., Laaksonen, A., Kulmala, M.: SO_2 oxidation products other than H_2SO_4 as a trigger of new particle formation. Part 1: Laboratory investigations. Atmos. Chem. Phys. 8, 6365-6374 (2008).

85. Laaksonen, A., Kulmala, M., Berndt, T., Stratmann, F., Mikkonen, S., Ruuskanen, A., Lehtinen, K.E.J., Dal Maso, M., Aalto, P., Petäjä, T., Riipinen, I., Sihto, S.-L., Janson, R., Arnold, F., Hanke, M., Ücker, J., Umann, B., Sellegri, K., O'Dowd, C.D., Viisanen, Y.: SO_2 oxidation products other than H_2SO_4 as a trigger of new particle formation. Part 2: Comparison of ambient and laboratory measurements, and atmospheric implications. Atmos. Chem. Phys. 8, 7255-7264 (2008).

86. González-García, N., Olzmann, M.: Kinetics of the chemically activated HSO_5 radical under atmospheric conditions – a master-equation study. Physical Chemistry Chemical Physics. 12, 12290 (2010).

87. Kurtén, T., Berndt, T., Stratmann, F.: Hydration increases the lifetime of HSO_5 and enhances its ability to act as a nucleation precursor – a computational study. Atmos. Chem. Phys. 9, 3357-3369 (2009).

88. González-García, N., Klopper, W., Olzmann, M.: Thermochemistry of the $HOSO_2$+O_2 association reaction and enthalpy of formation of $HOSO_4$: A quantum chemical study. Chemical Physics Letters. 470, 59-62 (2009).

89. Klopper, W., Tew, D.P., González-García, N., Olzmann, M.: Heat of formation of the $HOSO_2$ radical from accurate quantum chemical calculations. The Journal of Chemical Physics. 129, 114308 (2008).

90. Fliegl, H., Glöß, A., Welz, O., Olzmann, M., Klopper, W.: Accurate computational determination of the binding energy of the $SO_3 \cdot H_2O$ complex. The Journal of Chemical Physics. 125, 054312 (2006).

91. Sipilä, M., Berndt, T., Petäjä, T., Brus, D., Vanhanen, J., Stratmann, F., Patokoski, J., Mauldin, R.L., Hyvärinen, A.-P., Lihavainen, H., Kulmala, M.: The Role of Sulfuric Acid in Atmospheric Nucleation. Science. 327, 1243 -1246 (2010).

92. Martin, D., Jourdain, J.L., Le Bras, G.: Discharge flow measurements of the rate constants for the reaction OH + SO_2 + He and $HOSO_2$ + O_2 in relation with the atmospheric oxidation of sulfur dioxide. The Journal of Physical Chemistry. 90, 4143-4147 (1986).

93. Fulle, D., Hamann, H.F., Hippler, H.: The pressure and temperature dependence of the recombination reaction HO+SO_2+M→$HOSO_2$+M. Physical Chemistry Chemical Physics. 1, 2695-2702 (1999).

94. Wine, P.H., Thompson, R.J., Ravishankara, A.R., Semmes, D.H., Gump, C.A., Torabi, A., Nicovich, J.M.: Kinetics of the reaction OH + SO_2 + M .fwdarw. $HOSO_2$ + M. Temperature and pressure dependence in the fall-off region. The Journal of Physical Chemistry. 88, 2095-2104 (1984).

95. Hippler, H., Nahr, D., Plach, H.J., Troe, J.: Excitation dependence of the ultraviolet absorption spectrum of sulfur dioxide. The Journal of Physical Chemistry. 92, 5503-5506 (1988).

96. Heymann, M., Hippler, H., Nahr, D., Plach, H.J., Troe, J.: UV absorption study of collisional energy transfer in vibrationally highly excited sulfur dioxide molecules. The Journal of Physical Chemistry. 92, 5507-5514 (1988).

97. Danielache, S.O., Eskebjerg, C., Johnson, M.S., Ueno, Y., Yoshida, N.: High-precision spectroscopy of ^{32}S, ^{33}S, and ^{34}S sulfur dioxide: Ultraviolet absorption cross sections and isotope effects. J. Geophys. Res. 113, D17314 (2008).

98. Wilson, M.W.: Multiphoton photofragmentation of SO_2 at 248 nm. The Journal of Chemical Physics. 77, 1837 (1982).

99. Okabe, H.: Fluorescence and predissociation of sulfur dioxide. Journal of the American Chemical Society. 93, 7095-7096 (1971).

100. Hebert, G.R., Hodder, R.V.: Intensity measurements in emission on 29 bands of the SO $B^3\Sigma^- - X^3\Sigma^-$ band system. Journal of Physics B: Atomic and Molecular Physics. 7, 2244-2255 (1974).

101. Cobos, C.J., Hippler, H., Troe, J.: Falloff curves of the recombination reaction O + SO + M .fwdarw. SO_2 + M in a variety of bath gases. The Journal of Physical Chemistry. 89, 1778-1783 (1985).

102. Atkinson, R., Baulch, D.L., Cox, R.A., Crowley, J.N., Hampson, R.F., Hynes, R.G., Jenkin, M.E., Rossi, M.J., Troe, J.: Evaluated kinetic and photochemical data for atmospheric chemistry: Volume I - gas phase reactions of O_x, HO_x, NO_x and SO_x species. Atmospheric Chemistry and Physics. 4, 1461-1738 (2004).

103. Calvert, J.G., Atkinson, R., Becker, K.H., Kamens, R.M., Seinfeld, J.H., Wallington, T.J., Yarwood, G.: The Mechanisms of Atmospheric Oxidation of the Aromatic Hydrocarbons. Oxford University Press, USA (2002).

104. Blake, D.R., Smith, T.W., Chen, T.-Y., Whipple, W.J., Rowland, F.S.: Effects of biomass burning on summertime nonmethane hydrocarbon concentrations in the Canadian wetlands. J. Geophys. Res. 99, 1699-1719 (1994).

105. Isidorov, V.A., Zenkevich, I.G., Ioffe, B.V.: Volatile organic compounds in solfataric gases. Journal of Atmospheric Chemistry. 10, 329-340 (1990).

106. Lonneman, W.A., Bellar, T.A., Altshuller, A.P.: Aromatic hydrocarbons in the atmosphere of the Los Angeles basin. Environmental Science & Technology. 2, 1017-1020 (1968).

107. Nehr, S., Bohn, B., Fuchs, H., Hofzumahaus, A., Wahner, A.: HO_2 formation from the OH + benzene reaction in the presence of O_2. Physical Chemistry Chemical Physics. 13, 10699 (2011).

108. Bloss, C., Wagner, V., Bonzanini, A., Jenkin, M.E., Wirtz, K., Martin-Reviejo, M., Pilling, M.J.: Evaluation of detailed aromatic mechanisms (MCMv3 and

MCMv3.1) against environmental chamber data. Atmos. Chem. Phys. 5, 623-639 (2005).

109. Jenkin, M.E., Saunders, S.M., Wagner, V., Pilling, M.J.: Protocol for the development of the Master Chemical Mechanism, MCM v3 (Part B): tropospheric degradation of aromatic volatile organic compounds. Atmos. Chem. Phys. 3, 181-193 (2003).
110. Atkinson, R., Aschmann, S.M., Arey, J., Carter, W.P.L.: Formation of ring□retaining products from the OH radical initiated reactions of benzene and toluene. International Journal of Chemical Kinetics. 21, 801-827 (1989).
111. Atkinson, R., Aschmann, S.M.: Products of the gas□phase reactions of aromatic hydrocarbons: Effect of NO_2 concentration. International Journal of Chemical Kinetics. 26, 929-944 (1994).
112. Volkamer, R., Klotz, B., Barnes, I., Imamura, T., Wirtz, K., Washida, N., Becker, K.H., Platt, U.: OH-initiated oxidation of benzene. Physical Chemistry Chemical Physics. 4, 1598-1610 (2002).
113. Noda, J., Volkamer, R., Molina, M.J.: Dealkylation of Alkylbenzenes: A Significant Pathway in the Toluene, o-, m-, p-Xylene + OH Reaction. The Journal of Physical Chemistry A. 113, 9658-9666 (2009).
114. Berndt, T., Böge, O.: Formation of phenol and carbonyls from the atmospheric reaction of OH radicals with benzene. Physical Chemistry Chemical Physics. 8, 1205 (2006).
115. Fernandes, R.X., Luther, K., Troe, J., Ushakov, V.G.: Experimental and modelling study of the recombination reaction H + O_2 (+M) → HO_2 (+M) between 300 and 900 K, 1.5 and 950 bar, and in the bath gases M = He, Ar, and N_2. Physical Chemistry Chemical Physics. 10, 4313 (2008).
116. Kovács, T., Blitz, M.A., Seakins, P.W., Pilling, M.J.: H atom formation from benzene and toluene photoexcitation at 248 nm. The Journal of Chemical Physics. 131, 204304 (2009).
117. Jain, C., Parker, A.E., Schoemaecker, C., Fittschen, C.: HO_2 Formation from the Photoexcitation of Benzene/O_2 Mixtures at 248 nm: An Energy Dependence Study. ChemPhysChem. 11, 3867-3873 (2010).
118. Fally, S., Carleer, M., Vandaele, A.C.: UV Fourier transform absorption cross sections of benzene, toluene, meta-, ortho-, and para-xylene. Journal of Quantitative Spectroscopy and Radiative Transfer. 110, 766-782 (juin).

119. Yokoyama, A., Zhao, X., Hintsa, E.J., Continetti, R.E., Lee, Y.T.: Molecular beam studies of the photodissociation of benzene at 193 and 248 nm. The Journal of Chemical Physics. 92, 4222 (1990).

120. Reilly, J.P., Kompa, K.L.: Laser induced multiphoton ionization mass spectrum of benzene. The Journal of Chemical Physics. 73, 5468 (1980).

121. Atkinson, D.B., Hudgens, J.W.: Rate Coefficients for the Propargyl Radical Self-Reaction and Oxygen Addition Reaction Measured Using Ultraviolet Cavity Ring-down Spectroscopy. The Journal of Physical Chemistry A. 103, 4242-4252 (1999).

122. Raoult, S., Rayez, M.-T., Rayez, J.-C., Lesclaux, R.: Gas phase oxidation of benzene: Kinetics, thermochemistry and mechanism of initial steps. Physical Chemistry Chemical Physics. 6, 2245 (2004).

123. Kanno, N., Tonokura, K., Tezaki, A., Koshi, M.: Nitrogen- and water-broadening coefficient measurements in the $\tilde{A}^2A'$ --> X^2A'' 000-000 band of HO_2 using high-resolution diode laser two-tone frequency modulation spectroscopy. Journal of Molecular Spectroscopy. 229, 193-197 (2005).

124. Trace gas detection with cavity ring down spectroscopy. Review of Scientific Instruments. 66, 2821-2828.

125. Scherer, J.J., Paul, J.B., O'Keefe, A., Saykally, R.J.: Cavity Ringdown Laser Absorption Spectroscopy: History, Development, and Application to Pulsed Molecular Beams. Chemical Reviews. 97, 25-52 (1997).

126. Fiddler, M.N., Begashaw, I., Mickens, M.A., Collingwood, M.S., Assefa, Z., Bililign, S.: Laser Spectroscopy for Atmospheric and Environmental Sensing. Sensors. 9, 10447-10512 (2009).

127. Corner, L., Barry, H.R., Hancock, G.: Comparison of cross-section measurements of the 2[nu]5 overtone band of formaldehyde determined by cavity ringdown and cavity enhanced spectroscopy. Chemical Physics Letters. 374, 28-32 (2003).

128. He, Y., Orr, B.J.: Ringdown and cavity-enhanced absorption spectroscopy using a continuous-wave tunable diode laser and a rapidly swept optical cavity. Chemical Physics Letters. 319, 131-137 (2000).

129. Volkamer, R., Sheehy, P., Molina, L.T., Molina, M.J.: Oxidative capacity of the Mexico City atmosphere – Part 1: A radical source perspective. Atmos. Chem. Phys. 10, 6969-6991 (2010).

130. Liao, W., Case, A.T., Mastromarino, J., Tan, D., Dibb, J.E.: Observations of HONO by laser-induced fluorescence at the South Pole during ANTCI 2003. Geophysical Research Letters. 33, (2006).

131. Hellebust, S., Roddis, T., Sodeau, J.R.: Potential Role of the Nitroacidium Ion on HONO Emissions from the Snowpack. The Journal of Physical Chemistry A. 111, 1167-1171 (2007).

132. Monge, M.E., D'Anna, B., George, C.: Nitrogen dioxide removal and nitrous acid formation on titanium oxide surfaces: an air quality remediation process? Physical Chemistry Chemical Physics. 12, 8991 (2010).

133. Langridge, J.M., Gustafsson, R.J., Griffiths, P.T., Cox, R.A., Lambert, R.M., Jones, R.L.: Solar driven nitrous acid formation on building material surfaces containing titanium dioxide: A concern for air quality in urban areas? Atmospheric Environment. 43, 5128-5131 (2009).

134. Rohrer, F., Bohn, B., Brauers, T., Brüning, D., Johnen, F.-J., Wahner, A., Kleffmann, J.: Characterisation of the photolytic HONO-source in the atmosphere simulation chamber SAPHIR. Atmos. Chem. Phys. 5, 2189-2201 (2005).

135. Djehiche, M., Tomas, A., Fittschen, C., Coddeville, P.: First Direct Detection of HONO in the Reaction of Methylnitrite (CH_3ONO) with OH Radicals. Environmental Science & Technology. 45, 608-614 (2011).

136. Perner, D., Platt, U.: Detection of nitrous acid in the atmosphere by differential optical absorption. Geophys. Res. Lett. 6, (1979).

137. Karlsson, R.S., LjungstrÖm, E.B.: Laboratory Study of ClNO: Hydrolysis. Environmental Science & Technology. 30, 2008-2013 (1996).

138. Yamano, D., Yabushita, A., Kawasaki, M., Perrin, A.: Absorption spectrum of nitrous acid for the $\nu_1+2\nu_3$ band studied with continuous-wave cavity ring-down spectroscopy and theoretical calculations. Journal of Quantitative Spectroscopy and Radiative Transfer. 111, 45-51 (2010).

139. Guilmot, J.M., Melen, F., Herman, M.: Rovibrational Parameters for cis-Nitrous Acid. Journal of Molecular Spectroscopy. 160, 401-410 (1993).

140. Guilmot, J.M., Godefroid, M., Herman, M.: Rovibrational Parameters for trans-Nitrous Acid. Journal of Molecular Spectroscopy. 160, 387-400 (1993).

141. Sironneau, V., Orphal, J., Demaison, J., Chelin, P.: High-Resolution Infrared Spectroscopy of trans- and cis-$H^{18}ON^{18}O$: Equilibrium Structures of the Nitrous Acid Isomers. The Journal of Physical Chemistry A. 112, 10697-10702 (2008).

142. Stockwell, W.R., Calvert, J.G.: The near ultraviolet absorption spectrum of gaseous HONO and N_2O_3. Journal of Photochemistry. 8, 193-203 (1978).

143. Febo, A., Perrino, C., Gherardi, M., Sparapani, R.: Evaluation of a High-Purity and High-Stability Continuous Generation System for Nitrous Acid. Environmental Science & Technology. 29, 2390-2395 (1995).

144. Stutz, J., Kim, E.S., Platt, U., Bruno, P., Perrino, C., Febo, A.: UV-visible absorption cross sections of nitrous acid. J. Geophys. Res. 105, 14585-14592 (2000).

145. Barney, W.S., Wingen, L.M., Lakin, M.J., Brauers, T., Stutz, J., Finlayson-Pitts, B.J.: Infrared Absorption Cross-Section Measurements for Nitrous Acid (HONO) at Room Temperature. The Journal of Physical Chemistry A. 104, 1692-1699 (2000).

146. Varma, R., Curl, R.F.: Study of the dinitrogen trioxide-water-nitrous acid equilibrium by intensity measurements in microwave spectroscopy. The Journal of Physical Chemistry. 80, 402-409 (1976).

147. Vaghjiani, G.L., Ravishankara, A.R.: Absorption Cross Sections of CH_3OOH H_2O_2, and D_2O_2 Vapors Between 210 and 365 nm at 297 K. J. Geophys. Res. 94, 3487-3492 (1989).

148. Forster, R., Frost, M., Fulle, D., Hamann, H.F., Hippler, H., Schlepegrell, A., Troe, J.: High pressure range of the addition of HO to HO, NO, NO_2, and CO. I. Saturated laser induced fluorescence measurements at 298 K. The Journal of Chemical Physics. 103, 2949 (1995).

149. Butkovskaya, N.I., Kukui, A., Pouvesle, N., Le Bras, G.: Formation of Nitric Acid in the Gas-Phase HO_2 + NO Reaction: Effects of Temperature and Water Vapor. The Journal of Physical Chemistry A. 109, 6509-6520 (2005).

150. Burkholder, J.B., Mellouki, A., Talukdar, R., Ravishankara, A.R.: Rate coefficients for the reaction of OH with HONO between 298 and 373 K. International Journal of Chemical Kinetics. 24, 711-725 (1992).

151. Macko, P., Romanini, D., Mikhailenko, S.N., Naumenko, O.V., Kassi, S., Jenouvrier, A., Tyuterev, V.G., Campargue, A.: High sensitivity CW-cavity ring down spectroscopy of water in the region of the 1.5 [mu]m atmospheric window. Journal of Molecular Spectroscopy. 227, 90-108 (2004).

152. Wojdyr, M.: *Fityk* : a general-purpose peak fitting program. Journal of Applied Crystallography. 43, 1126-1128 (2010).

153. Stone, D., Rowley, D.M.: Kinetics of the gas phase HO_2 self-reaction: Effects of temperature, pressure, water and methanol vapours. Physical Chemistry Chemical Physics. 7, 2156 (2005).

154. Johnson, T.J., Wienhold, F.G., Burrows, J.P., Harris, G.W., Burkhard, H.: Measurements of line strengths in the hydroperoxy .nu.1 overtone band at 1.5 .mu.m using an indium gallium arsenide phosphide laser. The Journal of Physical Chemistry. 95, 6499-6502 (1991).

155. Fink, E.H., Ramsay, D.A.: High-Resolution Study of the $\tilde{A}^2A'$ --> X^2A'' Transition of HO_2: Analysis of the 000-000 Band. Journal of Molecular Spectroscopy. 185, 304-324 (1997).

156. Kanno, N., Tonokura, K., Tezaki, A., Koshi, M.: Water Dependence of the HO2 Self Reaction: Kinetics of the HO_2−H_2O Complex. The Journal of Physical Chemistry A. 109, 3153-3158 (2005).

157. DeSain, J.D., Ho, A.D., Taatjes, C.A.: High-resolution diode laser absorption spectroscopy of the O-H stretch overtone band (2,0,0)<--(0,0,0) of the HO_2 radical. Journal of Molecular Spectroscopy. 219, 163-169 (2003).

158. Fink, E.H., Ramsay, D.A.: High-Resolution Study of the $\tilde{A}^2A'$ --> X^2A'' Transition of DO_2: Analysis of the 000-000 Band. Journal of Molecular Spectroscopy. 216, 322-334 (2002).

159. Rothman, L.S., Gordon, I.E., Barbe, A., Benner, D.C., Bernath, P.F., Birk, M., Boudon, V., Brown, L.R., Campargue, A., Champion, J.-P., Chance, K., Coudert, L.H., Dana, V., Devi, V.M., Fally, S., Flaud, J.-M., Gamache, R.R., Goldman, A., Jacquemart, D., Kleiner, I., Lacome, N., Lafferty, W.J., Mandin, J.-Y., Massie, S.T., Mikhailenko, S.N., Miller, C.E., Moazzen-Ahmadi, N., Naumenko, O.V., Nikitin, A.V., Orphal, J., Perevalov, V.I., Perrin, A., Predoi-Cross, A., Rinsland, C.P., Rotger, M., Simecková, M., Smith, M.A.H., Sung, K., Tashkun, S.A., Tennyson, J., Toth, R.A., Vandaele, A.C., Vander Auwera, J.: The HITRAN 2008 molecular

spectroscopic database. Journal of Quantitative Spectroscopy and Radiative Transfer. 110, 533-572 (juin).

160. Christensen, L.E., Okumura, M., Sander, S.P., Friedl, R.R., Miller, C.E., Sloan, J.J.: Measurements of the Rate Constant of HO_2 + NO_2 + N2 → HO_2NO_2 + N_2 Using Near-Infrared Wavelength-Modulation Spectroscopy and UV−Visible Absorption Spectroscopy. The Journal of Physical Chemistry A. 108, 80-91 (2004).

161. Martin, N.A., Thrush, B.A.: The disproportionation of DO_2 radicals studied by infrared laser spectroscopy. Chemical Physics Letters. 153, 200-202 (1988).

Appendix A- Full spectra

Full spectra of H_2O_2 and HONO in the near infra-red region (6623-6645 cm^{-1}) measured by the cw-CRDS technique are given in this section.

A.1 H_2O_2 spectrum

H_2O_2 spectrum has been measured using commercial H_2O_2 (Sigma Aldrich 50% by weight water) at 40 Torr helium pressure. This is a spectrum of mixture of H_2O_2 and water. Water absorption spectrum is also added for the comparison. Arrows show the H_2O_2 absorption lines calibrated in the present work.

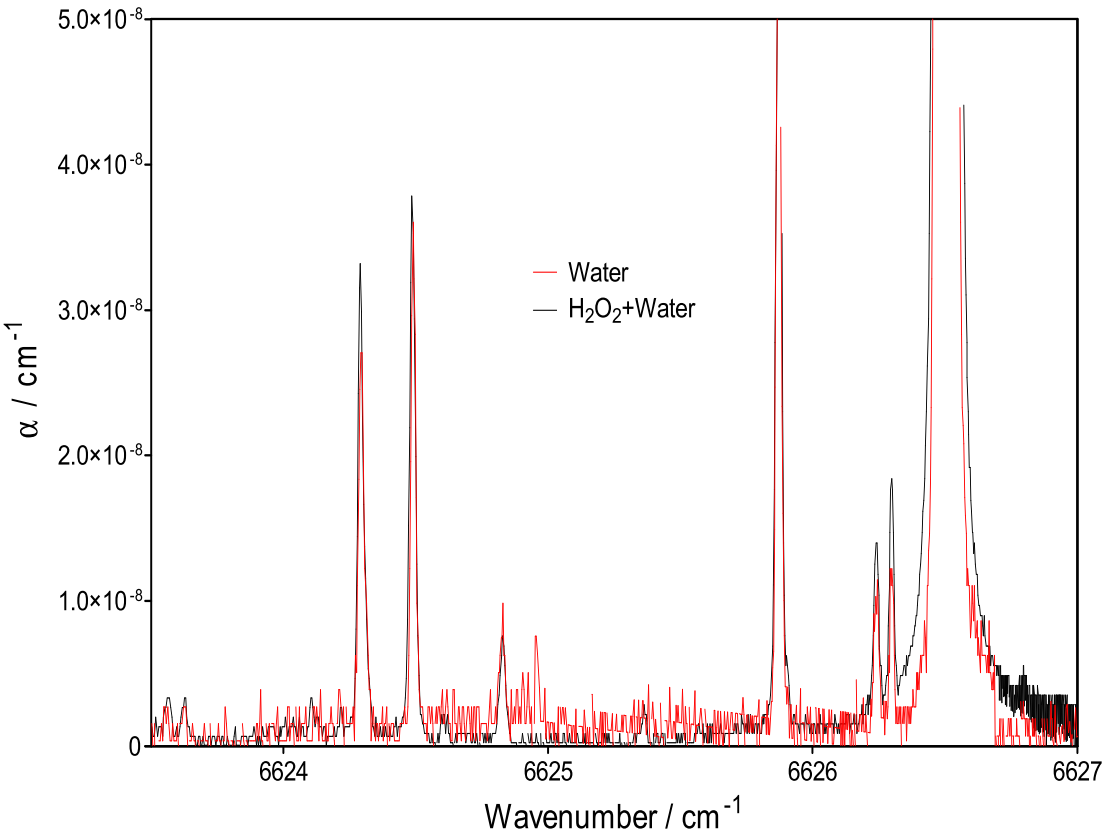

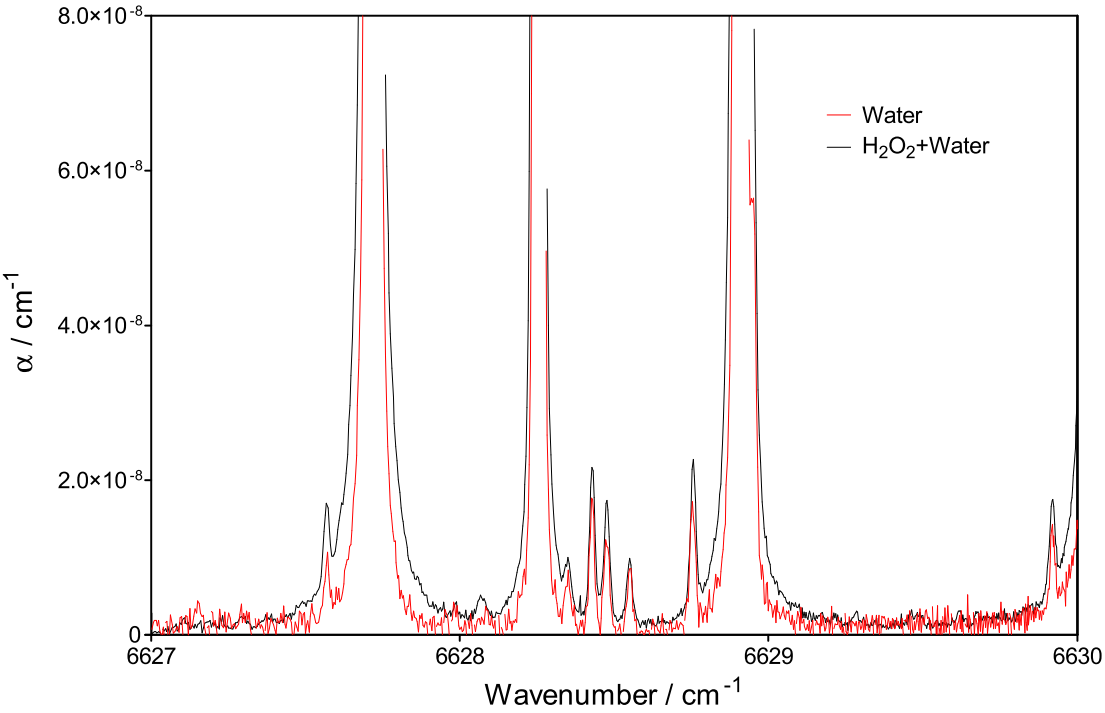

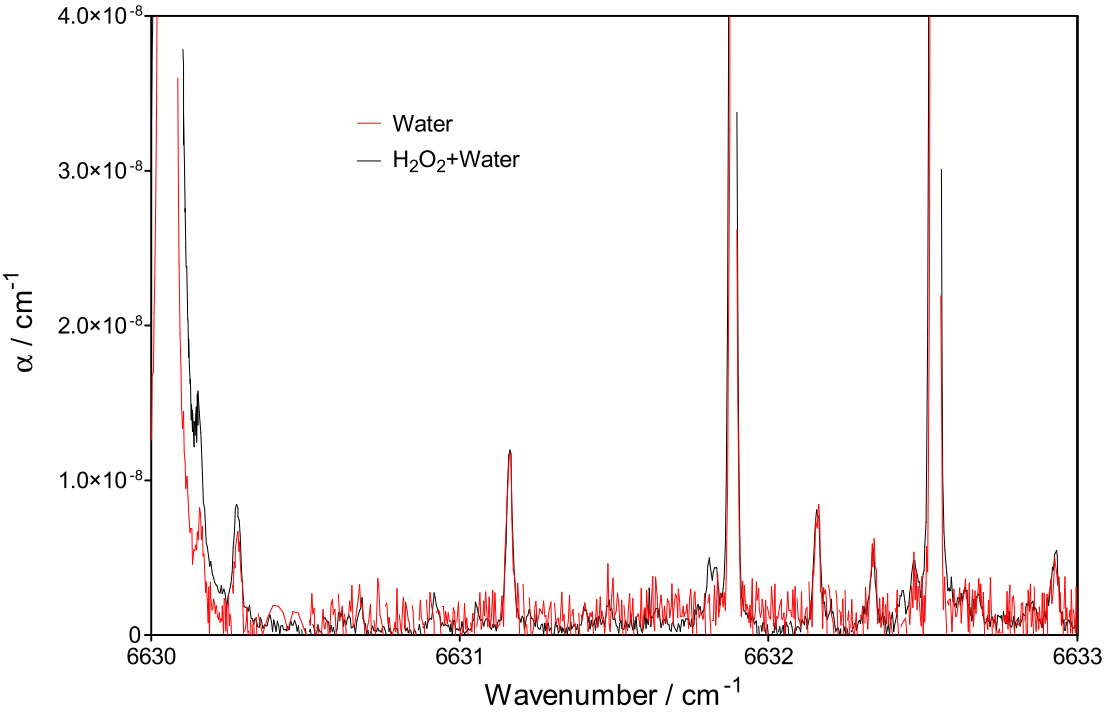

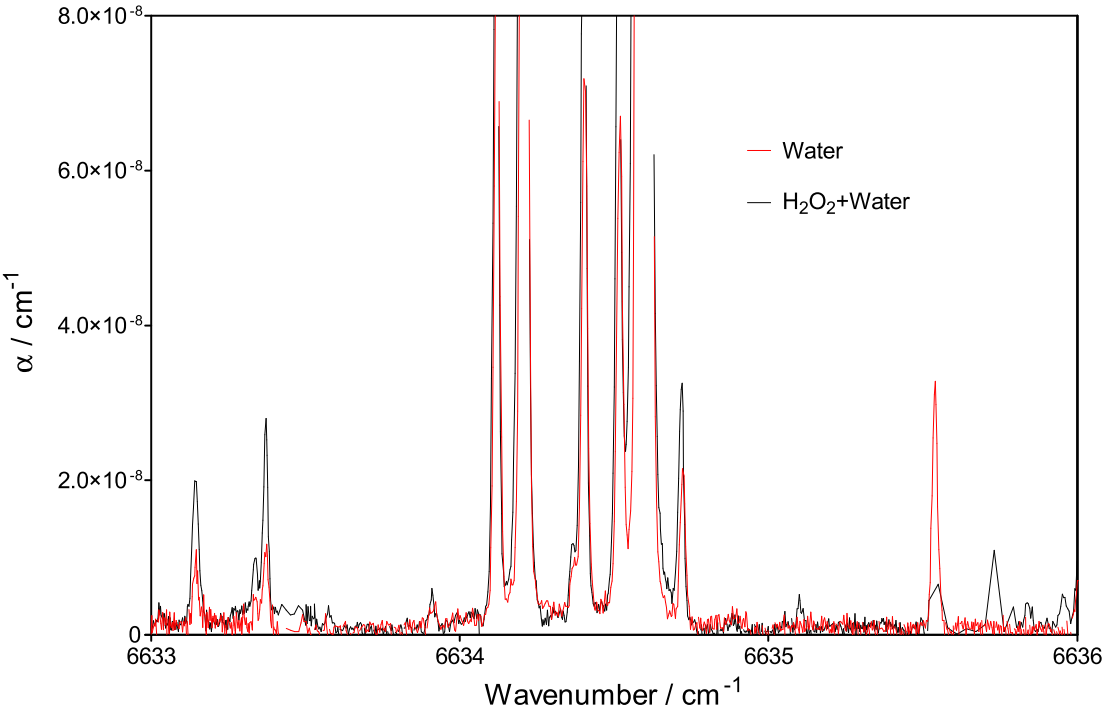

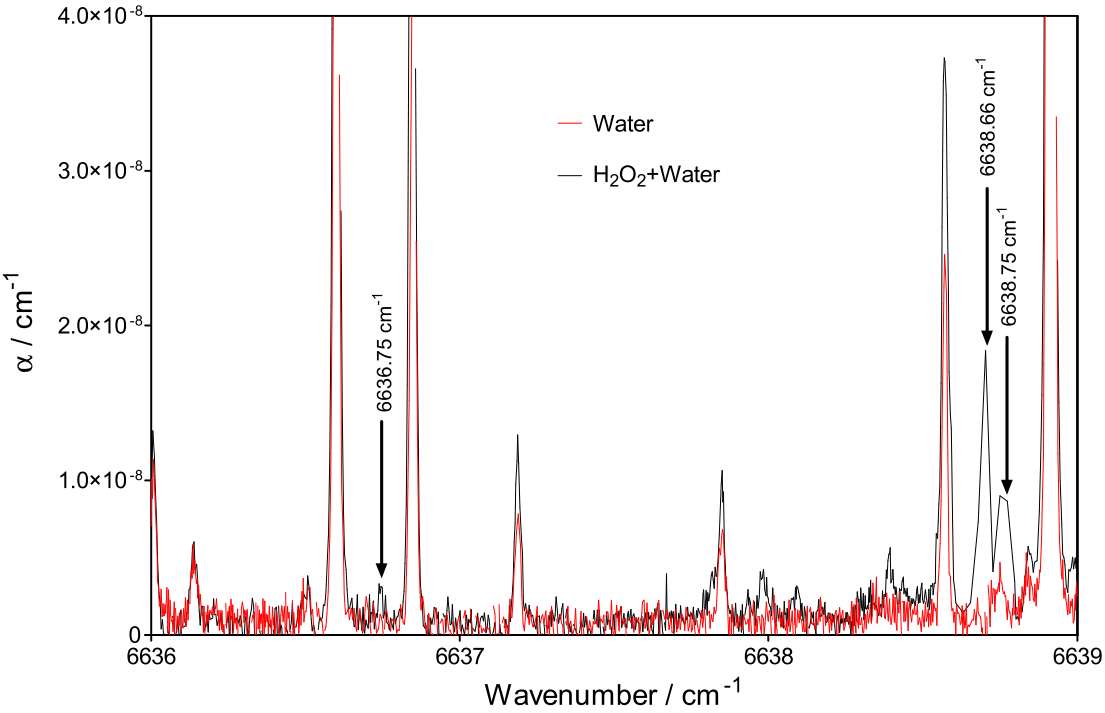

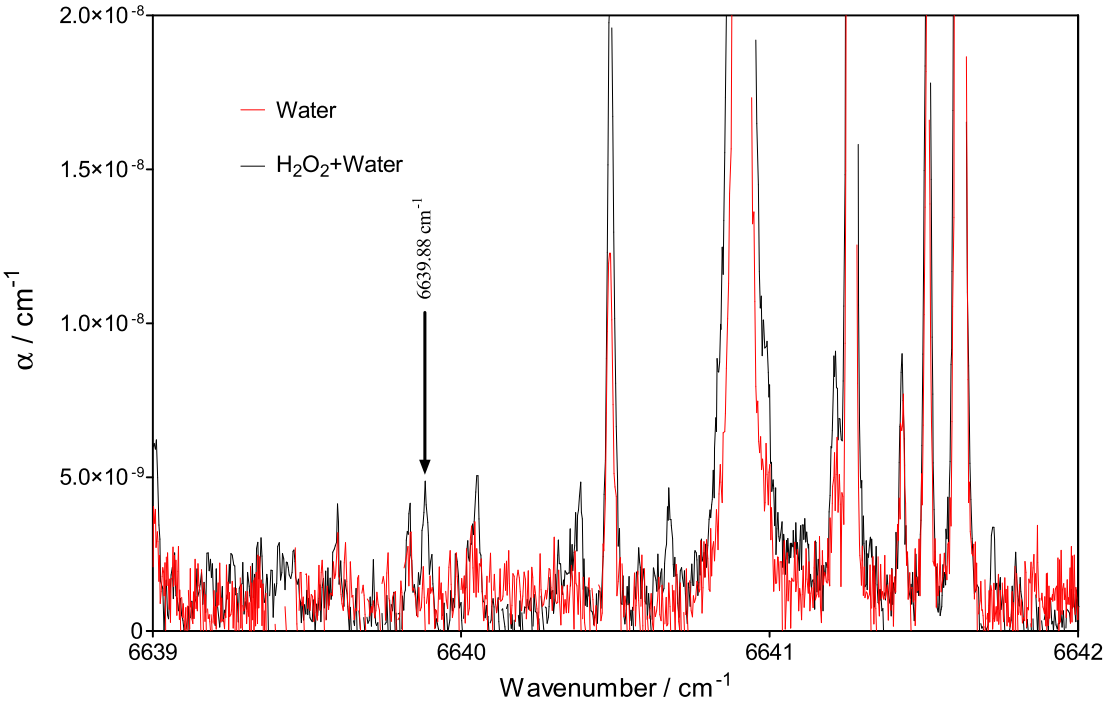

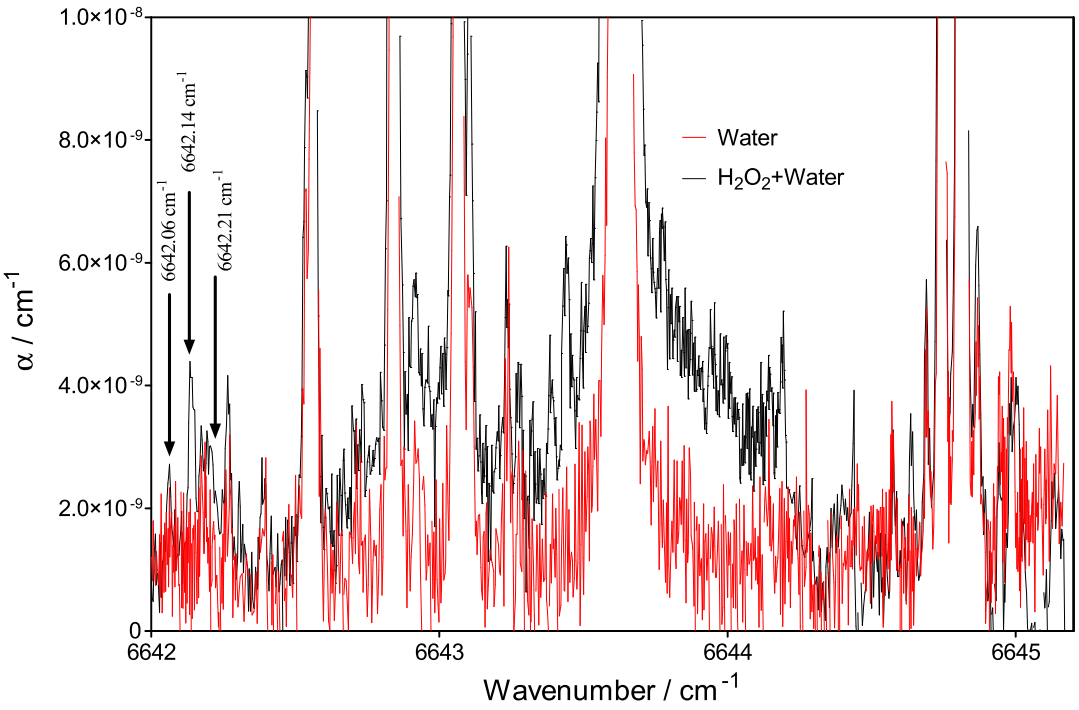

A.2 Six larger lines from the full spectrum of HONO in the range 6623-6645.5 cm-1

These are the selected lines which are measured again with the better resolution using pulsed photolysis method.

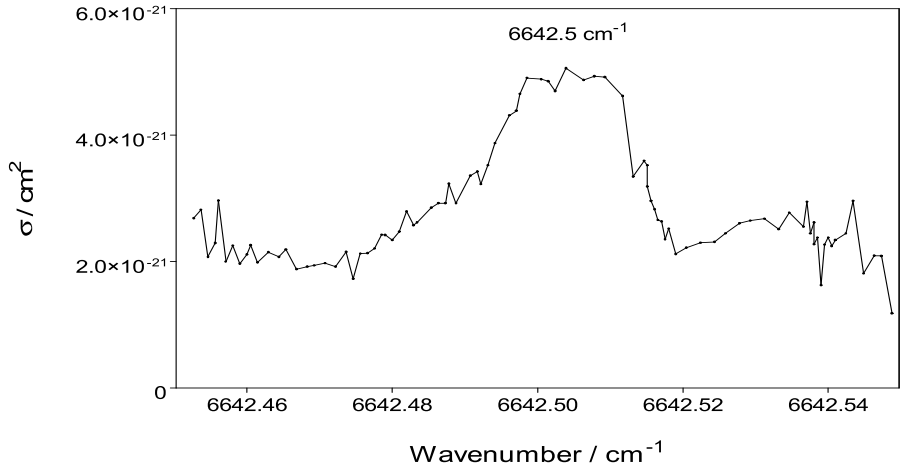

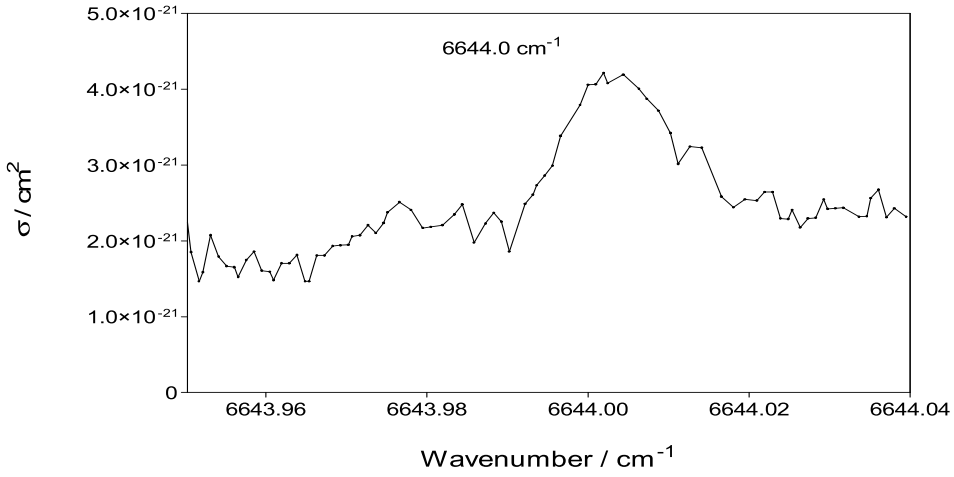

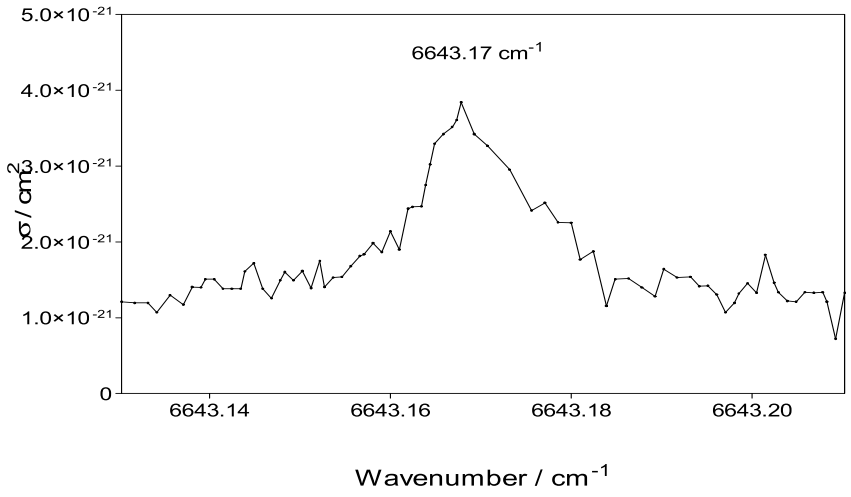

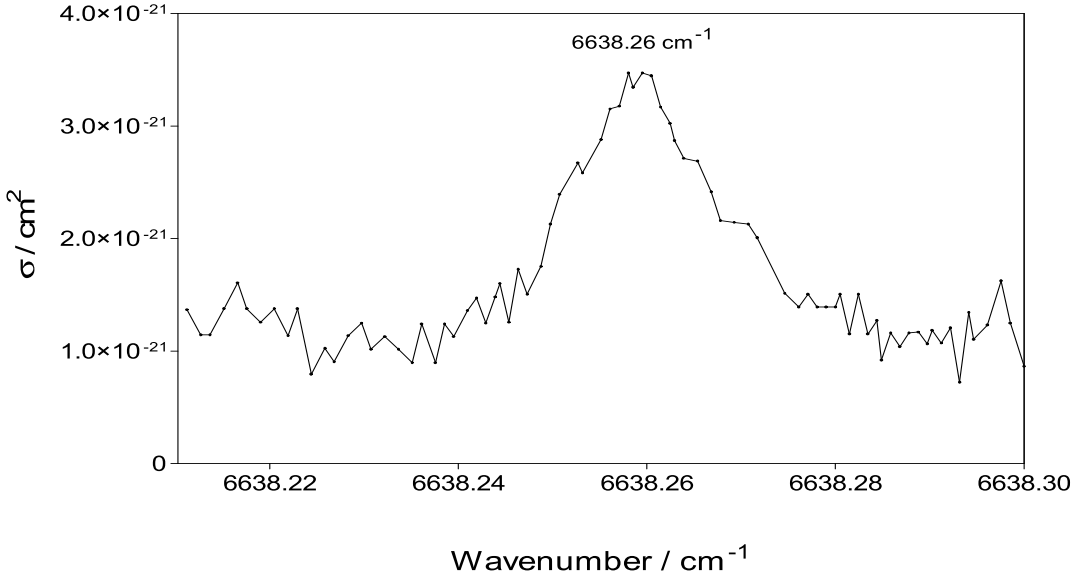

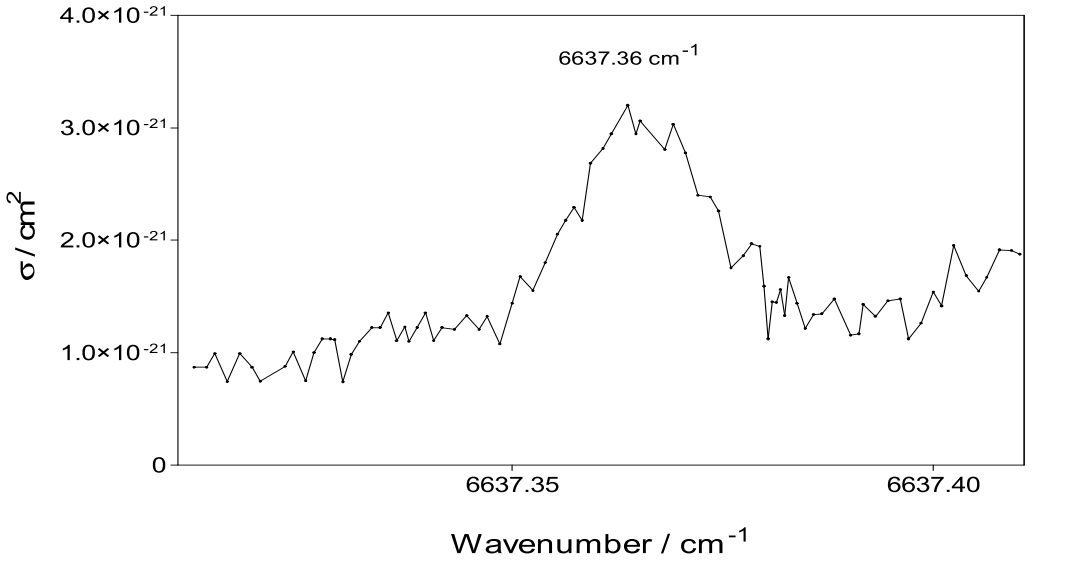

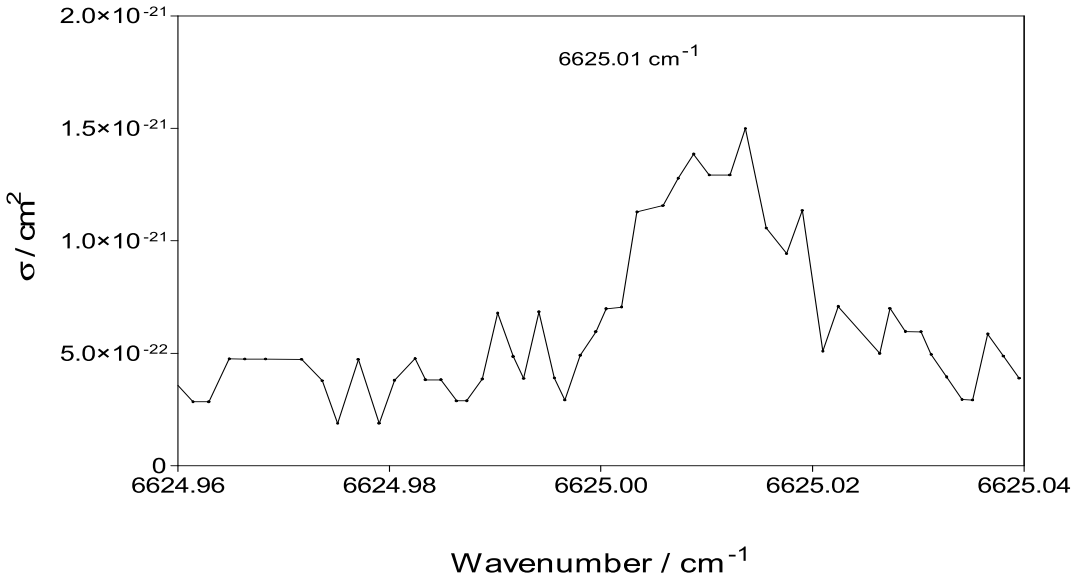

A.3 Full HONO spectrum

The full spectrum of HONO obtained by both methods: green line shows the spectrum obtained by laser photolysis method; black line shows the spectrum obtained by continuous HONO production stick spectrum shows H_2O spectrum obtained by Macko *et al.* [151].

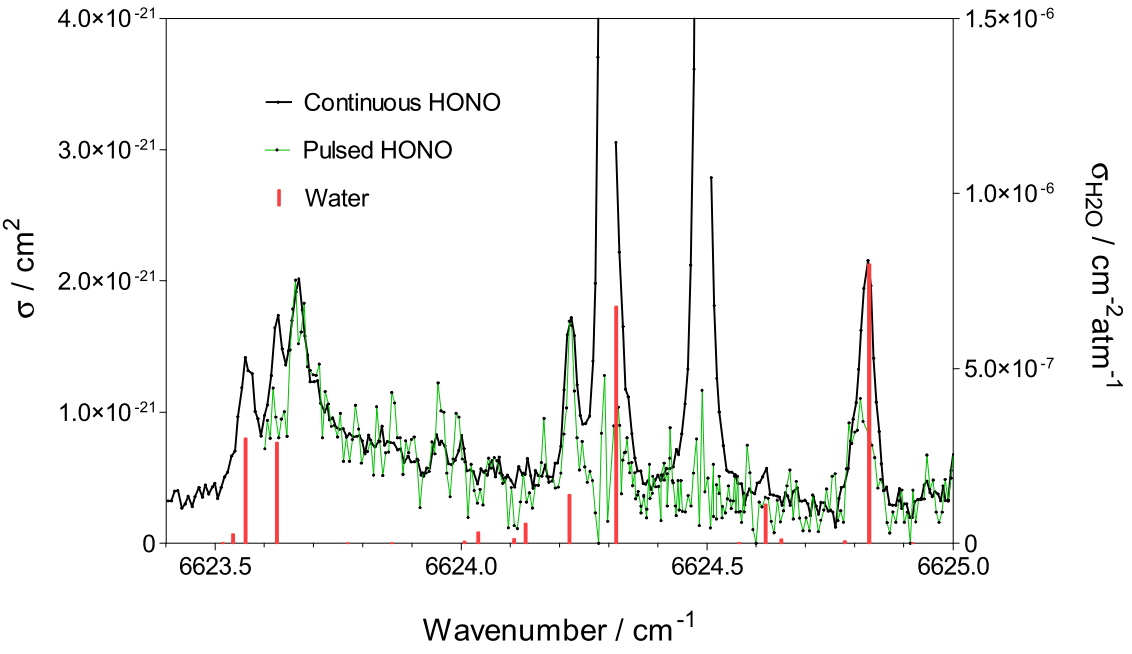

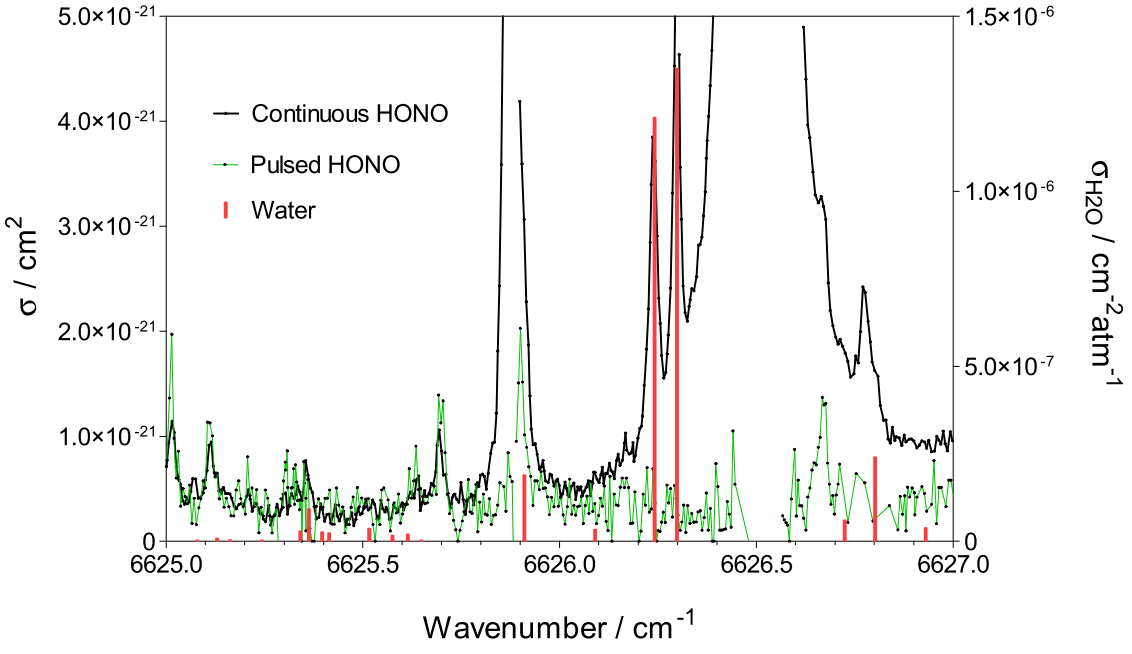

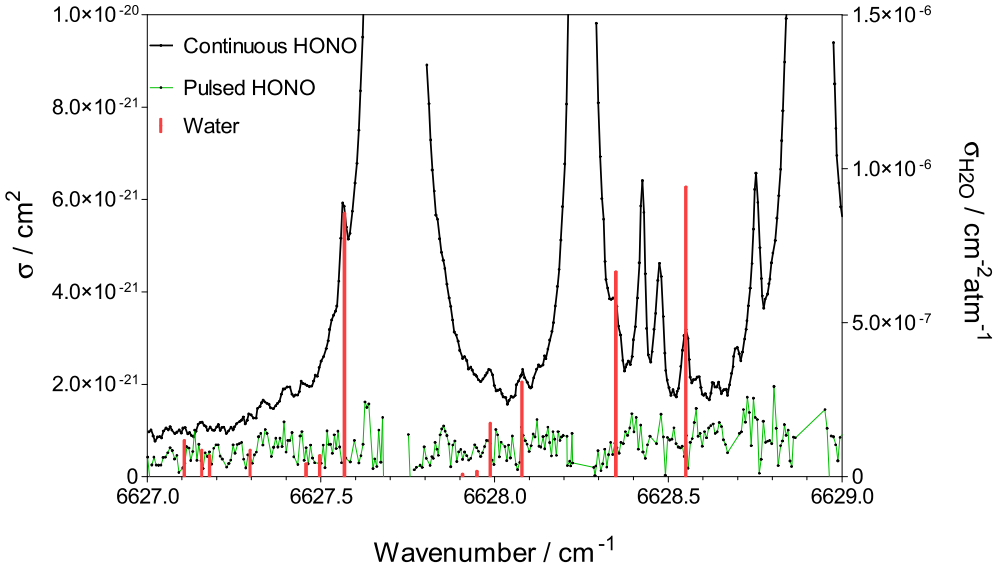

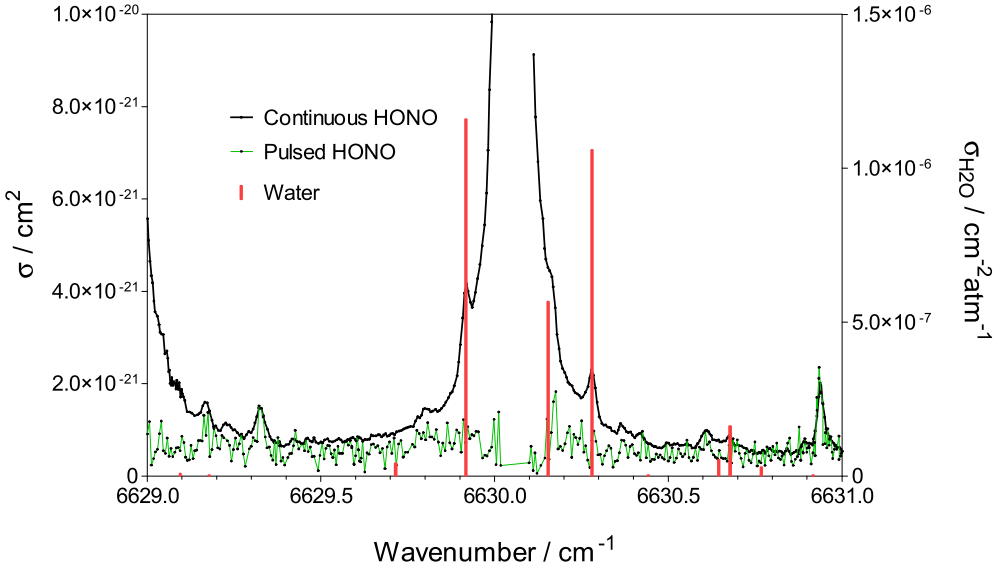

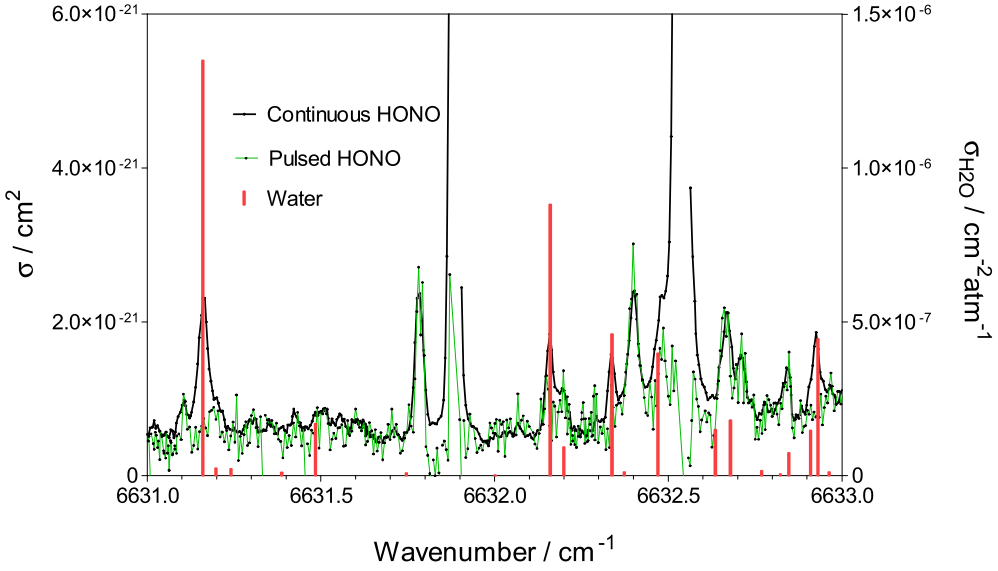

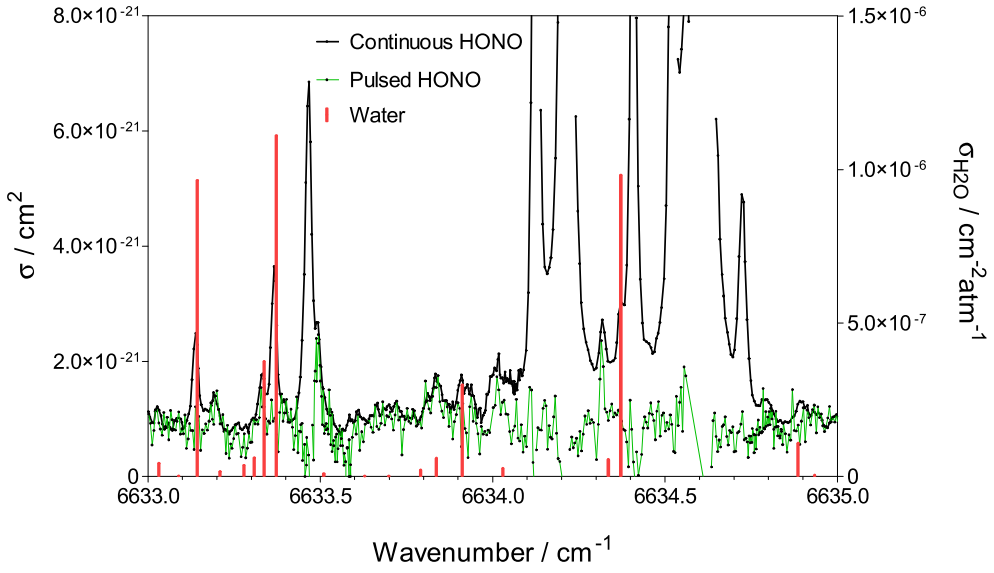

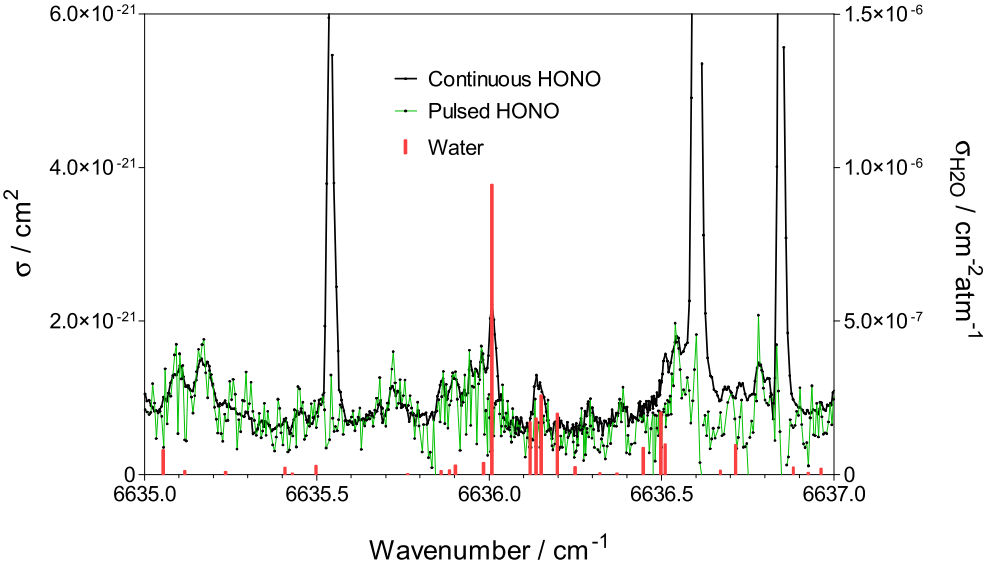

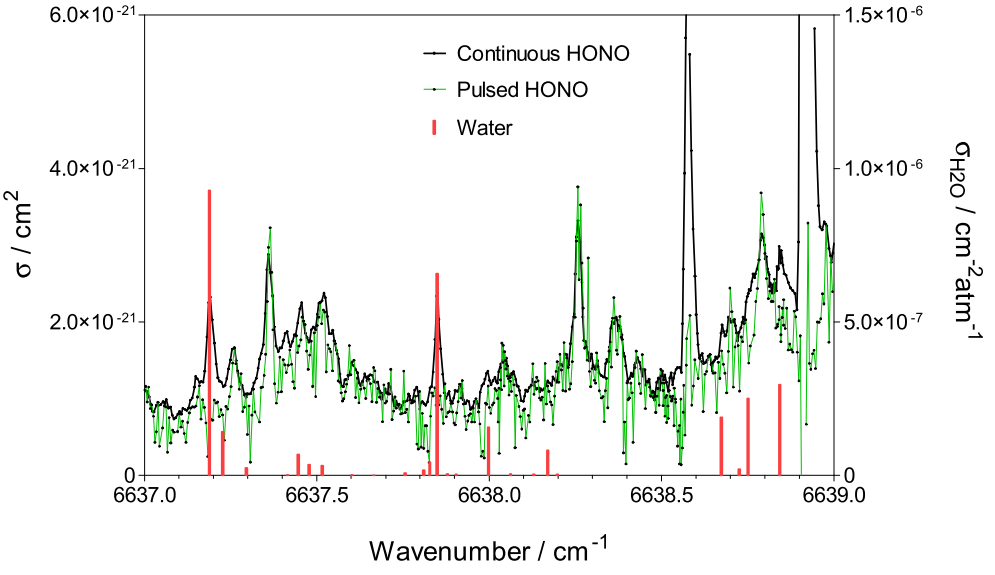

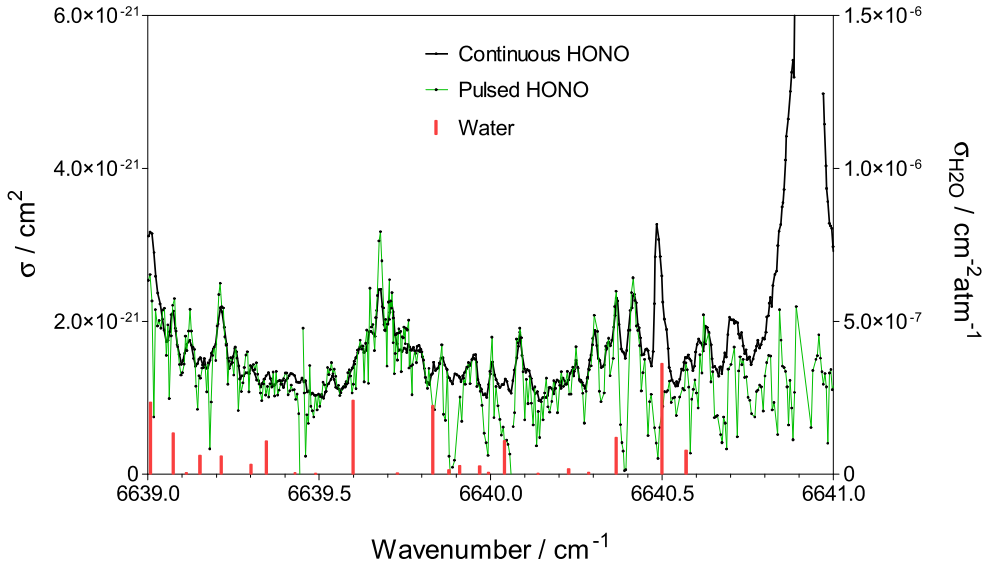

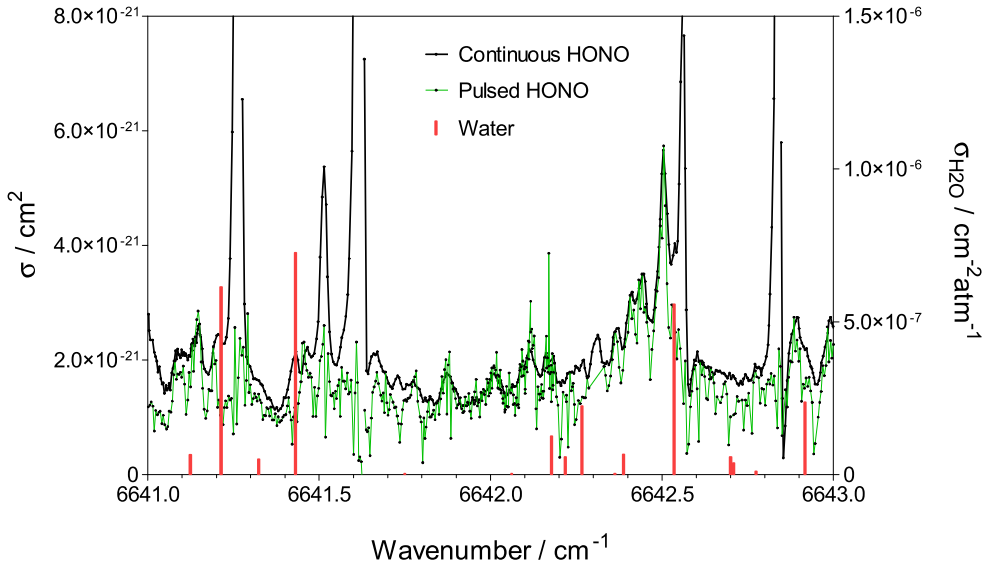

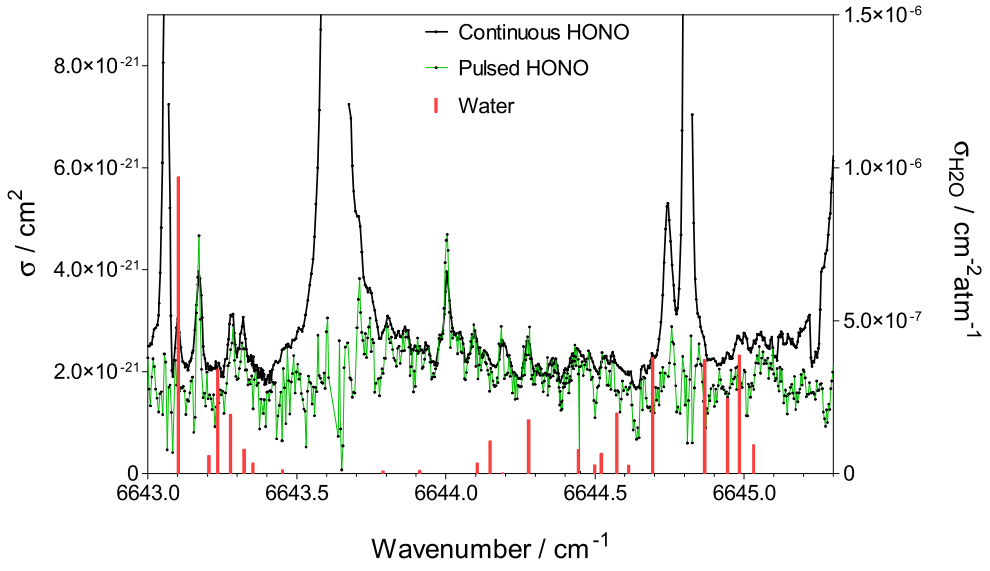

Appendix B- Academic Records

B.1 Publications

1. Parker, A.E., Jain, C., Schoemaecker, C., Fittschen, C.: Kinetics of the reaction of OH radicals with CH_3OH and CD_3OD studied by laser photolysis coupled to high repetition rate laser induced fluorescence. Reaction Kinetics and Catalysis Letters. 96, 291-297 (2009).
2. Parker, A.E., Jain, C., Schoemaecker, C., Szriftgiser, P., Votava, O., Fittschen, C.: Simultaneous, time-resolved measurements of OH and HO_2 radicals by coupling of high repetition rate LIF and cw-CRDS techniques to a laser photolysis reactor and its application to the photolysis of H_2O_2. Applied Physics B. 103, 725-733 (2010).
3. Jain, C., Parker, A.E., Schoemaecker, C., Fittschen, C.: HO_2 Formation from the Photoexcitation of Benzene/O_2 Mixtures at 248 nm: An Energy Dependence Study. ChemPhysChem. 11, 3867-3873 (2010).
4. Jain, C., Morajkar, P., Schoemaecker, C., Viskolcz, B., Fittschen, C.: Measurement of absolute absorption cross sections for HONO in the near infrared region by cw-CRDS technique coupled to laser photolysis: J. Phys. Chem. A. 115, 10720-10728 (2011).
5. Jain, C., Schoemaecker, C., Fittschen, C.: Yield of HO2 radicals in the OH-initiated oxidation of SO_2: accepted by Zeitschrift für Physikalische Chemie, doi: 10.1524/zpch.2011.0169 (2011).

B.2 Oral presentations

1. Journée des Doctorants, Douai, 16th March 2009 “Study of Atmospherically relevant reactions using LIF and CRDS techniques coupled to Photolysis laser”.
2. Journée des Doctorants, Lille, 10th January 2010 “Etude de la réactivité des radicaux OH et HO_2 dans des réactions d’intérêt atmosphérique par technique de photolyse laser, détection par cw-CRDS et FIL”.

3. Journée des doctorants IRePSE, Lille, 18th March 2011 "Experimental methods for better understanding of atmospheric Chemistry". Best oral presentation award.
4. Interface Chimie-Spectrsopie Atmospheriques, Lille, 31st May 2011 "Measurement of absolute absorption cross sections for HONO in the near IR by cw-CRDS technique coupled to laser photolysis".

B.3 Poster presentations

1. "TOTECAT: Aspects of homogeneous atmospheric chemistry" Monitoring Event for EST Contracts, Paris 5th February 2009.
2. "SO_2 oxidation under atmospheric conditions" at atmospheric spectroscopy summer school held at Jaca, Spain 29-June-2009 to 10-July-2009.
3. "SO_2 oxidation under atmospheric conditions" at Cavity Enhanced Absorption Spectroscopy winter school held at Leiden, The Netherlands, 2-6 November 2009.
4. "Direct formation of HO_2 radicals from the reaction of excited benzene with oxygen" at annual photochemistry meeting, Wimereux, 9 and 10 June 2010.
5. "Direct formation of HO_2 radicals from the reaction of excited benzene with oxygen" at 21st International symposium on Gas Kinetics, Leuven, Belgium, 18-23 July-2010. Best poster prize sponsored by Royal Society of Chemistry.
6. "Direct formation of HO_2 radicals from the reaction of excited benzene with oxygen" at Journée IRENI, Douai, 8the July 2011.

B.4 Conferences and meetings attended

1. Monitoring Event for MEST Contracts, Paris 5th February 2009.
2. Journée des Doctarants, Douai 16th March 2009.
3. Conférence annuelle de Cinétique et de Photochimie, Créteil, 17 and 18-June 2009.
4. Summer school "Spectroscopy of the Atmosphere", Jaca (Spain) 29-June-2009 to 10-July-2009.
5. Cavity Enhanced Absorption Spectroscopy winter school, Leiden, The Netherlands, 2-6 November 2009.
6. Journée des Doctarants, Lille, 22nd January 2010

7. Conférence annuelle de Cinétique et de Photochimie, Wimereux, 9 and 10 June-2010.
8. 21st International symposium on Gas Kinetics, Leuven, Belgium, 18-23 July 2010.
9. Journée des doctorants IRePSE, Lille, 18th March 2011.
10. Journée des Doctarants, Douai 8th May 2011.
11. Journée IRENI, Douai, 8th July 2011.
12. Réunions du Groupe de Cinétique et Photochimie en Phase Gazeuse, (GFCP) et Interface Chimie-Spectroscopie Atmosphériques (ICSA), Lille, 30 and 31st May 2011.

N° d'ordre : 40628

Laser photolysis coupled to detection by LIF and cw-CRDS: Application to spectroscopic and kinetic studies of OH, HO_2 and HONO

OH and HO_2 radicals play a vital role in many oxidation processes in the atmosphere. The degradation of volatile organic compounds under tropospheric conditions is generally induced by the reaction with hydroxyl radicals, followed by reaction with oxygen. This thesis involved the study of the mechanisms and reaction pathways of some of these reactions using an experimental system of laser photolysis coupled to Laser Induced Fluorescence (LIF, for OH) and continuous wave Cavity Ring-Down Spectroscopy (cw-CRDS, for HO_2) detection techniques. The coupling of these detection techniques allowed studying the simultaneous, time resolved kinetics of OH and HO_2 radicals and spectroscopic measurements for different species by the cw-CRDS technique.

Different chemical systems studied using the above experimental technique include: 1) kinetics of the reaction of OH radicals with CH_3OH and CD_3OD, 2) HO_2 yield in the OH-initiated oxidation of SO_2, 3) an energy dependence study on the direct formation of HO_2 radicals from the photoexcitation (at 248 nm) of various aromatic hydrocarbons (benzene, toluene, xylene or mesitylene) in the presence of oxygen. In addition the spectroscopic application of the cw-CRDS technique has been used to measure the absorption cross-sections of selected absorption lines of H_2O_2, HONO, HO_2 and DO_2 in the near infrared region.

Keywords: Atmospheric chemistry – Radicals – Hydroxyl – Laser Induced Fluorescence – Flash Photolysis – Hydroperoxyl – CRD spectroscopy

Photolyse laser couplée à la détection par LIF et cw-CRDS : Application pour l'etude spectrscopique et cinetique de OH, HO_2 et HONO

Les radicaux OH et HO_2 jouent un rôle essentiel dans beaucoup de processus d'oxydation dans l'atmosphère. La dégradation d'espèces chimiques dans les conditions troposphériques est généralement initiée par la réaction avec les radicaux OH, suivie par la réaction avec l'oxygène. Dans le cadre de cette thèse, deux techniques optiques de détection d'OH et HO_2 ont été appliquée à des études cinétiques et spectroscopiques. Pour cela, nous utilisons un système expérimental de photolyse laser couplée à des techniques de détection par continuous wave Cavity Ring-Down Spectroscopy (cw-CRDS, pour HO_2) et Fluorescence Induite par Laser (FIL, pour OH). Ce couplage permet de mesurer les cinétiques des radicaux OH et HO_2 simultanément, résolues dans le temps pour l'étude des mécanismes réactionnels.

Différents systèmes chimiques ont été étudiés en utilisant ce dispositif expérimental: 1) les cinétiques de la réaction d'OH avec CH_3OH et CD_3OD, 2) le rendement de HO_2 dans l'oxydation de SO_2 initiée par OH et 3) la formation des radicaux HO_2 par photoexcitation (à 248 nm) de différents hydrocarbures aromatiques (benzène, toluène, xylene ou mésitylène) en présence d'oxygène. Des applications spectroscopiques de la cw-CRDS pour mesurer les sections efficaces de H_2O_2, HONO, HO_2 et DO_2 dans le proche Infrarouge ont également été réalisées.

Mots-clefs : Chimie de l'atmosphère - Radicaux (Chimie) – Hydroxyle - Fluorescence Induite par Laser - Photolyse éclaire- Hydropéroxyle - Spectroscopie CRDS